

EPATAN project

Final Report

Julien Delanoë¹⁾, Silke Groß²⁾, Florian Ewald²⁾, Quitterie Cazenave^{1), 2)}, Jacques Pelon¹⁾, Eleni Marinou²⁾, Abdenour Irbah¹⁾

¹⁾ Laboratoire Atmosphères, Milieux, Observations Spatiales (LATMOS), 11 Boulevard d'Alembert 78280 Guyancourt, France

²⁾ Deutsches Zentrum für Luft- und Raumfahrt, Institut für Physik der Atmosphäre, Münchner Str. 20, 82234 Oberpfaffenhofen, Germany

ESA Contract No. 4000119015/NL/CT/gp
Earthcare Pre-Launch Campaigns Activity:
EarthCARE Preparation campaign (EPATAN)



Content

ACRONYMS & ABBREVIATIONS.....	4
1. INTRODUCTION / OVERVIEW	5
2. EPATAN PROJECT AND DATA	7
2.1 EPATAN.....	7
2.2 LATMOS instruments	11
2.3 DLR instruments deployment.....	20
2.3.1 HALO aircraft	20
2.3.2 Cloud Radar	21
2.3.3 WALES Lidar	21
2.3.4 SpecMACS.....	23
2.4 Auxiliary data	24
2.5 EPATAN data.....	25
3. DATA PROCESSING AND STRUCTURE	25
4. DATA ANALYSIS.....	25
4.1 Cloud characterization	25
4.1.1 Statistics of cloud classification (HALO study during NAWDEX).....	25
4.1.2 Statistics of cloud dynamic and microphysics from W-band radar (F-Falcon study during EPATAN).....	32
4.2 Analysis of multi-wavelengths radar-lidar measurements	35
4.2.1 Comparison of Level 1 measurements between HALO and FF20	35
4.2.2 Comparison of Level-2 retrieval (VarCloud) results of ice cloud microphysics	36
4.3 CC – underpasses and comparisons	38
4.3.1 Underpass #1 : 2016/10/02 (F7-French Falcon)	39
4.3.2 Underpass #2 : 2016/10/05 (F9-French Falcon)	42
4.3.3 Underpass #3 : 2016/10/14 (F18-French Falcon)	46
4.3.4 Conclusions and remarks regarding the satellite underpasses	50
4.4 EarthCARE resolution.....	50
4.5 Closure study – comparing retrieval results and passive measurements	53
4.5.1 Method	53
4.5.2 Homogeneous cloud structure	54
4.5.3 Inhomogeneous cloud structure with high updrafts	57

5	SUMMARY AND CONCLUSION	60
	Acknowledgement	61
	References	62
	Annex 1: DATA ACQUISITION REPORT (DAR)	62

ACRONYMS & ABBREVIATIONS

ADM	Atmospheric dynamic mission
BASTA	Bistatic rAdar SysTem for Atmospheric studies
CALIPSO	Cloud-Aerosol Lidar and Infrared Pathfinder Satellite Observations
CC	CloudSat-CALIPSO
CLIMAT	Conveyable Low-Noise Infrared Radiometer for Measurements of Atmosphere and Ground Surface Targets
DARDAR	raDAR liDAR
EarthCare	Earth Clouds, Aerosol and Radiation Explorer
EC	EarthCare
ECSIM	EarthCare Simulator
EPATAN	Earthcare PrepAraTion cAmpaign
EUFAR	EUropean Facility for Airborne Research
HAMP	HALO microwave package
LIDAR	Light Detection And Ranging
NAWDEX	North Atlantic Waveguide and Downstream Impact Experiment
NEAREX	Norwegian Mesoscale Ensemble and Atmospheric River Experiment
RALI	RAdar LIdar
HALO	High Altitude and LOng
RADAR	RAdio Detection And Ranging
RASTA	Radar Airborne System Tool for Atmosphere
WALES	Water vapor lidar experiment in space

1. INTRODUCTION / OVERVIEW

This document describes the work performed in the frame of the EarthCARE preparation campaign (EPATAN). It covers the tasks in response to the Statement of Work (SoW) from ESA (EOP-SM/2985/DS-s of 17 August 2016). The description of the data and the algorithms used in this activity are described in the DAR (Data Acquisition Report) which is given in annex I.

The main scientific objectives of EPATAN 2016 (**E**arthcare **P**rep**A**ra**T**ion **c**ampaig**N**) are derived from the scientific objectives of EarthCARE. The EarthCARE mission will advance our understanding of the role that clouds and aerosols play in reflecting incident solar radiation back into space and trapping infrared radiation emitted from Earth's surface by providing vertical cloud and aerosol profile information in connection with collocated broadband solar and thermal radiance measurements (Illingworth et al. 2015).

In the context of general ESA campaign objectives, EPATAN 2016 campaign addresses directly the programmatic needs of EarthCARE Mission Development, particularly relating to the development and refinement of Geophysical Product Algorithms.

The main objectives of EPATAN 2016 project are as follows:

- In collaboration with appropriate International Scientists and Agencies, design, plan and conduct a field campaign extension to the existing NAWDEX 2016 experiment dedicated to the preparation of EarthCare launch.
- Contribute to a better understanding of EarthCARE measurements and perform testing of L2 algorithms.
- Provide EarthCARE like measurements (W-band and 355 nm HSRL), with a spatial coverage scales and product resolution similar to that of the EarthCARE mission.
- Provide the most possible independent measurements from EarthCARE and then compare the retrievals using only the measurements on board EarthCARE.
- Perform dedicated CloudSat-CALIPSO overpass flights that will be utilized as reference.
- Perform a first rehearsal of the validation/calibration strategy ensuring readiness of the cal/val setup after launch
- Provide collocated observations from the different lidar systems of aerosol under varying aerosol conditions (load and type). Note that unfortunately the Icelandic conditions were not favourable for aerosols studies. As a consequence, this has not been addressed in the report.

Airborne platforms are ideal to complete the ground-based systems allowing direct satellite underpasses. German and French aircraft, respectively HALO and French Falcon 20 have very complementary payloads (see section 3) and are perfectly designed for the preparation, the calibration and the validation of EarthCare (EC hereafter). Both aircraft board a high spectral resolution lidar (355 nm on the French Falcon and 532 nm on the HALO), a Doppler radar at 36 GHz (HALO) and 95 GHz (Falcon) and in-situ measurements. At European level they are the most complete possible setup to mimic and to complete EarthCare payload. Furthermore, the associated scientific teams have a very large experience in algorithm development, especially synergistic radar-lidar retrieval for cloud and aerosol retrieval. Note that any cloud studies using airborne radar-lidar-radiometer synergy is relevant for EC preparation, as we want as many various cases as possible for training algorithms and to improve our understanding of

W-band Doppler cloud radar and High spectral resolution at 355 nm measurements. The EC preparation field campaign is expected to provide EC like measurements (i.e. W band and 355 nm HSR), which will contribute to better understand the unprecedented nature of EC measurements and will bring material for testing L2 algorithms. Prior to this project there were almost no dedicated observations that can be provided to the L2 algorithm development teams. This unique combination provides the community with an EC like data set supported by extra radar-lidar-radiometry measurements airborne systems. The strategy is to provide the most possible independent measurements from EC and then compare the retrievals using only the measurements on board EC. In addition to that we need to have dedicated CloudSat-CALIPSO (CC hereafter) overpass flights are our reference. Note that currently, many future EC algorithms are running on CC data.

The EPATAN 2016 activity benefited from the international NAWDEX campaign framework. NAWDEX stands for North Atlantic Waveguide and Downstream Impact experiment; it aims at increasing our knowledge of the effects of diabatic processes (mainly moist and radiative processes) on atmospheric disturbances along the North Atlantic jet stream (also called North Atlantic waveguide). These diabatic processes, such as those involved in cloud microphysics, are not well represented in current meteorological forecast models. This misrepresentation often leads to forecast error growth, which may have dramatic consequences in the case of high-impact weather events over Europe. The field campaign, held in fall 2016 (19 September to 16 October 2016), included state-of-the-art airborne measurements and ground-based measurements to provide a unique observational dataset, sampling the key dynamics and processes associated with the triggering, propagation and downstream impact of disturbances along the North Atlantic waveguide. It is used to test and validate parameterization schemes within numerical weather prediction models with the general objective to improve the accuracy of one-day to two-week high impact weather forecasts. The observational payload is therefore mostly dedicated to cloud, precipitation, wind, and humidity characterization. More details of the NAWDEX project can be found here: <http://nawdex.org>.

To achieve these above-mentioned objectives the following work has been performed:

- The team designed, planned and conducted a field campaign extension to the existing NAWDEX 2016 experiment.
- The French F20 carried out 15 flights (about 46 flight hours), radar-lidar data have been collected during these flights, including joint flights with HALO, German F20 and FAAM aircraft.
- The measurements have been calibrated and processed in order to provide target classification, wind retrieval (RASTA radar only) and ice cloud properties. The processing details, including calibration processes, have been reported in the Data Acquisition Report (DAR).
- Within these French F20 flights 3 CloudSat-CALIPSO underpasses (2nd, 5th and 14th of October) have been carried out. The collected data have been compared against CloudSat-CALIPSO measurements and synergistic products (DARDAR).
- We carried out an analysis of the cloud properties retrieved using HALO measurements during NAWDEX campaign. This work includes the target classification statistical analysis (cloud phase study for instance).

- An analysis of the ice cloud and dynamical properties of the cloud sampled by the French F20 during NAWDEX experiment.
- An analysis of the multiwavelength radar-lidar measurements. With a focus on level 1 data from the HALO and the French F20 and level 2 ice clouds microphysics retrievals (Varcoud).
- A simulation of the EarthCare's measurements using HALO data at EarthCare's resolution.
- A closure analysis using passive measurements on board HALO aircraft.

2. EPATAN PROJECT AND DATA

2.1 EPATAN

The previous objectives were achieved through the collection and analyses of airborne Lidar and Radar data sets at different frequencies together with correlative ground-based and satellite-based data acquired during NAWDEX 2016 campaign. Airborne measurements were collected from the French and German Falcon 20, HALO and FAAM (with ISMAR). Characteristics of the payloads of the French and German aircraft are given in section 3.

In order to achieve the above-mentioned objectives 15 flights (F5 to F18 can be used for scientific purposes, F3 and F19 are dedicated to calibration and tests and not distributed) with a total of 46.5 scientific flights hours (excluding transfer flight hours) were performed with the French Falcon during the NAWDEX 2016 campaign (Figure 1). Note that national or EUFAR funding completed ESA support for that campaign.

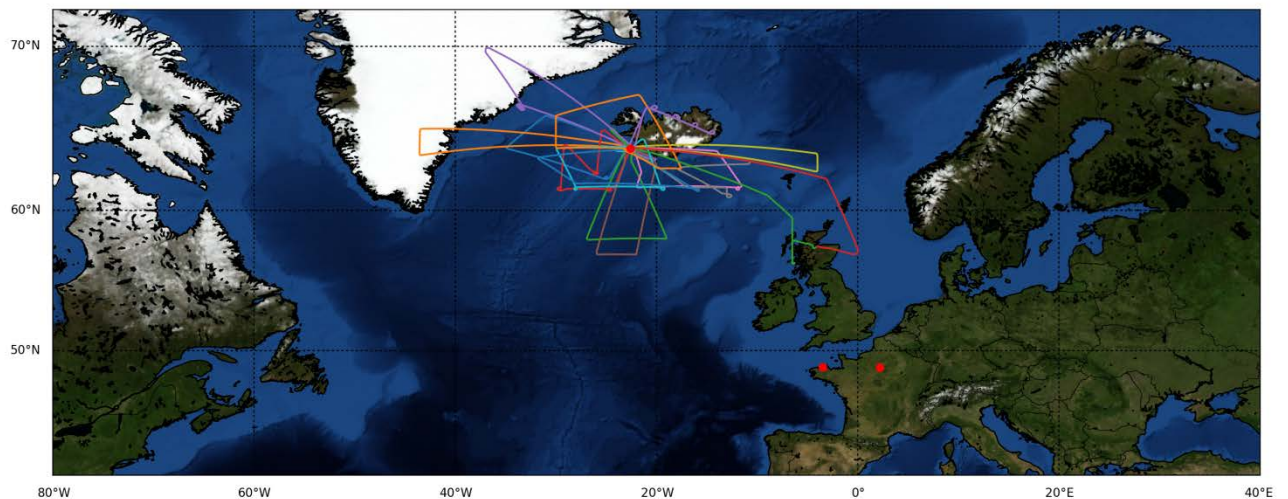


Figure 1 French F20 flight tracks during NAWDEX

The list of the flights with a short description is given in Table 1

EPATAN in a few words:

- From 28th of September to 17th of October 2016

- Number of scientific flights: 15 (Figure 1)
- Number of scientific flight hours: 46.5
- Number of released dropsondes: 59
- Number of CloudSat-CALIPSO underpasses: 3
- Number of co-located flights: 5

During the campaign four common flight legs were performed together with the German HALO research aircraft (Figure 2) with similar payload as the French F20 (see Section 2.3). These flights are crucial to investigate the effects of different wavelengths on measured atmospheric parameters and on retrieval results. In addition to the combination of French F20 and HALO the first common flight track of the research flight on 14 October 2017 was planned as coordinated flight of French F20, HALO and the British FAAM, the last performing in-situ sampling of cloud properties below the two other aircraft. These additional measurements help to evaluate radar-lidar retrieval results. The second common flight track of the research flight on 14 October 2017 was planned as A-Train underpass to learn and develop strategies for future EarthCARE cal/val activities. The motivation and aims of these joint flights are highlighted in the NAWDEX overview paper (Schäfler et al., 2018 accepted for BAMS).

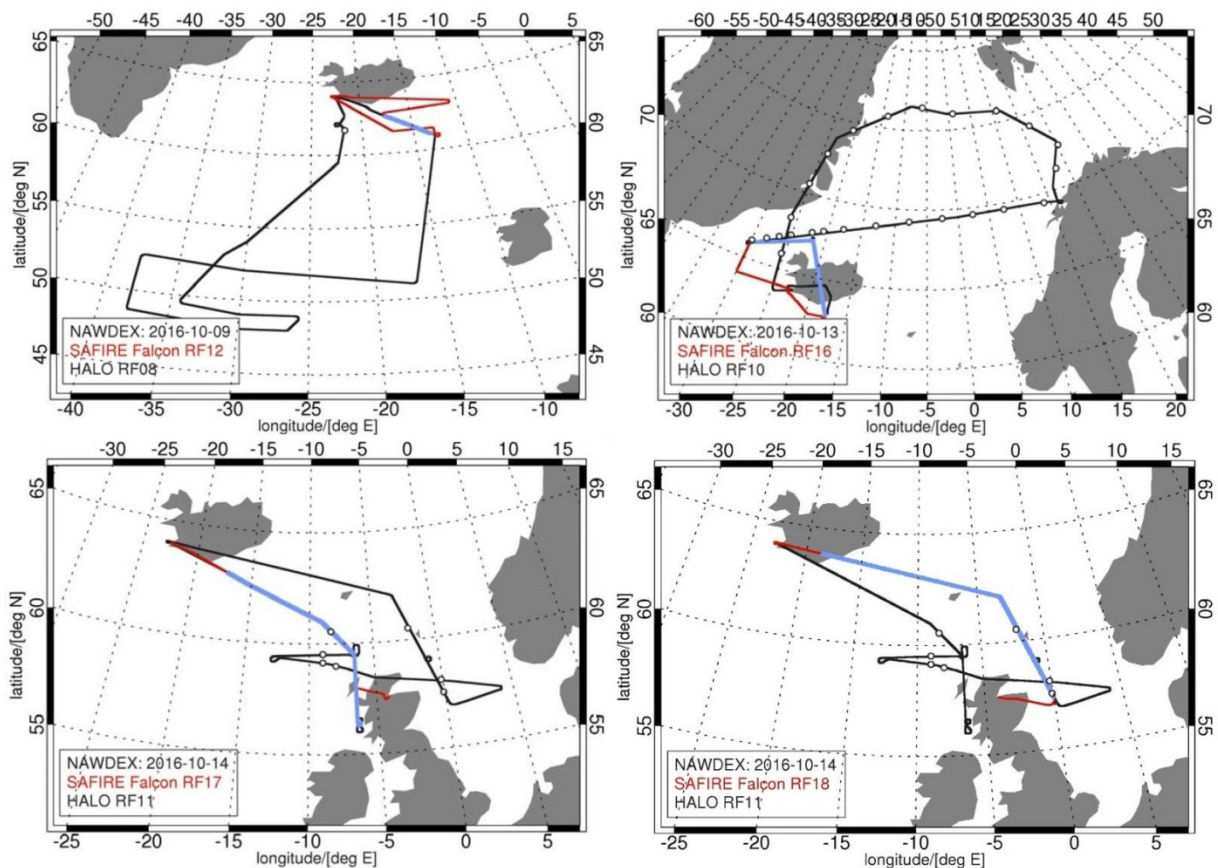


Figure 2 Common flights of French F20 (red) and HALO (black) during NAWDEX. Common flight tracks are marked blue.

Flight number	Date and flight duration	Comments	Overpass	joint legs	Ds
---------------	--------------------------	----------	----------	------------	----

	Take off-landing				
3	21/09/2016	Test flight in Toulouse area – radar calibration	no	no	1
5	01/10/2016	Deep low in Northern Atlantic, arriving on Iceland during the night. Less active structure west of Iceland with fairly thick clouds.	no	no	3
	2.7h				
	15:13-17:36	Test flight on the area west of Iceland, to make a cross-section of the cloud structure to observe different cloud layers and test the instruments response. Crossing of the jet stream and launch of 3 dropsondes.			
6	02/10/2016	Cyclone approaching the vicinity of Iceland (Saturday Storm) associated with active fronts and thick clouds.	no	yes with GF20	9
	3.5h				
	8:37-11:50	Outflow of the Warm Conveyor Belt (WCB) associated with the Saturday Storm; analysing the tropopause fold and the PV gradient. Coordinated flight with the DLR Falcon above Greenland (A2D validation).			
7	02/10/2016	Cyclone approaching the vicinity of Iceland (Saturday Storm) associated with active fronts and thick clouds. Strong winds forecast for the evening in Keflavik.	Overpass with ground-based radar BASTA at 13:34	no	0
	3.5h		Overpass with satellite at 14:07:35		
	13:01-16:16	Sampling the inflow of the WCB (same structure as for the previous flight). Overpass with Cloudsat-CALIPSO.	Overpass with ground-based radar BASTA at 18:24 in the descent (FL105)		
8	04/10/2016	Ridge over Iceland linked to an anticyclonic situation in western Europe. Deep low between Iceland and Newfoundland.	Overpass with ground-based radar BASTA at 18:24 in the descent (FL105)	no	5
	3.4h				
	15:45-18:45	Sampling the outflow of the WCB at the edge of the ridge and the negative PV region. Problems to start the new acquisition of RASTA (a few minutes not available)			
9	05/10/2016	Diabatic Rossby wave in North-west Atlantic evolving into a very deep low between Iceland and Greenland.	Overpass with Cloudsat only, CALIPSO payload turned off for maintenance manoeuvre.		4
	4h				
	13:18-16:31	Cyclonic outflow of the WCB, in the same system as the previous flight, close to the centre of the low. Satellite underpass with Cloudsat over Greenland in a region with moisture advection and orographic precipitation.			
10	07/10/2016	Iceland under a south-east flux between the low south of Greenland and the high pressure levels over Norway, associated with moisture advection.	no	no	7
	3.1h				
	12:03-14:54	Atmospheric rivers south of Iceland.			
11	09/10/2016	A low is located over Iceland (named “Brigitte”) associated with frontal structures south of Iceland.	no	no	4
	2.7h				
	10:19-15:50	Crossing the flow associated with the WCB We will study its evolution with the 2 nd flight in the afternoon and the flight of the following day.			

12	09/10/2016	The frontal structure is now located east of Iceland.	no		DLR Falcon2 0 and HALO	4
	2.7h	Several cross sections of the frontal area where its activity is the most intense. Common leg with the DLR aircraft from the center to the edge of the front.				
	17:08-20:08					
13	10/10/2016	The system of the previous day has evacuated northward. Iceland is in a southwesterly flow created by the opposition of the anticyclonic system on western Europe and the low pressure levels over Greenland. Atmospheric river of relatively weak intensity related to the remains of the system observed in the previous flights and its connection to the deep low located further south in the Atlantic.	no		no	6
	3.2h	Only thin cirrus and a few supercooled layers observed in the atmospheric river resulting in a weak radar signal.				
	10:11-13:08					
14	11/10/2016	Very active system west of Iceland associated with low tropopause levels	no		no	4
	2.9	Inflow of the WCB associated with the system passing over Iceland.				
	16:16-18:44					
15	12/10/2016	Very active system located to the south of Iceland, resulting in strong winds and heavy rainfall in Iceland. Targeting the WCB inflow and the strong moisture flow south of Iceland (Atmospheric River).	no		no	7
	3h					
	15:47-18:34					
16	13/10/2016	Anticyclonic edge of the WCB over Iceland, associated with orographic waves on the northern part of the flight plan. This flight plan was made to fit with the flight plan of HALO to have a common leg on its way back to Keflavik.	no		FF20 and HALO	1
	3h					
	13:03-15:52					
17	14/10/2016	Anticyclonic situation on the northern Atlantic with few cyclonic activities.	no		HALO and FAAM	1
	3.2h	The cloudy region north of Scotland, favourable for intercomparisons between the aircraft.				
	8:19-11:30					
18	14/10/2016	"" second flight of the day		CALIPSO overpass 12:52:31	yes at HALO	1
	2.8h					
	12:24-14:58					
19	16/10/2016	Ridge over Iceland, under the influence of the high-pressure levels over northern Europe.	no		no	2
	2.4h	A low located on the British Isles brings moisture in the upper levels.				
	09:56-12:13	Measurements in the cirrus over Iceland, associated to the system on the British Isles. Only one antenna for RASTA (testing integration time impact)				

Table 1 Flights summary

Note that RASTA and LNG worked continuously during the campaign. A few flights were affected by misalignment of LNG but there was no degradation during the campaign.

2.2 LATMOS instruments

2.2.1 Airborne platform

The RALI platform was mounted on board the French Falcon 20. The F20 aircraft (Figure 3) was operated by SAFIRE¹ (Service des Avions Français Instrumentés pour la Recherche en Environnement). RALI consists of a combination of the multi beam 95 GHz Doppler radar RASTA (RAdar SysTem Airborne) and the LNG (Leandre New Generation). Both instruments were developed at LATMOS (<http://rali.projet.latmos.ipsl.fr/>, Delanoë et al 2013). LNG, in its backscatter configuration, operates at three wavelengths (355 nm, 532 nm, 1064 nm), including depolarization at 355 nm. Since 2010 the LNG lidar has had a high spectral resolution capability added at 355 nm. Since 2006 at least one of the two instruments flew under CloudSat and CALIPSO tracks (AMMA (2006)/ CIRCLEII (2007)/ POLARCAT (2008)/MT-AFRICA (2010) / LNG-CALIPSO (2010), CALOSIRIS (2014), HAIC-CAYENNE (2015), RALI test campaign (December 2015)) and now NAWDEX (2016).



Figure 3 French Falcon 20

2.2.2 Airborne payload

a. RASTA Doppler cloud radar

RASTA can measure the Doppler velocity and the reflectivity at 95 GHz (Table 2) along a radial defined by the pointing direction of the antenna. The RASTA radar includes 3 downward-looking beams (nadir, 28 degrees off-nadir and opposite the aircraft motion, and 20 degrees off-nadir perpendicular to the aircraft motion, Figure 4). This unique configuration allows for the retrieval of the three-dimensional wind.

¹ <http://www.safire.fr>

3 antennas	RASTA characteristics
Frequency (GHz)	95 (3.2 mm)
Vertical resolution (m)	60
Horizontal resolution (m)	225 to 300 depending on aircraft speed
Range (km)	15
Integration time (ms)	250 (measurement every 750ms for each antenna)
Energy (kW)	2 (pulse 0.4 μ s)
Ambiguous velocity (m s ⁻¹)	8
Antenna size (cm)	45 (0.5° beam width)
Sensitivity at 1km (dBZ)	Down backward: -30 / Nadir: -30 / Down transverse: -30
Weight (kg)/dimensions (cm)	110/82x102x150

Table 2 RASTA characteristics

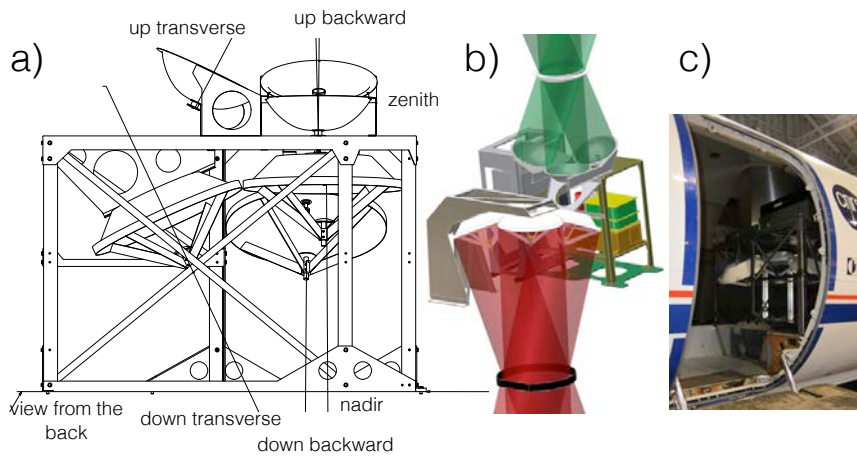


Figure 4 RASTA configuration on-board F20

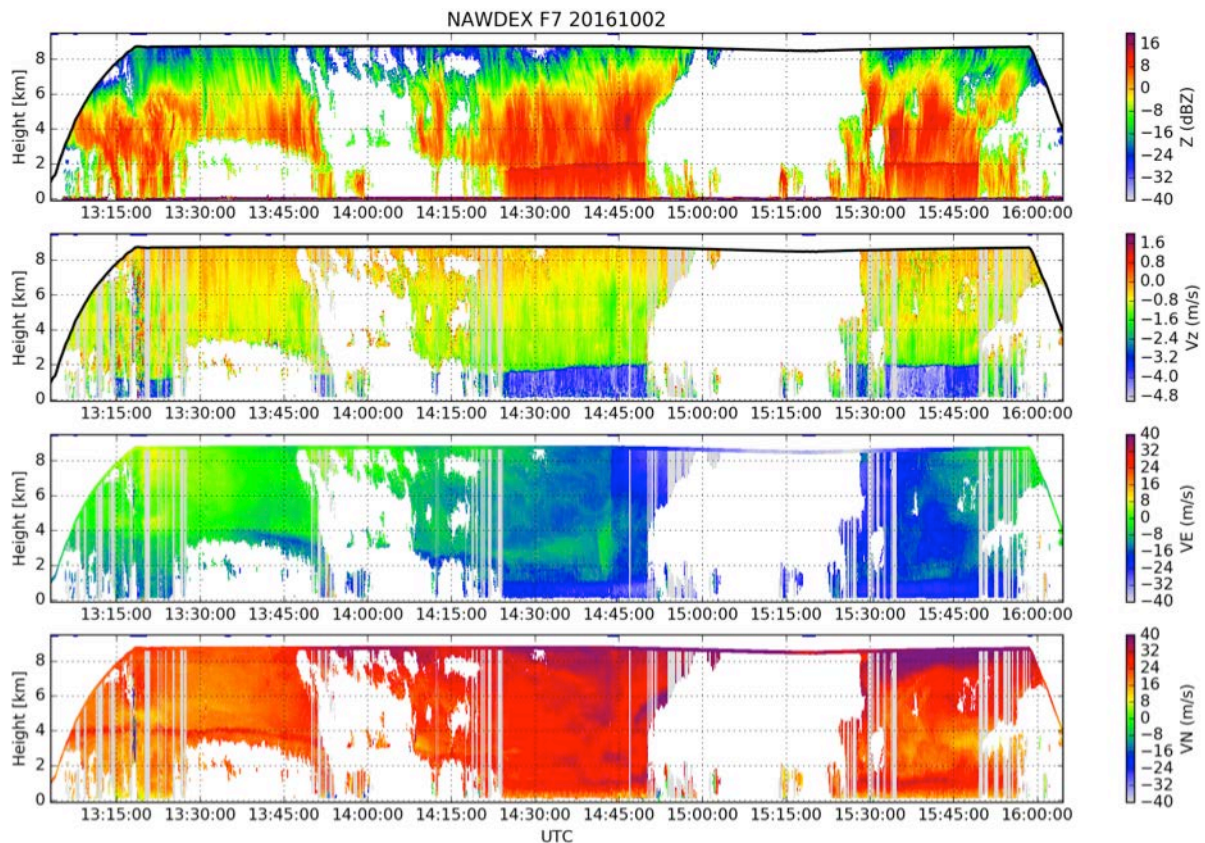


Figure 5 Example of 3D retrieval for NAWDEX campaign (F7, 02/10/2016), top panel describes the measured reflectivity below the aircraft. Second panel from top is the vertical velocity, which is a combination of the terminal fall velocity and the vertical air motion. Third and fourth plots from top illustrate both zonal (VE, or U) and meridional (VN or V) wind components. The in-situ wind (from the F20 measurements) is over-plotted at the altitude of the aircraft showing a very good consistency with RASTA's retrievals. Grey strips correspond to radial, which cannot be used in the retrieval.

RASTA nadir reflectivity is calibrated using the ocean surface return technique (Li et al. 2005; Tanelli et al. 2008). The calibration of the other antennas is either directly derived using ground surface (in a similar manner as the nadir) or by comparing with nadir reflectivity. In the case of an available CloudSat overpass the latter is also used to retrieve the radar calibration.

After calibration RASTA sensitivity as a function of the range from the aircraft (nadir, backward and transverse antennas) is presented in Figure 6.

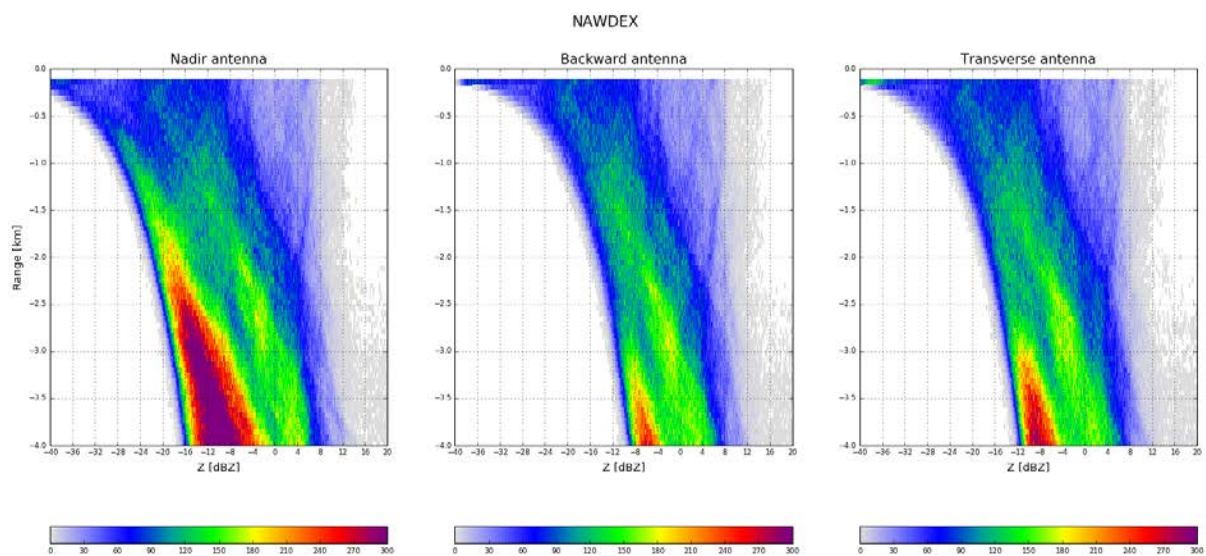


Figure 6 RASTA sensitivity for the three antennas as a function of the distance from aircraft.

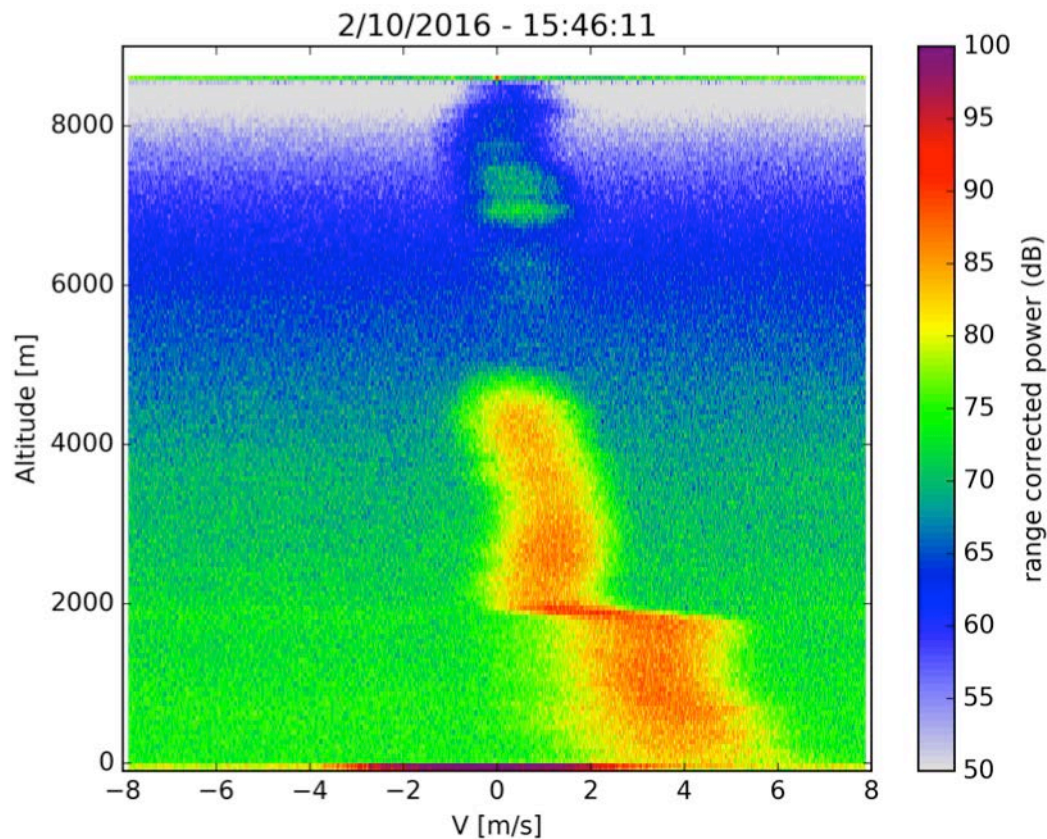


Figure 7: Doppler spectrum, range corrected power (not calibrated) as a function of velocity and range from the aircraft.

RASTA I and Q are archived for each flight and each antenna, it is therefore possible to process raw data and derive the Doppler spectrum. Figure 7 illustrates the Doppler spectrum measured on the 2nd of October during the NAWDEX campaign.

b. LNG multi-wavelength lidar (high spectral resolution UV)

The LEANDRE New Generation (LNG) airborne Lidar system (Figure 8) is based on a two-wave interferometry [Mach–Zehnder Interferometer (MZI)] to provide both the determination of optical parameters of aerosol and clouds and along-sight wind in the troposphere (Bruneau et al., 2003, 2015). It operates in a direct detection mode (measurement of the backscattered light intensity), which has the advantage of relying on both particulate and molecular scattering, and allows extended ranges and capabilities.

The direct detection technique has been chosen for space observations of winds for the ADM-AEOLUS space mission using UV-Fabry Perot Interferometer, and comparisons have shown that wind measurements were in very good agreement between the two techniques as well as with theoretical performance (Bruneau et al., 2004). The design of the MZI is well adapted to the quantification of aerosol and cloud properties, as well as Line-of-sight wind measurements on particles.

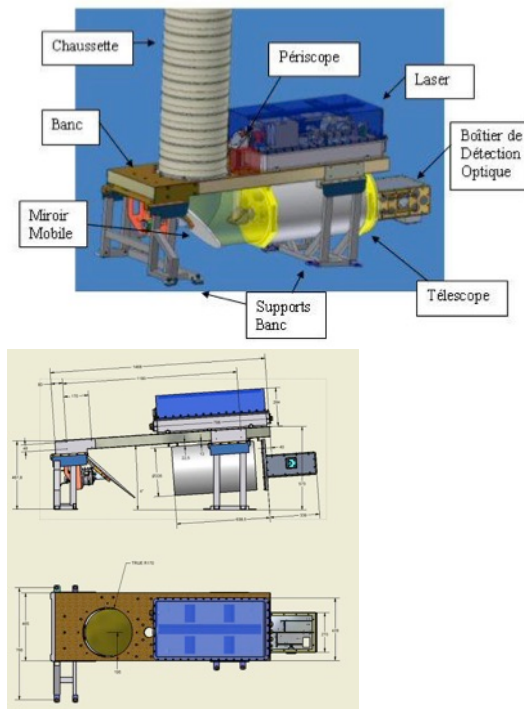


Figure 8 Left panel, Lidar implementation aboard the SAFIRE F20 showing the laser source and telescope/detection parts installed below the bench supporting the laser source. Right panel: LNG optical bench illustration, optical bench, mobile mirror and laser

LNG is a three-wavelength (1064, 532, and 355 nm, Table 3) backscatter lidar with polarization analysis at 355 nm. The HSR capability, based on a MZI, has been added at 355 nm following a previous concept analysis ([Bruneau and Pelon, 2003](#)). A view of the lidar on board the SAFIRE Falcon 20 is presented in Figure 8.

The HSR analysis within LNG performed by a Mach–Zehnder interferometer allows phase and intensity analysis simultaneously. In contrast to conventional HSR devices, our approach is not to separate the molecular and particulate signals in two distinct channels but to determine the interference contrast given by the backscattered light, which is linked to the backscatter ratio. The contrast is unambiguously determined by the signals given by four detection channels in phase quadrature, whatever the spectral positioning of the laser frequency with regard to the transmission function of the MZI. This way no frequency stabilization is necessary either for the laser or the interferometer. Calibration is performed using laser signal injected in the MZI.

The signals, in phase quadrature, are delivered by the four detectors. The analysis allows us to retrieve intensity and phase shift of the backscattered signal with respect to the laser emission. As a result, backscattering signals are derived at the three emitted wavelengths and the HSR signals allow one to separate the attenuated particulate and molecular backscattering, as for ADM-Aeolus.

Wavelength	1064nm, 532nm and 355nm
Class	IV
Lighting power	6 Watts (average)
Type	ND : YAG pulsed (20Hz)
Beam visibility	Not visible inside cabin but visible outside the aircraft at night-time

Focused beam	No
Eye safe minimum distance	About 600m

Table 3 Laser characteristics

Some examples of LNG Doppler measurements which were collected during 2014 test campaign are shown in Figure 9. In the left panel, the ground surface echo velocity is compared to the speed of the aircraft as the F20 was flying at a constant altitude. The mean difference is 0.12 m s^{-1} and the standard deviation is about 1.4 ms^{-1} . The pitch of the F20 is about 3° upward.

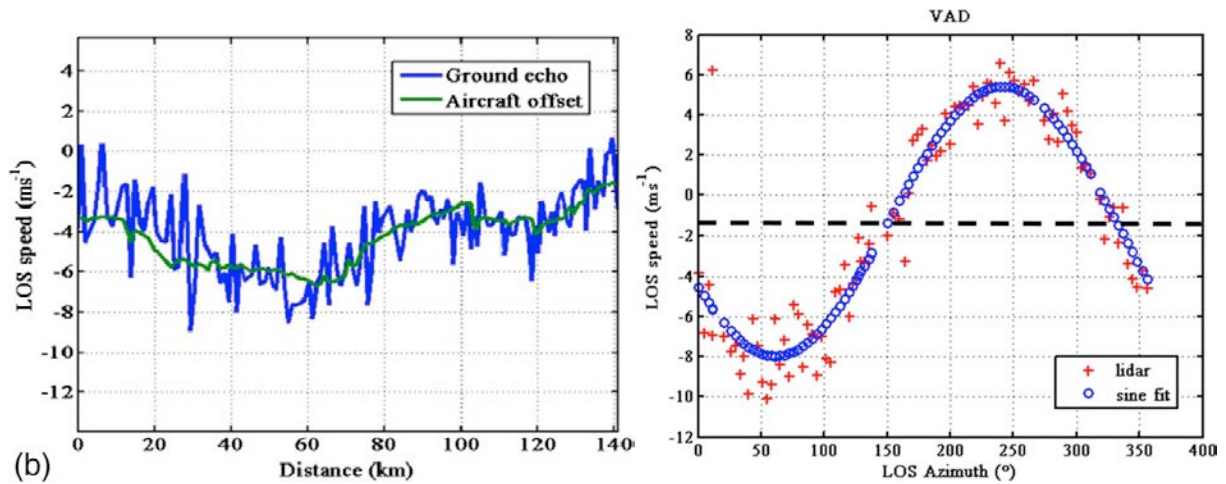


Figure 9 Left, LNG-HSR measurements of the ground echo, apparent speed derived from measurements (blue) and from inertial navigation system (green). Right, Velocity-azimuth display of the corrected LOS (line-of-sight) wind speed

Right panel in Figure 9 present the results of a 360° turn carried out by the F20 and was performed at a constant roll angle of 27° over cirrus clouds between 9.5 and 10.5 km. We display the corrected LOS wind speed as a function of the LOS azimuth angle, after having corrected the aircraft navigation offset. Assuming stationarity in the probed volume, this velocity-azimuth display (VAD) of the conical scan allows for the retrieval of the speed and direction of the horizontal wind as well as the vertical wind speed. A sine fit to the data shows a retrieved horizontal wind speed of 15 ms^{-1} with a direction of 240° . The measurement aboard the aircraft (at 12.5 km) gives a wind speed of 20 ms^{-1} with a direction of 270° . An offset of 1.5 ms^{-1} in the mean VAD was evidenced, larger than the estimated bias requiring further analysis.

In addition to the classical nadir and zenith views LNG has a slant measurement capability. In December 2015, the system has been modified to allow 37° sideward pointing. The laser viewing can be changed during flight.

Figure 10 illustrates the “wind” measurements collected by RALI (radar and lidar). The multibeam radar configuration allows us to retrieve vertical and horizontal wind field where clouds are detected by the instrument. In bottom panel, the wind component on the line-of-sight measured by LNG is reported as the F20 was flying forth and back to Greenland (first turn at 10:00 UTC and second one at 10:25 UTC). Nadir view was used from landing until around 10:30 and then LNG was depointed in order to make the most of its additional slant viewing

which is giving access to products directly comparable to Aeolus ones. LNG was back to its nadir configuration after the second turn and as heading back to Iceland. We clearly see the impact of the wind velocity projection (including aircraft speed projection) while radar wind retrieval highlights similar wind structures during the flight.

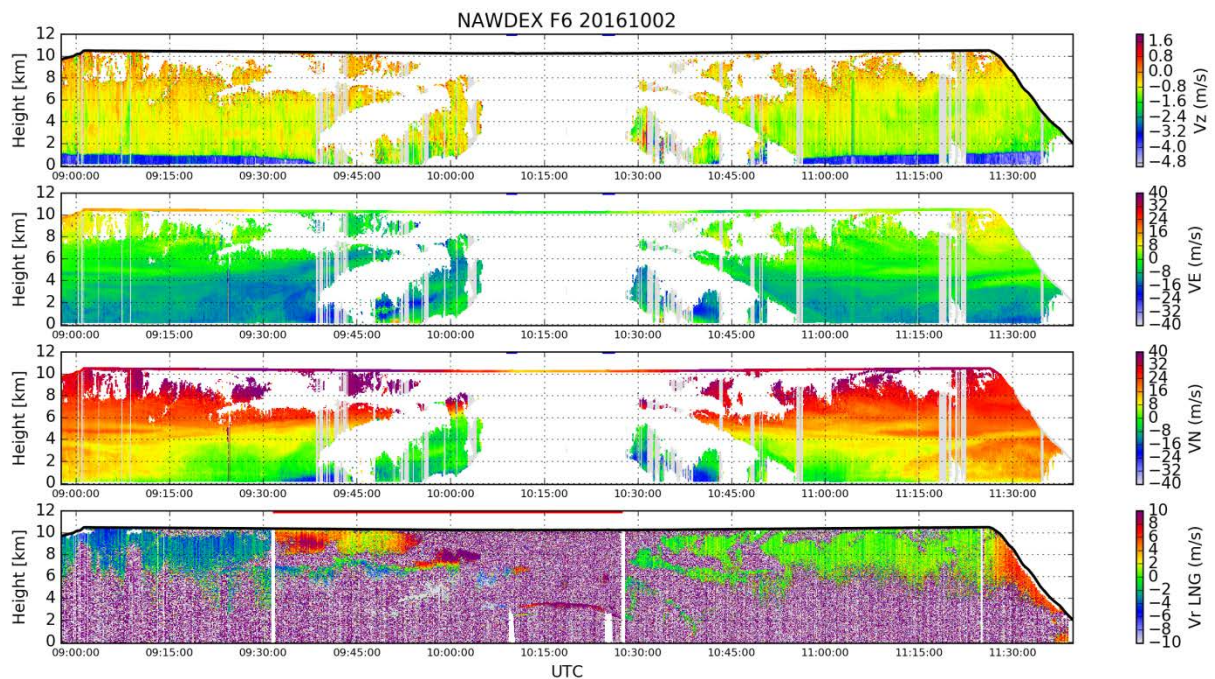


Figure 10 RALI wind measurements. First three top panels show radar wind retrievals, vertical velocity, eastwards wind and northwards wind respectively. Bottom panel shows LOS wind measured by LNG-HSR in nadir and 37° slant viewing configurations (37° configuration is highlighted by a red line between 9:32 and 10:27 UTC)

c. Measurements of Atmosphere and Ground Surface Targets - CLIMAT

Brightness temperature can be used to constrain cloud microphysics in clouds with Optical depths smaller than 6-8. The aircraft is equipped with the thermal infrared radiometer Conveyable Low-Noise Infrared Radiometer for Measurements of Atmosphere and Ground Surface Targets (CLIMAT)-Airborne Version (AV) (Legrand et al. 2000; Brogniez et al. 2003; Brogniez et al. 2005). It uses a 7-Hz sampling frequency and performs measurements within a 50-mrad field of view, which corresponds to a footprint of about 50 m at a 1-km range. Radiances are measured simultaneously in three narrowband channels centred at 8.7, 10.8, and 12.0 micron, with about 1 mm of full width at half maximum. Climat is very similar to the CALIPSO IIR system. Spectral band passes of CLIMAT-AV and IIR are presented in Figure 11 (from Sourdeval et al. 2012).

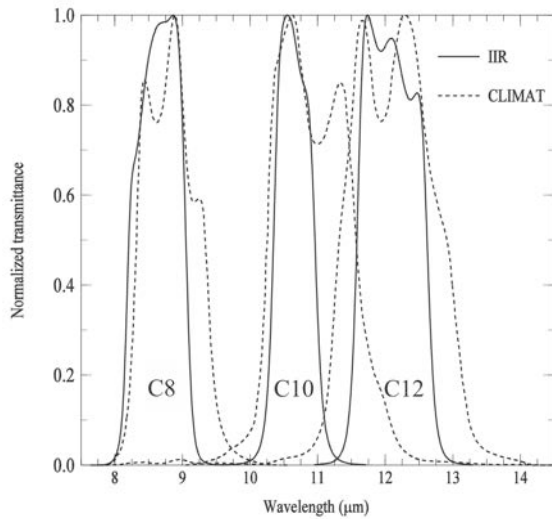


Figure 11 Normalized spectral band transmissions in channels C8, C10, and C12 of CLIMAT-AV and IIR. (Sourdeval et al. 2012).

The absolute accuracy of brightness temperature measurements derived from CLIMAT-AV is about of 0.1 K, whereas its sensitivity is of the order of 0.05 K (Brogniez et al. 2003).

Infrared measurements were collected during each F20 flights and co-located with radar and lidar data as shown in Figure 12.

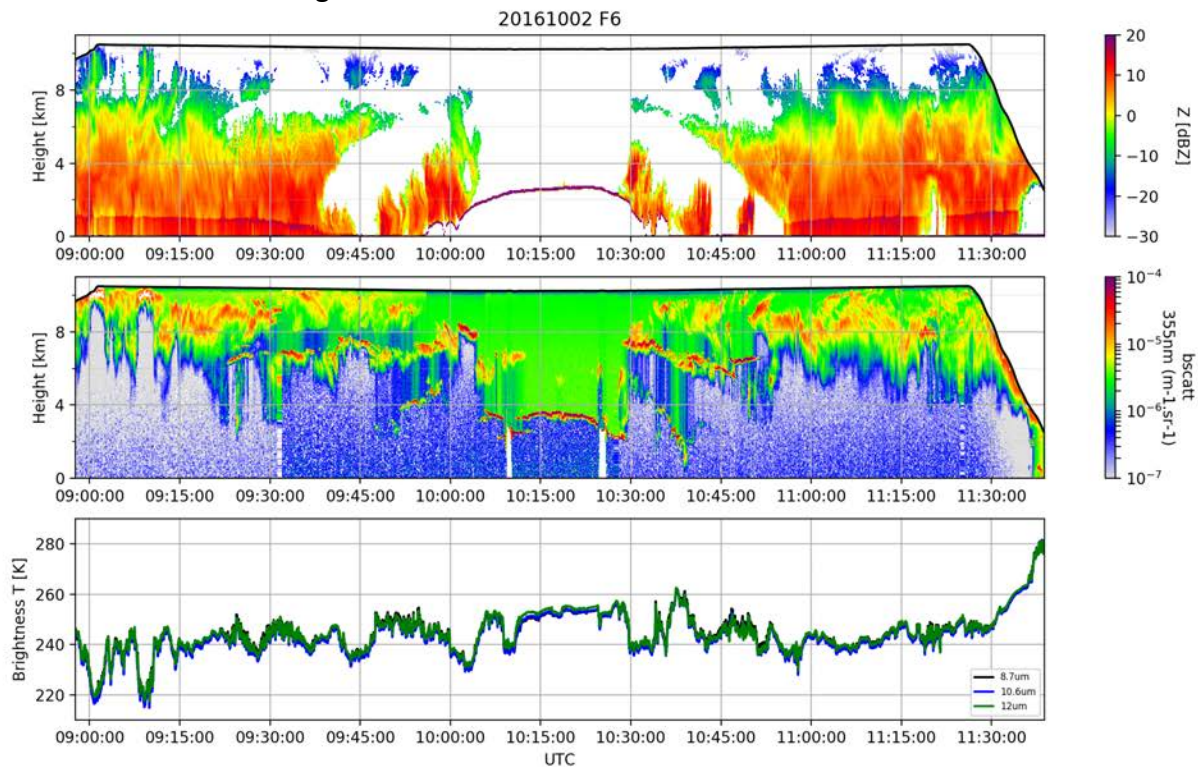


Figure 12 Example of radiative measurements collected during flight 6 on the 2nd of October 2016. Top and middle panels represent radar and 355 nm lidar measurements respectively. Bottom panel shows the CLIMAT brightness temperature at three wavelengths (8.7, 10.6 and 12 μm).

d. Dropsondes



Figure 13 Dropsonde launcher on-board the F20.

59 Vaisala AVAPS dropsondes were launched during the experiment. Some of the dropsondes in cloud conditions were used for characterizing atmospheric state to complete remote sensing measurements. However most of them were used in the framework of NEAREX objectives and LNG wind retrieval validation.

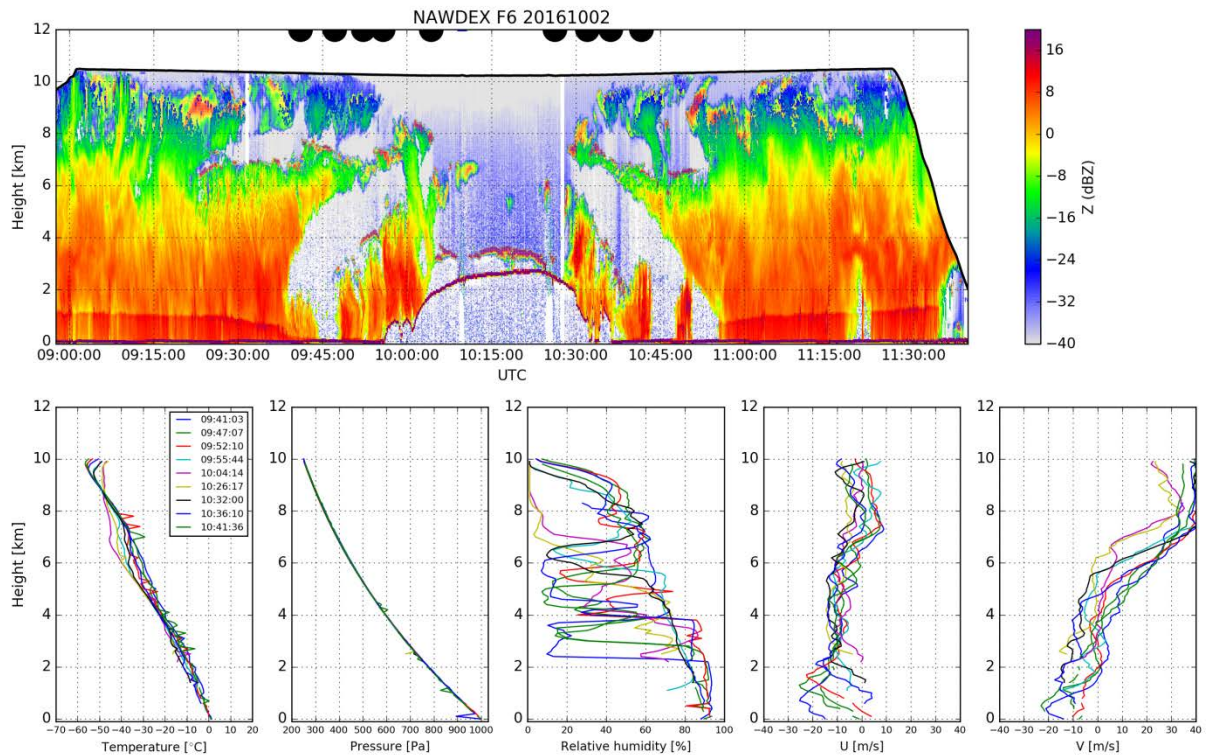


Figure 14 Examples of raw dropsonde measurements collected during flight 6. Top panel is a radar-lidar merged plot giving the cloud situation (black dots indicate dropsonde launches). Bottom panels show the dropsondes measurements, such as temperature, pressure, relative humidity, zonal and meridional winds.

e. Example of measurements collected during the EPATAN-NAWDEX

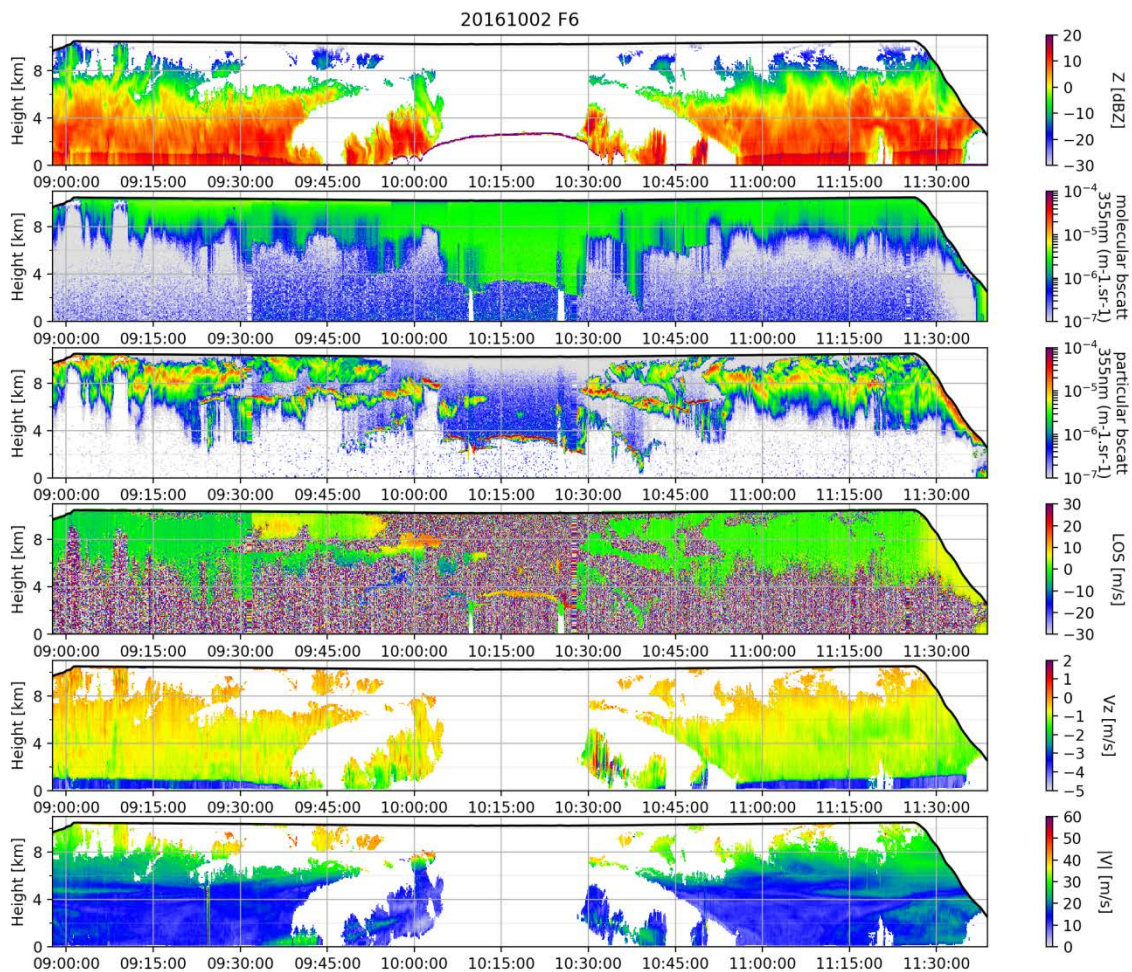


Figure 15 Example of RALI measurements and retrievals (from top to bottom panels: 95GHz radar reflectivity, molecular backscatter at 355 nm, particular backscatter at 355nm, radial Doppler velocity from lidar, vertical cloud velocity module from radar and module of the horizontal cloud velocity).

Examples above show complementarity of lidar and radar observations within RALI allowing to fully describing the vertical structure of clouds, including thin ice clouds at top, thick ice clouds, water clouds, and precipitation regions.

2.3 DLR instruments deployment

2.3.1 HALO aircraft

During NAWDEX the German high altitude and long-range research aircraft HALO (see Figure 16) was employed. HALO is a modified Gulfstream G550 business jet with an endurance of more than 10 flight hours, a maximum range of about 8000 km, and a maximum cruising altitude of more than 15 km.



Figure 16 HALO (High Altitude and LOng range) aircraft. Photo adopted from <http://www.halo.dlr.de/>.

HALO was equipped with an extensive set of remote sensing instrumentation combining the differential absorption and high spectral resolution lidar (532 nm) system WALES (DLR), the cloud radar MIRA36 at 35 GHz (DLR, MPI-M Hamburg, University of Hamburg) and the spectral imager specMACS (LMU Munich) with microwave radiometer (MPI-M, University of Hamburg, University of Cologne) and radiation measurements (University of Leipzig). Additionally, in-situ measurements of the meteorological properties along the flight track are measured.

2.3.2 Cloud Radar

MIRA36 is a commercial standard METEK Ka-band (35 GHz) cloud radar with polarization and Doppler capability to determine vertical velocity in clouds and precipitation. Technical details are summarized in Table 4.

Frequency	35.5 GHz
Peak Power	35 kW
Diameter of Antenna	1.1 m
Antenna Beam Width	0.5 deg.
Sensitivity at 5 km	-44.5 dBZ

Table 4 System parameters of the MIRA36 cloud radar

Together with microwave radiometers in the K-, V-, W-, F-, and G-band the MIRA36 is part of the HALO microwave package (HAMP) (Mech et al., 2014).

2.3.3 WALES Lidar

The lidar system WALES (Figure 17) is a combined differential absorption and high spectral resolution lidar (HSRL) system developed and built at the Deutsches Zentrum für Luft- und Raumfahrt (Wirth et al., 2009; Esselborn et al., 2008).

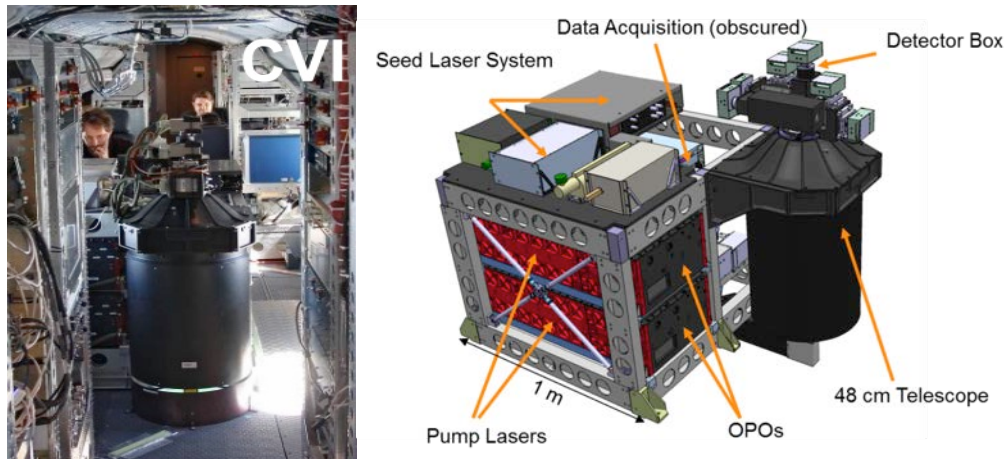


Figure 17 Lidar implemented in the HALO aircraft showing the telescope and the detector box and parts of the laser source (left panel), and sketch of the WALES lidar system (right panel).

The WALES lidar system consists of two transmitters, both based on an injection-seeded optical parametric oscillator (OPO) pumped by the second harmonic of a Q-switched, diode pumped Nd:YAG laser. WALES is capable to nearly simultaneously emit four wavelengths, three online and one offline, in the water vapour absorption band between 935 and 936 nm. The three online wavelengths achieve the necessary sensitivity needed for measurements over the whole range of tropospheric water vapour concentration. A complete water vapour profile of the troposphere is composed by using the information of the partly overlapping line contributions. The single pulse energy at 935 nm is 35 mJ with a repetition rate of 200 Hz (or 50 Hz for each quadruple). The vertical resolution of the raw data is 15 m. In addition to the 935 nm channel, the receiver is equipped with polarization-sensitive aerosol channels at 532 and 1064 nm, the first one with High Spectral Resolution capabilities using an iodine filter in the detection path ([Esselborn et al., 2008](#)). Typical transmitted pulse energies are 60 mJ at 532 nm and 120 mJ at 1064 nm. This allows for collocated measurements of humidity and optical depth, as well as studies of clouds and aerosol optical properties. System parameters of the WALES system are listed in Table 20. For a detailed technical description see [Wirth et al. \(2009\)](#).

Transmitter type	Nd:YAG laser pumped OPO
Pulse energy 935 nm (mJ)	35
Pulse energy 532 nm (mJ)	60
Pulse energy 1064 nm (mJ)	120
Pulse rate (Hz)	200
Wavelength (nm)	532, 935, 1064
Strong absorbing line (nm)	935.6846
Medium absorbing line (nm)	935.6083
Weak absorbing line (nm)	935.5612
Telescope diameter (cm)	48
Vertical resolution (m)	150
Horizontal resolution (km)	0.2 (1s)

Table 5 System parameters of the WALES lidar

An example of a WALES high spectral resolution lidar measurement during NAWDEX is shown in Figure 18

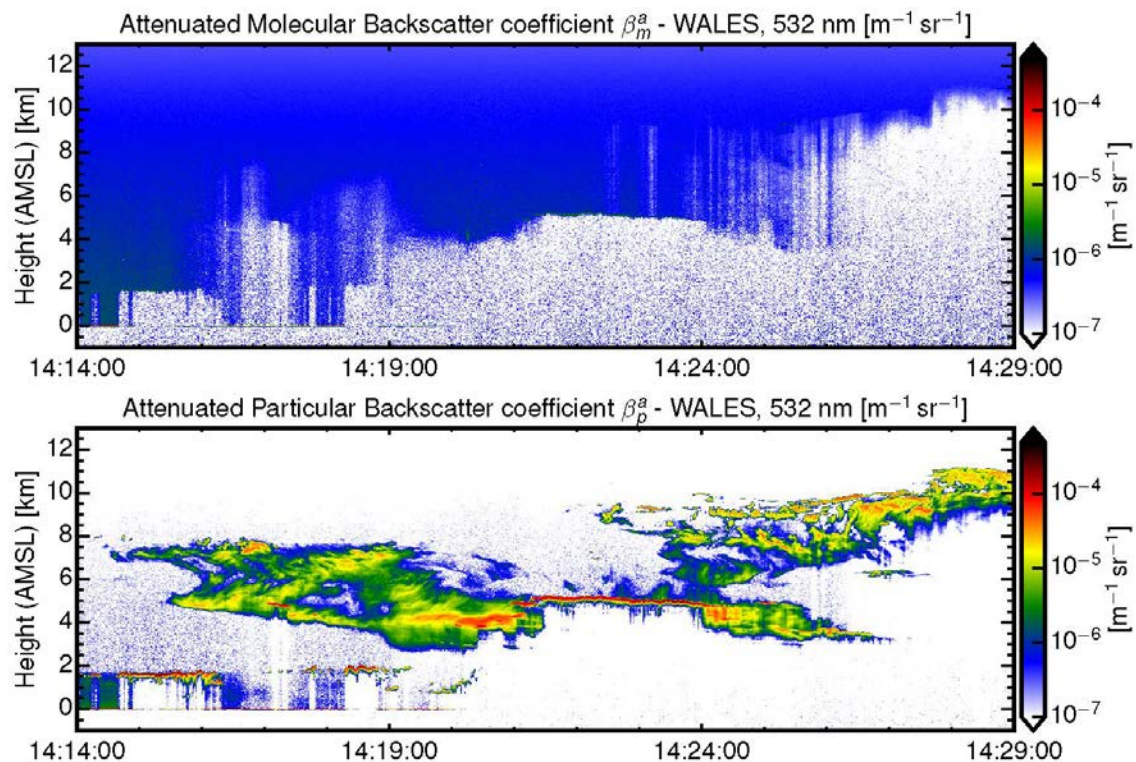


Figure 18 WALES high spectral resolution lidar measurements during NAWDEX on 13 October 2016.

2.3.4 SpecMACS

SpecMACS is an imaging cloud spectrometer consisting of two commercial spectral camera systems in the visible near-infrared (VNIR: 400-1000 nm) and in the shortwave infrared (SWIR:

1000-2500 nm) manufacturer SPECIM, Finland. The nominal spectral resolution is 3nm and 10 nm for the VNIR and for the SWIR, respectively. SpecMACS produces a spectrally resolved line image. For the NAWDEX campaign this spatial line will be mounted across-track resulting in a push-broom image with a spatial resolution in the order of 10 m for cloud objects at a distance of about 10 km for a typical data acquisition rate of 30 Hz. Technical details are summarized in Table 6.

	VNIR	SWIR
Detector	SiO ₂ DMOS	HgCdTe CMOS
Spectral range (nm)	417 – 1016	1015 – 2496
Spectral bandwidth (nm)	typ. 2.5 – 4	typ. 7.5 – 12
FOV	32.7°	35.5°
IFOV (across track) (mrad)	typ. 1.4	typ. 3.8
IFOV (along track) (mrad)	typ. 2.0	typ. 1.8
Maximum frame rate (Hz)	145	103
Temp. Control (K)	uncooled	200

Table 6 System parameters of the specMACS imager

The specMACS system is well characterized and calibrated ([Ewald et al., 2016](#)). It was first operated on board the HALO aircraft during the ACRIDICON-SHUVU campaign in Brazil in September 2014. (Figure 19) shows an example of specMACS measurements during NAWDEX.

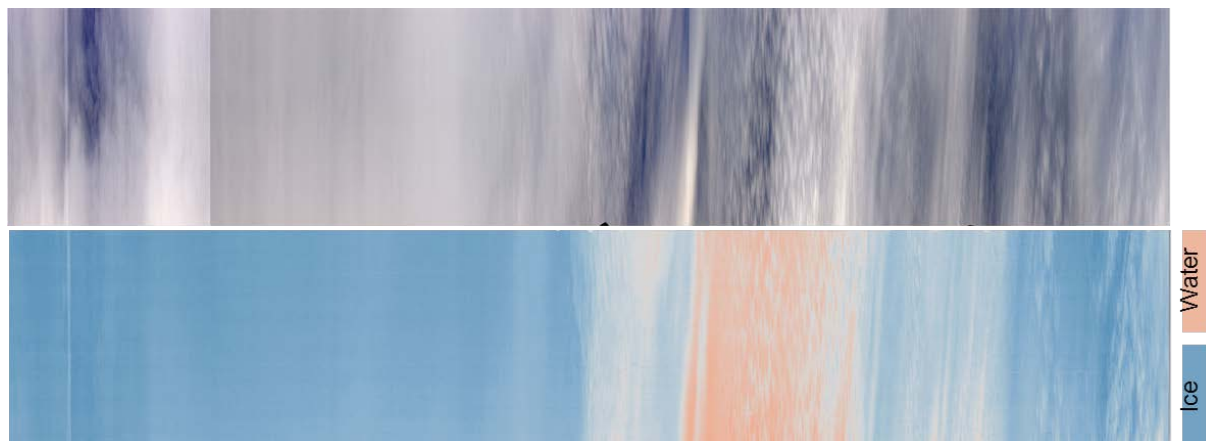


Figure 19 RGB and ice index derived from specMACS measurements on 1 October 2016.

2.4 Auxiliary data

To derive backscatter coefficient and backscatter ratio from the WALES and LNG lidar measurements auxiliary information on temperature and pressure are mandatory. For the data processing of WALES model analysis data from ECMWF is used. This data is interpolated in space and time to match the WALES and LNG measurements. For more information the reader should refer to the DAR (annex I).

2.5 EPATAN data

During EPATAN multiple active and passive instruments were operated on board the HALO and the F20. The full description of the data can be found in Annex I (DAR).

3. DATA PROCESSING AND STRUCTURE

The description of the data, information on data quality and processing, system calibration, as well as on data products and formats can be found in the Data Acquisition Report in Annex I (DAR).

4. DATA ANALYSIS

4.1 Cloud characterization

4.1.1 Statistics of cloud classification (HALO study during NAWDEX)

In order to derive statistics of the cloud phases observed above the North Atlantic during the campaign period, the lidar and radar observations onboard HALO are analysed with the cloud classification algorithm introduced in (Ceccaldi et al. 2013). The algorithm combines the lidar attenuated backscatter coefficient, the radar reflectivity and the ECMWF thermodynamic variables of temperature and pressure to provide information on the phase of the cloud (e.g. ice, liquid, supercooled, supercooled and ice). Hereon, three flights are discussed and the general NAWDEX statistics are provided.

CASE A: 1 October 2016

In Figure 20 (left), we see the atmospheric circulation over the North Atlantic and Europe on 1st of October 2016. The isohypses at 500 hPa (black lines) provide us the information of the circulation in the upper troposphere. Additionally, the surface pressure isobars (white lines) provide us the information of the location of surface high and low pressure systems. From the 500 hPa isobars we see three upper level troughs: one over the North-East Atlantic; a second one over the British Isles and a third one over northern Scandinavia. The trough over Scandinavia is connected with the remaining of the extratropical cyclone “Walpurga” which was firstly observed on 26th of September. The trough over North-West Atlantic is associated with a surface low system in the same area (white isobars) known as the “Stalactite” cyclone. The cyclone caused a lot of clouds that can be seen in satellite image in Figure 20 (right). The red line in this figure indicates the HALO flight path of that day. In the first part of the flight, the observations correspond to the clouds related to another weak low off the coast of Greenland. Southwards, HALO overflew part of the outflow of the Stalactite cyclone. In this part of the flight, southwest winds across a warm front resulted in the up-glide of moist air masses leading to saturation and cloud formation. Figure 21 shows the HALO observations of the WALES total attenuated backscatter coefficient and the MIRA radar reflectivity. The up-glide of the moist air is observed during 8:55 – 9:15 UTC and 10:05 – 10:20 UTC (latitudes 59 -

63 °N). In these observations, the cloud base rises from 3 km (9:15 and 10:05 UTC) to 6 km (8:55 and 10:25 UTC). At the same time, cloud top is between 8 and 11 km. During 9:25 – 9:50 UTC (latitudes 56 - 59 °N), lower cloud tops are observed (6 – 8 km) with several thin layers of high lidar attenuation backscatter coefficient and low radar reflectivity. Below these layers, relatively high (for this scene) radar reflectivities are observed with values up to 10 dBZ.

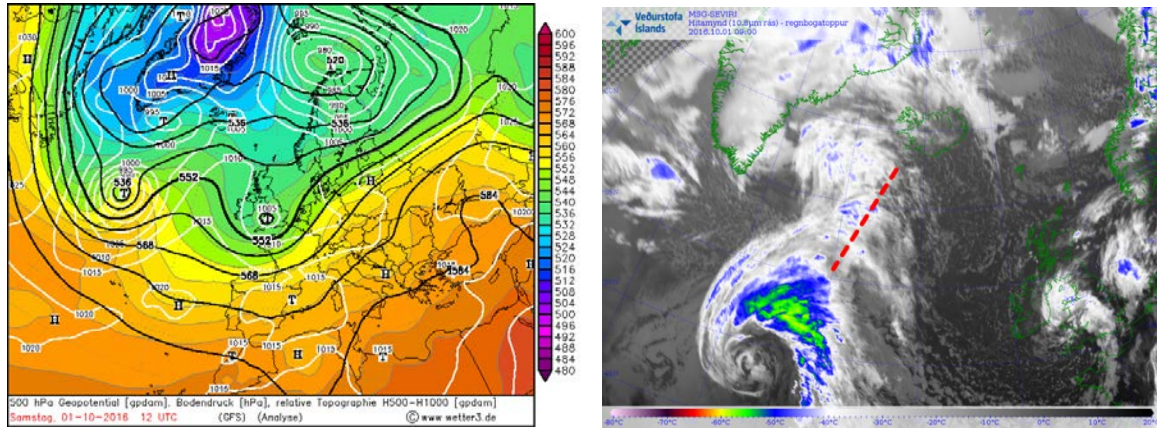


Figure 20 Left panel: Synoptic scale conditions during 1st of October 2016. Black contours show the 500 hPa geopotential heights and white contours the surface pressure (source: wetter3.de). Right panel: MSG-SEVIRI at 9 UTC and HALO flight path (source: brunnur.vedur.is).

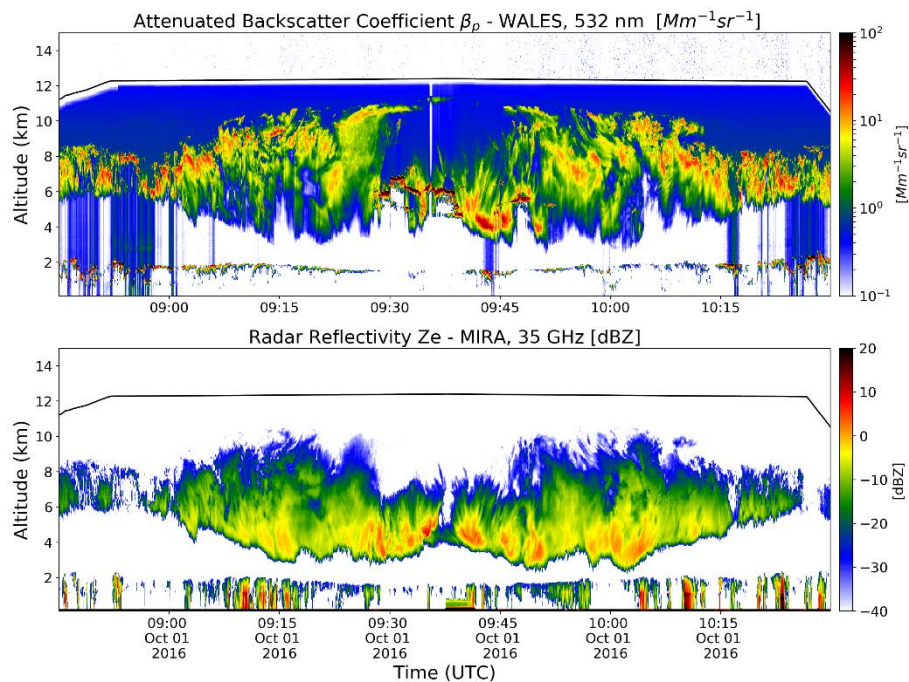


Figure 21 WALES total attenuated backscatter coefficient (upper panel) and MIRA radar reflectivity (lower panel) observations during 1st of October 2016.

The results of the cloud classification algorithm are provided in Figure 22. The two lower panels show the cloud phase statistics of the flight per 1°C (left panel: number of observations, right panel: percentage of observations). From the simplified cloud classification curtain (Figure 22-upper panel) is evident that the majority of the observations are ice clouds. The

distinctive layers in the middle of the scene are characterized as supercool layers with ice (mixed phase) with one exception in the centre of the scene that is characterized as supercooled water only. In particular, supercooled layers with ice are observed in 22.5% of the flight profiles. Some observations in the top of the marine shallow layers are also characterized as supercool water (4.4% of the profiles). The supercool layers with ice are located at 3 – 7 km height where the temperatures are between -30 to -10 °C. The number of “supercool & ice” observations in the aforementioned temperature regime range from 200 obs. (at -20 °C) to 15 obs. (at -30 °C) and represent the 5% (at -20 °C) to 0.4% (at -30 °C) of the total cloud observations in this flight.

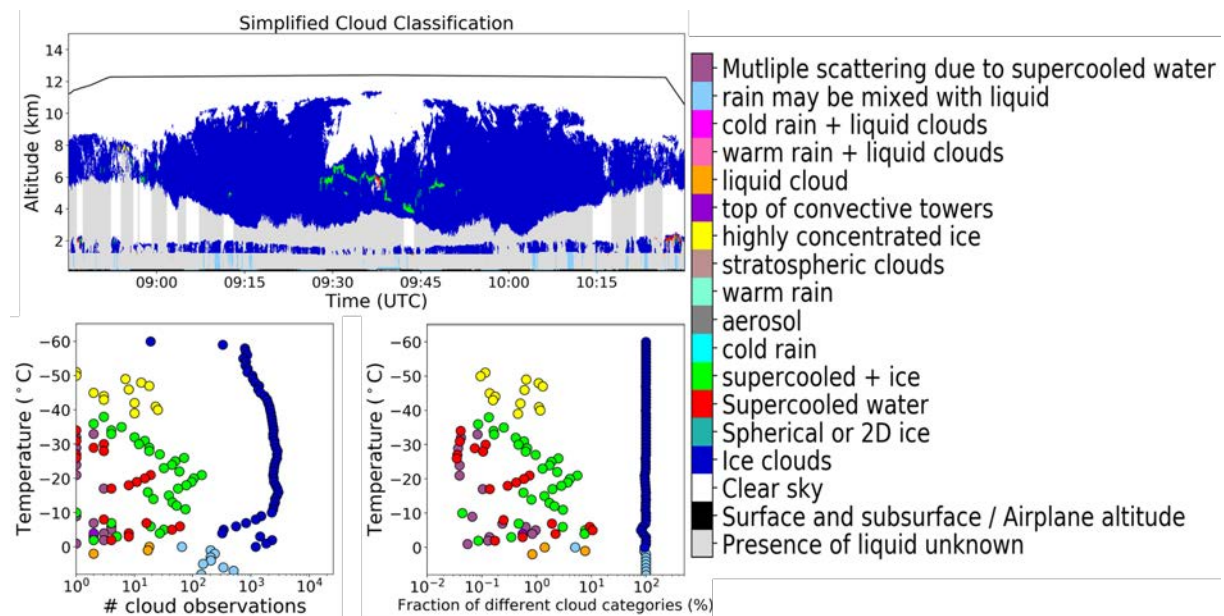


Figure 22 Simplified cloud classification (upper panel) and statistics of the cloud phases observed (lower panels) during 1st of October 2016.

CASE B: 13 October 2016

Figure 23 (left panel) shows the synoptic situation on 13th of October 2016. In the isobars at 500 hPa (black lines), we see south of Iceland a deep trough extending towards Greenland. Downstream, an upper-level ridge covers large parts of the northern North Atlantic and northern Scandinavia, identified as a northward excursion of the jet stream. In the surface pressure isobars, we see the existence of a cyclone south of Greenland, which lifted air masses towards the North and caused saturation. At upper-levels the cirrus clouds that are visible in Figure 23 (right) are advected with the jet stream towards Scandinavia. The HALO flight path, visible in the right panel of Figure 23 followed the jet stream (until location 8; 11:30 UTC) before it crosses the high-pressure system from Norway to Iceland, and then cross the frontal clouds two times between 13 and 15 UTC. Figure 24 shows the corresponding lidar and cloud radar observations (for the path between the map locations 3 and 12 of Figure 23). In the parts of the flight that crossed the frontal clouds (9:00 – 10:30 and 13:00 – 15:15 UTC), convection and precipitation is observed with cloud top heights between 4 and 11 km. Additionally, in the flight path between 9:10 – 11:30 UTC (loc. 4 - 5), high lidar attenuation backscatter coefficients and low radar reflectivities are observed. In the flight path between 11:30 to 13 UTC, when

HALO was crossing above the high-pressure system, broken clouds are observed at altitudes below 2 km and cirrus clouds at altitudes between 8 and 12 km.

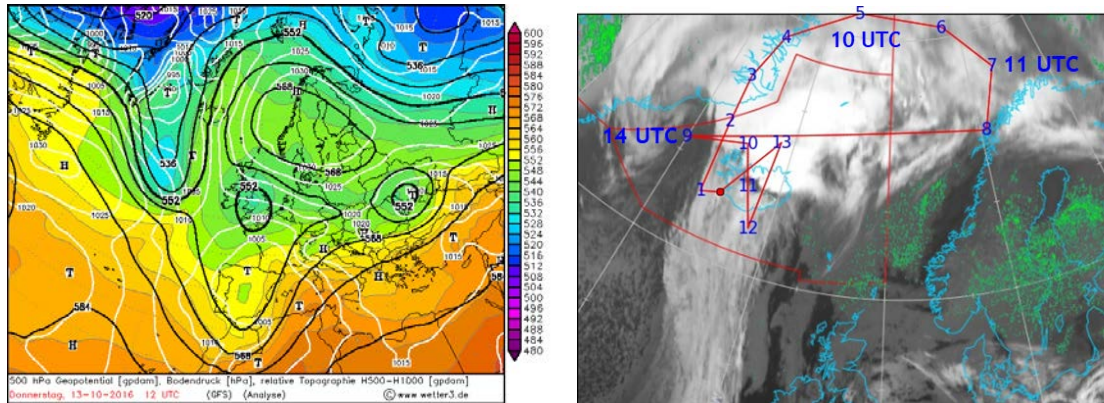


Figure 23 Left panel: Synoptic scale conditions during 13th of October 2016. Black contours show the 500 hPa geopotential heights and white contours the surface pressure (source: wetter3.de). Right panel: MSG-SEVIRI at 10 UTC and HALO flight path (source: brunnur.vedur.is).

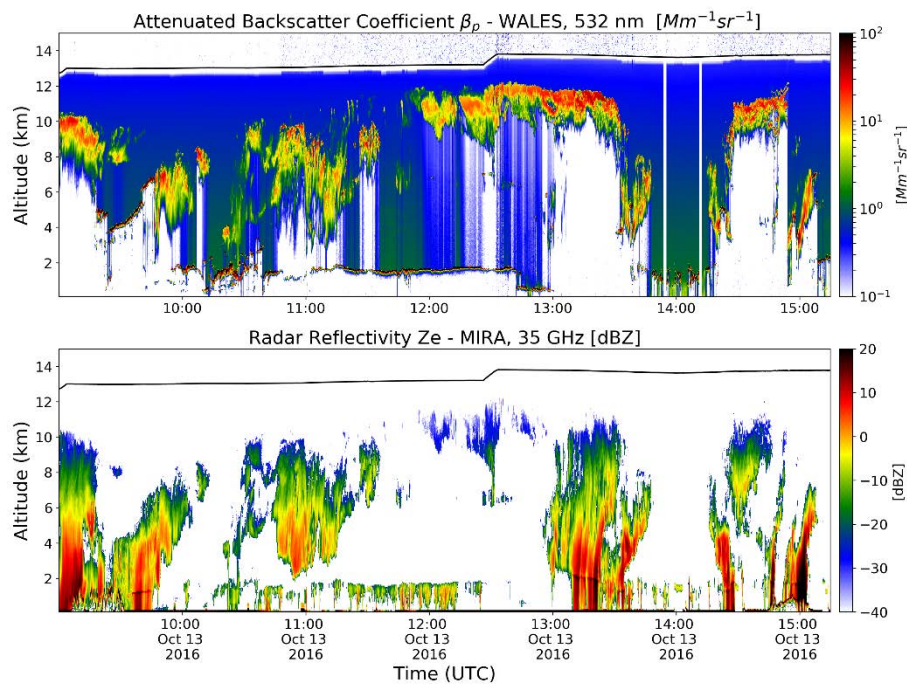


Figure 24 WALEs total attenuated backscatter coefficient (upper panel) and MIRA radar reflectivity (lower panel) observations during 13th of October 2016.

The results of the cloud classification algorithm are provided in Figure 25. In the upper panel, the box highlights the collocated observations with Falcon. In the area of the high-pressure system (between 11 and 13 UTC), the low clouds formed are characterized as ice or liquid clouds. In more detail, 48% of the profiles in this region are observed to have liquid-phase features at temperatures $[0, 1]$ °C, 14% of the observations are characterized as liquid clouds and 83% as ice clouds (Figure 25 – low left panel). The 99% of the high clouds are characterized as pure ice.

In the part of the flight crossing the frontal clouds (9:00 – 11:00 and 13:00 – 15:15 UTC), precipitation is additionally observed below the convective clouds. The precipitation observed is characterized as worm rain between 13:00 – 15:15 UTC and as cold rain between 9:00 – 10:30 UTC. An interesting segment of this flight is the part between 9:00 – 10:30 UTC, where the classification reveals a high concentration ice layer of 200 m depth located in the top of the up-lifting cloud and at temperatures between -30 and -10 °C. Additionally, some areas with high ice concentrations are observed between 13:00 – 15:15 UTC, this time prominently at [-60, -50] °C. Throw-out the frontal clouds observed, 29% of the profiles had high concentration ice layers, 3.8% had supercool and ice layers and 3.3% had supercool and water layers. Overall, at [-30, -10] °C, the high concentration ice observations corresponded to about 1.5% of the cloud observations in this flight (Figure 25 – low right panel).

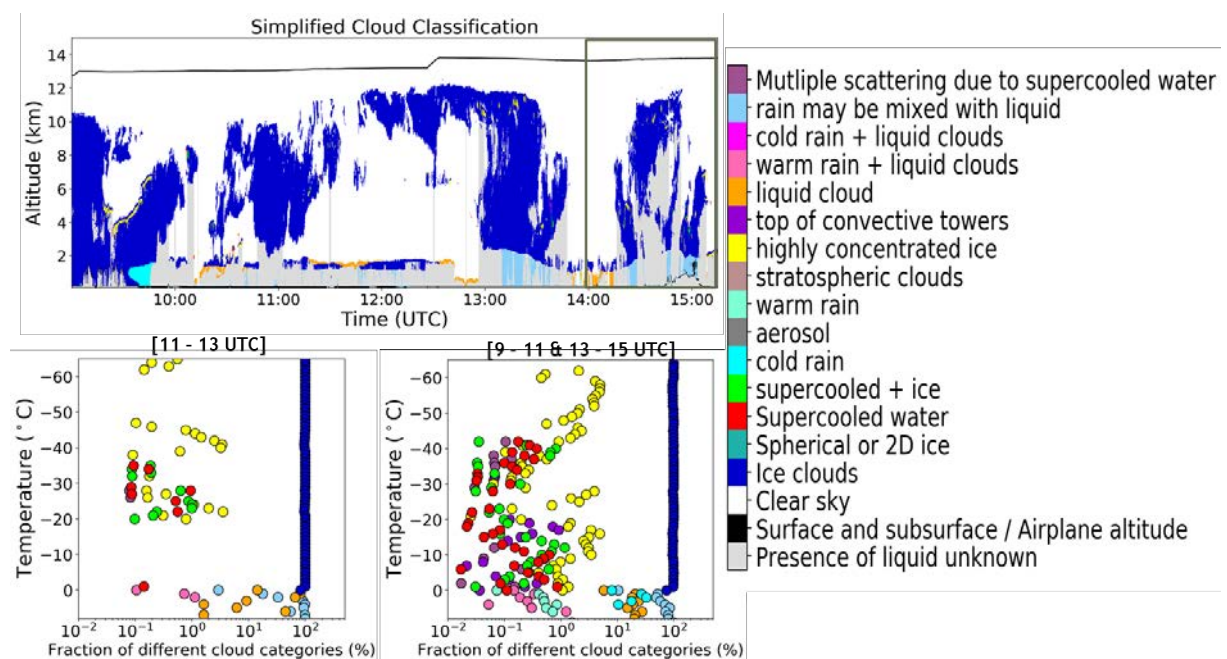


Figure 25 Simplified cloud classification (upper panel) and statistics of the cloud phases observed (lower panels) during 13th of October 2016.

CASE C: 14 October 2016

Figure 26 shows the atmospheric circulation over the North Atlantic and Europe (left panel) and the flight path of HALO superimposed on a satellite image (right panel) during 14th of October 2016. In the black isolines at 500 hPa we notice the location of a cut-off low-pressure system west of the British Isles and a ridge to the north of it. The cyclone caused lifting and cloud formation to the North of UK as visible from clouds in the satellite image (Figure 26 right). The complex flight track was planned to cover the thicker clouds between Iceland and northern UK. Figure 27 shows the corresponding lidar and cloud radar observations. In the part of the flight over the ridge (9:00 – 9:30 and 13:30 – 14:30), clouds at 2 km altitude are observed. In the part of the flight covering the thicker clouds, connected with the cyclone, complex cloud structures are observed with cloud tops between 5 to 9 km and several layers of high backscatter coefficient values with low radar reflectivities.

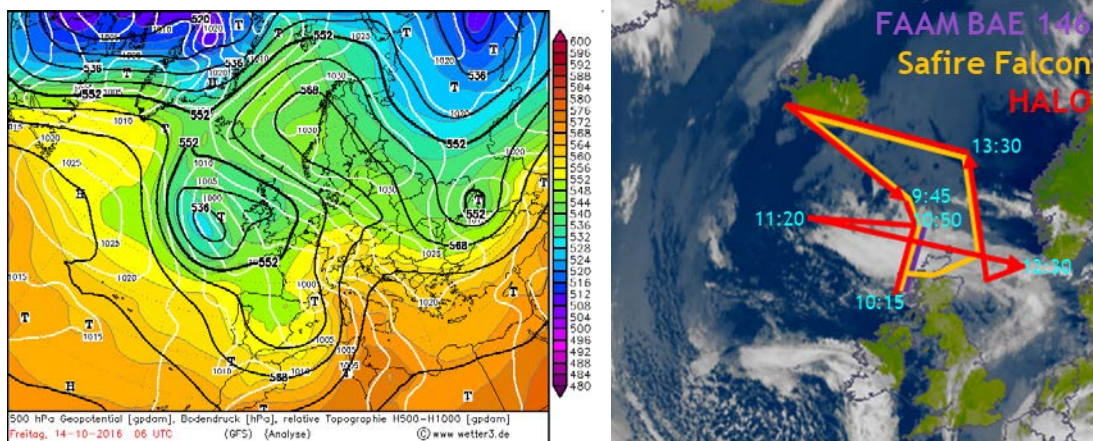


Figure 26 Left panel: Synoptic scale conditions during 14th of October 2016. Black contours show the 500 hPa geopotential heights and white contours the surface pressure (source: wetter3.de). Right panel: MSG-SEVIRI at 12 UTC and flight paths of HALO (red) Safire Falcon (orange) and FAAM BAE 146 (purple) (source: brunnur.vedur.is).

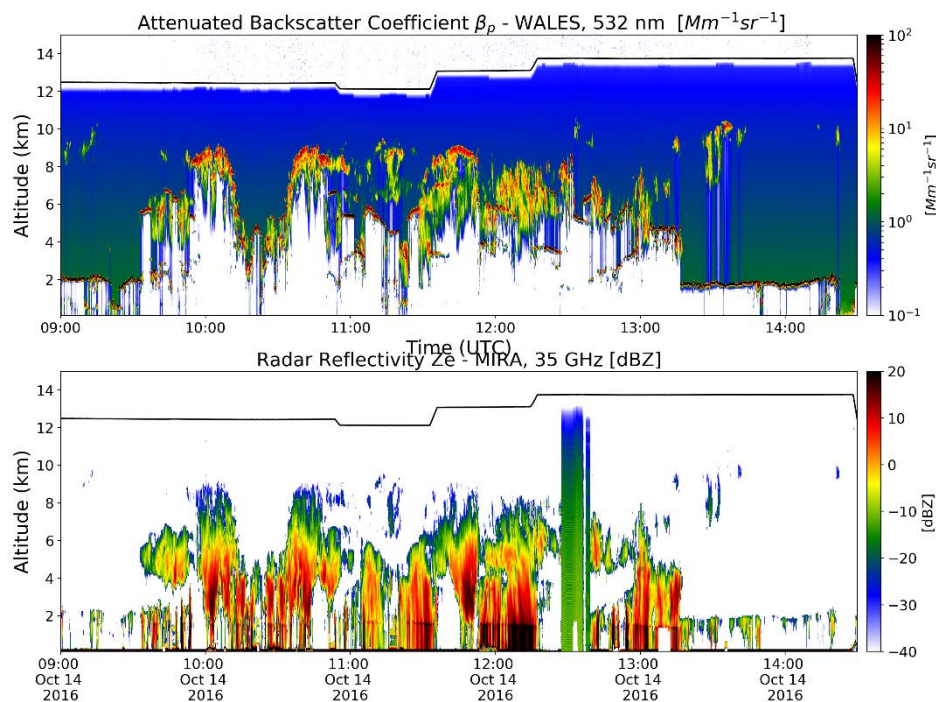


Figure 27 WALES total attenuated backscatter coefficient (upper panel) and MIRA radar reflectivity (lower panel) observations during 14th of October 2016.

The results of the cloud classification algorithm are shown in Figure 28. In the upper panel, the two boxes highlight the collocated flight tracks with Falcon. In the area over the ridge, all clouds are below 0 °C and in 33% of these profiles high concentrated ice layers are observed. These high concentration ice observations represent the 15% of the total cloud observations at [-3,-1] °C (Figure 28 - low left panel). In the domain connected with the cyclone, 46% of the cloud profiles contain high concentration ice layers, 27% contain supercool and ice layers and 6% contain supercool water layers. The layers with high concentration ice in this case, represent the 2 – 6 % of the total cloud observations at [-30, -5] °C and the 4 – 10 % of the total cloud observations at [-60, -40] °C (Figure 28 - low right panel).

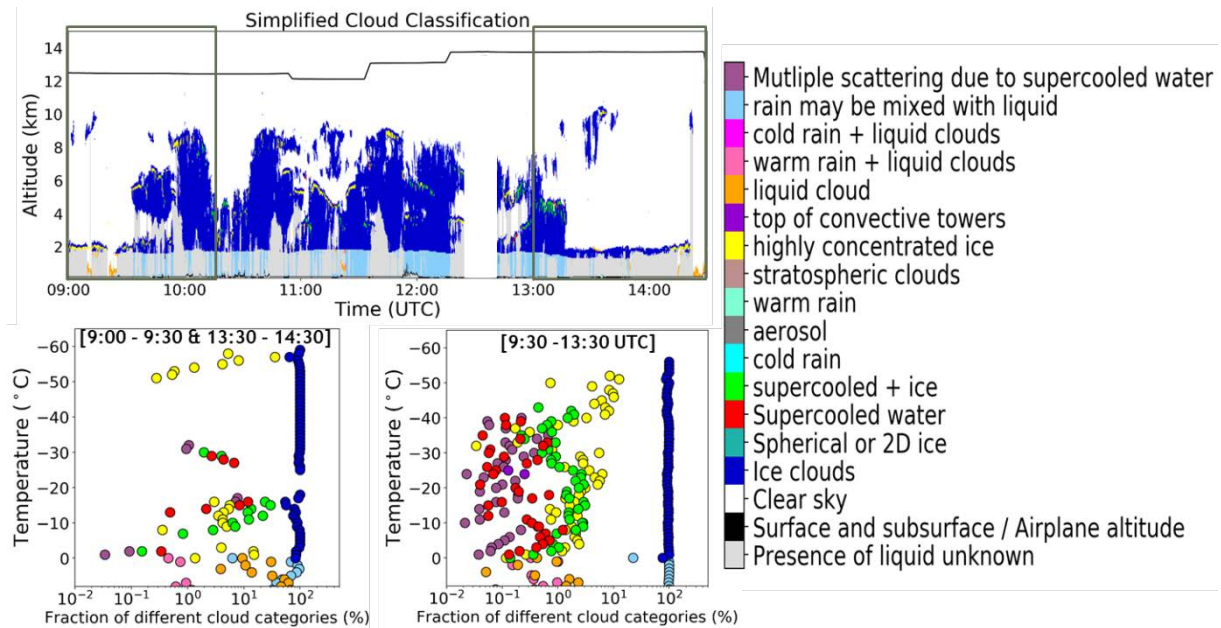


Figure 28 Simplified cloud classification (upper panel) and statistics of the cloud phases observed (lower panels) during 14th of October 2016.

Overall statistics during NAWDEX

During NAWDEX complex and varied cloud structures were observed in the vicinity of 5 extratropical cyclones and one anticyclone (Schäfler et al, 2018). Analysing the 16 HALO flights, we see that the clouds observed at altitudes with temperatures below 0°C are dominated by ice with frequent observations of thin layers of (a) high ice number concentrations, (b) ice coexisting with supercool water and (c) supercool water. Overall, from the 37469 cloud profiles analyses, pure ice phase is observed in 81% of them, high ice number concentration layers are embedded in 17% of them, and ice coexisting with supercool water in 12% of them. Additionally, supercool water layers are observed in 5% of the cloud profiles. The high concentration ice layers are observed at all temperatures below 0 °C, in 2% of the observations at [-22, 0] °C, 1% at [-48, -22] °C and 0.5% at [-65, -48] °C (Figure 29). The ice coexisting with supercool water layers are observed at [-40, 0] °C, with the highest occurrence at [-25, -10] °C representing the 1.3% of the observations in these temperatures. The pure supercool water layers are observed at the same temperature ranges, with highest occurrence at [-10, -1] °C (in 0.74% of the observations). Nevertheless, as presented in the previous three cases of this section, the fraction of layers with high ice concentrations or with coexistence of ice and supercool water were significantly higher than the campaign mean conditions in specific flights, hence the embedded layers were occasionally associated with larger contribution to the overall cloud structure.

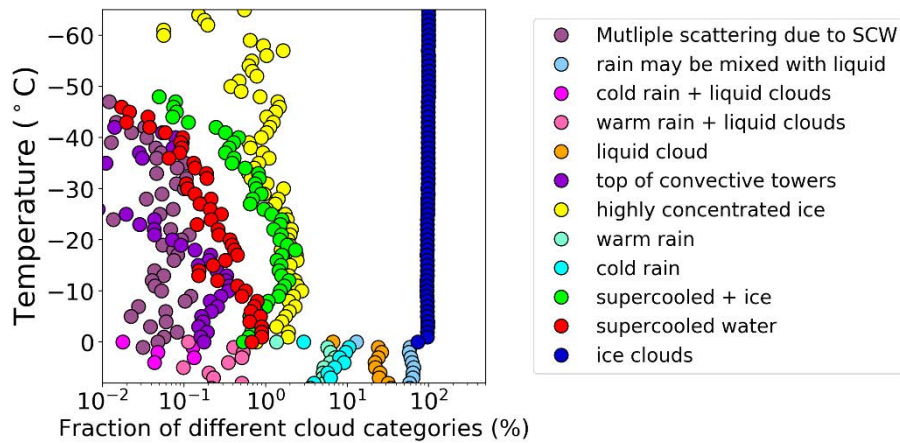


Figure 29 Overall cloud classification statistics per 1 °C as observed during the 16 NAWDEX HALO flights.

4.1.2 Statistics of cloud dynamic and microphysics from W-band radar (F-Falcon study during EPATAN)

RASTA Doppler capabilities allow us to retrieve both ice cloud microphysics and dynamic simultaneously. Figure 30 illustrates the probability density function of reflectivity, vertical velocity (sum of vertical air motion and terminal fall velocity), wind direction and intensity as a function of temperature (from the ground up to tropopause altitude) collected during the campaign. The temperature is provided by the ERA-I temperature co-located with RASTA measurements. These measurements tell us about the dynamic conditions of the campaign and also the link with microphysics.

We clearly identify the partition between ice and liquid (rain) on both reflectivity and vertical velocity, the rain considerably attenuates the W-band signal compared to ice and the velocity leaps from about -1m/s to about -4 m/s. The vertical velocity in ice increases with temperature as the size of the hydrometeors statistically increases due to aggregation process. We note that at these latitudes the ice vertical velocity ranges between -2 and 0 m/s. Larger vertical velocity are attributed to snow falls.

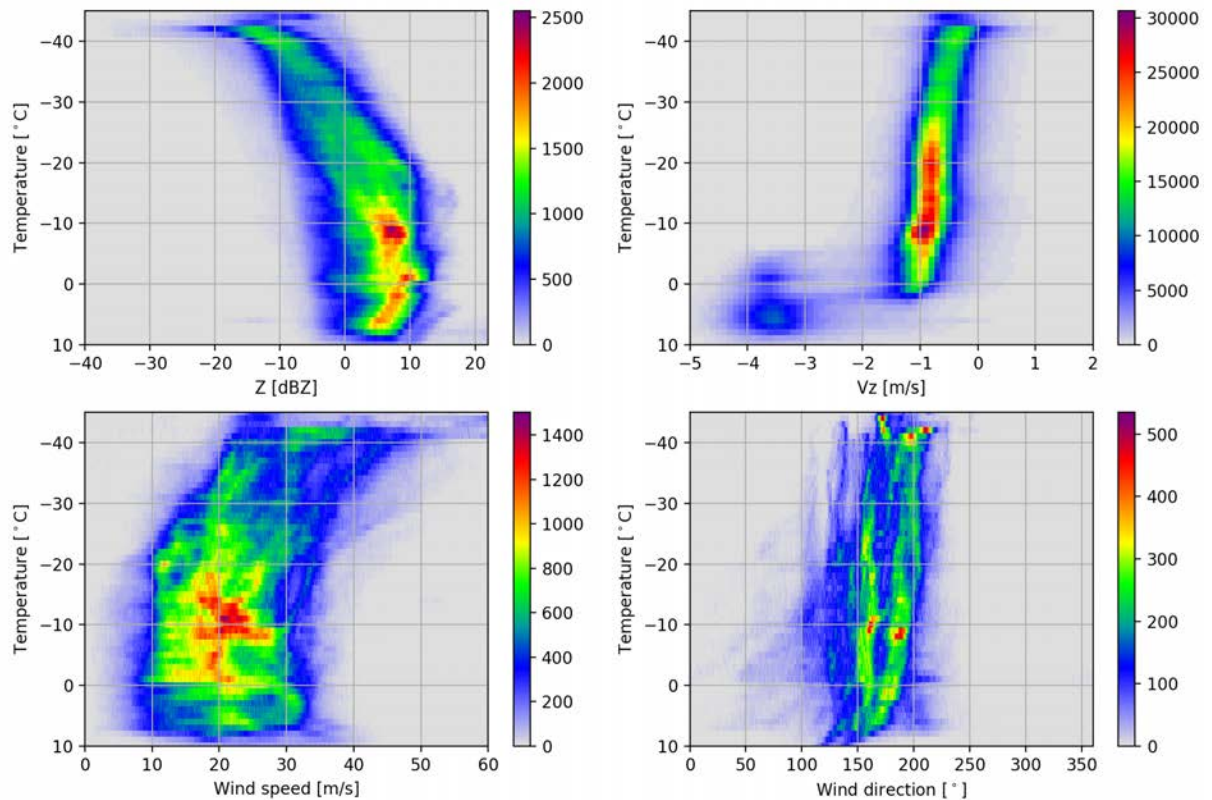


Figure 30: Statistical distribution of RASTA nadir reflectivity, vertical velocity, horizontal wind speed and direction retrieved from the combination of the nadir/backward/transverse antennas as a function of temperature.

The horizontal wind spans mainly between 5 and 35 m/s below -20°C and gradually increases at colder temperature (when getting closer the jet). Due to the sampling strategy and the scientific objectives of NAWDEX the wind direction encountered was most of the time around 180° (southerly).

The radar measurements are also used to derive IWC. Figure 31 exhibits the distribution of IWC in logarithm scale as a function of temperature. The ice water content is increasing up to -10°C and then slightly decreasing above this limit. Thanks to the Doppler capability of RASTA we can also infer the relationship between IWC and the vertical velocity. As explained earlier, V_z is the combination of both V_t and W however when looking at the IWC- V_z pdf we can consider that the trend of V_z corresponds to the trend of V_t (assuming that on a few kilometers length updrafts and downdrafts are cancelling out). The right-hand side panel shows a relationship between IWC and V_z , nonetheless it remains difficult to derive a robust parameterization as the terminal fall velocity (V_t) intensity is driven by the size of the particles. For instance, for the same water content we can have large particles with a low concentration or small particles highly concentrated.

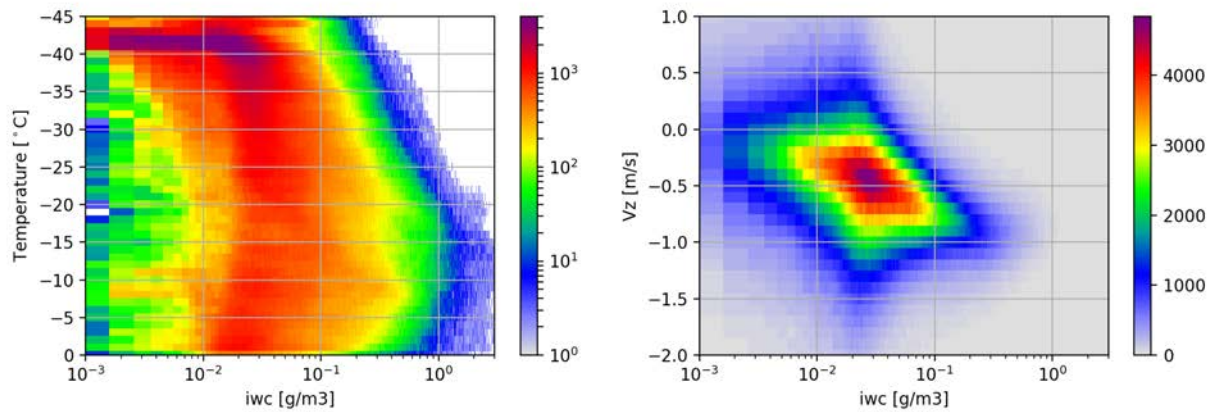


Figure 31: Distribution of IWC (radar-only) as a function of temperature and statistical relationship between IWC and vertical velocity.

More than 50 dropsondes were launched during the field campaign, while a few of them were not launched in cloudy conditions others were co-located with radar measurements. Figure 32 represents the distribution of Z, IWC and Vz as a function of the relative humidity (respectively panels a), b) and c)). Relative humidity and the three variables are correlated, an increase in humidity is favourable to higher IWC then higher Z and Vz.

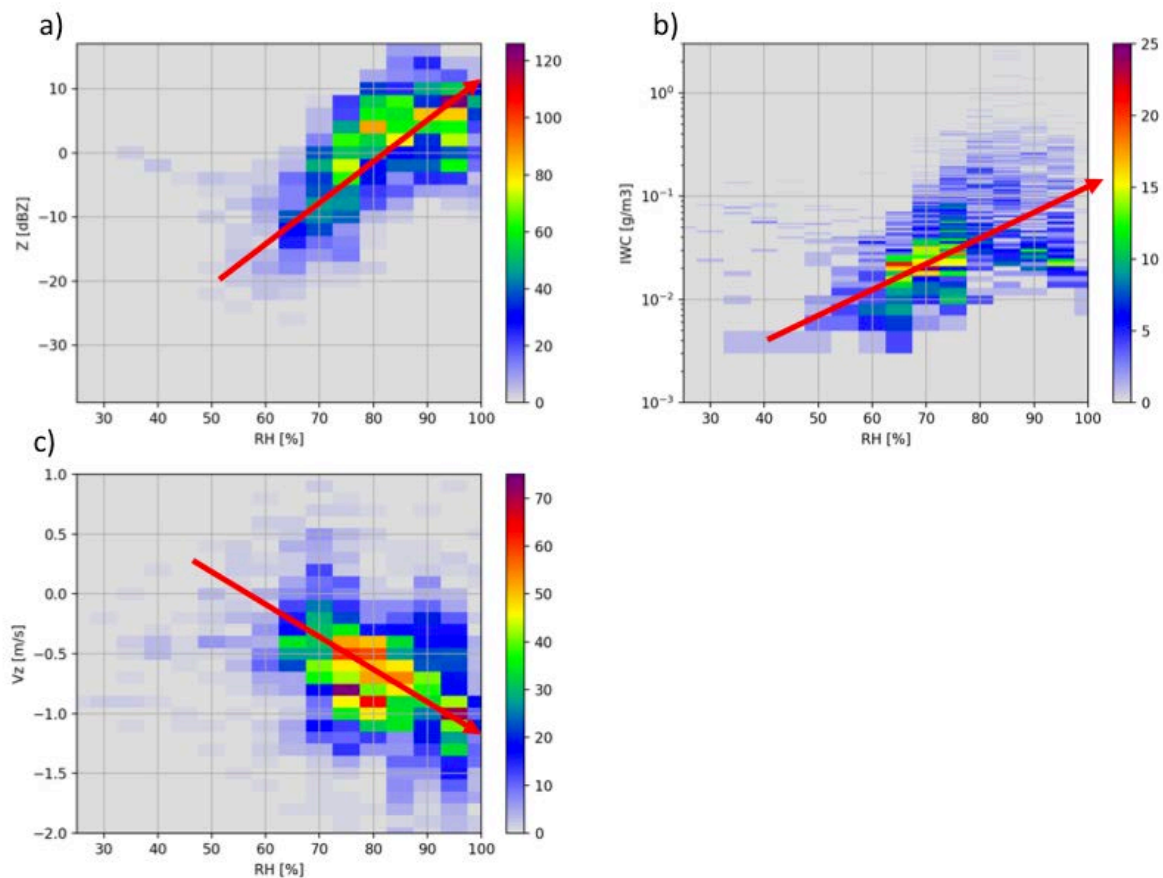


Figure 32: Radar reflectivity and retrieval as a function of relative humidity (measured from the dropsondes)

4.2 Analysis of multi-wavelengths radar-lidar measurements

4.2.1 Comparison of Level 1 measurements between HALO and FF20

The first common flight leg with HALO and the French Falcon for a comparative analysis of radar and lidar measurements (MIRA/RASTA and WALES/LNG) took place south of Iceland on 9th October 2016 between 18:22 UTC and 18:44 UTC (see Figure 2 for flight tracks). For the first 3 minutes, the lateral distance of the flight tracks was larger than 1 km and went below 250 m for the remaining common flight leg. HALO flew ahead so the French Falcon measurements were recorded 180 seconds later in the beginning of the common leg and 260 seconds at the end of the leg. The flight leg was placed above a large cloud band associated with a warm conveyor belt with heavy precipitation in the beginning and ascending air masses in the second part. The panels in Figure 33 show Level 1 measurements with MIRA and WALES on HALO (left) and RASTA and LNG on the French Falcon (right) during this inter-comparison flight. In the panel on the top of Figure 33, radar measurements from MIRA at 35 GHz on HALO are compared to RASTA measurements at 94 GHz on the French Falcon. While the overall cloud features are quite similar in both measurements, the higher sensitivity of MIRA and reflectivity differences associated with the different radar wavelengths become evident. While MIRA measurements seem to resolve the cloud top well (compared with WALES measurements) with radar reflectivity down to -35 dBZ, RASTA measurements do not contain cloud tops with a minimum measured radar reflectivity of -25 dBZ. Secondly, radar reflectivities agree quite well in the upper cloud parts, while RASTA radar reflectivities in comparison are smaller towards lower cloud parts. This observation can be explained by the larger hydrometeor attenuation at 95 GHz and larger particle sizes. Especially in the precipitation region, the scattering at 95 GHz changes from the Rayleigh to the Mie regime. The centre panel in Figure 33 compares the attenuated total backscatter coefficient measurements of WALES at 532 nm flown on HALO with LNG measurements at 355 nm flown on the French Falcon. Besides the different spatial resolution (WALES: 15m (vertical) x 300 m (horizontal), LNG: 6 m (vertical) x 1000 m (horizontal)) the higher clear air backscatter at 355 nm is the most striking difference. While the lidar penetration depth is quite similar for both, the signal gradient and contrast between adjacent profiles is higher for WALES with its higher horizontal resolution. The bottom panel in Figure 33 shows the instrument masks for the WALES/MIRA (left) and LNG/RASTA (right) combination. The overlap region with radar and lidar measurements is the gray area, the radar only region is the blue area and the lidar only region is the green area. Both instrument combinations have a measurement overlap for most profiles. Due to the high sensitivity of MIRA, the overlap region is larger in measurements from HALO, where the radar sensitivity for ice clouds is obviously quite close to the lidar sensitivity.

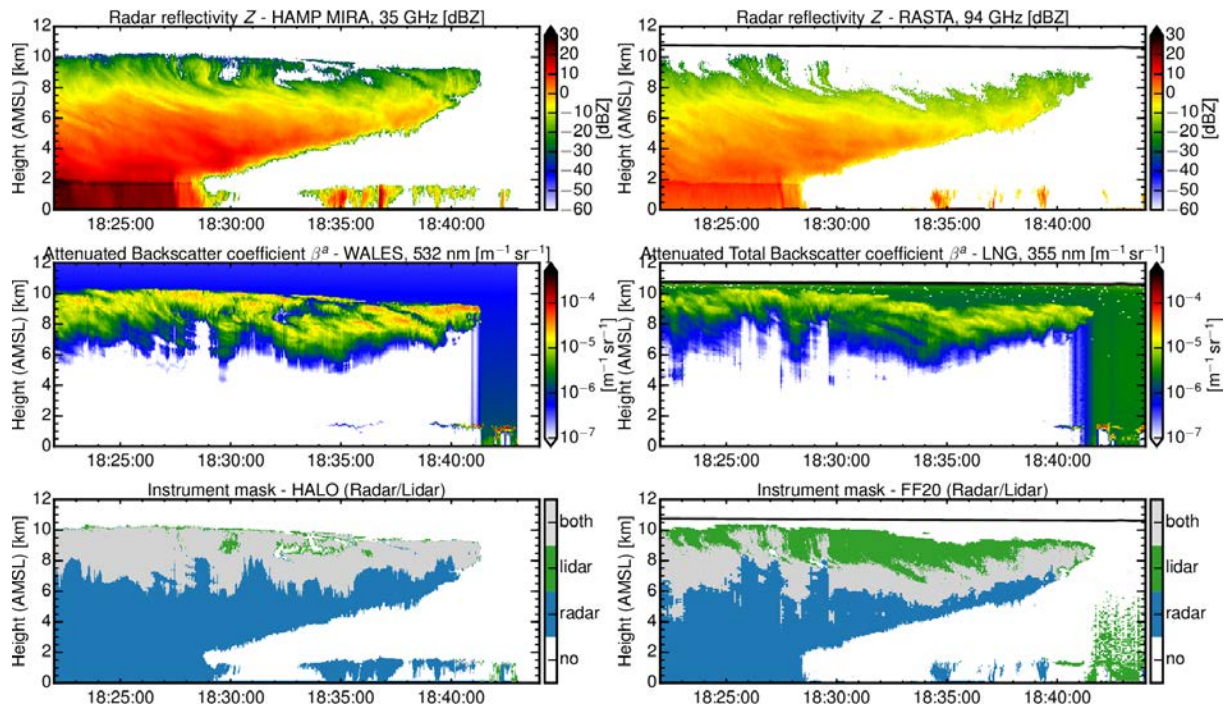


Figure 33. Comparison of Level 1 radar+lidar data which was measured with MIRA and WALES on HALO (left) and RASTA and LNG on the French Falcon (right) during a common flight leg on 9th October 2016 south of Island. Radar measurements are compared for 35 GHz and 94 GHz (top), lidar measurements for 532 nm and 355 nm (center). (Bottom) Comparison of different instrument overlaps.

4.2.2 Comparison of Level-2 retrieval (VarCloud) results of ice cloud microphysics

The following analysis will apply the previously mentioned VarCloud retrieval of ice cloud microphysics to the radar/lidar measurements during the common flight leg of HALO and the French Falcon shown in Section 4.2a. Three retrieved ice cloud properties are compared between HALO (left) and FF20 (right) in Figure 34, namely the retrieved ice water content (top), the retrieved effective radius (center) and the retrieved extinction (bottom). In the following, retrieval results with the HALO wavelength combination will be called ‘VarCloud (v3)’. The retrieval results with the French Falcon wavelength combination will be called ‘RALI (v3)’. The overall retrieval results are quite similar with increasing IWC and reff from 20 micron at cloud top towards lower cloud regions with reff larger than 80 microns. A closer inspection reveals differences especially in the lower cloud part. Here, the retrieved ice water content is lower using measurements on HALO compared to the retrieval results on the French Falcon. Conversely, the retrieved effective radius is larger on HALO in this region. In addition, the retrieved effective radius on cloud tops is mostly smaller HALO results. Similar to the retrieved ice water content, the retrieved optical extinction in the lower cloud region is smaller in HALO results.

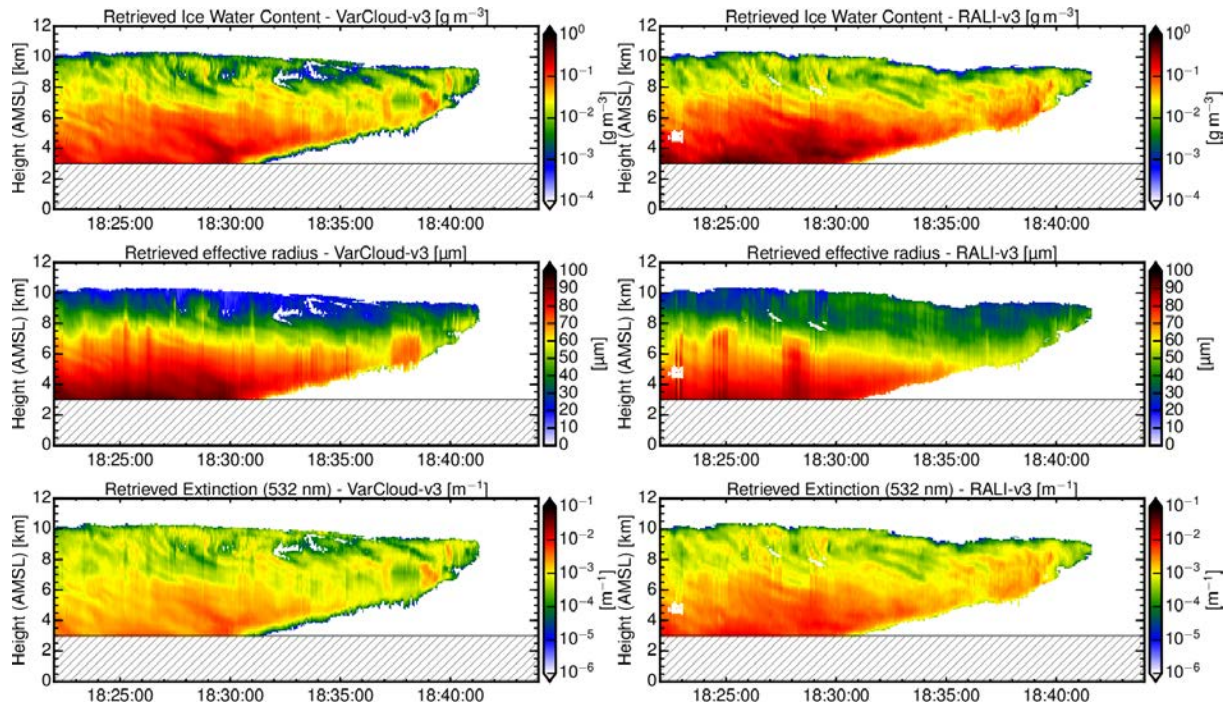


Figure 34. Comparison of Level 2 retrieval results from VarCloud (v3) of ice cloud microphysics using L1 data on HALO (left) and French Falcon (right) shown in Figure 33. The comparison is made for ice water content (top), effective radius (center) and optical extinction (bottom).

The lower optical extinction on HALO becomes also evident when the retrieved fields are used to calculate the optical thickness between 3 km and 12 km. In Figure 35, the retrieved optical thickness is compared using measurements from HALO (green) and the French Falcon (red). In the optically thicker cloud region measured during the first half of the common leg, the optical thickness peaks at around 10 for VarCloud (v3) on HALO while the optical thickness from RALI on FF20 peaks reaches values over 20. The retrieval in this optical thick cloud region is strongly dominated by the radar measurements. The largest part of the optical thickness difference should therefore be attributed to differences / limitations in the radar only part of the retrieval.

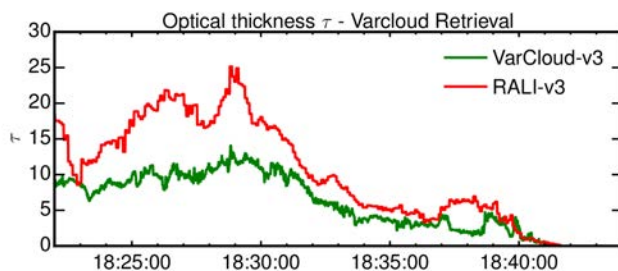


Figure 35. Comparison of retrieved optical thickness using VarCloud (v3) on HALO (green) and French Falcon (red) data corresponding to the retrieval results shown in Figure 34.

As the optical thickness of the cloud decreases and thus the influence of the radar only region, the absolute and relative difference between VarCloud (v3) and RALI decreases too. Closer inspection showed a very good agreement of optical thickness limited to a region between 6 km and 12 km throughout the common flight leg with relative differences between VarCloud (v3) and RALI smaller than 20%. This good agreement is also visible in Figure 35 for the whole

scene after 18:40 UTC where both instrument combinations have a large overlap. Figure 36 shows a more in-depth comparison of the retrieval results. On the left in Figure 36, the distribution of the retrieved ice water content is compared between VarCloud (v3) on HALO (green) and RALI on the French Falcon (red). The respective median value is marked by the vertical line. Like in the previous analysis, RALI on FF20 shows slightly larger IWC values with a median IWC of $3.9 \times 10^{-2} \text{ gm}^{-3}$ than VarCloud (v3) on HALO with a median of $2.9 \times 10^{-2} \text{ gm}^{-3}$. The largest differences become apparent at high IWC values, where VarCloud retrieves a maximum IWC of $2.8 \times 10^{-1} \text{ gm}^{-3}$, while RALI IWC values peak at $7.1 \times 10^{-1} \text{ gm}^{-3}$. In contrast, the probability for smaller IWC values between 10^{-3} and 10^{-2} gm^{-3} is larger for VarCloud on HALO. This can be explained by the higher sensitivity of MIRA but also by the slightly different cloud top structure in the HALO measurements at around 18:35 UTC caused by the lateral flight path mismatch of 250 m. The shapes of the retrieved effective radius distributions are similar with slightly different medians of $60 \text{ }\mu\text{m}$ (VarCloud) and $53 \text{ }\mu\text{m}$ (RALI). The distribution from VarCloud is slightly broader and is a little bit skewed towards larger effective radii. In contrast, the RALI distribution is more skewed towards smaller values. These differences originate mainly again from the lower, optically thicker cloud regions with radar-only results.

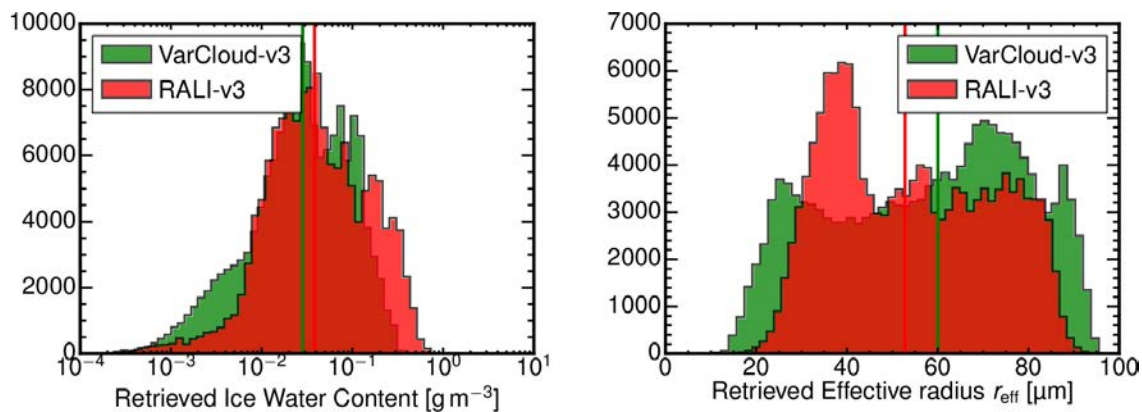


Figure 36. Comparison of retrieved ice water content distribution (left) and retrieved effective radius distribution (right) using HALO (green) and French Falcon (red) data.

4.3 CC – underpasses and comparisons

In this section we focus on 3 CloudSat-CALIPSO underpasses carried out by the French F20 on the 2nd, 5th and 14th of October 2016. Note that CALIPSO was not operating during the 5th of October and therefore there is no available DARDAR product for this flight. The aircraft data are compared against DARDAR product (MASK-V2 and CLOUD-V2). DARDAR (CloudSat-CALIPSO) merged products are available through AERIS/ICARE website (<http://www.icare.univ-lille1.fr>). For each flight we present a map including the A-Train and F20 tracks. The calibrated reflectivity measured by CloudSat and RASTA, the lidar backscatter at 532 nm from CALIPSO (when available) and LNG are also presented. CloudSat and RASTA do not use the same convention for the calibration. The dielectric constant for water ($|Kw2|$) is set to 0.75 for CloudSat while RASTA uses a different convention and $|Kw2|$ is set to 0.93. Therefore the CloudSat reflectivity (in $\text{mm}^6 \text{ m}^{-3}$) has been multiplied by a constant (0.75/0.93) to account for the difference in calibration assumptions for RASTA and CloudSat. In addition

to these measurements, the synergistic radar-lidar cloud products are shown for both A-Train and F20. A full description of the radar-lidar processing is given in Annex 1 (Data Acquisition Report).

4.3.1 Underpass #1 : 2016/10/02 (F7-French Falcon)

On the second of October 2016, there was a cyclone approaching the vicinity of Iceland associated with active fronts and thick clouds. There was a strong wind forecast for the evening in Keflavik. The Overpass with satellite occurred at 14:09 (Figure 37) in the south west of the Icelandic island, the granule number (CloudSat reference) is 2016276130250_55491. The F20 was sampling the inflow of a warm conveyor belt in cloudy conditions just below 9 km. CloudSat and CALIPSO were flying from south to north while the F20 was sampling the scene in the opposite direction.

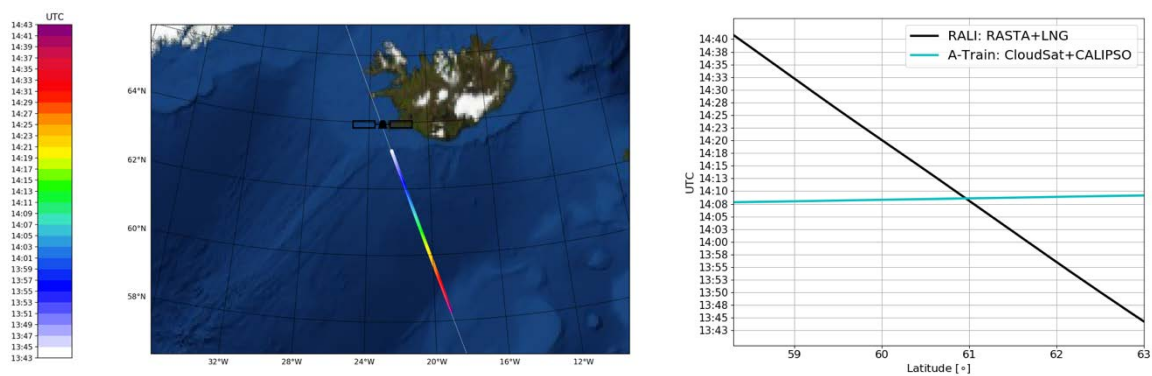


Figure 37: F20 and CloudSat-CALIPSO tracks for 2nd of October 2016. White line represents the satellites tracks and coloured line shows the F20 track as a function of time. The right-hand side plot shows the time as a function of latitude.

The measurements collected by RALI and the A-Train are shown in Figure 38, the attenuated backscatter, reflectivity and the merged target classification are given as a function of latitude and height. At the start of the scene (~58° latitude) the time difference was about 30 min between aircraft and satellite measurements, at the end of the scene (63°) the time shift was about 25 min. The best co-location time was obtained at 61°. As the aircraft was flying during daytime CALIPSO background signal suffered from a strong contamination. The narrower field of view of LNG limits this contamination and therefore the sensitivity of the airborne lidar is much higher. This contamination by the solar photons mainly affects the aerosol and the ice cloud detection while the liquid layers are reflective enough to remain above the background noise. We have a good agreement between the two lidars in case of strong backscatter, especially between 60° and 60.5° at 7km and 61° and 62.5° between 4 and 5 km. RASTA and CloudSat also exhibit very similar patterns and the differences are more pronounced on the right edge of the scene due to the time shift and the less homogeneous situation. We can notice that the sensitivity of CloudSat remains almost constant with range while RASTA is much less sensitive as we go away from the radar. The DARDAR and RALI target classifications agree for the large pictures and the main discrepancies originate from the time shift and the

melting layer location leading to an artificial increase in IWC, extinction and effective radius near 2 km altitude between 58 and 59.5°.

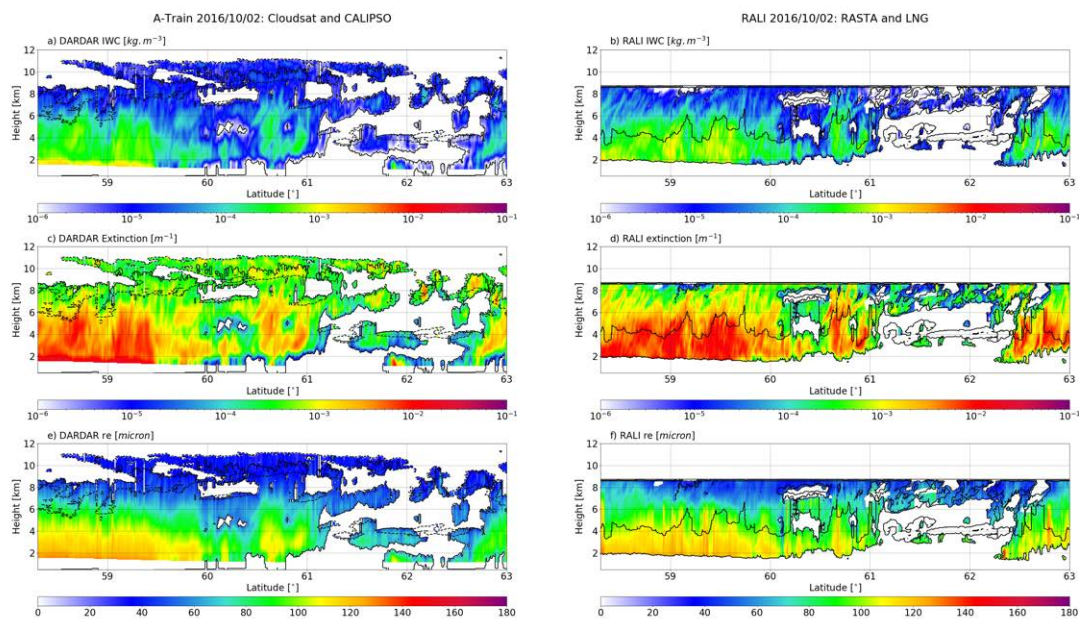


Figure 39: Synergistic cloud retrievals results as a function of latitude for the 2nd of October, IWC, visible extinction and effective radius correspond to the top, middle and bottom plots respectively (DARDAR on the left-hand side and RALI on the right-hand side).

While the Latitude x height distribution of the cloud parameters presented in Figure 39 allows us to compare qualitatively the retrievals, it remains difficult to carry out direct comparisons due to co-location issues (in time and space). In Figure 40 we propose to look at the distribution of IWC (panels e and f) as a function of altitude (the colour bar indicates the number of hits in each altitude and IWC intervals, 500m and 0.1 g/m³ in logarithm scale respectively). Note that these statistics are built on gridded data in order to compare the products with similar resolutions. DARDAR and RALI mean values are computed for each 0.01° latitude bin (for the horizontal scale) and 500m bin (for the vertical scale).

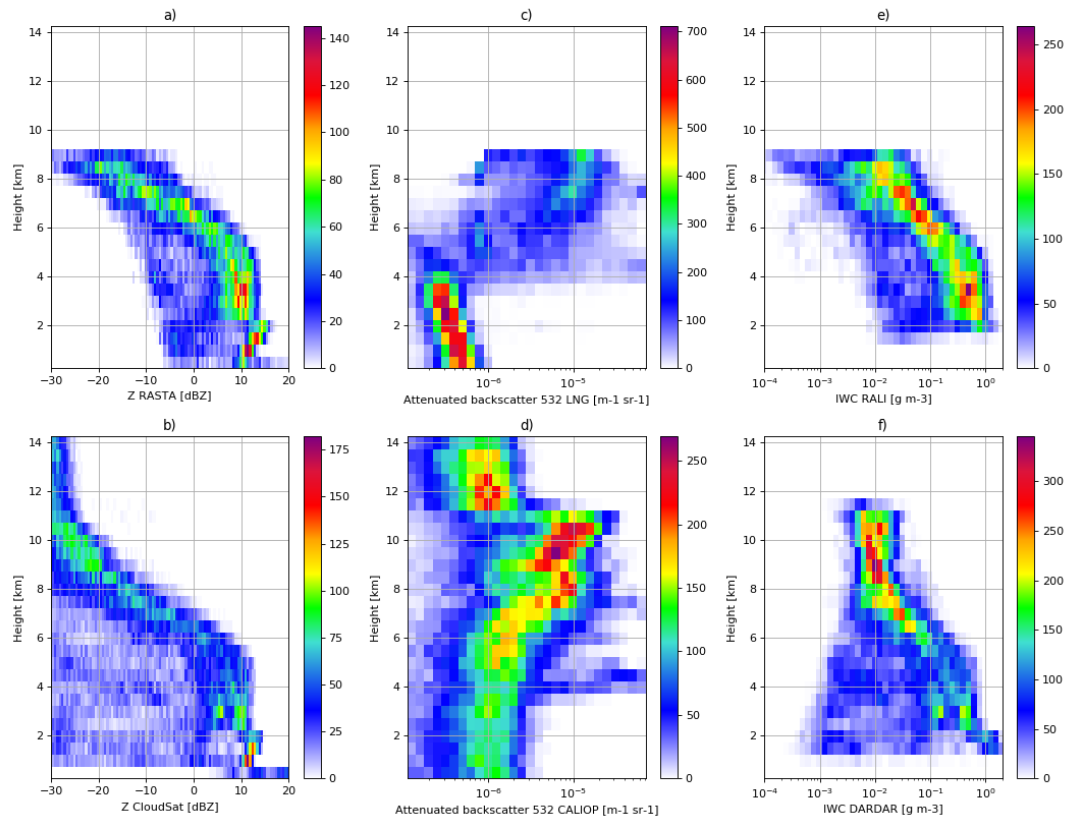


Figure 40: Vertical distribution of measured reflectivity (a and b), attenuated backscatter at 532nm (c and d) and retrieved IWC (e and f) for both RALI and DARDAR.

From this figure we can see that the two distributions related to the largest values of IWC (i.e. larger than 10^{-2} g/m^3) are very consistent. The lowest values of IWC, on the other hand, show large differences which are explained by the lack of the sensitivity of the RASTA compared to CloudSat. This is confirmed in panels a and b (RASTA and CloudSat respectively) showing the distributions of the reflectivity as a function of height. The distributions of the largest reflectivity are very similar but the detection threshold of RASTA does not allow us to measure the same range of reflectivity. Unfortunately, the lidar measurements cannot compensate the lack of sensitivity of the radar in this situation as the lidar is most of the time already extinguished. Panels c and d illustrate LNG and CALIOP attenuated backscatters respectively. The impact of the solar contamination is obvious on the CALIOP signal with a flat molecular signal below 4 km.

4.3.2 Underpass #2 : 2016/10/05 (F9-French Falcon)

On the fifth of October a diabatic Rossby wave in North-west Atlantic was evolving into a very deep low between Iceland and Greenland. The cyclonic outflow of the warm conveyor belt was close to the centre of the low. The satellite underpass with Cloudsat (only) was located over Greenland in a region with moisture advection and orographic precipitation. The corresponding CloudSat granule number for that underpass is the following: 2016279133339_55535. The overpass configuration is presented in Figure 41, the area of

interest was located between 66.5° and 69.7° of latitude (15:05 and 14:28 UTC respectively), the meeting point was reached at about 14:42 i.e. about 68.5° of latitude.

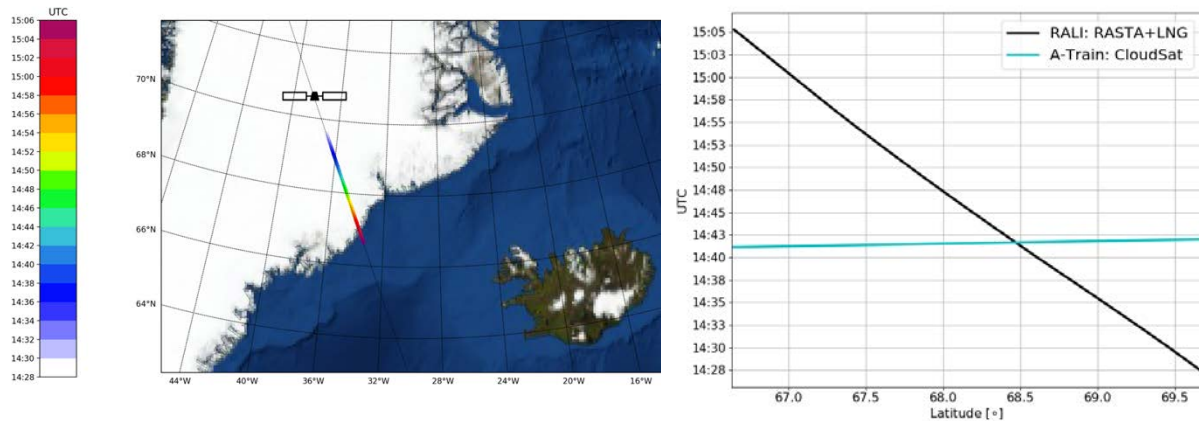


Figure 41: Same as Figure 37 for the 5th of October 2016

The RALI measurements, the associated target classification and CloudSat reflectivity are given in Figure 42. A very strong backscatter is observed at the cloud top in addition to the very low reflectivity (detected by Cloudsat) it suggests that the particles are small and highly concentrated. When the lidar attenuated backscatter gradient is getting to sharp there is a potential signature of supercooled layer before 66.8° and around 67° of latitude. The lack of sensitivity of RASTA does not allow us to consider the mixed phase category. Despite this sensitivity issue, RASTA and CloudSat reflectivities agree well. The CloudSat reflectivity is clearly affected by the surface clutter above Greenland and the very low-level clouds are not detected while RASTA can pick very low-level clouds which are embedded in the ground clutter. There is an area between 2 and 5 km with high reflectivity which is observed by both RASTA and CloudSat, this area probably corresponds to very large snowflakes or highly concentrated large ice crystals. The slight reflectivity enhancement seen on CloudSat could be due to multiple scattering. The RALI retrieved extinction, IWC and re values are increasing in this area as shown in Figure 43. The reflectivity distribution as a function of altitude supports the hypothesis of multiple scattering effects (Figure 44 a, b, c), since the reflectivity profile is consistent above 6 km but below this altitude CloudSat reflectivity appears larger. This effect is also shown in panel d), the scatter plot confirms that there is no bias between RASTA and CloudSat reflectivities but a blob appears for large reflectivities (i.e larger than 10dBZ).

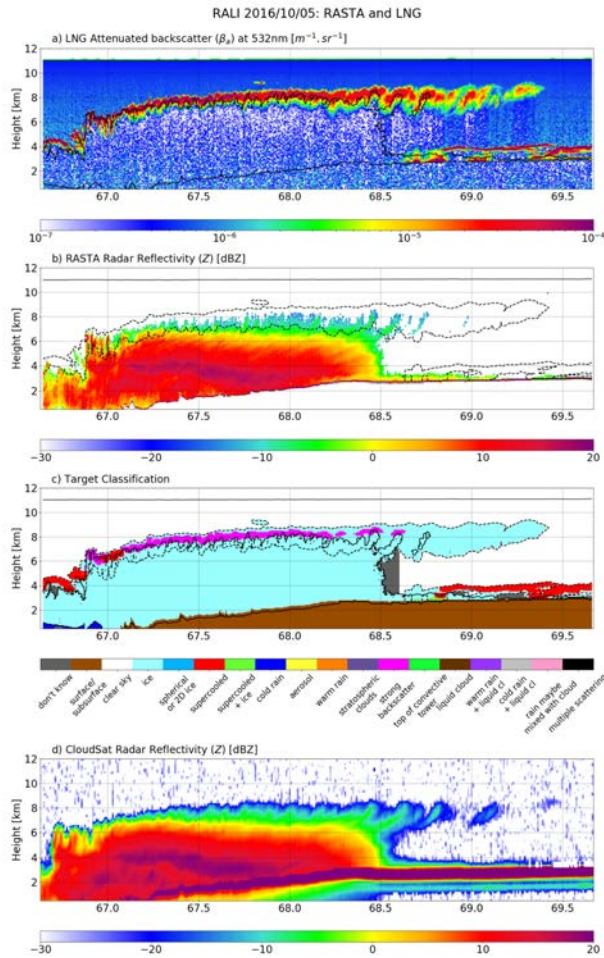


Figure 42 : RALI and CloudSat measurements for the 5th of October. LNG attenuated backscatter at 532nm, RASTA reflectivity, RALI synergistic classification and CloudSat reflectivity are shown in panels a), b), c) and d) respectively.

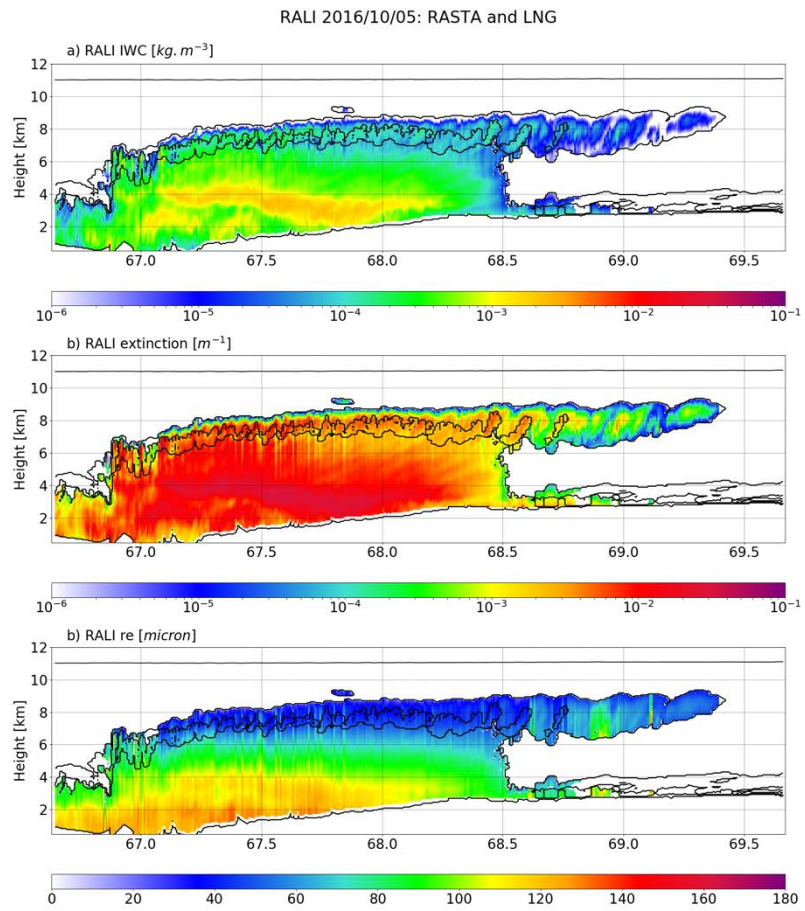


Figure 43: RALI retrieval as a function of latitude for the 5th of October. IWC, visible extinction and effective radius are shown in panels a), b) and c) respectively.

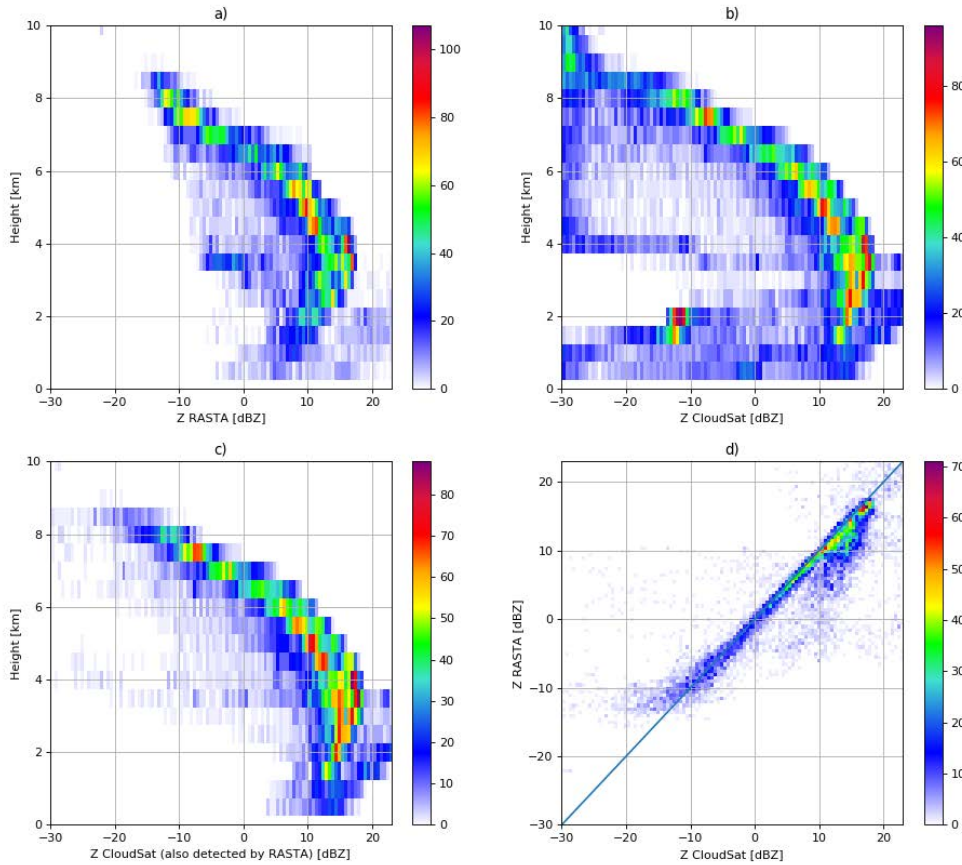


Figure 44: Vertical distribution of reflectivity as function of height, measured by RASTA and CloudSat, panels a) and b) respectively. Panel c) is the derived using CloudSat reflectivity when RASTA also detects an echo. Panel d) illustrates the RASTA reflectivity as a function of CloudSat reflectivity

4.3.3 Underpass #3 : 2016/10/14 (F18-French Falcon)

On the 14th of October 2016 there was an anticyclonic situation on the northern Atlantic with a cyclonic activity around British Islands (meteorological context is given in section 4.14.1.1). The cloudy region located in the north of Scotland was favourable for intercomparisons between the aircraft and the A-Train underpass (at around 12:54, Figure 45). The CloudSat granule number for that underpass is 2016288114840_55665.

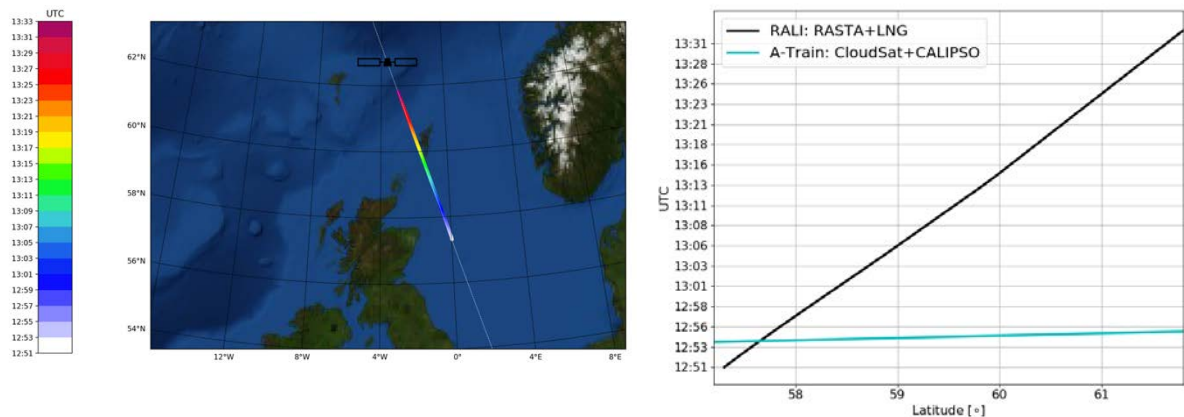


Figure 45: Same as Figure 37 for the 14th of October 2016

The segment of interest was located between 57° and 62° of latitude and this time the aircraft and the satellite were flying in the same direction. As the aircraft took off at 12:24 the satellite ground track was joined only a few minutes before the meeting point.

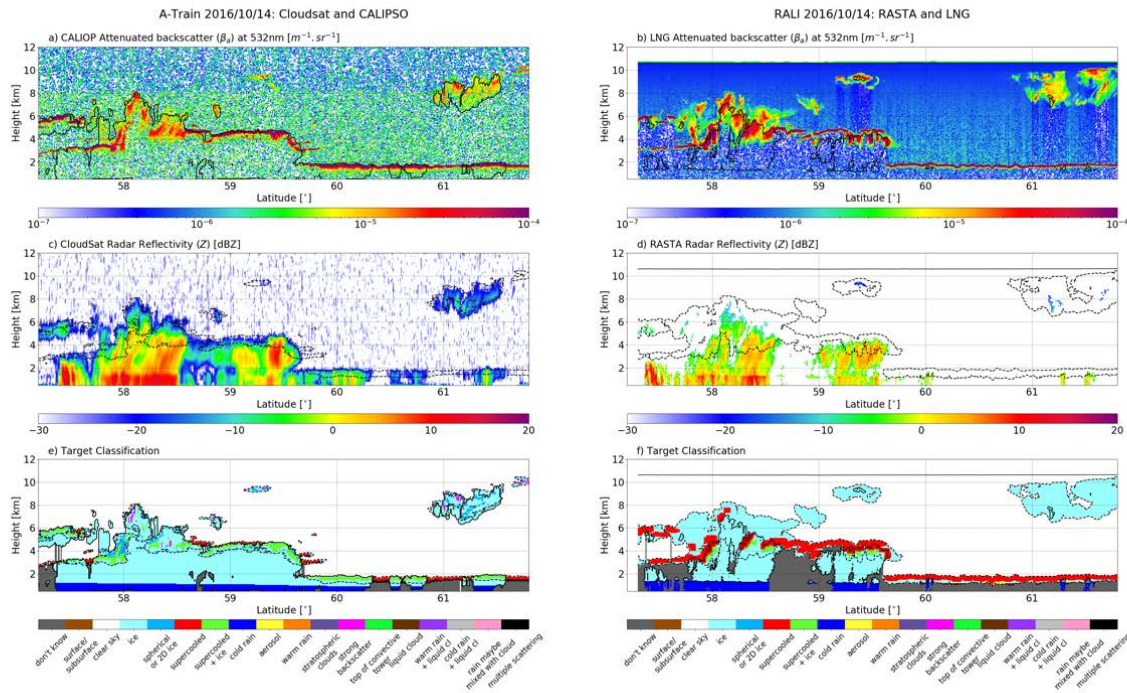


Figure 46: Same as Figure 38 for the 14th of October 2016

The observed situation is very complicated with heterogeneous cloud layers, even between 57° and 58° where we have a time shift which does not exceed 5 min. The observed cloud structures are unexpectedly very different despite the difference in sensitivity between RASTA and CloudSat. This is confirmed by the statistics of the reflectivity profiles shown in Figure 47. The distributions of CloudSat reflectivity (only where there is a possible detection by RASTA) and RASTA reflectivity are consistent above 4km if we only focus on the largest values however below this altitude there are large differences. Panel d) represents a scatter plot between CloudSat and RASTA reflectivity and there is a disagreement between the two radars up to 5 dB. There is no obvious bias that could be due to a calibration issue so we could assume that the differences are due to mis-location of the cloud/precipitation system. In some cases, RASTA observes larger Z and in other cases lower values than CloudSat.

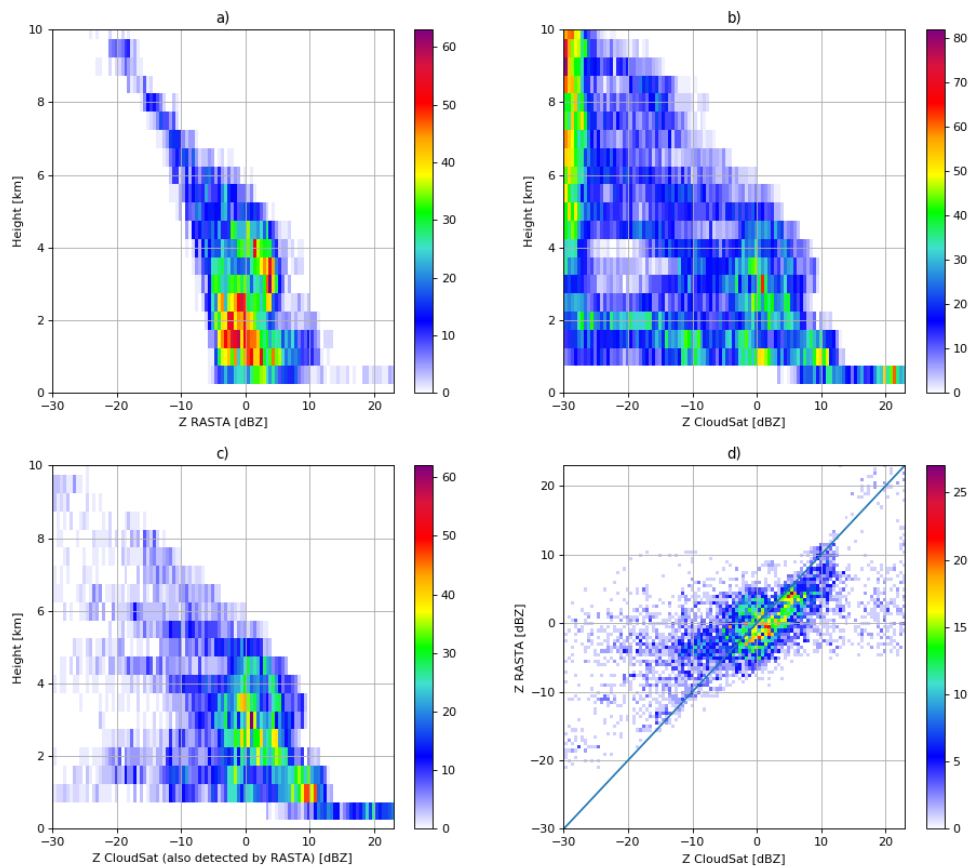


Figure 47 : Same as Figure 44 for the 14th of October 2016

As a result, we cannot expect a good agreement between the retrieved properties. The differences in reflectivity are also critical here as the lidar contribution is rather limited due to the strong extinction coming from the supercooled located at cloud top. Figure 48 presents the ice cloud properties retrieved using RALI and CloudSat and CALIPSO. As expected we notice that the order of magnitude for the retrieved properties is consistent but the location of the cloud structure is not consistent. Looking at the IWC distribution for the whole common leg (Figure 49) we can see that the envelop for the largest IWC remains consistent with a very similar slope. The distribution for the lowest values, on the other hand, is very different. This is mainly due to the sensitivity difference between the radars for the lowest altitude levels (advantage to CloudSat) and the lidars for the highest altitudes (advantage to LNG).

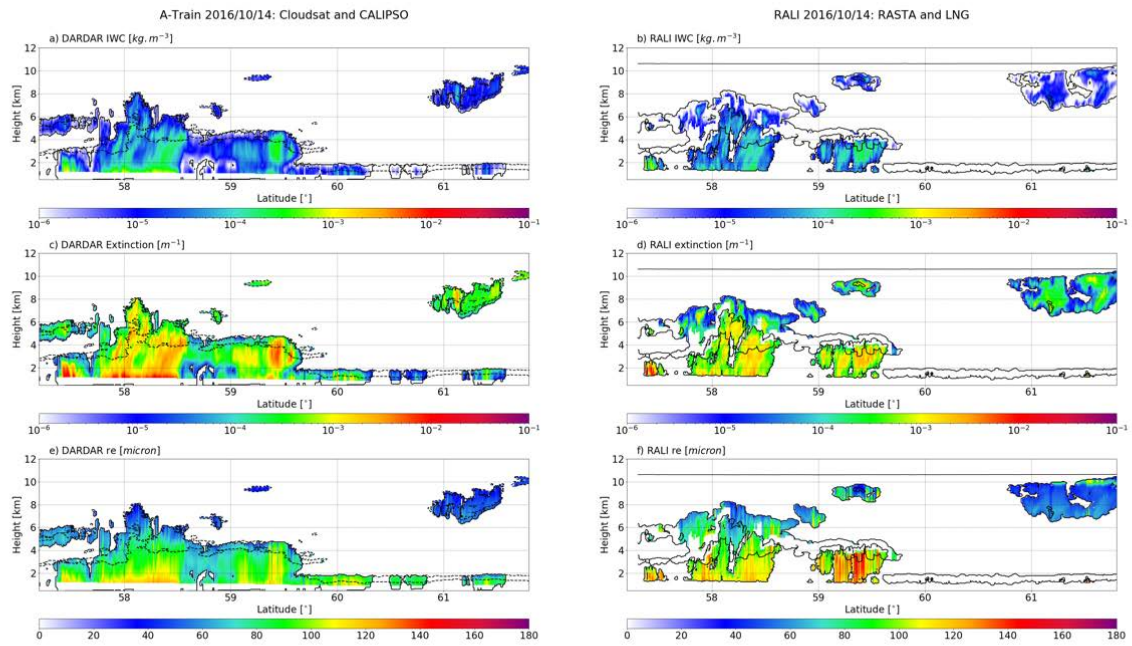


Figure 48: Same as Figure 39 for the 14th of October 2016

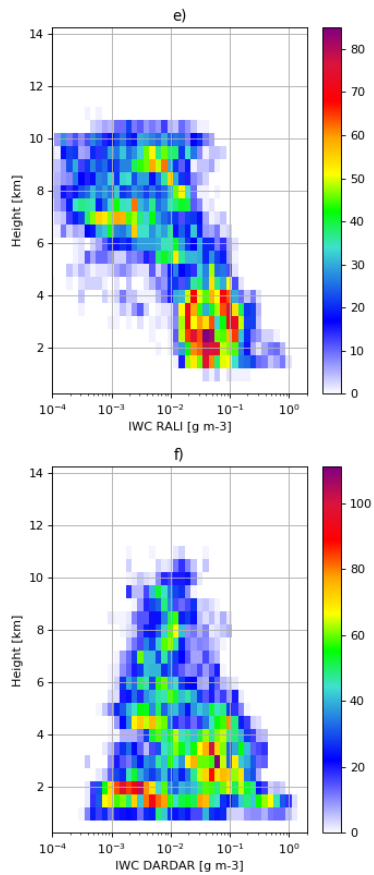


Figure 49: Same as Figure 40 for the 14th of October 2016 with a focus IWC retrievals

4.3.4 Conclusions and remarks regarding the satellite underpasses

Satellites underpasses are crucial for direct instrument calibration and validation of products however it remains a difficult exercise even for very experimented teams. There is a strong dependence on the meteorological conditions for instance a homogeneous system is much simpler to sample (for example the case over Greenland, 7th of October 2016) than a sparse one (14th of October 2016). It is also recommended to carry out many joint legs in order to increase the statistics and improve the assessment of the satellite measurements and products. As the velocity of the aircraft is not comparable to the spacecraft the co-location in time is very challenging. Perhaps we could suggest to slow down the satellite but then it would dive into the atmosphere and crash...

We also notice that the sensitivity of the radar could be an issue for cloud products but it has no impact on the calibration exercise. With these co-located measurements, it is also possible to investigate the multiple scattering contribution which is now well forward modelled but still depends on microphysics assumptions and the constraints brought from space measurements may be limited in these situations. The solar photons contamination can also be an issue as seen for CALIPSO and the airborne lidar is less sensitive to this due to its smaller foot print. The finest resolutions, both horizontal and vertical, of the airborne system is also an advantage compare to the coarser resolution of the spacecraft's instruments. We also showed that the higher resolution can have an impact on the target classification. Despite the difference in instruments characteristics (technology, resolution...) it is important to be able to run very similar algorithm on both platforms, including the target classification.

4.4 EarthCARE resolution

The next analysis will compare airborne measurements from WALES and MIRA with spaceborne measurements from CALIOP and CloudSat on the A-Train first on their native resolution and then on the resolution of EarthCARE. To this end, an A-Train underpass with HALO is used which was performed during NAWDEX on 14th October 2016 over the North Sea. The common flight leg was performed between 57°N, 0°E and 62°N, 3°E beginning at 12:53 UTC and ending at 13:33 UTC. The flight leg cut through a precipitating band of convection of an occluded front which was associated with a cut-off low pressure system west of the British Isles. Figure 50 compares radar measurements from MIRA on HALO (top) and the spaceborne CloudSat (bottom). The centre plot shows MIRA data down-sampled from its native resolution (vertical: 30m x horizontal: 300m) to EarthCARE's CPR resolution (vertical: 500m @ 100m x horizontal: 750m @ 1000m).

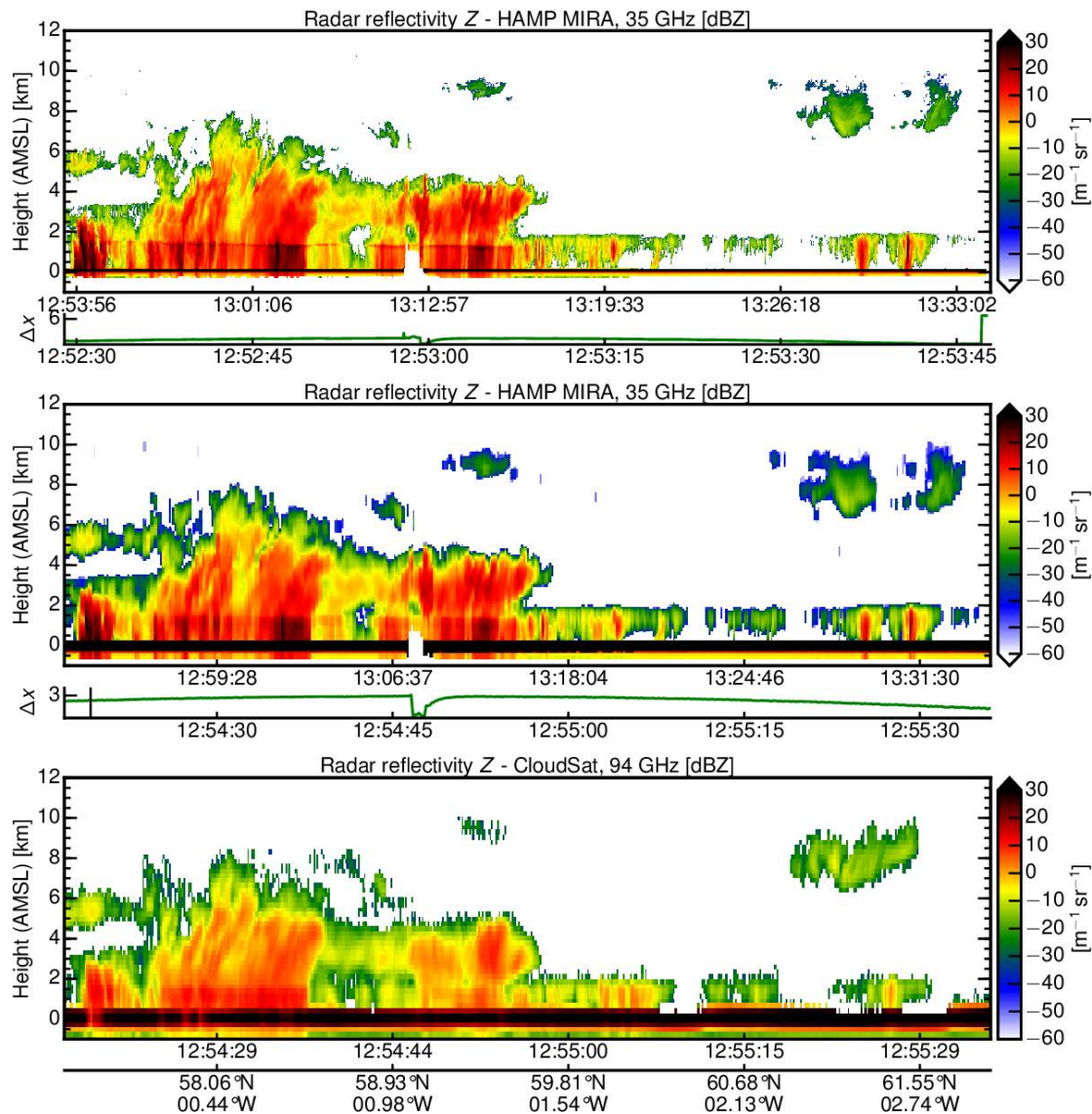


Figure 50. Comparison of radar measurements from MIRA on HALO (top) and the spaceborne CloudSat (bottom) during the A-Train underpass on 14th October 2016 over the North Sea. The centre plot shows MIRA data down-sampled from its native resolution (30m x 80m) to EarthCARE's CPR resolution (500m@100m x 750m@1000m). The additional axes show geographical location, lateral and time mismatch.

The additional axes show the lateral mismatch between the footprints of the airborne and spaceborne instrument (green), the respective time and the geographical location. For the first part of the flight leg, where the time difference between aircraft and satellite is smaller than 20 minutes, MIRA measurements match very well with CloudSat measurements. Measurements with a larger time difference show similar cloud structures but greater differences. With the down-sampling of MIRA data to the larger vertical footprint of CPR (centre panel in Figure 50), the resolution of cloud structures and the ground return becomes more similar with CloudSat. The analogue comparison between airborne and spaceborne lidar instrument is done in the next step. Figure 51 shows lidar measurements from WALES on HALO (top) and the spaceborne CALIOP (bottom) during the A-Train underpass already discussed in Figure 50. The centre plot shows WALES data down-sampled from its native resolution (vertical: 15m x horizontal: 300m) to EarthCARE's ATLID resolution (vertical: 100m x horizontal: 285m). Like in the last discussion, the additional axes give lateral and time

mismatch as well as geographical location. Since the resolution of WALES and ATLID is not that different, only minor difference are visible between the native WALES resolution (top panel) and its resampled version (centre panel).

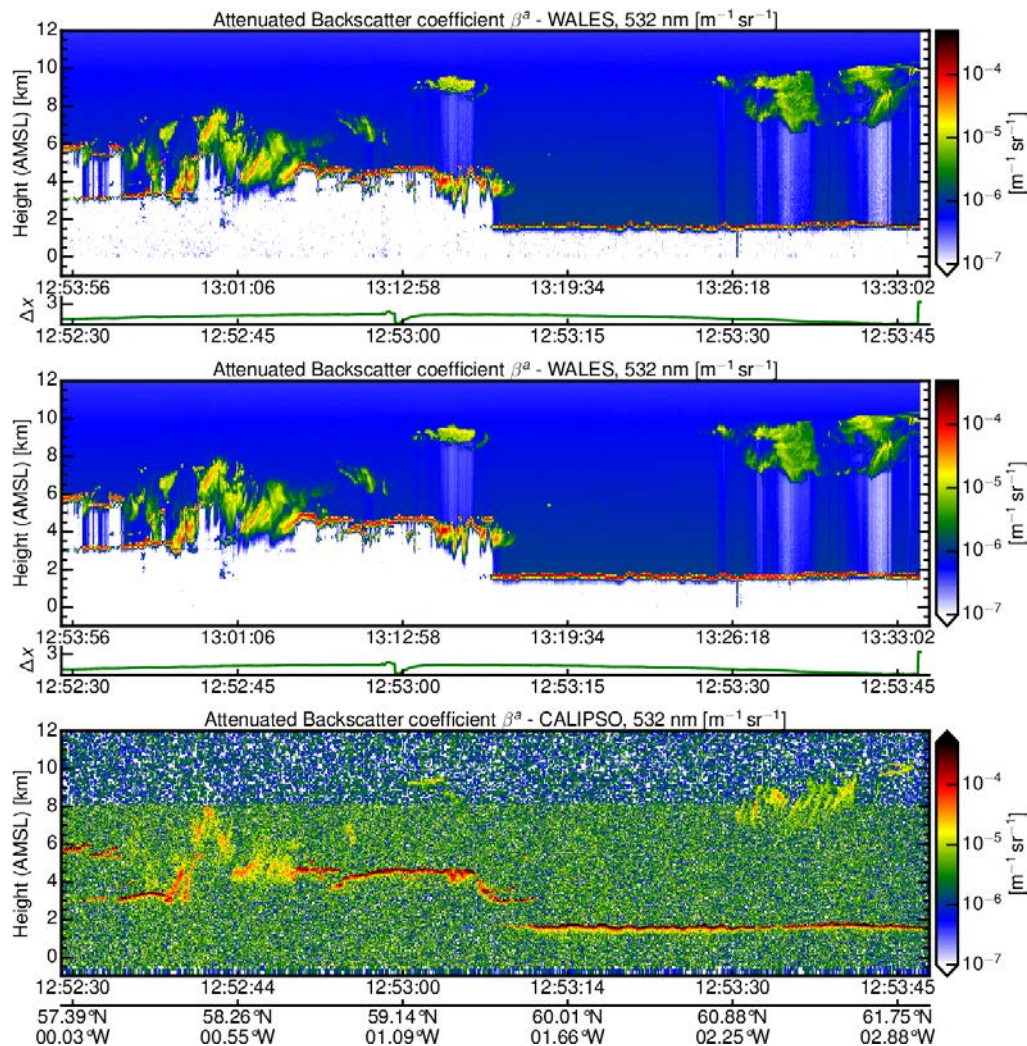


Figure 51. Comparison of lidar measurements from WALES on HALO (top) and the spaceborne CALIOP (bottom) during the A-Train underpass shown in Figure 50. The centre plot shows WALES data down-sampled from its native resolution (15m@15m x 20m@300m) to EarthCARE's ATLID resolution (100m@100m x 30m@285m). The additional axes show geographical location, lateral and time mismatch.

As an example, sharp cloud boundaries get smeared out so that the maximum observed backscatter is smaller. In contrast to the comparable radar results, the signal quality between WALES and CALIOP differs significantly. While the backscatter from thin ice clouds and clear air is very well resolved in WALES measurements, the CALIOP signal is very noisy due to daylight contamination and the much larger distance of the spaceborne instrument. Nevertheless, the stronger backscatter from water clouds agrees very well between both instruments.

4.5 Closure study – comparing retrieval results and passive measurements

4.5.1 Method

To evaluate the performance of the synergistic radar-lidar algorithm to retrieve ice microphysical properties a closure study was performed. Similar as it will be done for the future EarthCARE measurements we retrieved ice water content and ice effective radius for the ice cloud detected by lidar and radar using the optimal estimation retrieval described by Delanoë et al., 2008 and Cazenave et al., 2018 (submitted). In a next step we used the retrieved ice microphysics to calculate the spectral radiance on top of the cloud. This is done by radiative transfer calculations using the libRadtran (Mayer 2009; Buras and Mayer 2011; Emde et al., 2016) software package. The retrieved spectral radiances are then compared to measured radiances onboard the HALO aircraft with the specMACS imaging cloud spectrometer (Ewald et al., 2016). An overview of the method and the included assumptions is given in Figure 52.

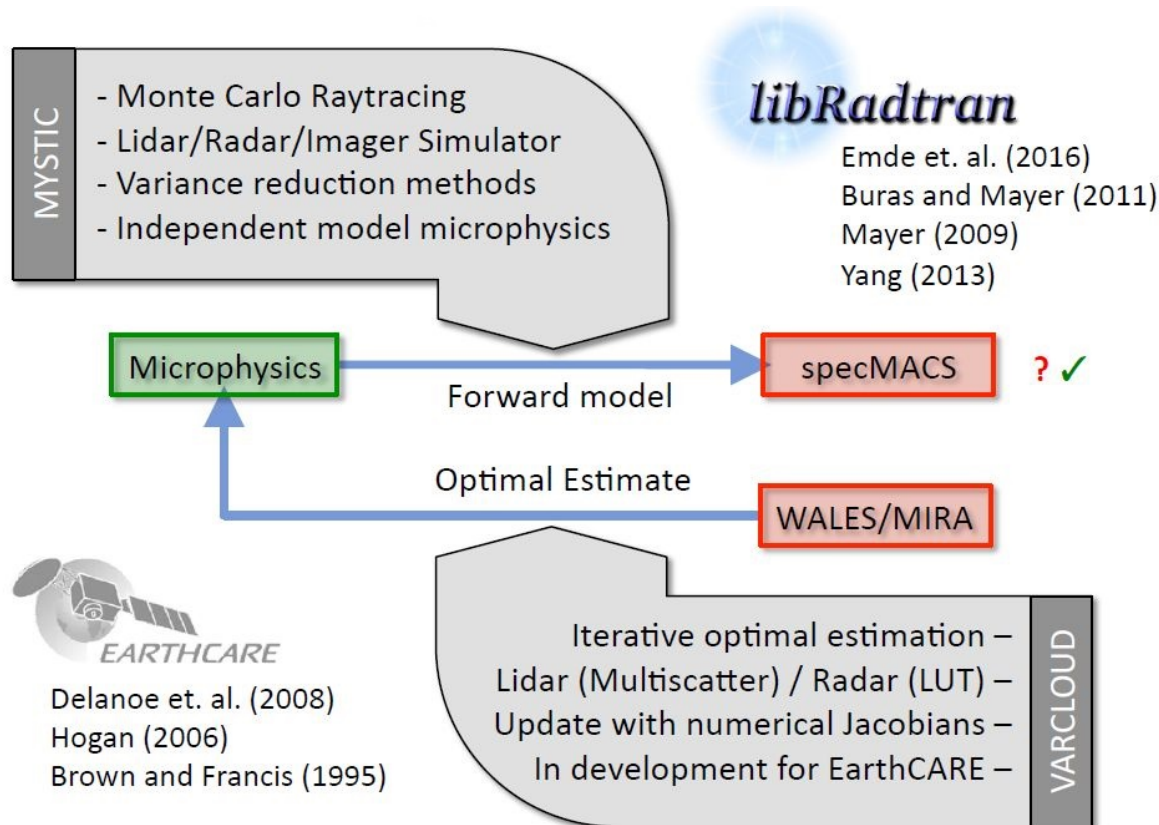


Figure 52: Schematic description of the performed closure study.

To exclude the influence of water clouds in lower layers the use of spectral measurements at 1900 nm are most appropriate. As it is shown from simulations of the 2-way transmission at different altitude (Figure 53) different wavelengths are differently affected by water vapor in the atmosphere. E.g. at 870 nm the measurements are nearly unaffected by absorption due to atmospheric water vapor and thus information throughout the atmosphere contributes equally to the measured signal. On the other hand, measurements at e.g. 1900 nm are most affected by absorption in the atmosphere and thus the contribution of different height layers is different. As it is shown in Figure 53 information from the lowermost height regions (up to

about 4 km) do almost not contribute to the measured signal. Thus the influence of the low level clouds below 2 km height detected by radar and lidar (Figure 55) in the first measurement examples are not considered in the comparison of simulated radiances and measured radiances when using 1900 nm.

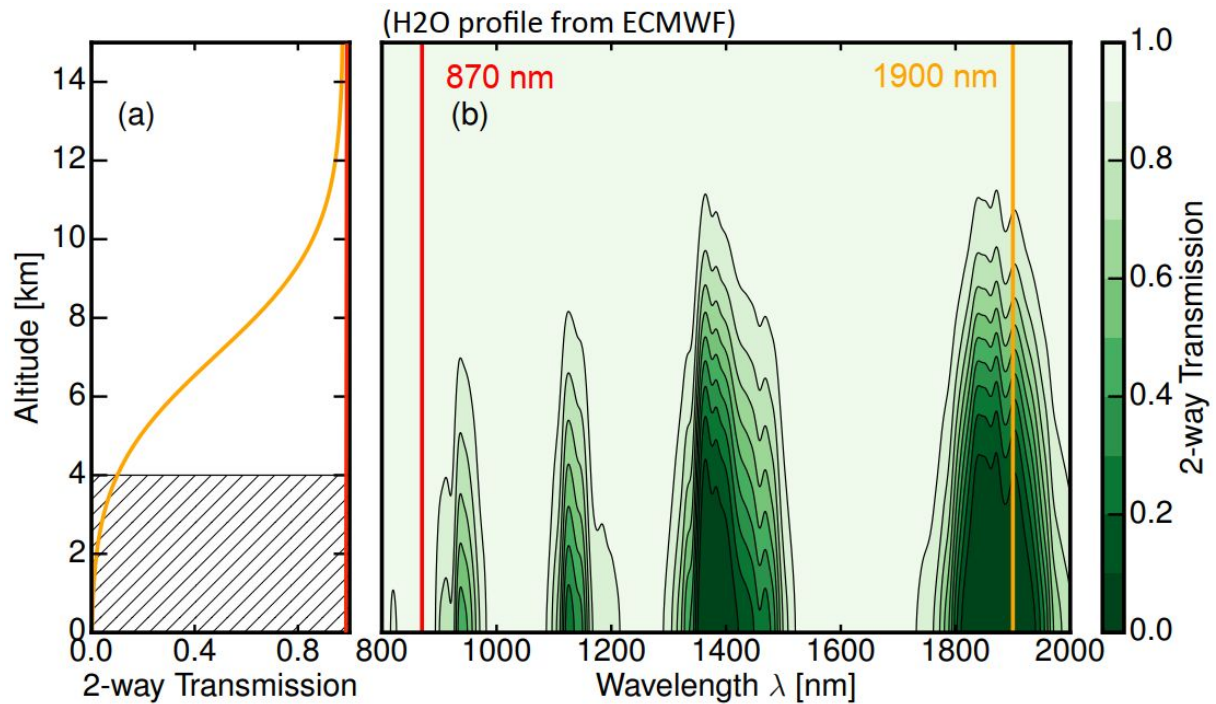


Figure 53: Simulated 2-way transmission through the atmosphere for different wavelengths.

4.5.2 Homogeneous cloud structure

For a first closure we used the measurements of the flight performed on 1 October 2016 starting in Iceland in southward direction (Figure 54). The flight crossed a homogenous cloud structure connected to the frontal zone of an extra-tropical low-pressure system.

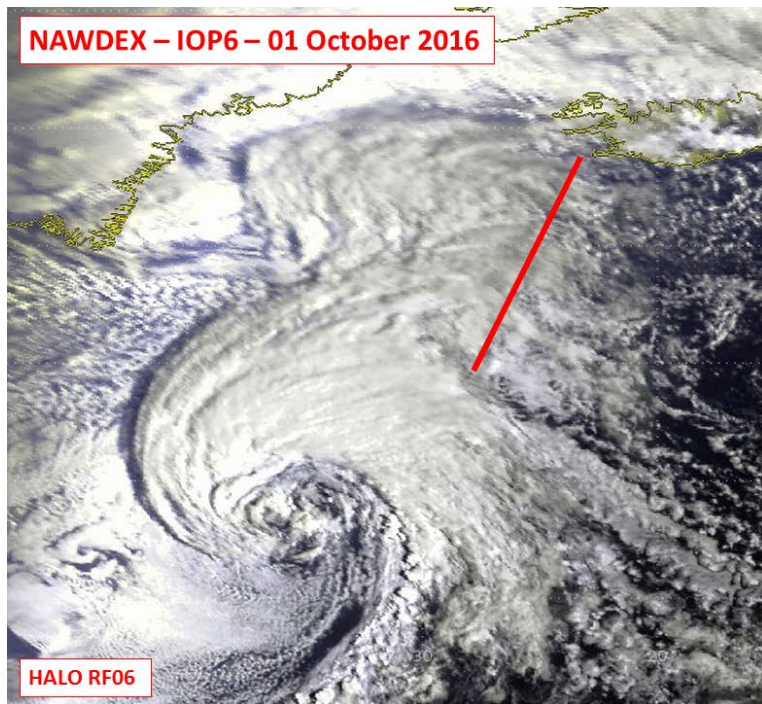


Figure 54: Satellite image of the cloud situation on 1 October 2016 southwest of Iceland and overlaid flight track (red line).

Both active remote sensing measurements on HALO, the lidar and the radar, provided good coverage of the cloud system (Figure 55). Thus both measurements could be used in almost the whole cloud cross section to retrieve the microphysical properties. At about 9:00 UTC we started to cross the cloud. In the beginning of our measurements, the cirrus cloud extended from about 6 km to about 8 km height. In the progress of our measurements the vertical extent of the cirrus cloud increased. The cloud base as identified by the radar was at about 4 km; the cloud top identified by the lidar was at about 10 km height. The radar reflectivity ranged between about 5 dBZ in the lower part of the cirrus and about -35 dBZ in the upper part. The corresponding attenuated backscatter coefficient at 532 nm at the upper part of the cirrus cloud was in the order of $10^{-4} \text{ m}^{-1}\text{sr}^{-1}$. At parts of the cloud with high reflectivity the attenuated backscatter coefficient showed signatures of saturation.

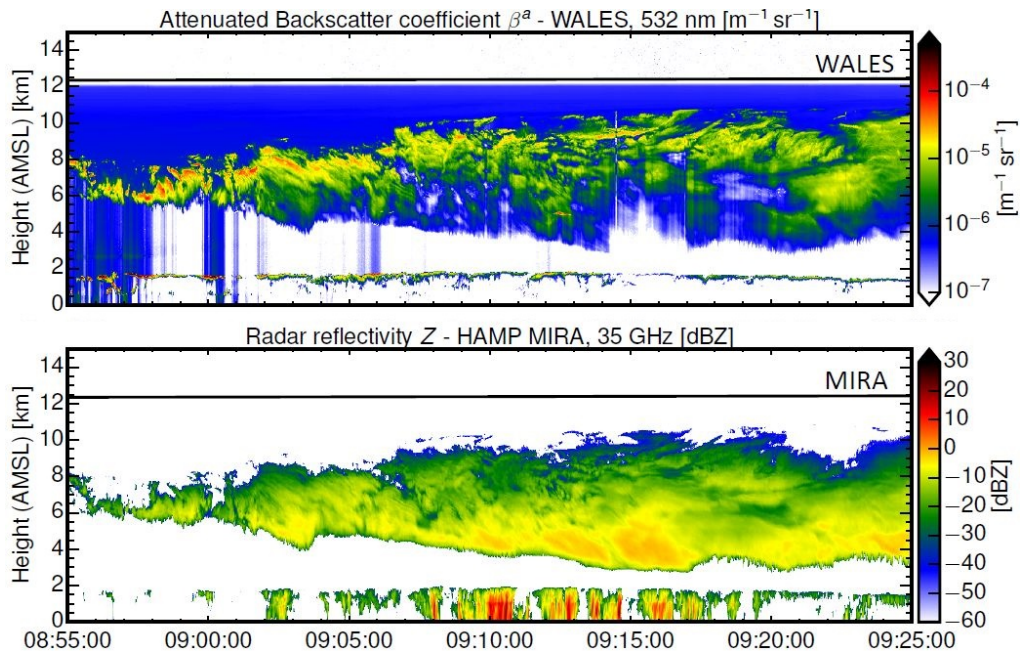


Figure 55: Measurements of the attenuated backscatter coefficient (upper panel) and the radar reflectivity measured during the flight shown in Figure 54.

Applying the synergistic radar-lidar retrieval based on the optimal estimation method (Section 4.5a) the ice microphysical properties, the ice water content and the effective radius are retrieved (Figure 56). Regions with high radar reflectivity are connected with high ice water content and large ice effective radii. Those areas are found in the lower part of the cirrus cloud. In the upper part of the cloud the smallest ice effective radii are found. While also small ice water content is found in the upper part of the cloud the vertical gradient of ice water content is not as distinguished as for the effective radius.

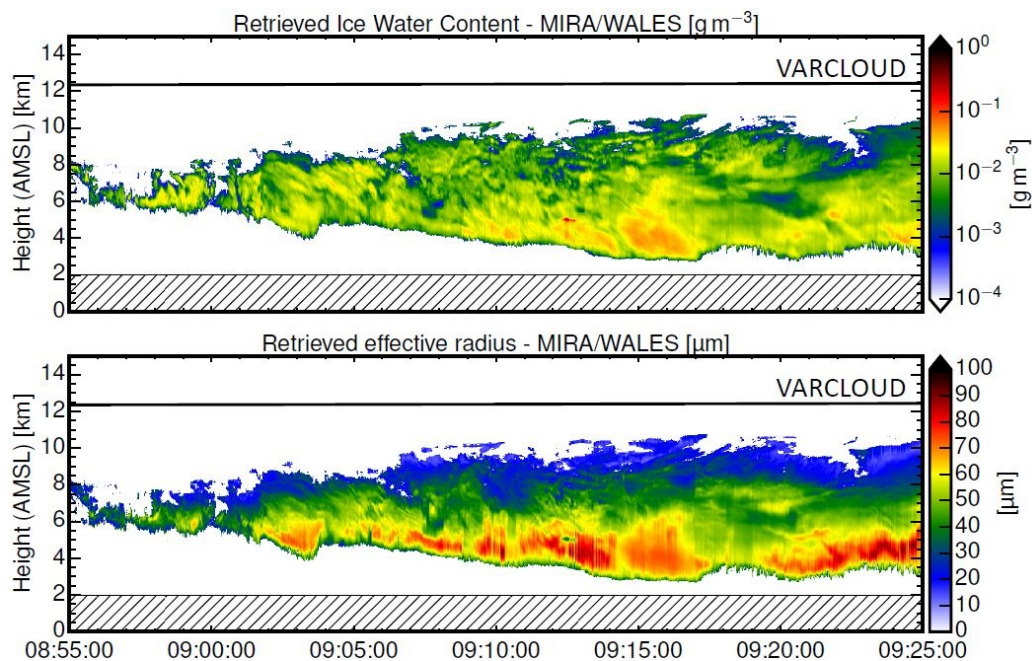


Figure 56: Retrieved ice water content (upper panel) and ice effective radius (lower panel) for the measurements performed on 1 October 2016 southwest of Iceland shown in Figure 54.

In the last step of the closure the spectral radiances are calculated from the retrieved ice microphysics (Section 4.5a). Comparing these modelled radiances at 1900 nm and the measured radiances at 1900 nm one can see that both agree very well (Figure 57). No significant differences are visible. At about 9:14 UTC the specMACS measurements show a high value of the spectral radiance. This is not captured by the retrieval. This high value is most probably caused by a contrail embedded in the cirrus which causes saturation of the lidar signal or which cannot be captured in the lidar/radar measurements. Overall this case demonstrated that in principle the whole method works well.

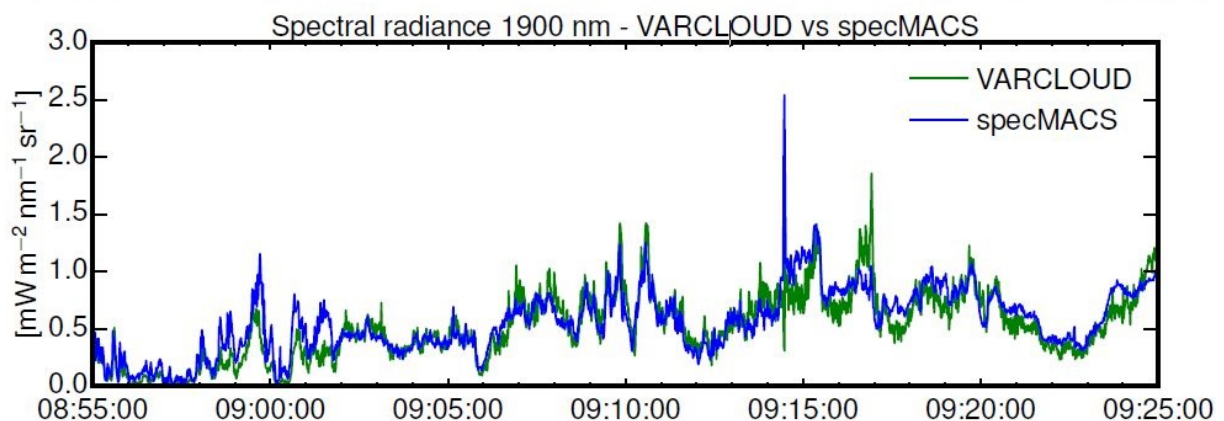


Figure 57: Measured (blue) and modelled (green) radiances above the cirrus cloud at 1900 nm for the flight performed on 1 October 2016 shown in Figure 54.

4.5.3 Inhomogeneous cloud structure with high updrafts

The same method was applied to a flight leg with inhomogeneous cloud structure and high updrafts. For this study, the common flight leg between HALO, French Falcon and FAAM BAe 146 was used which was performed on 14th October 2016. The common flight leg was flown over the seas west of Scotland between 95.5°N, 6.5°W and 61.2°N, 10.0°W beginning at 09:52 UTC and lasting until 10:15 UTC. During that period the lateral distance between the instrument footprints was below 100 m with the French Falcon flying 300 s behind HALO. The flight leg cut through an occluded front with an optically thick and precipitating cloud band which was associated with a cut-off low pressure system west of the British Isles. HALO and the French Falcon flew staggered at an altitude of 13 km and 11 km. First, the BAe 146 probed the cloud top at 9 km in the same direction and went then in a descent to obtain a profile of the ice cloud microphysics. Figure 58 shows a 3D representation of this common flight leg of HALO (green), French Falcon (red) and FAAM BAe 146 (blue). The curtain shows WALES and MIRA measurements over a corresponding satellite image from MODIS on Aqua.

NAWDEX RF06 – 14 October 2016

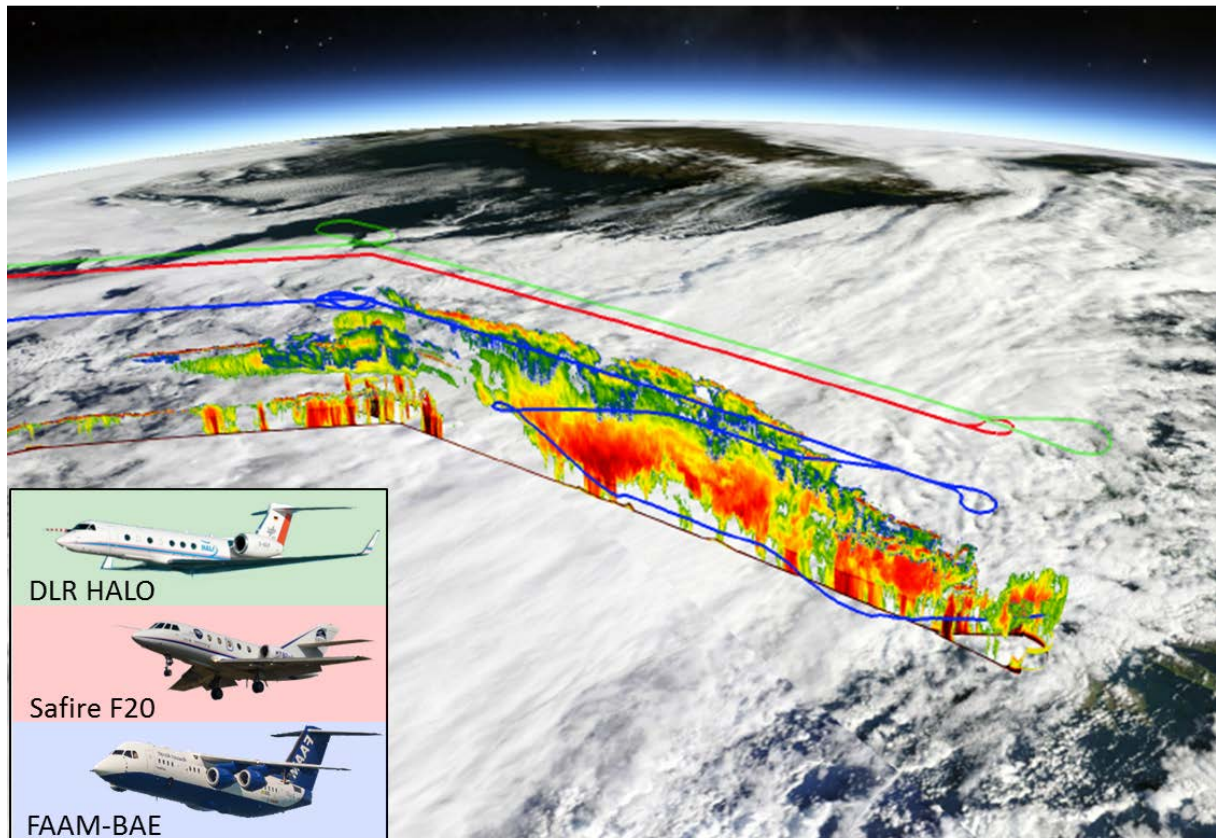


Figure 58. 3D representation of the common flight paths of HALO (green), French Falcon (red) and FAAM BAe 146 (blue) that was flown over the seas west of Scotland on 14th October 2016. The curtain shows WALES and MIRA measurements over a corresponding satellite image from MODIS on Aqua.

A more detailed look on the lidar measurement is given in the top panel Figure 59 , which shows the backscatter coefficient measured by WALES at 532. Striking features are the multiple cloud regions (e.g. 10:02 UTC or 10:05 UTC) with very high backscatter which could not be penetrated with the lidar. Analogous to the previous case, ice cloud microphysics are first retrieved using the radar/lidar synergy on HALO and FF20 and subsequently used for the forward simulation of solar radiances at 1900 nm. In the bottom panel of Figure 59, these forward simulated solar radiances (green line: HALO, red line: FF20) are compared to solar radiances measured with specMACS (blue line). In this case the much poor agreement between forward modelled and measured solar radiances is directly apparent. While the forward modelled radiances agree quite well between the different microphysics retrieved from HALO and FF20, they both strongly underestimate the actual measured radiances. This is especially true over the previously mentioned cloud regions with the high backscatter and short penetration depth in the lidar data. This correlation seems to indicate regions with very high cloud reflectance and for which the microphysical assumptions of VarCloud are not well suited for.

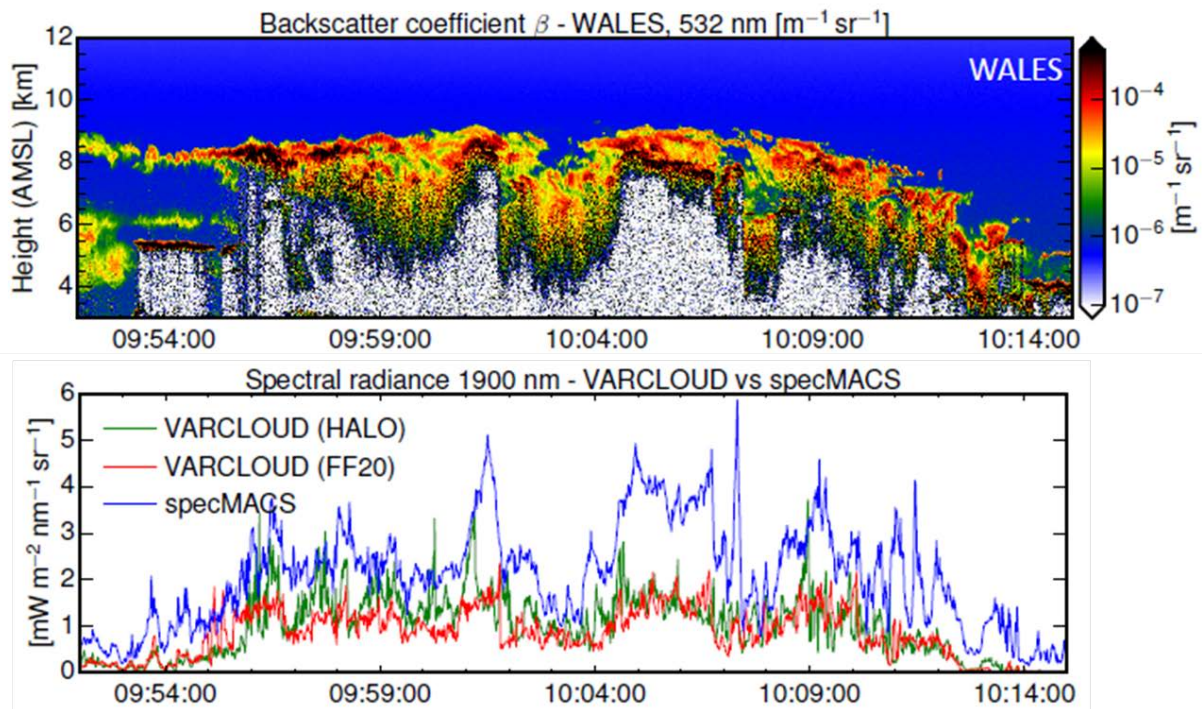


Figure 59. Top panel: Backscatter coefficient measured by the HSRL WALES at 532 nm for the common flight leg shown in Figure 58. Bottom panel: Measured and forward simulated solar radiance at 1900 nm using the specMACS instrument and the retrieved ice cloud microphysics from VarCloud.

More light is shed on these regions in Figure 60 where the retrieved ice crystal number concentration (2D field) is compared with the in-situ measured ice crystal number concentration by the FAAM BAe 146 (line). Directly at cloud top, the retrieval agrees quite well with the in-situ data. There, both show quite high ice number concentrations of 10^3 L^{-1} and more. Discrepancies become visible for deeper within the cloud at 10:05 UTC, where the in-situ data indicate extremely high concentrations of 10^4 L^{-1} and more. The cloud pockets of very high ice crystal number concentration match very well with the regions which could not be penetrated by the lidar. In contrast, the retrieval does not capture these features since lidar data is missing in these regions and the ice particles are too small to have a substantive impact on the radar reflectivity. Without the closure with solar radiance measurements, the optimal estimate to radar and lidar would converge to one result and would yield seemingly correct ice cloud microphysics. Here, the scientific user would be unaware of the apparent discrepancy with solar radiances, an indication that the retrieved microphysics are inconsistent with radiative fluxes. This case underlines the need to develop a unified framework to incorporate solar radiances into an optimal estimate of ice cloud microphysics. It furthermore highlights the advantage to fly a solar radiance spectrometer in combination with the radar/lidar remote sensing package.

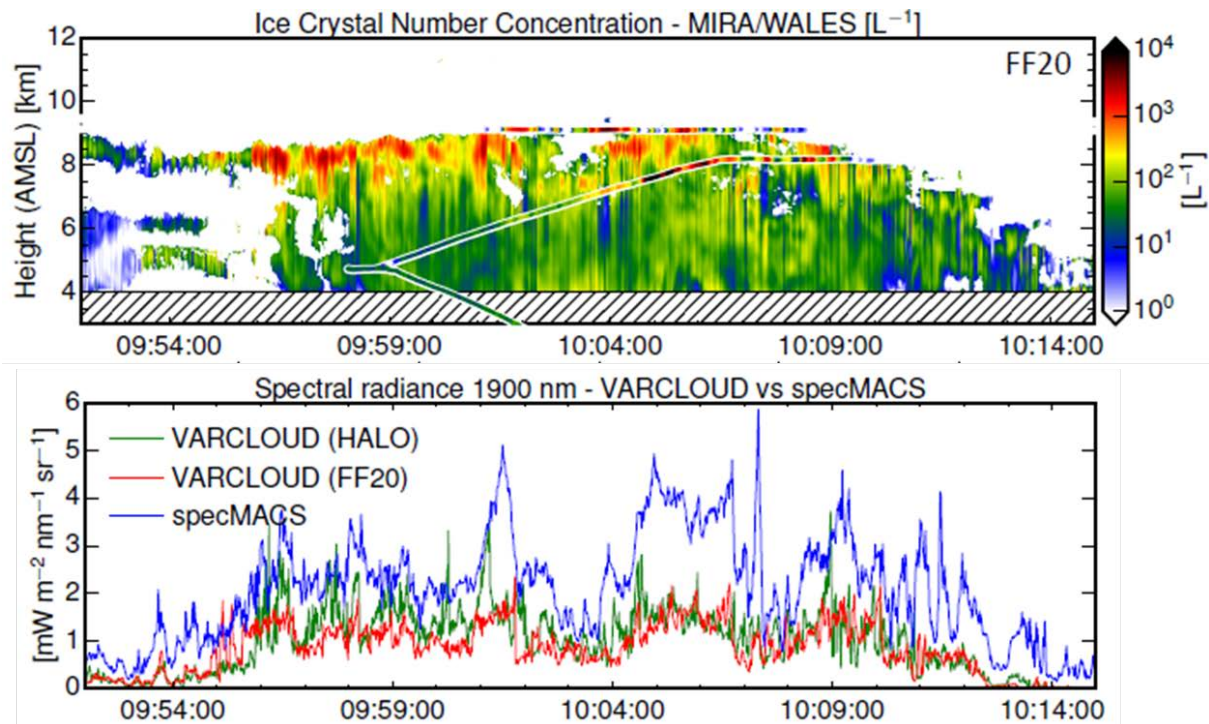


Figure 60. Top panel: Ice crystal number concentration retrieved by VarCloud (2D field) and in-situ ice crystal number concentration measured by FAAM BAe 146 (line). Bottom panel: Measured and forward simulated solar radiance at 1900 nm using the specMACS instrument and the retrieved ice cloud microphysics from VarCloud.

5 SUMMARY AND CONCLUSION

In order to achieve the main objectives of the EPATAN activity we have designed, planned and conducted a field campaign extension to the existing NAWDEX 2016 experiment. The French F20 carried out 15 flights (about 46 flight hours), radar-lidar data have been collected during these flights, including joint flights with HALO, German F20 and FAAM aircraft. The measurements have been calibrated and processed in order to provide synergistic target classifications, wind retrieval (RASTA radar only) and ice cloud properties. The processing details, including calibration processes, have been reported in the Data Acquisition Report. An analysis of the cloud properties retrieved using HALO measurements during NAWDEX campaign for three selected cases (1st; 13th and 14th October) and the whole flights has been done showing that the ice phase coexists with supercool water layers within in the range [-40, 0] °C, with the highest occurrence at [-25, -10] °C representing the 1.3% of the observations in these temperatures. The pure supercool water layers were observed at the same temperature ranges, with highest occurrence at [-10, -1] °C (in 0.74% of the observations). Using the RASTA radar only measurements we showed that horizontal wind spanned mainly between 5 and 35 m/s below -20°C and gradually increased at colder temperature (when getting closer the jet). Looking at the ice water content we discussed the distribution of IWC as a function of temperature and thanks to the Doppler capability of RASTA we also inferred the relationship between IWC and the vertical velocity.

Making the most of the two radar-lidar systems operating at different wavelengths, HALO (35GHz/532nm) and F20 (95GHz/355nm), we analysed the impact of the wavelengths on the measurements and the ice cloud retrievals. We showed that the radar frequency can slightly affect the IWC retrieval.

Within this activity we had the opportunity to compare CloudSat-CALIPSO against RALI measurements and products. Thanks to 3 CloudSat-CALIPSO underpasses (2nd, 5th and 14th of October) in very different meteorological conditions. We highlighted the fact that the meteorological conditions can have a large impact on the comparisons. For instance, a homogeneous system is much simpler to sample than an inhomogeneous. We clearly see the interest of having many joint legs in order to increase the statistics and improve the assessment of the satellite measurements and products. We also noticed that the sensitivity of the radar could be an issue for cloud products but it has no impact on the calibration exercise. With these co-located measurements, it is also possible to investigate the multiple scattering. The Doppler velocity is not assessed here as the CloudSat radar is not dopplerised but the airborne measurements will contribute to better understand the Doppler velocity measured by EarthCare-CPR.

To evaluate the performance of the synergistic radar-lidar algorithm to retrieve ice microphysical properties a closure study was performed. Similar as it will be done for the future EarthCare measurements we retrieved ice water content and ice effective radius for the ice cloud detected by lidar and radar and forward model spectral radiances that are compared against the real measurements made with the specMACS imaging cloud spectrometer. Two cases have been studied, one with a homogeneous structure and one with inhomogeneous structure with very different results. The first case gave a very good agreement between specMACS and the simulation but the second one was not as satisfactory. Retrieved properties from HALO and FF20 led to forward modelled radiances that strongly underestimated the actual measured radiances. Thanks to co-located in-situ measurements with the FAAM aircraft we showed that the problematic area was made of ice crystals with a high number concentration. This result highlights the advantage to fly a solar radiance spectrometer in combination with the radar/lidar remote sensing package.

In this activity we managed to team up the most advanced European radar-lidar platforms in order to prepare the future EarthCare mission throughout the calibration of its instruments and the validation of its products. The data produced are quite unique and are ideal for testing EarthCare synergistic products with a top-down view including more wavelengths than the satellite with Doppler capability for the radar and high spectral resolution for the lidar.

Acknowledgement

The authors thank the CALIPSO team at NASA Langley Research Centre and the CloudSat team at Colorado State University for the availability of the level-2 data used in DARDAR product. We also acknowledge AERIS ICARE Data and Services Centre (<http://www.icare.univ-lille1.fr>) for providing DARDAR data. Acknowledgments also go to ECMWF for the ERA-I reanalyse.

References

Ceccaldi, M., J. Delanoë, R. J. Hogan, N. L. Pounder, A. Protat, and J. Pelon: From CloudSat-CALIPSO to EarthCare: Evolution of the DARDAR cloud classification and its comparison to airborne radar-lidar observations, *J. Geophys. Res. Atmos.*, 118, 7962–7981, doi:10.1002/jgrd.50579, 2013.

Schäfler, A., G. Craig, H. Wernli, P. Arbogast, J. Doyle, R. McTaggart-Cowan, J. Methven, G. Rivière, F. Ament, M. Boettcher, M. Bramberger, Q. Cazenave, R., Cotton, S. Crewell, J. Delanoë, A. Dörnbrack, A. Ehrlich, F. Ewald, A. Fix, C., Grams, S. Gray, H. Grob, S. Groß, M. Hagen, B. Harvey, L. Hirsch, M. Jacob, T., Kölling, H. Konow, C. Lemmerz, O. Lux, L. Magnusson, B. Mayer, M. Mech, R., Moore, J. Pelon, J. Quinting, S. Rahm, M. Rapp, M. Rautenhaus, O. Reitebuch, C. Reynolds, H. Sodemann, T. Spengler, G. Vaughan, M. Wendisch, M. Wirth, B., Witschas, K. Wolf, and T. Zinner, 2018: The North Atlantic Waveguide and Downstream Impact Experiment. *Bull. Amer. Meteor. Soc.*, doi:10.1175/BAMS-D-17-0003.1, in press.

Ewald, Florian, et al. "Design and characterization of specMACS, a multipurpose hyperspectral cloud and sky imager." *Atmospheric Measurement Techniques* 5 (2016): 2015-2042.

Annex 1: DATA ACQUISITION REPORT (DAR)

Version 1.2 EPATAN DATA ACQUISITION REPORT

EPATAN Data acquisition report

EARTHCARE - EPATAN

ESA Contract No. 4000119015/NL/CT/gp

Prepared by:

Julien Delanoë (LATMOS)

Silke Gross (DLR)

Quitterie Cazenave (LATMOS/DLR)

Florian Ewald (DLR)

Jacques Pelon (LATMOS)

Abdenour Irbah (LATMOS)

Gwendal Rivière (LMD)



credits NAWDEX

Version 1.2 EPATAN DATA ACQUISITION REPORT

Document version	date	Modifications and comments
0.0	11/2016	first version of the document
0.1	05/2017	second version of the document, annexes have been removed from the main document
0.2	11/2017	Annexes are back in the main document as a single deliverable
1.0	02/2018	Document has been renamed as DAR (Data Acquisition Report)
1.1	02/2018	Contribution DLR and LATMOS
1.2	04/2018	Modifications suggested during PM2

Log table

This document aims at presenting the data collected during EPATAN campaign, which took place in Iceland from 28/09/2016 to 17/10/2016.

Note that this campaign has been funded through ESA, EUFAR and CNES grants:

- ESA-EPATAN
- EUFAR- Nearex project
- CNES-EECLAT and CNES-ADM

Index

EPATAN Actions and Risk Log (EPARL).....	5
1. Introduction and scope of EPATAN.....	7
2. Campaign summary.....	9
3. Instrumental deployment	13
3.1 LATMOS instruments deployment.....	13
3.1.1 Airborne platform.....	13
3.1.2 Ground based measurements deployed during the campaign	23
3.2 DLR instrument deployment.....	25
3.2.1 HALO aircraft.....	25
3.2.2 German F20 with wind lidars	28
4. French Falcon DATA description.....	31
4.1 RASTA Aircraft data	31
4.2 RASTA products	31
4.2.1 Single antenna level 2 product.....	31
4.2.2 Wind retrieval level 2 product.....	37
4.2.3 Microphysical product.....	41
4.2.4 Spectral analysis product (on demand only).....	42
4.2.5 RASTA measurement errors information	44
4.3 LNG products.....	44
4.3.1 Characteristics of LNG and pre-processing	44
4.3.2 Calibration of the lidar signals	46
4.3.3 Measurement errors	48
4.3.4 Masks.....	53
4.4 RALI products	54
4.4.1 Co-located measurements product.....	54
4.4.2 Phase categorization.....	55
4.4.3 Ice clouds retrieval	58
4.4.4 Reported errors in merge products	61
4.5 Dropsondes	62
5. HALO products	62
5.1 Basic of WALES Data Processing	63
5.2 Basic of MIRA Data Processing	65
5.2.1 Internal/Budget calibration.....	66
5.2.2 Radiometric calibration of the MIRA36.....	69
5.3 Co-located MIRA36 and WALES products and ice cloud retrieval	71
6. Satellite underpasses.....	72
6.1 Underpass #1 : 2016/10/02 (F7-French Falcon).....	72
6.2 Underpass #2 : 2016/10/05 (F9-French Falcon).....	73
6.3 Underpass #3 : 2016/10/14 (F18-French Falcon).....	74
References	75
Annexe A: Flights description.....	77
F5: 2016/10/01	78
F6: 2016/10/02	79
F7: 2016/10/02	80
F8: 2016/10/04	81

Version 1.2 EPATAN DATA ACQUISITION REPORT

F9: 2016/10/05	82
F10: 2016/10/07	83
F11: 2016/10/09	84
F12: 2016/10/09	85
F13: 2016/10/10	86
F14: 2016/10/11	87
F15: 2016/10/12	88
F16: 2016/10/13	89
F17: 2016/10/14	90
F18: 2016/10/14	91
Annexe B: content of the files	92
SAFIRE aircraft product	92
RASTA L2 single antenna product.....	100
RASTA wind product	104
RASTA microphysical product.....	114
RASTA Spectral product.....	121
Level 1 LNG file.....	124
File Description for MIRA36	128
File description for WALES.....	129
File Description for VARCLOUD Output on HALO	131
File Description for VARMASK Output on HALO.....	133

EPATAN Actions and Risk Log (EPARL)

Month Year	Actions	Remarks
September 2016	Campaign preparation and start of the campaign	
October 2016	Campaign	
November 2016	Preliminary processing of the data	
December 2016	Preliminary processing of the data	
January 2017	Preliminary processing of the data	
February 2017	Signature of the contract Preliminary processing of the data	
March 2017	Presentation at NAWDEX meeting	
April 2017	Preliminary processing of the data	
May 2017	Updated version of CIP Delivery of a first version of the documents: <ul style="list-style-type: none"> • Flight reports v1 • L2_RASTA_product_v0 • RALI_wind_product_v0 • RASTA_dynamics_microphysic_product_v0 • RASTA_spectral_analysis_product_v0 	PM1: Presentation of the results (see minutes) Link: https://mycore.core-cloud.net/public.php?service=files&t=d5e039282e8cd0ad580ddb5f7ddf5fc
June 2017	First progress meeting (13th of June) Delivery directory: <ul style="list-style-type: none"> • NAWDEX catalogue • Presentation material of PM1 	
July 2017	Reprocessing of the radar L2 data Draft of the minutes of PM1	
August 2017	Processing and quality analysis of MIRA Radar L1 data for joint flight legs	
September 2017	Processing and quality check of WALES lidar L1 data for joint flight legs First analysis of joint flights (data gridded, comparisons of radar reflectivity at different wavelengths, comparison of lidar att. Backscatter at different wavelengths, Radar-Radar masks, retrieving of ice cloud properties)	
October 2017	First analysis of joint flights (data gridded, comparisons of radar reflectivity at different wavelengths, comparison of lidar att. Backscatter at different wavelengths, Radar-Radar	

Version 1.2 EPATAN DATA ACQUISITION REPORT

	masks, retrieving of ice cloud properties	
November 2017	<p>First analysis of joint flights (data gridded, comparisons of radar reflectivity at different wavelengths, comparison of lidar att. Backscatter at different wavelengths, Radar-Radar masks, retrieving of ice cloud properties)</p> <p>New repository for distributing the document</p> <p>Presentation of EPATAN data during the HALO Topical Workshop: Scientific exploitation of the combined HALO/FAAM/Falcon flight during the NAWDEX campaign 2016 (14 October, IOP 11)</p>	<p>New link for documentation: https://owncloud.latmos.i-psl.fr/index.php/s/ydPWkgxkmAuinMF (pw: epatan)</p> <p>https://www.mi.uni-hamburg.de/en/arbeitsgruppen/strahlung-und-fernerkundung/events/2017-halo-faam-falcon.html</p>
February 2018	<p>RASTA L2 WIND product reprocessed – heading correction in the wind retrieval</p>	<p>only L2 and merge products impacted (only RASTA merge antenna wind product is modified, L2 single antenna is not changed)</p>
March 2018	<p>Presentation at NAWDEX workshop/ DAR V1.1 delivered</p> <p>LNG pointing angle refined</p>	<p>L1 LNG data (and merge product) are reprocessed</p>
April/Mai 2018	<p>LNG and RASTA wind products have been presented during EGU in Vienna.</p> <p>RASTA target classification has been improved</p>	<p>New classification, better detection of melting layer and phase.</p>

1. Introduction and scope of EPATAN

The main scientific objectives of EPATAN 2016 (**E**arthcare **P**rep**A**ra**T**ion **c**ampaig**N**) are derived from the scientific objectives of EarthCARE. The EarthCARE mission will advance our understanding of the role that clouds and aerosols play in reflecting incident solar radiation back into space and trapping infrared radiation emitted from Earth's surface by providing vertical cloud and aerosol profile information in connection with collocated broadband solar and thermal radiance measurements (Illingworth et al. 2015).

In the context of general ESA campaign objectives, EPATAN 2016 campaign addresses directly the programmatic needs of EarthCARE Mission Development, particularly relating to the development and refinement of Geophysical Product Algorithms.

The main objectives of EPATAN 2016 project are as follows:

- In collaboration with appropriate International Scientists and Agencies, design, plan and conduct a field campaign extension to the existing NAWDEX 2016 experiment dedicated to the preparation of EarthCare launch.
- Contribute to a better understanding of EarthCARE measurements and perform testing of L2 algorithms.
- Provide EarthCARE like measurements (W-band and 355 nm HSR), with a spatial coverage scales and product resolution similar to that of the EarthCARE mission.
- Provide the most possible independent measurements from EarthCARE and then compare the retrievals using only the measurements on board EarthCARE.
- Perform dedicated CloudSat-CALIPSO overpass flights that will be utilized as reference.
- Perform a first rehearsal of the validation/calibration strategy ensuring readiness of the cal/val setup after launch
- Provide collocated observations from the different lidar systems of aerosol under varying aerosol conditions (load and type).
- Provide spectral (nadir) radiance observations related to cloud cover, particle size and other EarthCARE relevant parameters.

Airborne platforms are ideal to complete the ground-based systems allowing direct satellite underpasses. German and French aircraft, respectively HALO and French Falcon 20 have very complementary payloads (see section 3) and are perfectly designed for the preparation, the calibration and the validation of EarthCare (EC hereafter). Both aircraft board a high spectral resolution lidar (355 nm on the French Falcon and 532 nm on the HALO), a Doppler radar at 36 GHz (HALO) and 95 GHz (Falcon) and in-situ measurements. At European level they are the most complete possible setup to mimic and to complete EarthCare payload. Furthermore, the associated scientific teams have a very large experience in algorithm development, especially synergistic radar-lidar retrieval for cloud and aerosol retrieval. Note that any cloud studies using airborne radar-lidar-radiometer synergy is relevant for EC preparation, as we want as many various cases as possible for training algorithms and to improve our understanding of W-band Doppler cloud radar and High spectral resolution at 355 nm measurements. The EC preparation field campaign is expected to provide EC like measurements (i.e. W band and 355 nm HSR), which will contribute to better understand the unprecedented nature of EC measurements and will bring material for testing L2 algorithms. Prior to this project there were almost no dedicated observations that can be provided to the L2 algorithm development teams. This unique combination provides the community with an EC like

data set supported by extra radar-lidar-radiometry measurements airborne systems. The strategy is to provide the most possible independent measurements from EC and then compare the retrievals using only the measurements on board EC. In addition to that we need have dedicated CloudSat-CALIPSO (CC hereafter) overpass flights are our reference. Note that currently many future EC algorithms are running on CC data.

The EPATAN 2016 activity benefited from the international NAWDEX campaign framework. NAWDEX stands for North Atlantic Waveguide and Downstream Impact experiment; it aims at increasing our knowledge of the effects of diabatic processes (mainly moist and radiative processes) on atmospheric disturbances along the North Atlantic jet stream (also called North Atlantic waveguide). These diabatic processes, such as those involved in cloud microphysics, are not well represented in current meteorological forecast models. This misrepresentation often leads to forecast error growth, which may have dramatic consequences in the case of high-impact weather events over Europe. The field campaign, held in fall 2016 (19 September to 16 October 2016), included state-of-the-art airborne measurements and ground-based measurements to provide a unique observational dataset, sampling the key dynamics and processes associated with the triggering, propagation and downstream impact of disturbances along the North Atlantic waveguide. It is used to test and validate parameterization schemes within numerical weather prediction models with the general objective to improve the accuracy of one-day to two-week high impact weather forecasts. The observational payload is therefore mostly dedicated to cloud, precipitation, wind and humidity characterisation. More details of the NAWDEX project can be found here: <http://nawdex.org>.

The trio of aircraft (HALO, DLR F20, French F20) were based in Iceland. This configuration allowed us to optimise the interaction between DLR and French F20 teams in order to provide the best possible characterisation of the atmosphere and share resources. In order to ensure a perfect interaction between the three aircraft and support the preparation/validation purposes we will focus on common scientific objectives. The scientific questions that were addressed in NAWDEX suited EC preparation and objectives:

- The **characterisation of mixed-phase deep clouds** (occurrence, altitude, ...)
- The **characterization of cloud processes in the lower troposphere**.
- The **characterization of clouds near the tropopause** is important to better estimate cloud radiative feedbacks on atmospheric dynamics.

The **relationship between the various kinds of clouds and the meteorological variables** like temperature, three-dimensional winds and potential vorticity.

The other objectives of the airborne radar-lidar system are to provide EC like measurements for ice and liquid clouds during the campaign. The region that has been sampled covers a wide range of meteorological situations, including mixed phase clouds. In a synergistic manner, NEAREX (Norwegian Mesoscale Ensemble and Atmospheric River Experiment), a EUFAR-funded project (covering 10 Flight hours), aimed at addressing these critical issues as an integral component of the international observational field campaign NAWDEX. The foci of NEAREX were on short-term forecasts and flood prediction. However, NEAREX results will also shed light on the representation of ARs in state of the art numerical models, providing essential information for a better understanding of seasonal and climate model projections.

2. Campaign summary

The previous objectives were achieved through the collection and analyses of airborne Lidar and Radar data sets at different frequencies together with correlative ground-based and satellite-based data acquired during NAWDEX 2016 campaign. Airborne measurements were collected from the French and German Falcon 20, HALO and FAAM (with ISMAR). Characteristics of the payloads of the French and German aircraft are given in section 3.

In order to achieve the above-mentioned objectives 46.5 scientific flights hours (excluding transfer flight hours), in other words 15 flights (F5 to F18 can be used for scientific purposes, F3 and F19 are dedicated to calibration and tests and not distributed), for the French Falcon were performed during the NAWDEX 2016 campaign within this activity. Note that national or EUFAR funding completed ESA support for that campaign.

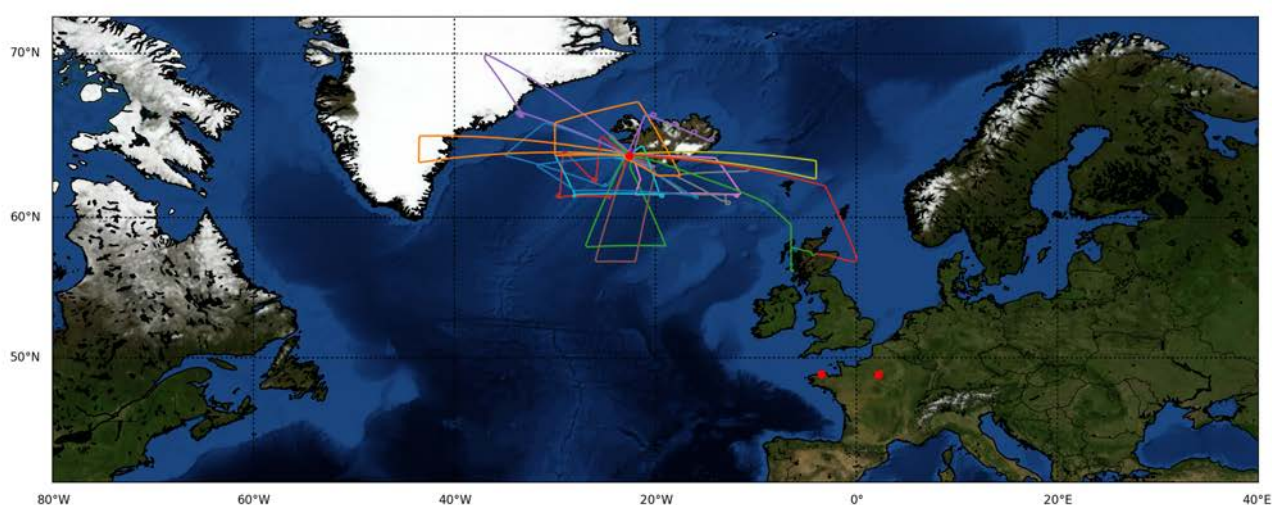


Figure 1 French F20 flight tracks during NAWDEX (separate flights)

The list of the flights with a short description is given in Table 1

EPATAN in a few words:

- From 28th of September to 17th of October 2016
- Number of scientific flights: 15 (Figure 1)
- Number of scientific flight hours: 46.5
- Number of released dropsondes: 59
- Number of CloudSat-CALIPSO: 3
- Number of co-located flights: 5

Quicklook data can be found in Annex A.

During the campaign four common flight legs were performed together with the German HALO research aircraft (Figure 2) with similar payload as the French F20 (see Section 3.2.1). These flights are crucial to investigate the effects of different wavelengths on measured atmospheric parameters and on retrieval results. Additionally to the combination of French F20 and HALO the first common flight track of the research flight on 14 October 2017 was planned as coordinated flight of French F20, HALO and the

British FAAM, the last performing in-situ sampling of cloud properties below the two other aircraft. These additional measurements help to evaluate radar-lidar retrieval results. The second common flight track of the research flight on 14 October 2017 was planned as A-Train underpass to learn for and develop strategies for future EarthCARE cal/val activities. The motivation and aims of these joint flights are highlighted in the NAWDEX overview paper (Schäfler et al., 2018 accepted for BAMS).

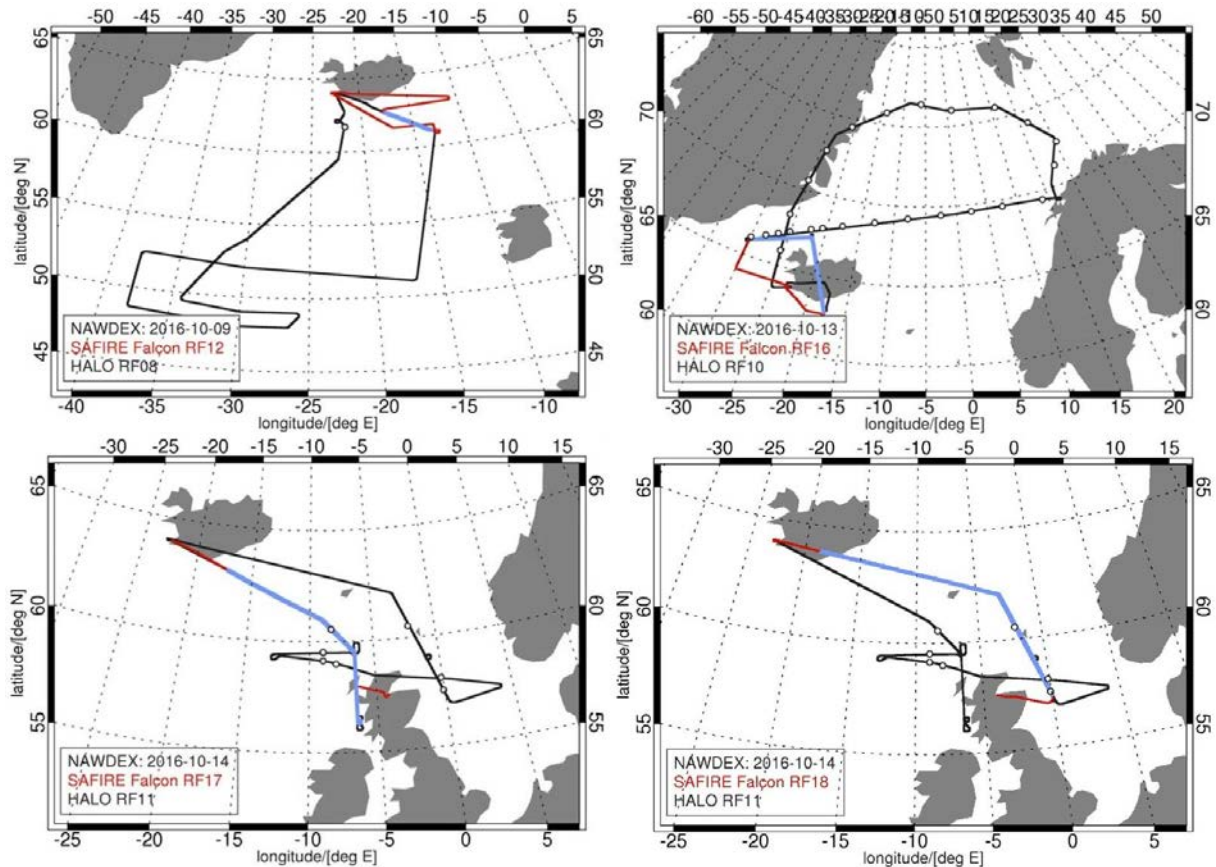


Figure 2 Common flights of French F20 (red) and HALO (black) during NAWDEX. Common flight tracks are marked blue.

Flight number	Date and flight duration Take off-landing	Comments	Overpass	joint legs	Ds
3	21/09/2016	Test flight in Toulouse area – radar calibration	no	no	1
5	01/10/2016 2.7h 15:13-17:36	Deep low in Northern Atlantic, arriving on Iceland during the night. Less active structure west of Iceland with fairly thick clouds. Test flight on the area west of Iceland, to make a cross-section of the cloud structure to observe different cloud layers and test the instruments response. Crossing of the jet stream and launch of 3 dropsondes.	no	no	3
6	02/10/2016 3.5h 8:37-11:50	Cyclone approaching the vicinity of Iceland (Saturday Storm) associated with active fronts and thick clouds.	no	yes with GF20	9

Version 1.2 EPATAN DATA ACQUISITION REPORT

		Outflow of the Warm Conveyor Belt (WCB) associated with the Saturday Storm; analysing the tropopause fold and the PV gradient. Coordinated flight with the DLR Falcon above Greenland (A2D validation).			
7	02/10/2016 3.5h 13:01-16:16	Cyclone approaching the vicinity of Iceland (Saturday Storm) associated with active fronts and thick clouds. Strong winds forecast for the evening in Keflavik. Sampling the inflow of the WCB (same structure as for the previous flight). Overpass with Cloudsat-CALIPSO.	Overpass with ground based radar BASTA at 13:34 Overpass with satellite at 14:07:35	no	0
8	04/10/2016 3.4h 15:45-18:45	Ridge over Iceland linked to an anticyclonic situation in western Europe. Deep low between Iceland and Newfoundland. Sampling the outflow of the WCB at the edge of the ridge and the negative PV region. Problems to start the new acquisition of RASTA (a few minutes not available)	Overpass with ground based radar BASTA at 18:24 in the descent (FL105)	no	5
9	05/10/2016 4h 13:18-16:31	Diabatic Rossby wave in North-west Atlantic evolving into a very deep low between Iceland and Greenland. Cyclonic outflow of the WCB, in the same system as the previous flight, close to the center of the low. Satellite underpass with Cloudsat over Greenland in a region with moisture advection and orographic precipitation.	Overpass with Cloudsat only, CALIPSO payload turned off for maintenance manoeuvre.		4
10	07/10/2016 3.1h 12:03-14:54	Iceland under a south-east flux between the low south of Greenland and the high pressure levels over Norway, associated with moisture advection. Atmospheric rivers south of Iceland.	no	no	7
11	09/10/2016 2.7h 10:19-15:50	A low is located over Iceland (named "Brigitte") associated with frontal structures south of Iceland. Crossing the flow associated with the WCB We will study its evolution with the 2 nd flight in the afternoon and the flight of the following day.	no	no	4
12	09/10/2016 2.7h 17:08-20:08	The frontal structure is now located east of Iceland. Several cross sections of the frontal area where its activity is the most intense. Common leg with the DLR aircraft from the center to the edge of the front.	no		DLR Falcon 20 and HALO 4
13	10/10/2016 3.2h 10:11-13:08	The system of the previous day has evacuated northward. Iceland is in a southwesterly flow created by the opposition of the anticyclonic system on western Europe and the low pressure levels over Greenland. Atmospheric river of relatively weak intensity related to the remains of the system observed in the previous flights and its connection to the deep low located further south in the Atlantic. Only thin cirrus and a few supercooled layers observed in the atmospheric river resulting in a weak radar signal.	no	no	6

Version 1.2 EPATAN DATA ACQUISITION REPORT

14	11/10/2016 2.9 16:16-18:44	Very active system west of Iceland associated with low tropopause levels Inflow of the WCB associated with the system passing over Iceland.	no	no	4
15	12/10/2016 3h 15:47-18:34	Very active system located to the south of Iceland, resulting in strong winds and heavy rainfall in Iceland. Targeting the WCB inflow and the strong moisture flow south of Iceland (Atmospheric River).	no	no	7
16	13/10/2016 3h 13:03-15:52	Anticyclonic edge of the WCB over Iceland, associated with orographic waves on the northern part of the flight plan. This flight plan was made to fit with the flight plan of HALO to have a common leg on its way back to Keflavik.	no	FF20 and HALO	1
17	14/10/2016 3.2h 8:19-11:30	Anticyclonic situation on the northern Atlantic with few cyclonic activity. The cloudy region north of Scotland, favourable for intercomparisons between the aircraft.	no	HALO and FAAM	1
18	14/10/2016 2.8h 12:24-14:58	"" second flight of the day	CALIPSO overpass at 12:52:31	yes HALO	1
19	16/10/2016 2.4h 09:56-12:13	Ridge over Iceland, under the influence of the high pressure levels over northern Europe. A low located on the British Isles brings moisture in the upper levels. Measurements in the cirrus over Iceland, associated to the system on the British Isles. Only one antenna for RASTA (testing integration time impact)	no	no	2

Table 1 Flights summary

Note that RASTA and LNG worked continuously during the campaign. A few flights were affected by misalignment of LNG but there was no degradation during the campaign.

DARDAR (CloudSat-CALIPSO) merged products are available through AERIS/ICARE website (<http://www.icare.univ-lille1.fr>).

3. Instrumental deployment

3.1 LATMOS instruments deployment

3.1.1 Airborne platform

The RALI platform was mounted on board the French Falcon 20. The F20 aircraft (Figure 3) was operated by SAFIRE¹ (Service des Avions Français Instrumentés pour la Recherche en Environnement). RALI consists of a combination of the multi beam 95 GHz Doppler radar RASTA (RADAR SysTEM Airborne) and the LNG (Leandre New Generation). Both instruments were developed at LATMOS (<http://rali.projet.latmos.ipsl.fr/>, Delanoë et al 2013). LNG, in its backscatter configuration, operates at three wavelengths (355 nm, 532 nm, 1064 nm), including depolarization at 355 nm. Since 2010 the LNG lidar has had a high spectral resolution capability added at 355 nm. Since 2006 at least one of the two instruments flew under CloudSat and CALIPSO tracks (AMMA (2006)/ CIRCLEII (2007)/ POLARCAT (2008)/MT-AFRICA (2010) / LNG-CALIPSO (2010), CALOSIRIS (2014), HAIC-CAYENNE (2015), RALI test campaign (December 2015)) and now NAWDEX (2016).



Figure 3 French Falcon 20

a. RASTA Doppler cloud radar

RASTA can measure the Doppler velocity and the reflectivity at 95 GHz (Table 2) along a radial defined by the pointing direction of the antenna. The RASTA radar includes 3 downward-looking beams (nadir, 28 degrees off-nadir and opposite the aircraft motion, and 20 degrees off-nadir perpendicular to the aircraft motion, Figure 4). This unique configuration allows for the retrieval of the three-dimensional wind.

¹ <http://www.safire.fr>

Version 1.2 EPATAN DATA ACQUISITION REPORT

3 antennas	RASTA characteristics
Frequency (GHz)	95 (3.2 mm)
Vertical resolution (m)	60
Horizontal resolution (m)	225 to 300 depending on aircraft speed
Range (km)	15
Integration time (ms)	250 (measurement every 750ms for each antenna)
Energy (kW)	2 (pulse 0.4μs)
Ambiguous velocity (m s ⁻¹)	8
Antenna size (cm)	45 (0.5° beam width)
Sensitivity at 1km (dBZ)	Down backward: -30 / Nadir: -30 / Down transverse: -30
Weight (kg)/dimensions (cm)	110/82x102x150

Table 2 RASTA characteristics

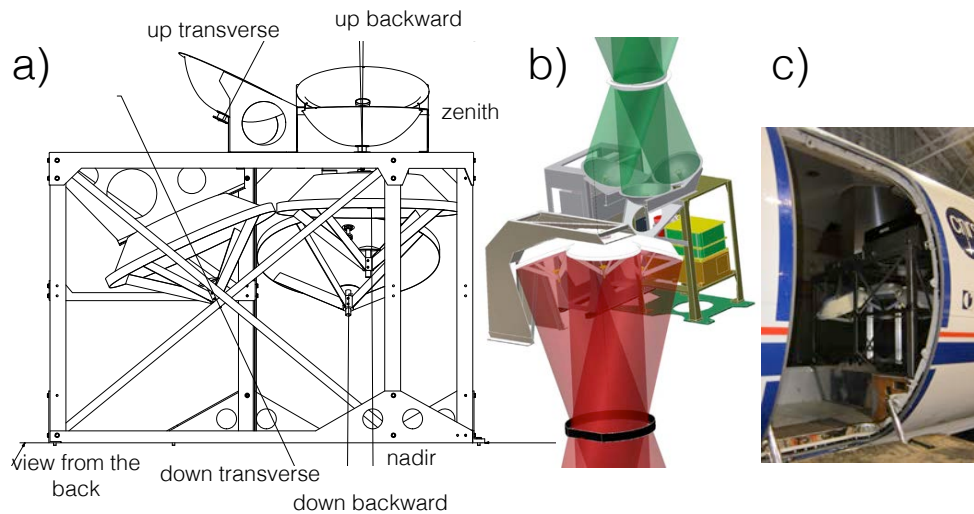


Figure 4 RASTA configuration on-board F20

As previously mentioned RASTA is capable of retrieving the 3D wind field, i.e. the three components of the wind on vertical plan below the aircraft when possible by combining independent measurements of the projected wind on radar radial. The independent Doppler radial velocities are provided by the multi-beam antenna system. An example of RASTA measurements and wind retrievals is shown in Figure 5 (see legend for description).

Version 1.2 EPATAN DATA ACQUISITION REPORT

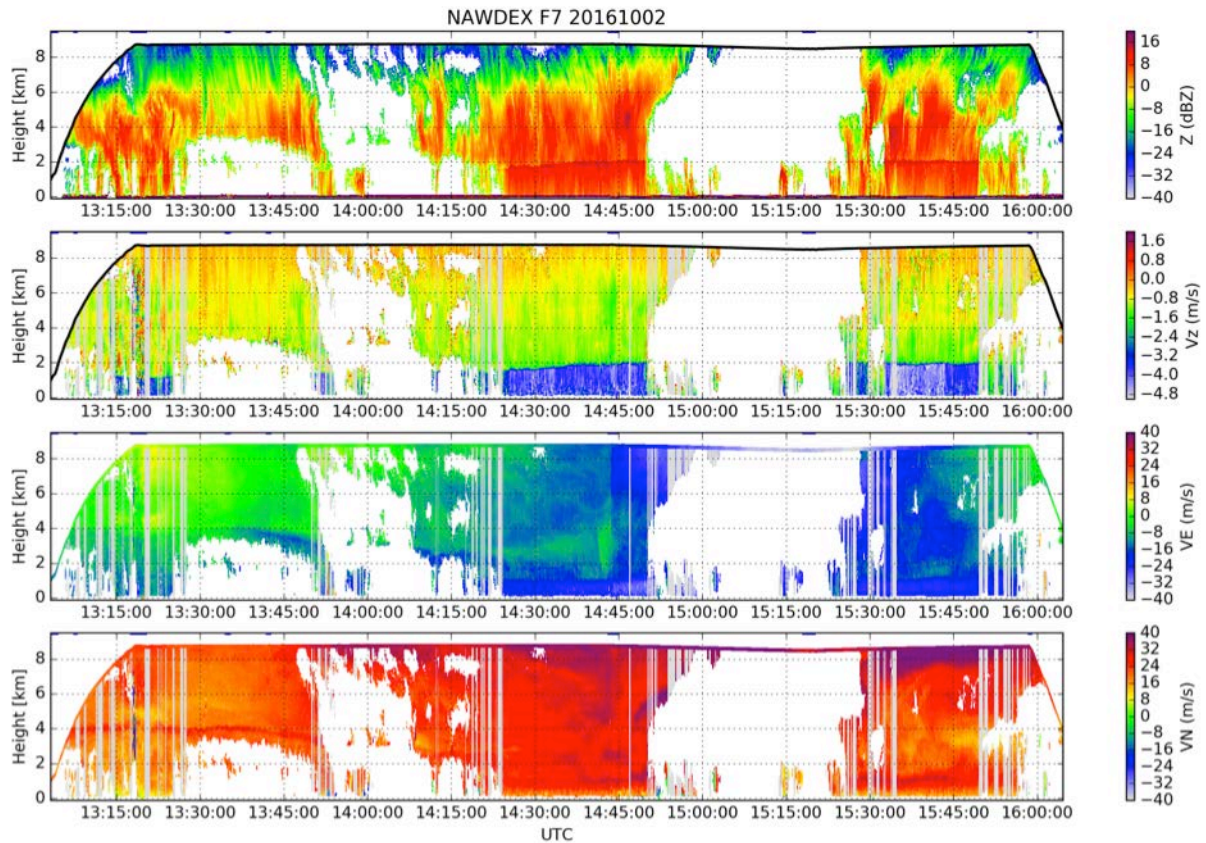


Figure 5 Example of 3D retrieval for NAWDEX campaign (F7, 02/10/2016), top panel describes the measured reflectivity below the aircraft. Second panel from top is the vertical velocity, which is a combination of the terminal fall velocity and the vertical air motion. Third and fourth plots from top illustrate both zonal (VE, or U) and meridional (VN or V) wind components. The in-situ wind (from the F20 measurements) is over-plotted at the altitude of the aircraft showing a very good consistency with RASTA's retrievals. Grey strips correspond to radial, which cannot be used in the retrieval.

RASTA nadir reflectivity is calibrated using the ocean surface return technique ([Li et al. 2005](#); [Tanelli et al. 2008](#)). The calibration of the other antennas is either directly derived using ground surface (in a similar manner as the nadir) or by comparing with nadir reflectivity. In the case of an available CloudSat overpass the latter is also used to retrieve the radar calibration.

After calibration RASTA sensitivity as a function of the range from the aircraft (nadir, backward and transverse antennas) is presented in Figure 6.

Version 1.2 EPATAN DATA ACQUISITION REPORT

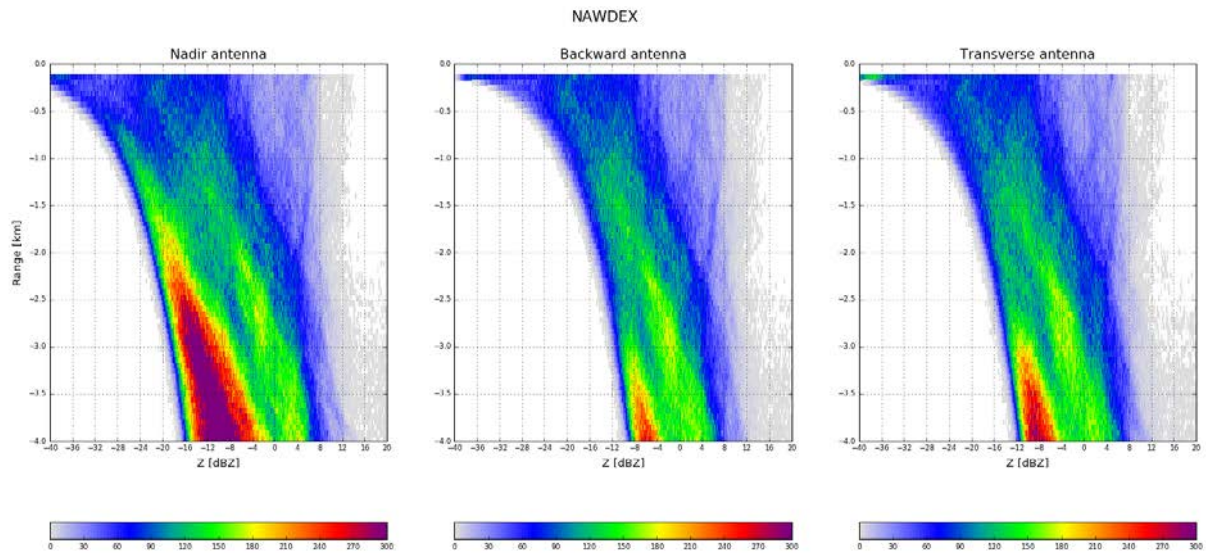


Figure 6 RASTA sensitivity for the three antennas as a function of the distance from aircraft.

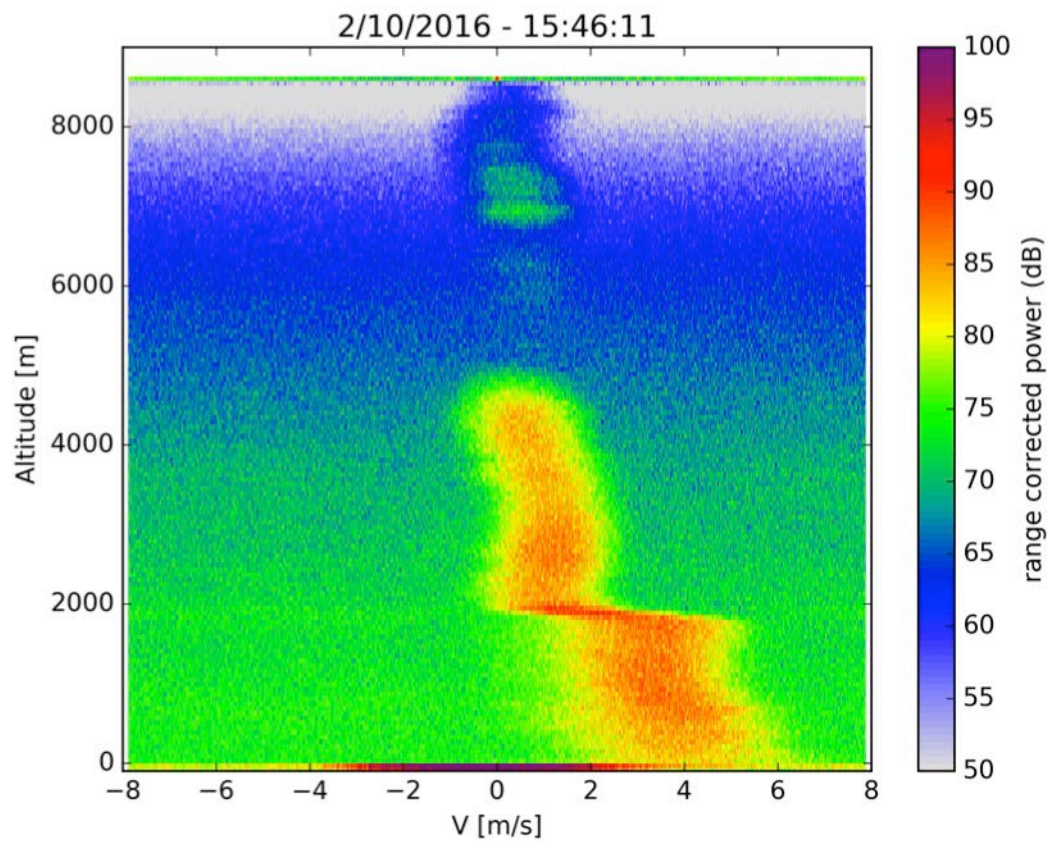


Figure 7: Doppler spectrum, range corrected power (not calibrated) as a function of velocity and range from the aircraft.

RASTA I and Q are archived for each flight and each antenna, it is therefore possible to process raw data and derive the Doppler spectrum. Figure 7 illustrates the Doppler spectrum measured on the 2nd of October during the NAWDEX campaign.

b. LNG multi-wavelength lidar (high spectral resolution UV)

The LEANDRE New Generation (LNG) airborne Lidar system (Figure 8) is based on a two-wave interferometry [Mach-Zehnder Interferometer (MZI)] to provide both the determination of optical parameters of aerosol and clouds and along-sight wind in the troposphere (Bruneau et al., 2003, 2015). It operates in a direct detection mode (measurement of the backscattered light intensity), which has the advantage of relying on both particulate and molecular scattering, and allows extended ranges and capabilities. The direct detection technique has been chosen for space observations of winds for the ADM-AEOLUS space mission using UV-Fabry Perot Interferometer, and comparisons have shown that wind measurements were in very good agreement between the two techniques as well as with theoretical performance (Bruneau et al., 2004). The design of the MZI is well adapted to the quantification of aerosol and cloud properties, as well as Line-of-sight wind measurements on particles.

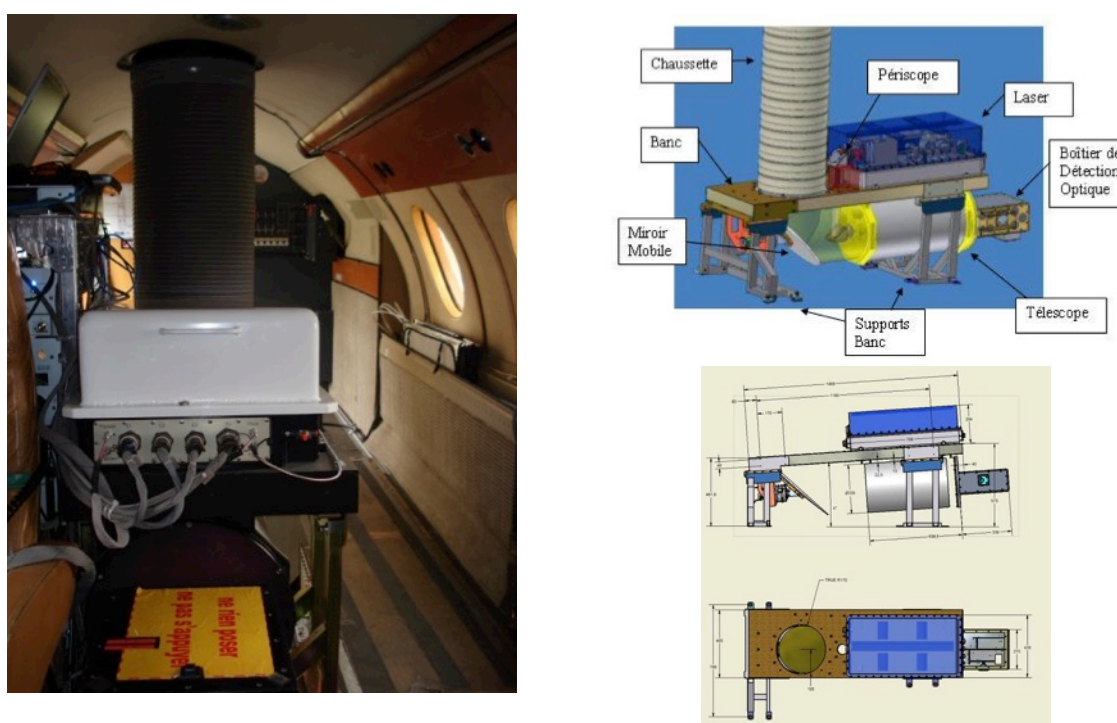


Figure 8 Left panel, Lidar implementation aboard the SAFIRE F20 showing the laser source and telescope/detection parts installed below the bench supporting the laser source. Right panel: LNG optical bench illustration, optical bench, mobile mirror and laser

LNG is a three-wavelength (1064, 532, and 355 nm, Table 3) backscatter lidar with polarization analysis at 355 nm. The HSR capability, based on a MZI, has been added at 355 nm following a previous concept analysis (Bruneau and Pelon, 2003). A view of the lidar on board the SAFIRE Falcon 20 is presented in Figure 8.

The HSR analysis within LNG performed by a Mach-Zehnder interferometer allows phase and intensity analysis simultaneously. In contrast to conventional HSR devices, our approach is not to separate the molecular and particulate signals in two distinct channels but to determine the interference contrast given by the backscattered light, which is linked to the backscatter ratio. The contrast is unambiguously determined by the signals given by four detection channels in phase quadrature, whatever the spectral positioning of the laser frequency with regard to the transmission function of the MZI. This way no

frequency stabilization is necessary either for the laser or the interferometer. Calibration is performed using laser signal injected in the MZI.

The signals, in phase quadrature, are delivered by the four detectors. The analysis allows us to retrieve intensity and phase shift of the backscattered signal with respect to the laser emission. As a result, backscattering signals are derived at the three emitted wavelengths and the HSR signals allow one to separate the attenuated particulate and molecular backscattering, as for ADM-Aeolus.

Wavelength	1064nm, 532nm and 355nm
Class	IV
Lighting power	6 Watts (average)
Type	ND : YAG pulsed (20Hz)
Beam visibility	Not visible inside cabin but visible outside the aircraft at night-time
Focused beam	No
Eye safe minimum distance	About 600m

Table 3 Laser characteristics

Some examples of LNG Doppler measurements which were collected during 2014 test campaign are shown in Figure 9. In the left panel, the ground surface echo velocity is compared to the speed of the aircraft as the F20 was flying at a constant altitude. The mean difference is 0.12 m s^{-1} and the standard deviation is about 1.4 ms^{-1} . The pitch of the F20 is about 3° upward.

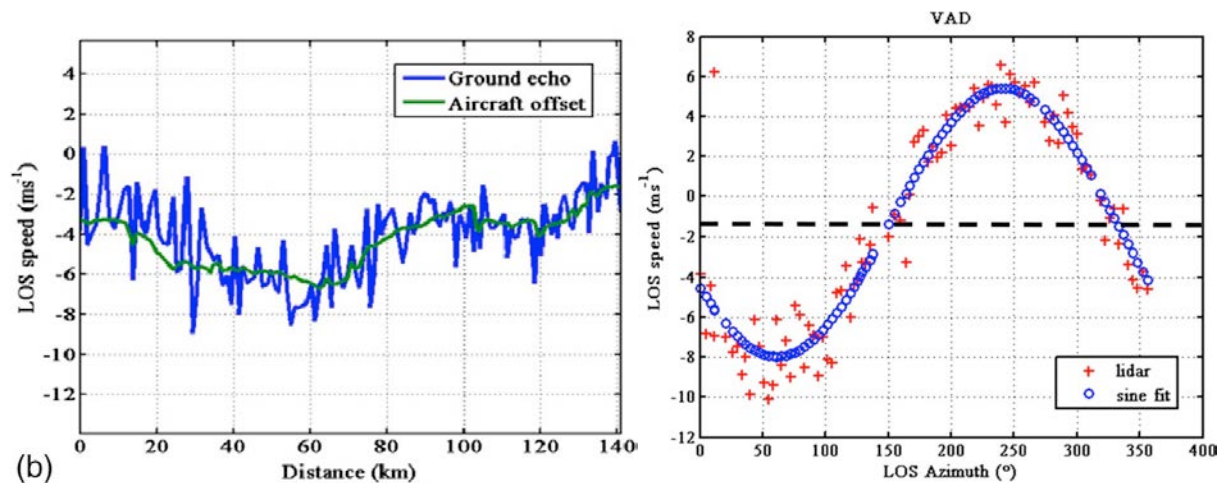


Figure 9 Left, LNG-HSR measurements of the ground echo, apparent speed derived from measurements (blue) and from inertial navigation system (green). Right, Velocity-azimuth display of the corrected LOS (line-of-sight) wind speed

Right panel in Figure 9 present the results of a 360° turn carried out by the F20 and was performed at a constant roll angle of 27° over cirrus clouds between 9.5 and 10.5 km. We display the corrected LOS wind speed as a function of the LOS azimuth angle, after having corrected the aircraft navigation offset. Assuming stationarity in the probed volume, this velocity-azimuth display (VAD) of the conical scan allows for the retrieval of the speed and direction of the horizontal wind as well as the vertical wind speed. A sine fit to the data shows a retrieved horizontal wind speed of 15 ms^{-1} with a direction of 240° . The

Version 1.2 EPATAN DATA ACQUISITION REPORT

measurement aboard the aircraft (at 12.5 km) gives a wind speed of 20 ms^{-1} with a direction of 270° . An offset of 1.5 ms^{-1} in the mean VAD was evidenced, larger than the estimated bias requiring further analysis.

In addition to the classical nadir and zenith views LNG has a slant measurement capability. In December 2015, the system has been modified to allow 37° sideward pointing. The laser viewing can be changed during flight.

Figure 10 illustrates the “wind” measurements collected by RALI (radar and lidar). The multibeam radar configuration allows us to retrieve vertical and horizontal wind field where clouds are detected by the instrument. In bottom panel, the wind component on the line-of-sight measured by LNG is reported as the F20 was flying forth and back to Greenland (first turn at 10:00 UTC and second one at 10:25 UTC). Nadir view was used from landing until around 10:30 and then LNG was depointed in order to make the most of its additional slant viewing which is giving access to products directly comparable to Aeolus ones. LNG was back to its nadir configuration after the second turn and as heading back to Iceland. We clearly see the impact of the wind velocity projection (including aircraft speed projection) while radar wind retrieval highlights similar wind structures during the flight.

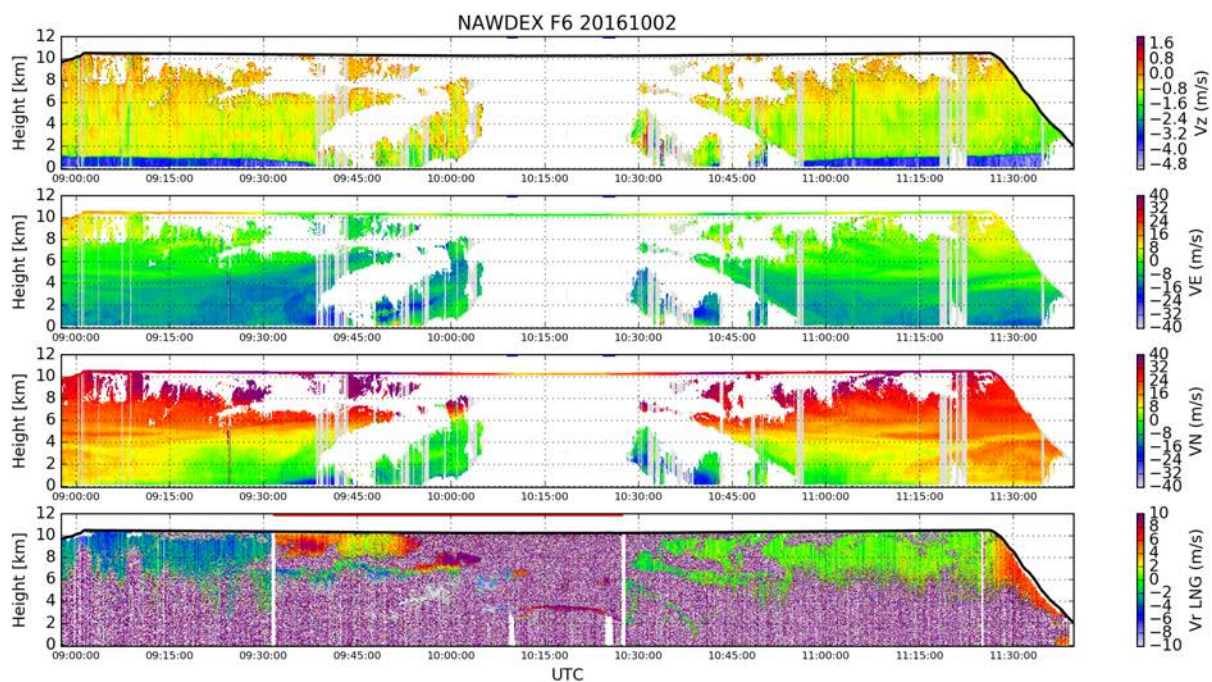


Figure 10 RALI wind measurements. First three top panels show radar wind retrievals, vertical velocity, eastwards wind and northwards wind respectively. Bottom panel shows LOS wind measured by LNG-HSR in nadir and 37° slant viewing configurations (37° configuration is highlighted by a red line between 9:32 and 10:27 UTC)

c. Measurements of Atmosphere and Ground Surface Targets - CLIMAT

Brightness temperature can be used to constrain cloud microphysics in clouds with Optical depths smaller than 6-8. The aircraft is equipped with the thermal infrared radiometer Conveyable Low-Noise Infrared Radiometer for Measurements of Atmosphere and Ground Surface Targets (CLIMAT)-Airborne Version (AV) (Legrand et al. 2000; Brogniez et al. 2003; Brogniez et al. 2005). It uses a 7-Hz sampling frequency and performs measurements within a 50-mrad field of view, which corresponds to a footprint of about 50 m at a 1-km range. Radiances are measured simultaneously in three narrowband channels centred at 8.7, 10.8, and 12.0 micron, with about 1 mm of full width at half maximum. Climat is very similar to the CALIPSO IIR system. Spectral band passes of CLIMAT-AV and IIR are presented in Figure 11 (from Sourdeval et al. 2012).

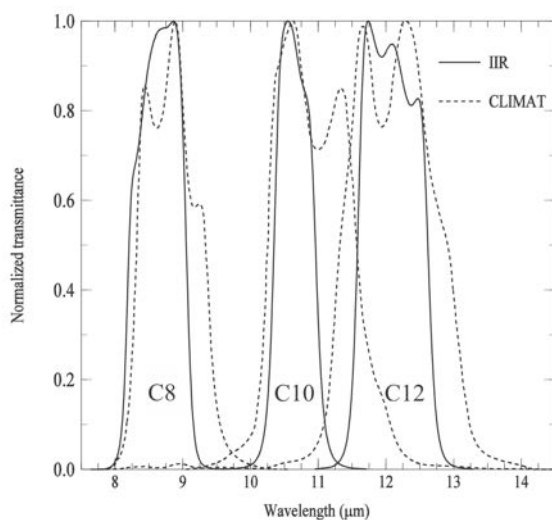


Figure 11 Normalized spectral band transmissions in channels C8, C10, and C12 of CLIMAT-AV and IIR. (Sourdeval et al. 2012).

The absolute accuracy of brightness temperature measurements derived from CLIMAT-AV is about of 0.1 K, whereas its sensitivity is of the order of 0.05 K (Brogniez et al. 2003).

Infrared measurements were collected during each F20 flights and co-located with radar and lidar data as shown in Figure 12.

Version 1.2 EPATAN DATA ACQUISITION REPORT

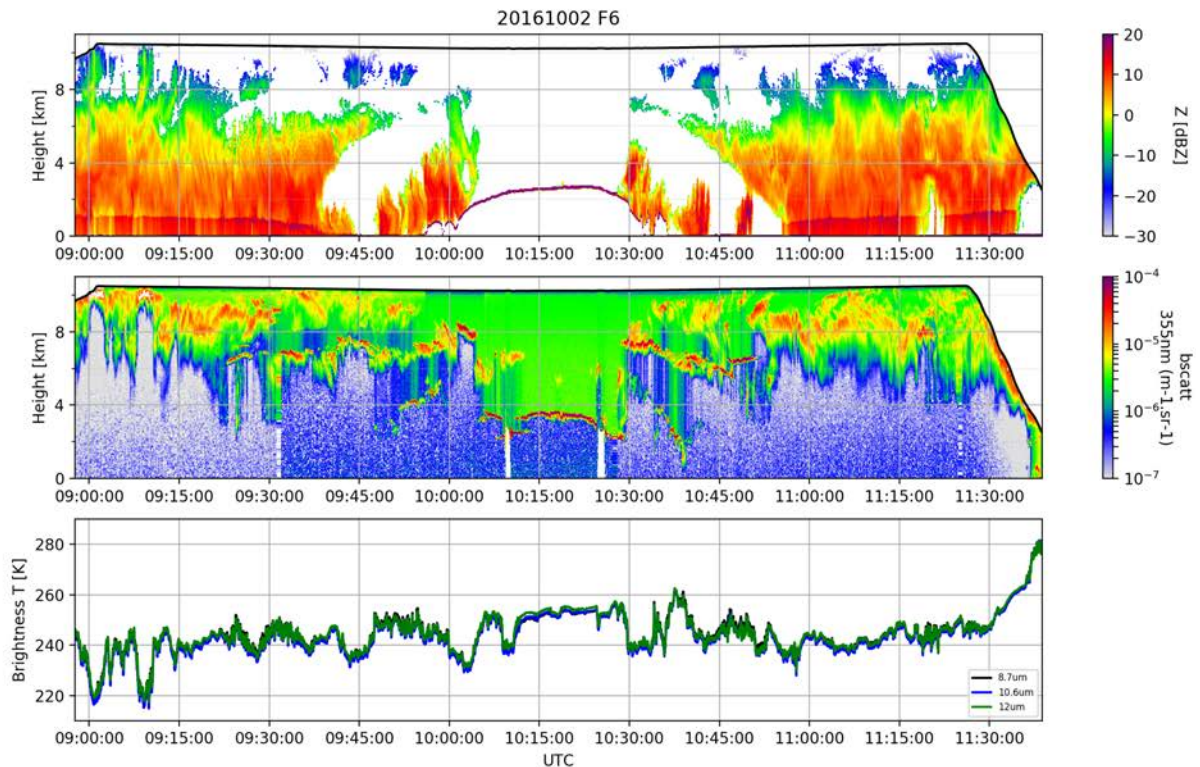


Figure 12 Example of radiative measurements collected during flight 6 on the 2nd of October 2016. Top and middle panels represent radar and 355 nm lidar measurements respectively. Bottom panel shows the CLIMAT brightness temperature at three wavelengths (8.7, 10.6 and 12 μm).

d. Dropsondes



Figure 13 Dropsonde launcher on-board the F20.

59 Vaisala AVAPS dropsondes were launched during the experiment. Some of the dropsondes in cloud conditions were used for characterizing atmospheric state to complete remote sensing measurements. However most of them were used in the framework of NEAREX objectives and LNG wind retrieval validation.

Version 1.2 EPATAN DATA ACQUISITION REPORT

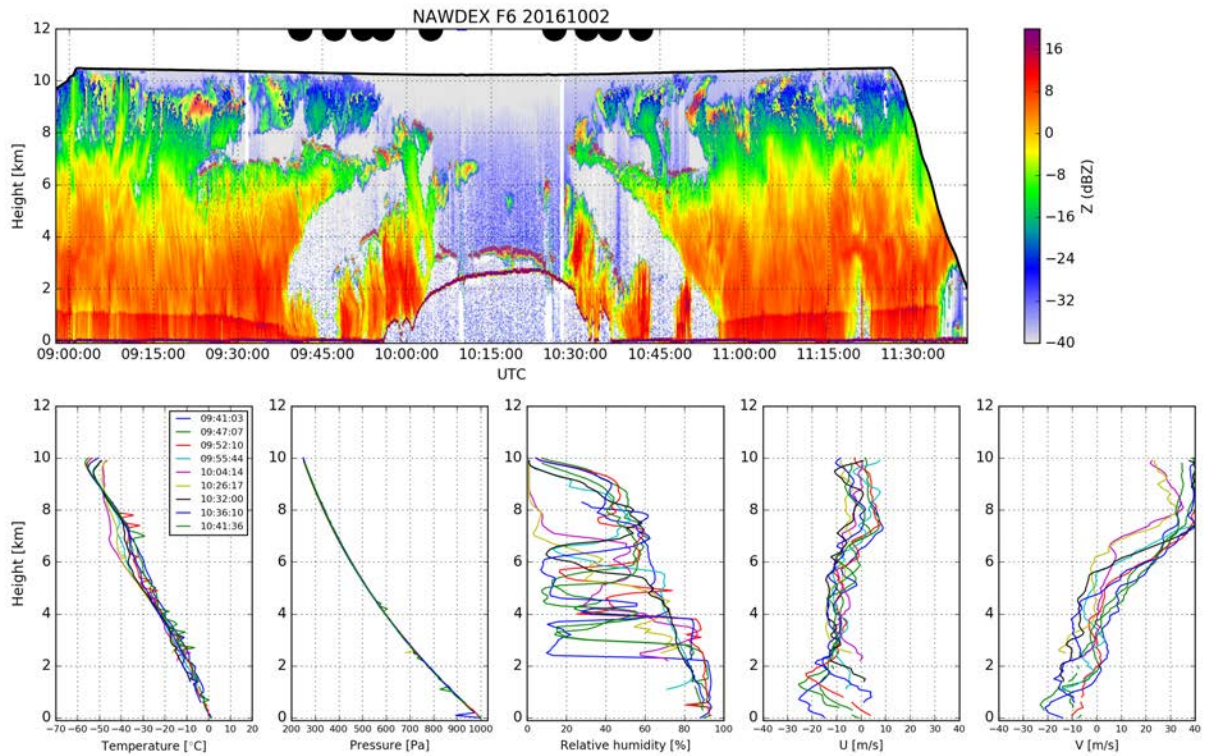


Figure 14 Examples of raw dropsonde measurements collected during flight 6. Top panel is a radar-lidar merged plot giving the cloud situation (black dots indicate dropsonde launches). Bottom panels show the dropsondes measurements, such as temperature, pressure, relative humidity, zonal and meridional winds.

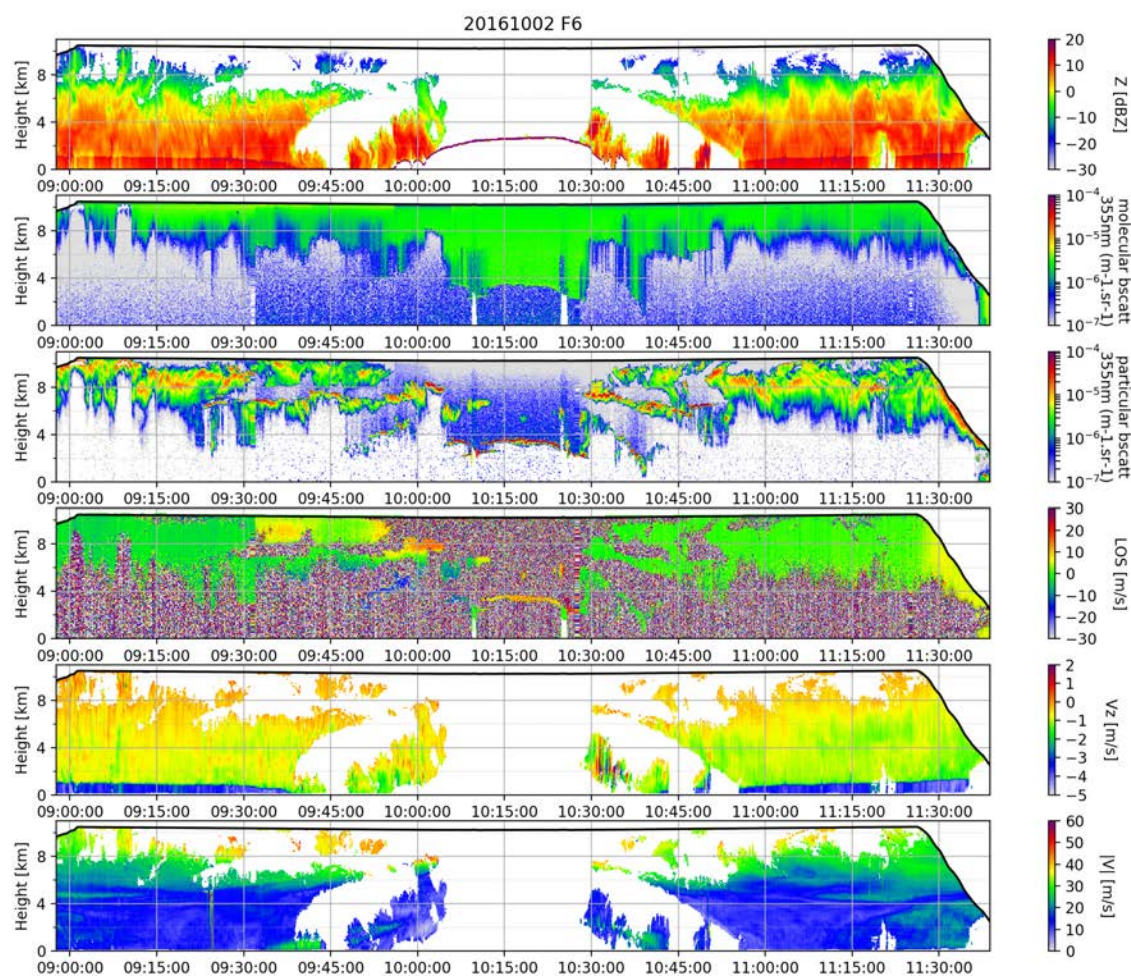
e. Example of measurements collected during the EPATAN-NAWDEX

Figure 15 Example of RALI measurements and retrievals (from top to bottom panels: 95GHz radar reflectivity, molecular backscatter at 355 nm, particular backscatter at 355nm, radial Doppler velocity from lidar, vertical cloud velocity module from radar and module of the horizontal cloud velocity).

Examples above show complementarity of lidar and radar observations within RALI allowing to fully describe the vertical structure of clouds, including thin ice clouds at top, thick ice clouds, water clouds, and precipitation regions.

3.1.2 Ground based measurements deployed during the campaign

The Doppler cloud radar mini BASTA ([Delanoë et al. 2016](#)) and the mini lidar were deployed in the vicinity of the airport. An example of radar measurements is presented in Figure 15 and the main characteristics of both radar and lidar are in Table 4.

Those instruments completed the airborne measurements with a bottom-up sampling of clouds and aerosols. The BASTA provided us with continuous observations (day and night operation) giving the general situation above Iceland during the campaign. The mini BASTA has been calibrated during the summer 2016 using a metallic reflector and could serve as reference for radar calibration. Note that the mini lidar was a prototype under

development and therefore only a few valid measurements were made during the targeted period.



Figure 16 Ground based radar-lidar system (mini BASTA and 808nm mini lidar) at Keflavik (hotel). From outside and inside the hotel room.

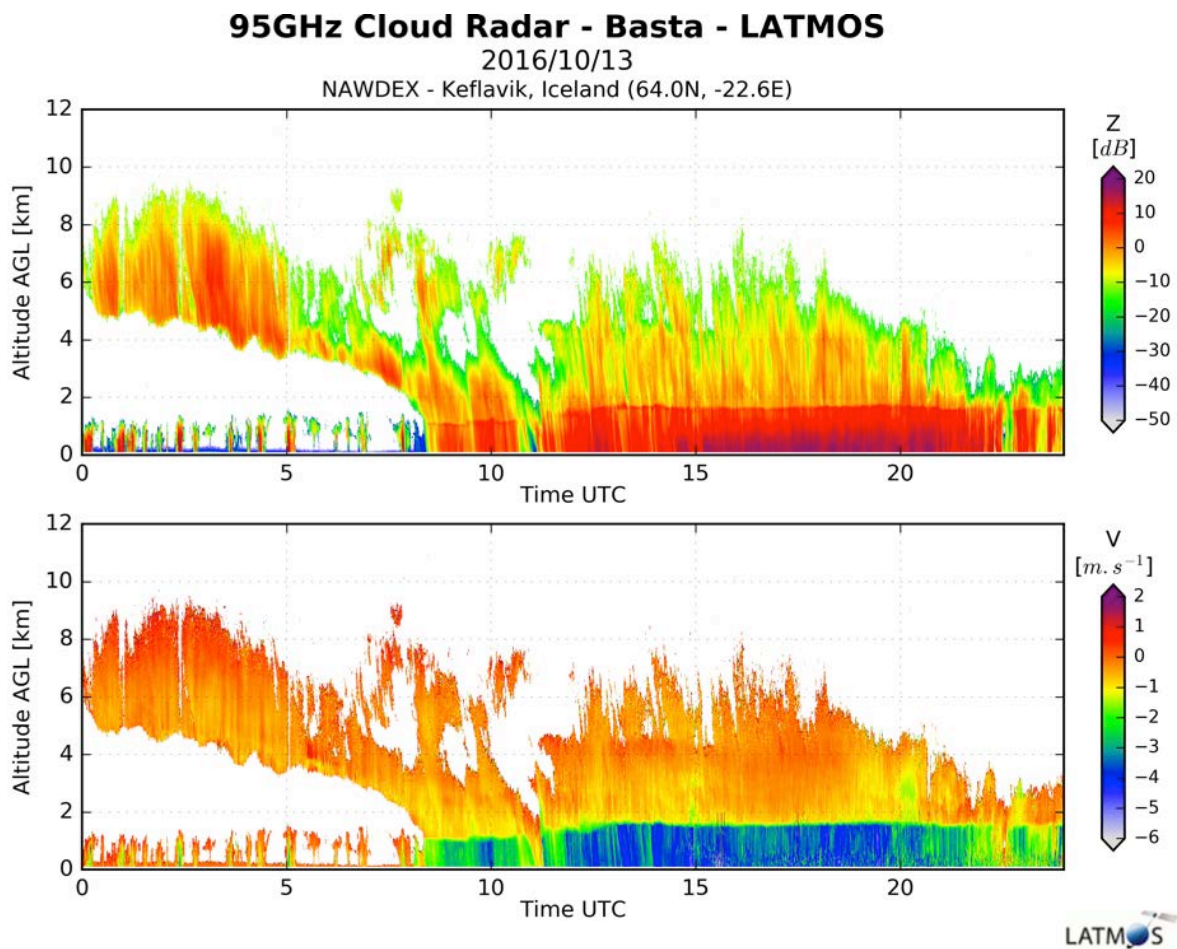


Figure 17 Example of measurements collected in Keflavik during NAWDEX campaign (13/10/2016). Top panel: reflectivity. Bottom panel: Doppler velocity.

	Mini BASTA	Mini-lidar
PI	J. Delanoë	J. Pelon
Weight (kg)	32	15
Size (cm)	82x52x45	Height=50 and diameter =25 cm
Wavelengths	3.2 mm (95 GHz)	808 nm
Measurements	Reflectivity and Doppler velocity	Attenuated backscatter

Table 4 Main characteristics of the ground-based radar and lidar

Note that the mini Lidar was in development during the deployment and the measurements are not suitable for scientific studies.

BASTA quicklooks are available here: <http://basta.projet.latmos.ipsl.fr/?bi=bif>, then select “Keflavik” and the mode you are interested in. Please contact Julien Delanoë (julien.delanoë@latmos.ipsl.fr) if you want to use the data.

3.2 DLR instrument deployment

3.2.1 HALO aircraft

During NAWDEX the German high altitude and long-range research aircraft HALO (see Figure 18) was employed. HALO is a modified Gulfstream G550 business jet with an endurance of more than 10 flight hours, a maximum range of about 8000 km, and a maximum cruising altitude of more than 15 km.



Figure 18 HALO (High Altitude and LOng range) aircraft. Photo adopted from <http://www.halo.dlr.de/>.

HALO was equipped with an extensive set of remote sensing instrumentation combining the differential absorption and high spectral resolution lidar (532 nm) system WALES (DLR), the cloud radar MIRA36 at 35 GHz (DLR, MPI-M Hamburg, University of Hamburg) and the spectral imager specMACS (LMU Munich) with microwave radiometer (MPI-M, University of Hamburg, University of Cologne) and radiation measurements (University of Leipzig). Additionally in-situ measurements of the meteorological properties along the flight track are measured.

3.2.1.1 Cloud Radar

MIRA36 is a commercial standard METEK Ka-band (35 GHz) cloud radar with polarization and Doppler capability to determine vertical velocity in clouds and precipitation. Technical details are summarized in Table 4.

Frequency	35.5 GHz
Peak Power	35 kW
Diameter of Antenna	1.1 m
Antenna Beam Width	0.5 deg.
Sensitivity at 5 km	-44.5 dBZ

Table 5 System parameters of the MIRA36 cloud radar

Together with microwave radiometers in the K-, V-, W-, F-, and G-band the MIRA36 is part of the HALO microwave package (HAMP) (Mech et al., 2014).

3.2.1.2 WALES Lidar

The lidar system WALES (Figure 19) is a combined differential absorption and high spectral resolution lidar (HSRL) system developed and built at the Deutsches Zentrum für Luft- und Raumfahrt (Wirth et al., 2009; Esselborn et al., 2008).

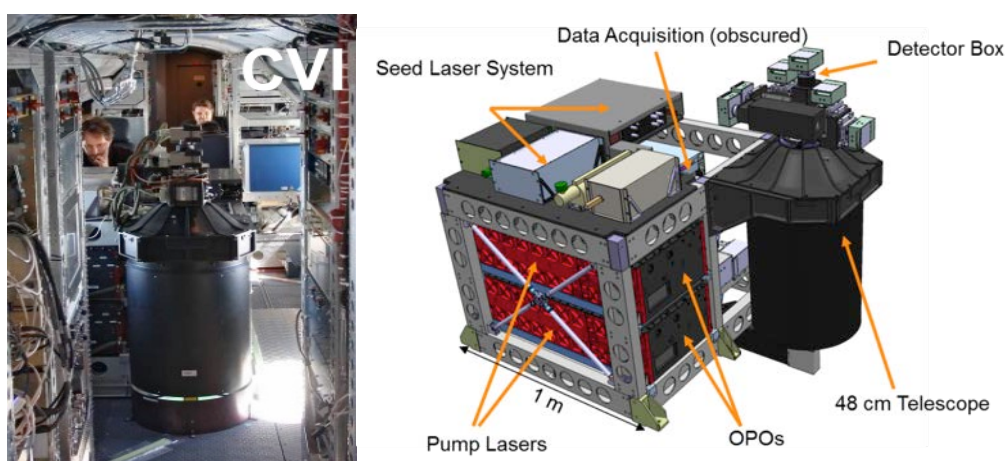


Figure 19 Lidar implemented in the HALO aircraft showing the telescope and the detector box and parts of the laser source (left panel), and sketch of the WALES lidar system (right panel).

The WALES lidar system consists of two transmitters, both based on an injection-seeded optical parametric oscillator (OPO) pumped by the second harmonic of a Q-switched, diode pumped Nd:YAG laser. WALES is capable to nearly simultaneously emit four wavelengths, three online and one offline, in the water vapour absorption band between 935 and 936 nm. The three online wavelengths achieve the necessary sensitivity needed for measurements over the whole range of tropospheric water vapour concentration. A complete water vapour profile of the troposphere is composed by using the information of the partly overlapping line contributions. The single pulse energy at 935 nm is 35 mJ with a repetition rate of 200 Hz (or 50 Hz for each quadruple). The vertical resolution of the raw data is 15 m. In addition to the 935 nm channel, the receiver is equipped with polarization-sensitive aerosol channels at 532 and 1064 nm, the first one with High Spectral Resolution capabilities using an iodine filter in the detection path (Esselborn et al., 2008). Typical transmitted pulse energies are 60 mJ at 532 nm and 120 mJ at 1064

nm. This allows for collocated measurements of humidity and optical depth, as well as studies of clouds and aerosol optical properties. System parameters of the WALES system are listed in Table 20. For a detailed technical description see [Wirth et al. \(2009\)](#).

Transmitter type	Nd:YAG laser pumped OPO
Pulse energy 935 nm (mJ)	35
Pulse energy 532 nm (mJ)	60
Pulse energy 1064 nm (mJ)	120
Pulse rate (Hz)	200
Wavelength (nm)	532, 935, 1064
Strong absorbing line (nm)	935.6846
Medium absorbing line (nm)	935.6083
Weak absorbing line (nm)	935.5612
Telescope diameter (cm)	48
Vertical resolution (m)	150
Horizontal resolution (km)	0.2 (1s)

Table 6 System parameters of the WALES lidar

An example of a WALES high spectral resolution lidar measurement during NAWDEX is shown in Figure 20

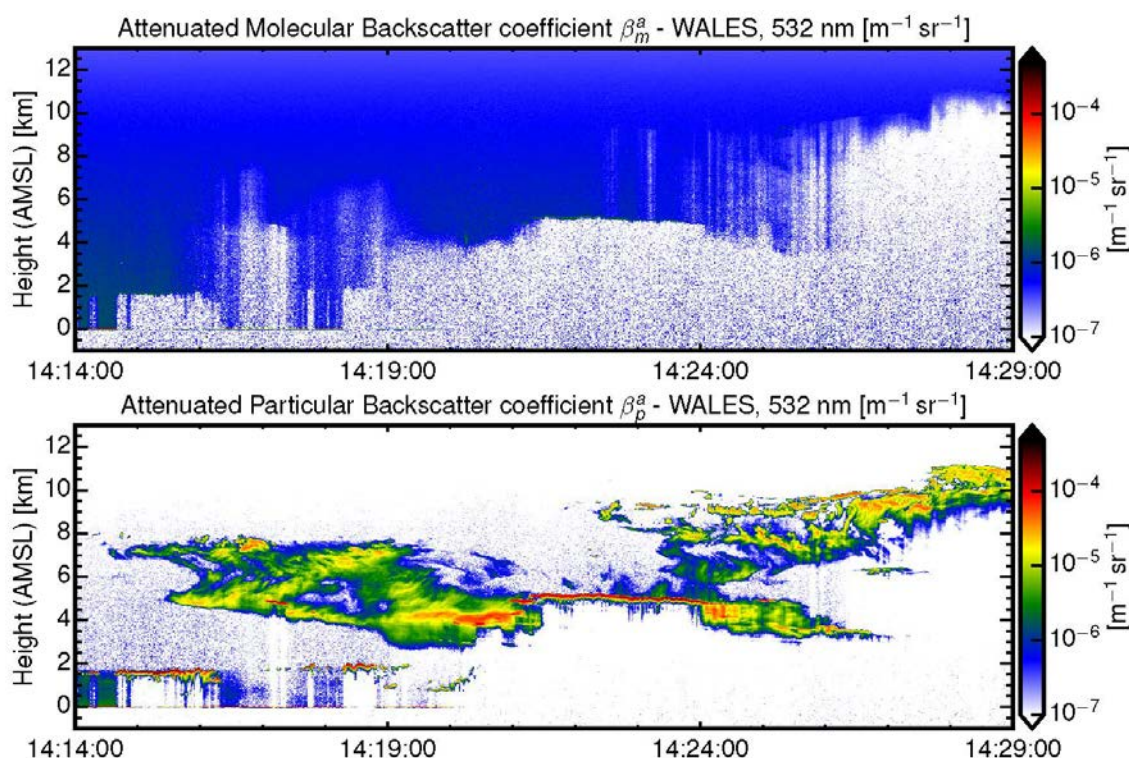


Figure 20 WALES high spectral resolution lidar measurements during NAWDEX on 13 October 2016.

3.2.1.3 SpecMACS

SpecMACS is an imaging cloud spectrometer consisting of two commercial spectral camera systems in the visible near-infrared (VNIR: 400-1000 nm) and in the shortwave infrared (SWIR: 1000-2500 nm) manufacturer SPECIM, Finland. The nominal spectral resolution is 3nm and 10 nm for the VNIR and for the SWIR, respectively. SpecMACS produces a spectrally resolved line image. For the NAWDEX campaign this spatial line will be mounted across-track resulting in a push-broom image with a spatial resolution in the order of 10 m for cloud objects at a distance of about 10 km for a typical data acquisition rate of 30 Hz. Technical details are summarized in Table 7.

	VNIR	SWIR
Detector	SiO ₂ DMOS	HgCdTe CMOS
Spectral range (nm)	417 – 1016	1015 – 2496
Spectral bandwidth (nm)	typ. 2.5 – 4	typ. 7.5 – 12
FOV	32.7°	35.5°
IFOV (across track) (mrad)	typ. 1.4	typ. 3.8
IFOV (along track) (mrad)	typ. 2.0	typ. 1.8
Maximum frame rate (Hz)	145	103
Temp. Control (K)	uncooled	200

Table 7 System parameters of the specMACS imager

The specMACS system is well characterized and calibrated ([Ewald et al., 2016](#)). It was first operated on board the HALO aircraft during the ACRIDICON-SHUVa campaign in Brazil in September 2014. (Figure 21) shows an example of specMACS measurements during NAWDEX.

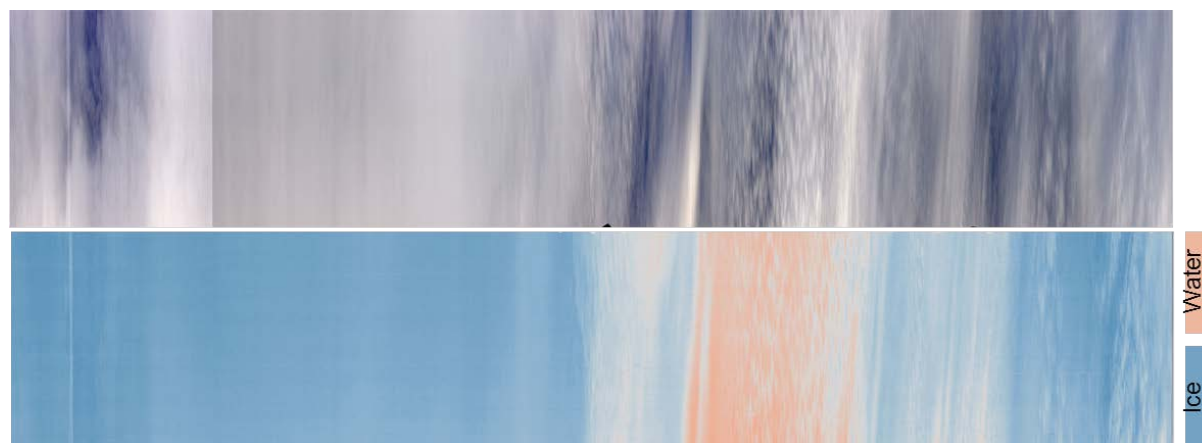


Figure 21 RGB and ice index derived from specMACS measurements on 1 October 2016.

3.2.2 German F20 with wind lidars

The DLR research aircraft Dassault Falcon 20-E5 will be operated from Keflavik Iceland. The well experienced airborne platform for atmospheric research have been deployed during several field campaigns over Iceland.



Figure 22 DLR Falcon instrumentation

Altitude [ft]	10 000	20 000	31 000	41 000
max. Range [NM]	1150	1500	1700	2000
max. Endurance [h:min]	04:10	04:15	04:45	05:00
max. Altitude			42 000 ft	12 800 m
max. Speed (VMO / MMO)			380 KCAS	0,865 Mach
Long Range Speed			410 KTAS	0,720 Mach
Takeoff Distance (MTOM, ISA, MSL)			2000 m	6562 ft

Table 8 DLR Falcon performance data

The following description of the Falcon instrumentation is taken from the Campaign Implementation plan of the WindVAL campaign 2015 (Reitebuch 2015).

The payload of the DLR Falcon aircraft will consist of the A2D (Reitebuch et al. 2009, Paffrath et al. 2009) and the 2- μ m Doppler wind lidar (DWL, Weissmann et al. 2005).

The A2D and the 2- μ m lidar will be pointing in the same line-of-sight LOS direction to the right side of the aircraft (in flight direction) with a nadir angle of 20°. The instruments are mounted as follows:

- The A2D aircraft frame is mounted with a pitch angle of -6° (pointing to the back) along the aircraft axis; the telescope is mounted such that it points towards the right with a roll angle of 20° and pointing back by -4°; thus the A2D telescope points backwards by -2° and 20° to the right side.
- The 2- μ m is mounted with a pitch angle of -2° (pointing to the back) along the aircraft axis. It is equipped with a double-wedge scanner, which allows to point towards -6° and a roll angle of 20°. Small offsets in the order of 0.1° of the 2- μ m pointing direction will be determined in flight.

The nominal operation of the 2- μ m lidar will be the measurement of the LOS wind and conical step-stare scans will be performed in order to measure the horizontal wind vector during flight. The vertical sampling of the A2D will be set such, that the ground layers are sampled with highest vertical resolution (2.1 μ s, 315 m range).

The 2- μ m DWL will measure time series of raw signal with a sampling rate of 500 MHz, which corresponds to a range resolution of 0.3 m for each emitted laser shot with a repetition rate of 500 Hz. This amounts to rather high raw-data rates of up to 60 GByte/hour depending on maximum range. The data will be processed on-ground to

Version 1.2 EPATAN DATA ACQUISITION REPORT

range-gates of 100 m resolution and temporal resolution of 1 s (500 shots). Standard meteorological parameters (pressure, horizontal wind vector, vertical wind speed, temperature, humidity (relative humidity, mixing ratio)) will be measured by in-situ sensors inside the Falcon nose-boom with a temporal resolution of up to 100 Hz and processed with resolution of 1 Hz. Thus vertical profile data are available for ascent and descent and flight-level data from cruising altitude. First quick-look data from these sensors will be available about 1 day after each flight during the campaign.

Parameter	DLR A2D	DLR 2- μ m DWL
Wavelength	354.89 nm	2022.54 nm
Laser energy	50 mJ	1-2 mJ
Pulse repetition rate	50 Hz	500 Hz
Pulse length	20 ns (FWHM)	400-500 ns (FWHM)
Telescope diameter	20 cm	10.8 cm
Vertical resolution	300 m – 2.4 km	100 m
Temporal averaging raw data (horizontal)	20 laser shots = 0.4 s	single shot = 2 ms
Temporal averaging product (horizontal)	14 s (+4 s data gap)	1 s LOS, 32 s scan (20-22 LOS)
Horizontal resolution @ 200 m/s=720 km/h = 12 km/min.	3.6 km (18 s)	0.2 km LOS, 6.4 km scan
Scanning capabilities	No, fixed 20° off nadir	Yes, double wedge, conical scan, fixed LOS and vertical
Precision (random error)	1.5 m/s Mie wind 2.5 m/s Rayleigh wind	< 1 m/s wind speed

Table 9 Main specifications and products from the 2 different direct-detection wind lidars

4. French Falcon DATA description

4.1 RASTA Aircraft data

The core meteorological instruments aboard the Falcon-20 are managed by SAFIRE. Most of them are sampled and recorded at frequencies above 1 Hz, and were averaged on a 1 s period in the dataset used for the present analysis.

Position, orientation and speed are measured by a GPS-coupled Inertial Navigation System (AIRINS model from IxBlue). Air pressure is measured by a Rosemount Model 1201 pressure transducer, air temperature by a Rosemount 102 B Total Air Temperature sensor. The 3-D air motion vector relative to the aircraft is measured by Rosemount 1221 differential pressures transducer connected to a Rosemount 858 flow angle sensor mounted at the tip of the boom, ahead of the aircraft, and by a pitot tube, which is part of the standard equipment of the aircraft.

Raw measurements, such as impact temperatures, relative air speed vector need to be processed to obtain atmospheric state variables. Adiabatic heating due to compression is removed from impact temperature to get static air temperature. Wind in local geographical coordinates is computed as the sum of the air speed vector relative to the aircraft, and the aircraft velocity vector relative to the ground. Both computations use classical formulas in the airborne measurement field described in Bange et al. (2013). These data are provided in netcdf format by SAFIRE and CNRM teams.

4.2 RASTA products

In this section we describe the different products derived from RASTA measurements. RASTA measures both power and velocity for each antenna (3 antennas looking down). However, these measurements cannot be used directly for scientific purpose. The radar reflectivity must be calibrated and range corrected in order to convert the it into dBZ. The background noise is also removed using thresholding technique knowing the background noise characteristics. Once the L1 data derived from the raw measurements and for each antenna it is possible to go to the next level.

There are several RASTA products available:

- L2 products for each antenna (note that this product also contains raw data)
- L2 WIND product
- Microphysical product
- Spectral analysis product (available only on demand)

4.2.1 Single antenna level 2 product

Before using the data and positioning the radar gates in space, it is crucial to know where the antennas are pointing. It has always been a challenging task (Testud et al. 1995; Haimov and Rodi 2013). Each antenna position must be known accurately on the aircraft. As a first guess we are using a pointing machine (operated by the technical division of CNRS-INSU) which allows us to measure the azimuth and elevation of each antenna (El_{ant} , Az_{ant}) in the aircraft's referential (vertical and the rail along the fuselage) as shown in **Figure 23** d and e. The downward antennas angles are checked using ground Doppler velocity that is expected to be close to zero once corrected from aircraft

motion and the projected in-situ wind measurements along the radar radial (not shown here). The upward antennas angles (when used) are only verified using the projected in-situ wind measurements along the radar radial direction. Note that we optimised the consistency with the aircraft's sensors and confirmed with the ground velocity.

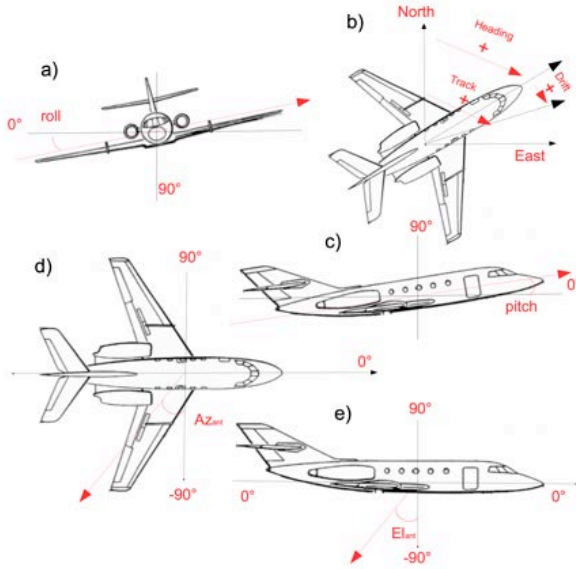


Figure 23 Description of the aircraft attitude angles (a to c) and the azimuth (Az_{ant}) and elevation (El_{ant}) of the antennas with the aircraft as a referential (d and e).

A radial is defined by the antenna pointing (aircraft's referential) and the attitudes of the aircraft defined in **Erreur ! Source du renvoi introuvable.** (roll (a), pitch (c), heading (b)). The first step is the calculation of the azimuth (Az) and the elevation (El) for each radar radial in the Earth referential:

$$Az = \arctan2(Y, X) + 360 - heading$$

$$El = \arctan2(Z, \sqrt{X^2 + Y^2}) \quad \text{(eq 1)}$$

where X , Y and Z are calculated using the following equations:

$$\begin{aligned} X &= \cos(El_{ant}) \cos(Az_{ant}) \cos(roll) + \sin(El_i) \sin(roll) \\ Y &= \cos(El_{ant}) \cos(Az_{ant}) \cos(roll) \cos(pitch) \\ &+ \cos(El_{ant}) \sin(Az_{ant}) \cos(pitch) - \sin(El_{ant}) \cos(roll) \sin(pitch) \\ Z &= -\cos(El_{ant}) \cos(Az_{ant}) \sin(roll) \cos(pitch) \\ &+ \cos(El_{ant}) \sin(Az_{ant}) \sin(pitch) - \sin(El_{ant}) \cos(roll) \cos(pitch) \end{aligned} \quad \text{(eq 2)}$$

Knowing Az and El angles for each antenna it is possible to calculate the coordinates (latitude, longitude, altitude) of each radar gate:

Version 1.2 EPATAN DATA ACQUISITION REPORT

$$\begin{aligned}
 Long[i, k] &= Long_{ac}[i] + r[k] \cos(Az[i]) \cos(El[i]) \frac{360}{2\pi R_T * \cos(Lat_{ac}[i])} \\
 Lat[i, k] &= Lat_{ac}[i] + r[k] \sin(Az[i]) \cos(El[i]) \frac{360}{2\pi R_T} \\
 Alt[i, k] &= Alt_{ac}[i] + r[k] \sin(El[i])
 \end{aligned}
 \tag{eq 3}$$

i is the radial index, k is the gate number, $R_T = 6378137$ m is the Earth radius, range is the distance between the radar and the gate. $Long_{ac}$ and Lat_{ac} are the longitude and the latitude of the aircraft, respectively. The range of each gate is represented by r .

RASTA nadir reflectivity is calibrated using the ocean surface return technique (Li et al. 2005; Tanelli et al. 2008). The calibration of the other antennas is either directly derived using ground surface (in a similar manner as the nadir) or by comparing with nadir reflectivity. This calibration was carried out during Flight 3 in Toulouse area on 21/09/2016 using the sea surface backscatter. An example is shown in Figure 24. The aircraft's flight track is presented in panel a. Panels b and c present the RASTA and LNG measurements respectively. The lidar measurement is used to ensure that we are not missing any liquid clouds between the sea surface and the aircraft that could strongly attenuate surface echo. σ_0 as a function of time and incidence angle (above sea) is displayed in panel d. The attenuation due to gases is computed using the dropsonde measurements (panel e)) collected during the flight, we estimate a loss of about 2dB. Knowing the wind surface, it is possible to estimate the theoretical σ_0 as a function of the incidence angle. Panel f shows the comparison between the RASTA and theoretical σ_0 .

Version 1.2 EPATAN DATA ACQUISITION REPORT

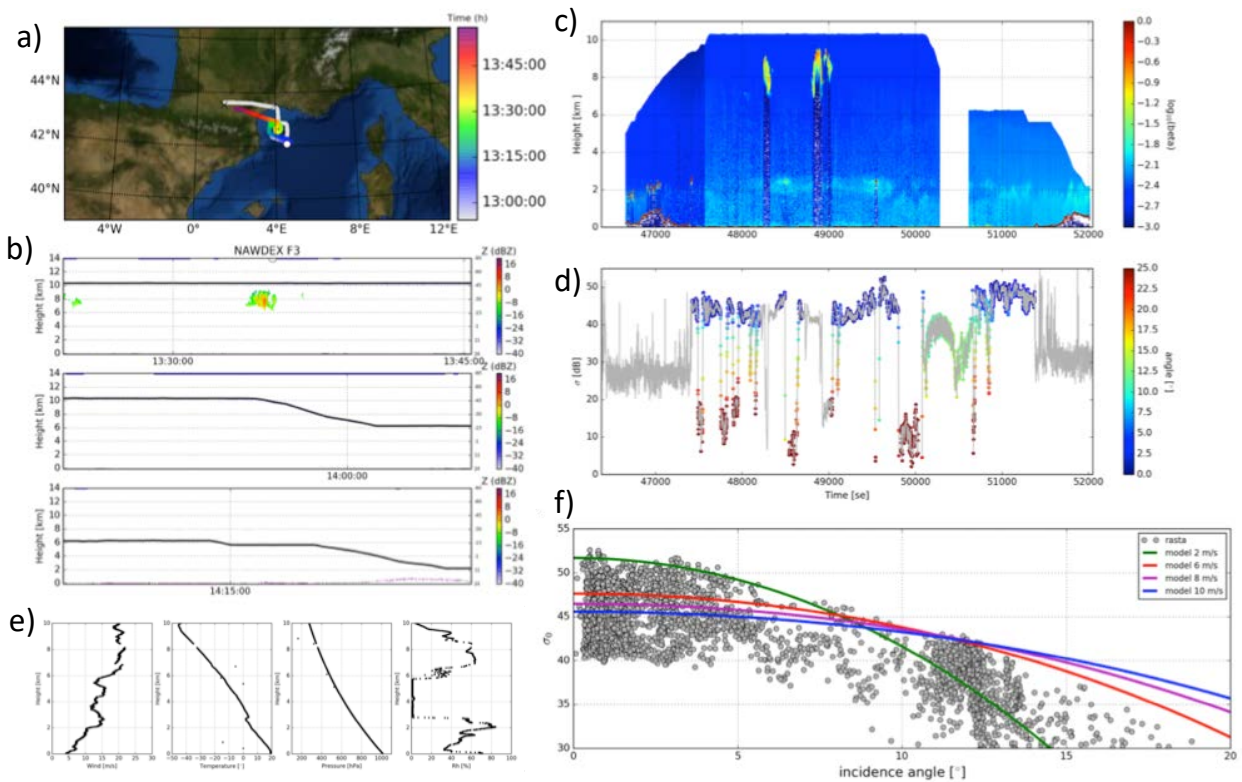


Figure 24 Example of calibration procedure for RASTA during the test flight in Toulouse

The BASTA radar was operating at the Keflavik airport and fortunately we carried out some overflights. This radar was calibrated prior to the campaign using a solid target. Figure 25 shows the co-located reflectivity and velocity between RASTA (top panels) and BASTA (middle panels) for a stratus ranging between 4 and 9 km. The black box corresponds to the closest window of observation for the ground-based radar with respect to the overpass time. We consider that the cloud close to surface does not strongly attenuate the signal (note that the radome was dry). Bottom right panel corroborates the good agreement between the radars, for both reflectivity and vertical velocity.

Version 1.2 EPATAN DATA ACQUISITION REPORT

Comparison RASTA and BASTA @ Keflavik : 20161002

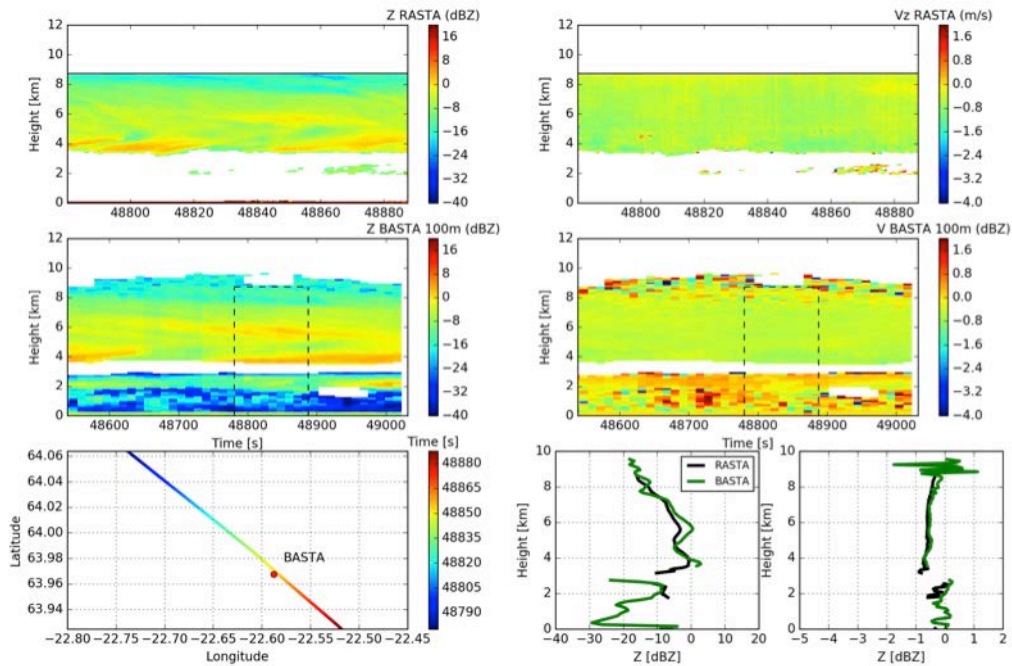


Figure 25 Comparison between RASTA and BASTA (ground based) measurements during an over flight

Due to its PRF (Pulse Repetition Frequency) and ambiguous distance, RASTA's Nyquist velocity is about 7.9 m/s ($V_{\text{Nyquist}} = \pm \text{PRF} \lambda/4$, with λ the radar wavelength 3.2 mm for RASTA). Therefore the Doppler velocity measured by RASTA must be corrected from "folding", which means that all Doppler velocities are measured into the Nyquist interval, ± 7.9 m/s. The aircraft motion vector is then projected along the radial direction, and added to the Doppler measurement to remove the aircraft motion component. This component is actually added, because the aircraft motion results in an apparent Doppler contribution of opposite sign. We then use the in-situ data at the closest range to the aircraft to unfold the first measured Doppler velocity along a radial direction. Then we apply a gate to gate correction along the radial, allowing for a maximum difference of 6 m s⁻¹ between successive range gates.

Figure 26 shows the raw measurements of each antenna as a function of range (from the aircraft). At this level there is no correction apply on the data, the reflectivity is not calibrated and not range corrected. The background signal is not removed as presented in Figure 26. The velocity contains the aircraft motion and we can distinguish areas where velocity has been folded.

Version 1.2 EPATAN DATA ACQUISITION REPORT

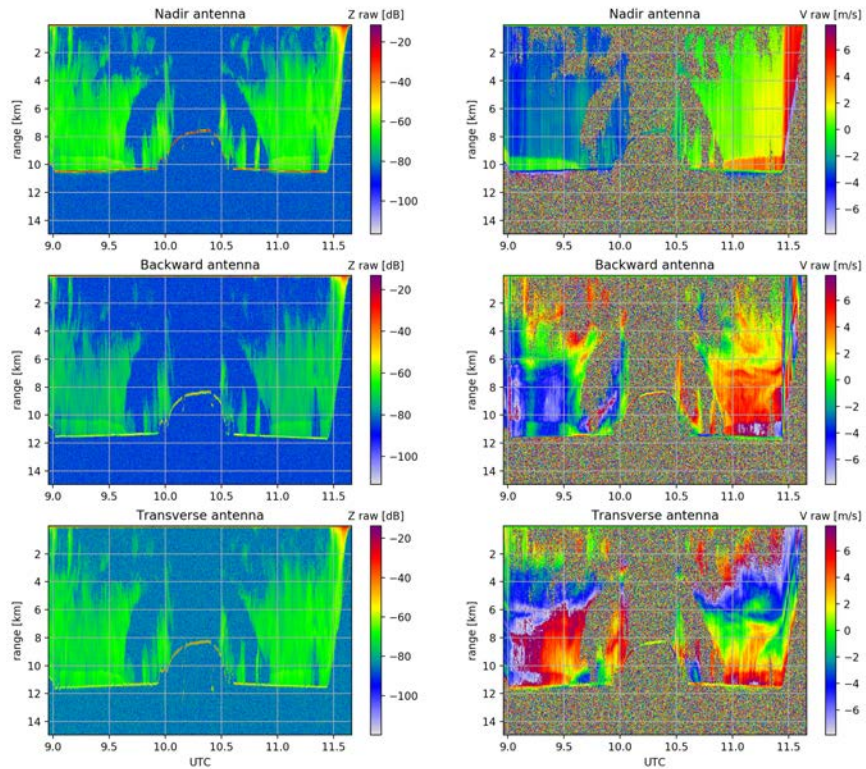


Figure 26 Raw measurements (power and Doppler velocity) from RASTA, nadir (top), backward (middle) and transverse (bottom) antennas

After processing, both reflectivity and velocity are corrected and the background noise is removed. Figure 27 shows reflectivity and velocity for each antenna after processing as a function of altitude above the earth surface. Note that all the radar gates have been positioned in space (latitude, longitude, altitude).

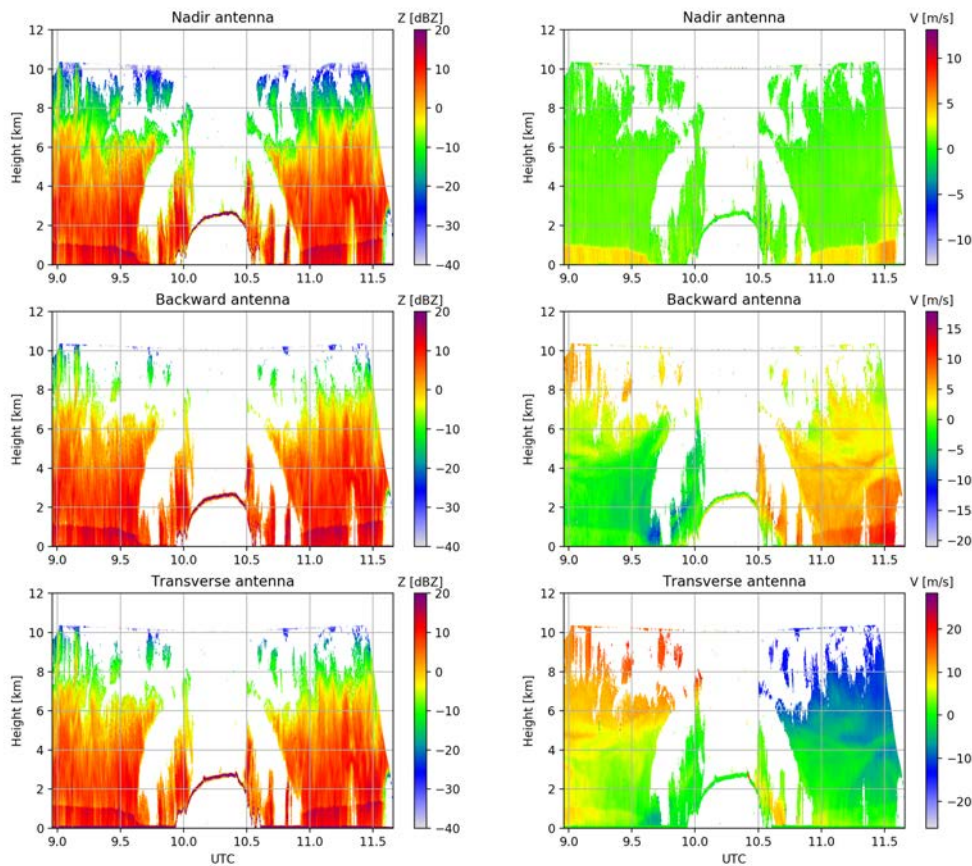


Figure 27 Calibrated radar reflectivity and unfolded Doppler velocity from RASTA, nadir (top), backward (middle) and transverse (bottom) antennas.

4.2.2 Wind retrieval level 2 product

As previously discussed, RASTA is capable of retrieving the 3D wind field, i.e. the three components of the wind on the vertical plane below the aircraft (3 antenna configuration), by combining independent Doppler velocity measurements from the multi-beam antenna system (we retrieved the 3 components of the wind in the aircraft's referential, V_x is the along track wind, V_y is the cross-track wind and V_z the vertical wind). Once the Doppler velocity is unfolded and corrected from aircraft's motion and the reflectivity calibrated it is possible to retrieve both dynamical and microphysical cloud properties. Figure 28 summarizes the whole process to retrieve cloud winds and some extra variables such as gaseous attenuation or phase discrimination.

Version 1.2 EPATAN DATA ACQUISITION REPORT

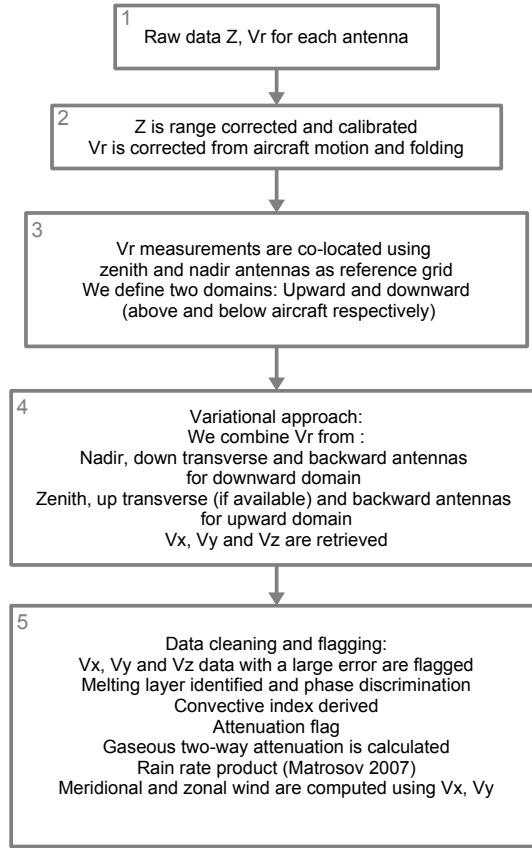


Figure 28 Flowchart describing the data processing for the wind retrieval.

The 3D wind is retrieved using an optimal estimation approach (inspired from Protat and Zawadzki, 1999), which consists in using an iterative process to adjust the state vector containing V_x (along track wind component), V_y (cross track) and V_z (vertical):

$$\mathbf{X} = \begin{pmatrix} V_x \\ V_y \\ V_z \end{pmatrix}, \quad (\text{eq 4})$$

to minimize δy the difference between the forward modelled Doppler velocity:

$$\mathbf{Y} = \begin{pmatrix} Vr_{vertical} \\ Vr_{backward} \\ Vr_{transverse} \end{pmatrix}, \quad (\text{eq 5})$$

and the measured one along each antenna.

Note that for the sake of clarity only one measurement from a random antenna is discussed here. When the transverse antenna is missing (this happened during the a few campaigns), only V_x and V_z can be retrieved. At each iteration, the state vector is updated using the following equation:

$$x_{k+1} = x_k + \mathbf{A}^{-1} \left[\mathbf{H}^T \mathbf{R}^{-1} \delta y \right], \quad (\text{eq 6})$$

where \mathbf{H} is the jacobian, \mathbf{A} the Hessian matrix and \mathbf{R} the covariance matrix error. After minimization of the cost function:

$$2J = \delta y^T \mathbf{R}^{-1} \delta y, \quad (\text{eq 7})$$

the optimal state vector contains the retrieved 3D wind components.

\mathbf{R} assumes that the errors are not correlated and is therefore diagonal. The forward model errors are arbitrary set to 0.5 m/s to include possible errors due to antenna mis-pointing.

Version 1.2 EPATAN DATA ACQUISITION REPORT

Note that the value of the error is not crucial as the same error is applied to all antennas. Some tests were made to use the collocation distance as weighting function but this resulted in retrieval instability. As the problem is well posed, 3 equations for 3 unknowns for a at least 3-antenna system, the convergence is reached after 3 iterations. Practically the retrieval method is not applied in one shot but only on ten continuous profiles to avoid processing of too large matrices at once, with the advantages of speeding up the process and limiting the required computing resources.

The forward model is straightforward and is defined by a single equation depending on the radial pointing and the three components of the wind as follows:

$$Vr_{ant} = V_x \cos(Az_{ant}) \cos(El_{ant}) + V_y \sin(Az_{ant}) \cos(El_{ant}) + V_z \sin(El_{ant}). \quad (\text{eq 8})$$

The “ant” index indicates that the formulae can be used for all antennas and for each radar gate. The jacobian (**H**) is diagonal as we assume the data gate to gate independent and is derived using the following equations:

$$\frac{\partial Vr_{ant}}{\partial V_x} = \cos(Az_{ant}) \cos(El_{ant}) \quad (\text{eq 9})$$

$$\frac{\partial Vr_{ant}}{\partial V_y} = \sin(Az_{ant}) \cos(El_{ant}) \quad (\text{eq 10})$$

$$\frac{\partial Vr_{ant}}{\partial V_z} = \sin(El_{ant}) \quad (\text{eq 11})$$

Indeed, V_y dependencies are removed when there are only two antennas available (upward or downward).

RASTA L2 product contains also some information regarding the nature of the hydrometeors. Temperature field from ERAI is used to support the ice/liquid distinction. The melting layer is detected using the vertical velocity as the rapid conversion of ice into rain leads to a strong vertical gradient in vertical velocity.

The radar mask contains the following information: 0 (no cloud) / 1 (ice) / 2 (rain) / 3 (ice but likely attenuated) / 4 (ground) / 5 (ghost ground) / 6 (interpolated). Note that label 6 is not relevant for EPATAN-NAWDEX configuration as it concerns only the campaigns when upwards antennas are used.

There are a few extra variables in this product (with recipe):

- **Convective index:** First we define the ice part and we keep only V_z (V_t+W) corresponding to ice.

n_vup = Sum of the pixels $V_z > 2$ (and V_z valid) updraft / n_vdown = Sum of the pixels $V_z < -3$ (and V_z valid) downdraft

Convective if n_vup or $n_vdown > 8$

- **Gaseous attenuation**

RH, T and P profiles are derived from in-situ and ECMWF reanalysis. The gaseous attenuation is computed using Liebe’s model (O₂ and H₂O). The variable saved is the cumulated attenuation for each radar gate as a function of the distance from the aircraft.

- **Melting layer/Phase discrimination**

Vertical gradients of Z and V_z are used. Horizontally averaged (running window), 10 radials

- V_z

Version 1.2 EPATAN DATA ACQUISITION REPORT

Melting zone $dVz/dz > 3$ and $-4 < T < 10$, variable set to 2

The melting layer is determined using the mean values and standard deviation of the melting zone altitude

The mean value is conserved only if the standard deviation is ≤ 0.2 km. Then the valid values are interpolated.

- Z

Melting zone : $dZ/dz < -8$ and with 200m of the melting zone Vz

Maximum altitude with this criterium

mean_melting=averaged(altitude_melt_Z) 'single value'

altitude_melt_Z is interpolated (only when difference between mean and melting line defined using Z is less than 500 m).

Ice altitude \geq altitude melting = 1

Rain or liquid $>$ altitude melting = 2

- **Rain rate (From Matrosov 2007)**

Compute the reflectivity gradient below the melting layer: $dZdr$ (most of the time below the aircraft but during take off or landing rain can be above the aircraft)

Rain rate is computed 500m below the melting layer only

rain_attenuation=0.5* $dZdr$ - gaseous_attenuation

$K=1.1*\rho_{\text{air}}^{(-0.45)}$, ρ_{air} is the air density kg/m³

RainRate = $K*1.4*\text{rain_attenuation}$

- **Attenuation**

- how many pixels below the melting layer (npix)

- can we detect the ground echo

- quick check of the cloud/rain thickness (above 500m) (npix cloud)

Attenuation in ice part if npix < 20 , ground echo not detected, roll $< 20^\circ$ and cloud thick enough (npix cloud > 25) => set to 1

Attenuation in ice part if aircraft below the melting layer => set to 1

- **attenuation_phase_flag:**

- 0 no cloud

- 1 ice

- 2 rain (attenuated)

- 3 ice but likely attenuated

- 4 ground

- 5 ghost ground

- 6 interpolated

- **radar_classification_flag :**

- -2: underground

- -1 : ground

- 0: no cloud

- 1: ice only Z

- 2: ice both Z and V

- 3: liquid and warm rain

- 4: melting layer

- 5: cold rain

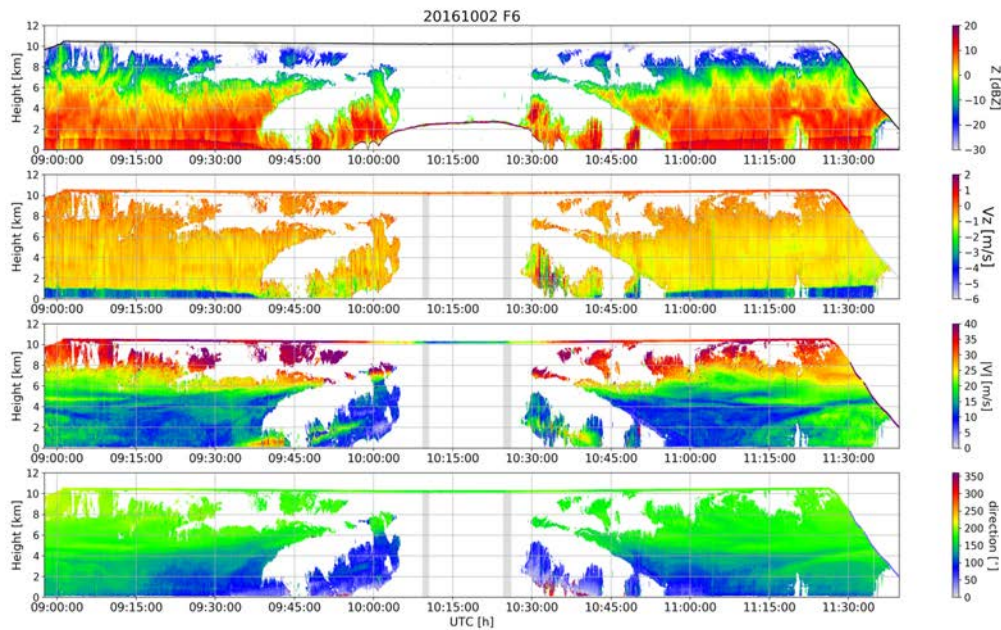


Figure 29 RASTA wind retrieval, top panel shows the nadir radar reflectivity, second panel from the top is the vertical velocity. Third and fourth panels illustrate horizontal wind intensity and direction respectively.

Level 2 velocity data can be combined to derive vertical and horizontal winds as shown in Figure 29. The nadir calibrated and range corrected reflectivity is represented in top panel. The vertical velocity (V_z which is a combination of the terminal fall velocity of hydrometeors and the vertical air motion) indicates that the cloud vertical velocity is around 1m/s and we can distinguish the ice/rain conversion (known as melting layer) at around 1km altitude. The vertical air motion measured by the aircraft's probes is plotted the altitude of the aircraft. The intensity of the horizontal wind is presented in the third panel, highlighting the variability of the wind intensity as a function of altitude due to wind shear. During that flight, the wind intensity was clearly increasing with the altitude with a maximum speed larger than 40 m/s which is corroborated by the aircraft probes (coloured line). The bottom plot shows that the wind direction is varying between 50° and 200° . Clear sky data are screened out and appear in white. Grey colour indicates the area where the retrieval cannot be trusted. For instance, the vertical component of the wind cannot be retrieved below the aircraft when the aircraft is turning on the left.

4.2.3 Microphysical product

The Radon technique proposed by Delanoë et al. (2007) uses the radar reflectivity and Doppler velocity to retrieve ice cloud properties. This technique is mainly based on the fact that the radar reflectivity once normalized by N_0^* (Delanoë et al. 2005, 2014) can be parameterized as a function of the mean volume diameter D_m . As the terminal fall velocity (V_t) is mainly a function of D_m , but is fairly independent on N_0^* , the V_t measurement is a

good constraint to retrieve D_m . Once D_m is calculated the relationship between Z/N_0^* and D_m is used to retrieve N_0^* . Knowing D_m , N_0^* and assuming a functional form for the normalized PSD, the different moments of the PSD can be calculated (N_t , extinction...). IWC is derived directly from the combination of D_m and N_0^* as explained in Delanoë et al. (2005, 2014). The new version of the Radon technique combines both the variational approach proposed in Delanoë and Hogan (2008) and the Delanoë et al. (2007) retrieval principle, hence the name “Radonvar”. However the definition of the state vector has been reconsidered to better fit the radar measurements and our current knowledge in ice cloud microphysics. N_0^* is replaced (Delanoë et al. 2014) by IWC. Therefore, we can directly use IWC bulk measurement as an a priori information. This has been possible thanks to the recent bulk measurements of IWC during HAIC campaigns. For the first time we had bulk measurements of reflectivity and IWC in deep convective ice clouds.

The state vector is composed of IWC and the vertical air motion (w). Note that the a priori information of w is set at 0 m/s. The vertical velocity V_z (sum of vertical air motion and terminal fall speed of hydrometeors) is not directly measured by the radar but the combination of at least two antennas (above and below the aircraft) pointing in different directions belonging to a plane at the vertical of the aircraft allows V_z to be retrieved. It is important to note that there are two independent measurements, Z and V_z , which in principle allow one to retrieve two parameters. An important issue in deep ice clouds resides in the attenuation of radar reflectivity due to dense and large hydrometeors. This will be discussed in the radar forward model section. Accounting for attenuation is one of the reasons why we considered using a variational approach. The strong vertical correlation of successive reflectivity measurements along the radial direction cannot be handled by classical methods such as radon. The previous gates affect each radar gate measurement.

As we start with a first guess of the cloud state (IWC, W) we can compute the associated reflectivity and vertical velocity via a “forward model”. The logarithm of IWC is used to prevent negative values in the IWC retrieval due to numerical instability or noise measurements effects. Radonvar uses an iterative process and therefore a first guess for the state vector is required. For consistency purpose we use the a priori information as a first guess, i.e. IWC as a function of temperature and reflectivity and W equal to 0 m.s⁻¹. The process is repeated until convergence and the latter is determined by a χ^2 convergence test.

4.2.4 Spectral analysis product (on demand only)

This product contains nadir antenna measurements (Z , V) but also higher-level products such as the 3D wind retrieval (combination of several antennas described above). I and Q data are available which allow users to make the most of the spectral analysis. FFT spectrum, V , Z and spectral width are derived from I and Q.

Version 1.2 EPATAN DATA ACQUISITION REPORT

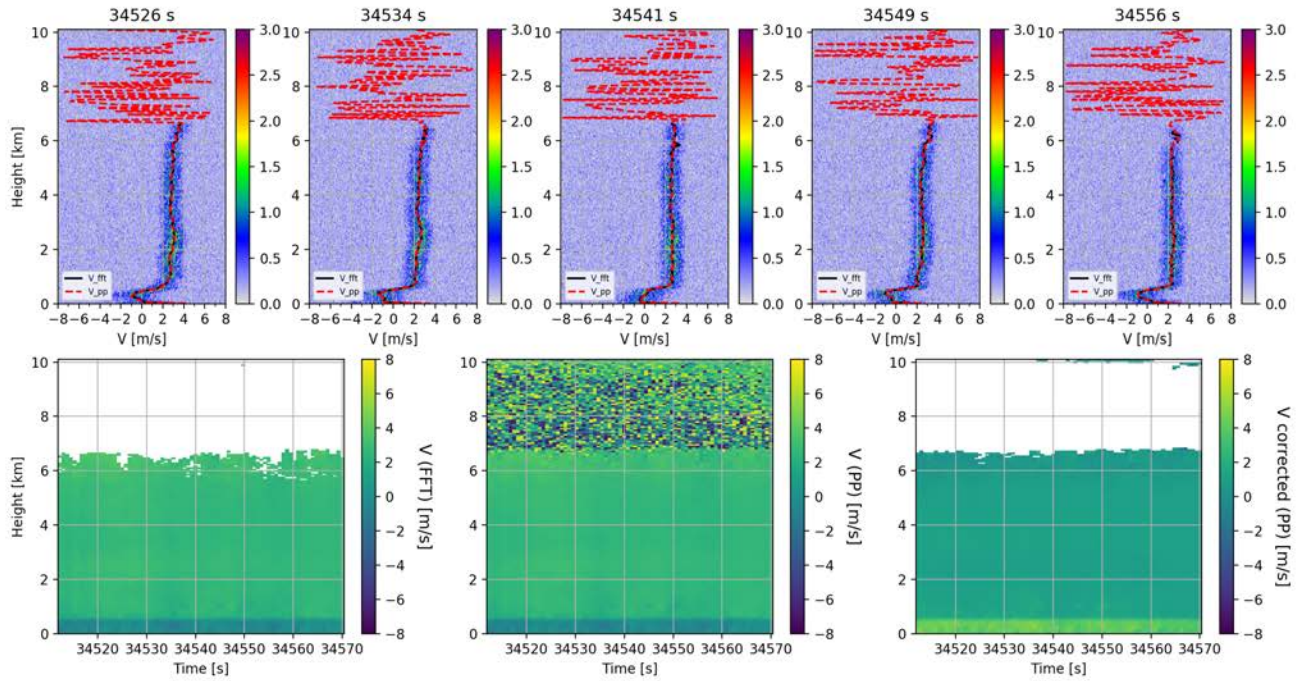


Figure 30 Example of spectral data: 2016/10/02 09h35. Top panels illustrate the FFT spectrum for different profiles (time in sec). Red and black lines represent the FFT and Pulse Pair Doppler velocities respectively. Bottom panels show the time-height representation of Doppler velocities (V_{FFT} , V_{PP}) and the right-hand graphic shows the Pulse Pair velocity corrected from aircraft velocity and folding.

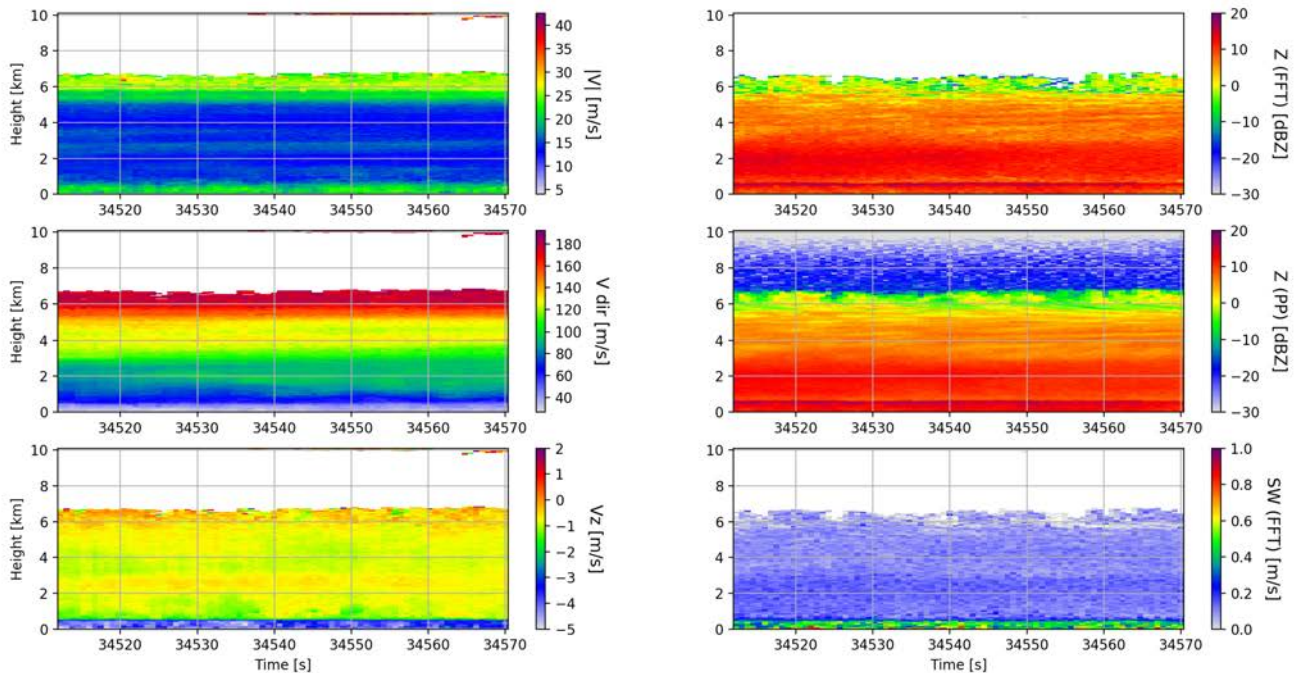


Figure 31 Time-height representation of Horizontal wind module ($|V|$) and direction (V_{dir}), vertical velocity retrieved combining 3 antennas. Reflectivity PP and FFT (range corrected and calibrated) and FFT spectral width

4.2.5 RASTA measurement errors information

The systematic error in RASTA reflectivity is assumed to be within 1dB according to our calibration technique. Radar pointing and errors in Doppler measurements are only assessed through a comparison between the Dropsondes measurements and RASTA 3D wind field retrieval.

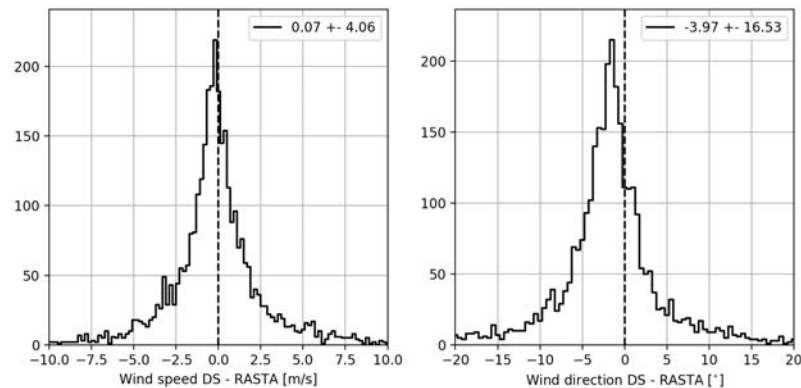


Figure 32 Histograms of the difference between DS and RASTA wind speeds and directions

The RASTA cloud winds have been co-located with the dropsonde wind profiles. We have shown that the bias on the horizontal wind speed was 0.07 m/s with a standard deviation of about 4 m/s. The wind direction is overestimated of about 4° with a standard deviation of 16° . The direction bias can be explained by the difficulty to estimate the radar antenna mounting angles. Note that we did not remove the outliers in these statistics, explaining the large standard deviation compared to the histogram presented in Figure 32.

4.3 LNG products

Calibrated LNG signals are available in the LIDAR Level 1 files and consist in total attenuated backscatters at 355 nm, 532 nm and 1064 nm as well as the particular and molecular attenuated backscatters at 355nm derived thanks to the HSRL measurements. The volume depolarization ratio and the particular depolarization ratio are also available at 355nm as the LIDAR emits at this wavelength in the linear polarization and the receiver separates the backscattered signal in the polarization parallel to the emission from the signal in the polarization perpendicular to the emission. The HSRL processing is performed on the parallel channel only. As a consequence, the final particular and molecular backscatters are a combination of the perpendicular channel and the HSRL outputs. The HSRL also allows for the retrieval of the radial wind on the LIDAR line of sight.

A calibration of the HSRL is performed before-hand to produce the Level 0 files and provide a calibrated measurement of the radial wind and the backscatter ratio in the 355 nm parallel channel. The final LIDAR backscatters available in the Level 1 files are calibrated over cloud and aerosol free regions using a reference model for the molecular backscatter at the corresponding wavelength.

4.3.1 Characteristics of LNG and pre-processing

Version 1.2 EPATAN DATA ACQUISITION REPORT

The LIDAR emits at 3 different wavelengths and has 4 reception channels as presented in Table 10 and Table 11. The 355 nm channels have a receiver filter of unknown spectral bandwidth (between 1.8 nm and 2.5 nm) and the central peak is not perfectly known either. This will lead to uncertainties when calibrating the depolarization ratio and the perpendicular channel relatively to the parallel one.

Table 10 : Main characteristics of the emitter

Wavelength (nm)	Energy (mj)	Divergence (mrd)
355 nm linear polarization	~40	0.16
532nm	~9	4
1064nm	~45	5.6

Table 11 Main characteristics of the receiver

Wavelength (nm)	Field of view (mrd)	Spectral bandwidth (nm)	Detector
355 nm parallel	0.5	~2	PM
355 nm cross	0.5	~2	PM
532nm	5	0.2	PM
1064nm	7	1	APD

The repetition rate of the emitter (a flashlamp-pumped Nd:YAG Q-switched oscillator) is 20 Hz (= 50 ms) and the spot separation distance is 10 meters assuming an aircraft speed of 200 m/s (Falcon 20).

The signal is averaged over a hundred of shots (~5s) to increase the signal-to-noise ratio, after the imperfectly seeded shots have been removed on a shot-to-shot basis and the signal of each channel has been corrected from the average value of the background noise of the corresponding detector (recorded prior to the signal itself).

Every profile is then corrected from the variation in energy of the laser source in the corresponding wavelength: $S_{355}(t) = S_{355,0}(t) * \frac{E_{355}(t)}{MEAN_{flight}(E_{355})}$. The measurement of energy is 10% accurate.

The HSR measurement is performed on the 355 nm parallel channel. To do so, the light is redirected to the input of a Mach-Zehnder interferometer (MZI) via a 600 μm silica/silica UV optical fibre and collected at the output by 4 detection channels (photomultipliers PM) in phase quadrature. A complex number is then derived to separate the molecular signal from the particular signal and determine the radial wind measured in the LIDAR line of sight ([Bruneau et al, 2015](#)).

The theoretical signal for each of the four channels of the interferometer is expressed as follows:

$$S_i = \frac{S_t}{4} a_i \left[1 + M_i M_a \sin \left(\varphi + (i - 1) \frac{\pi}{2} \right) \right] \quad \text{(eq12)}$$

With S_t , the total signal detected by the parallel channel at 355nm ($S_t = S_{par}$), M_a , the interference contrast due to the atmosphere (clear sky, clouds and aerosols) and M_i , the interference contrast due to the instrumental setup of the i^{th} channel, φ , the phase of the total signal, and a_i , an instrumental constant for the i^{th} channel.

After reconstruction of the signals, the L0 lidar files contain information on the total attenuated uncalibrated perpendicular signal S_{perp} , the total attenuated uncalibrated parallel signal S_{par} , the particular attenuated uncalibrated parallel signal $S_{par,part}$ and the molecular attenuated uncalibrated parallel signal $S_{par,mol} = S_{par} - S_{par,part}$, and finally, the Doppler measurement in the lidar line of sight V_{LOS} . Information on how to retrieve those signals from the MZI outputs can be found in [Bruneau et al. \(2015\)](#).

The raw signals presented in **Erreur ! Source du renvoi introuvable.** cannot be used directly and they require extra processing such as calibration.

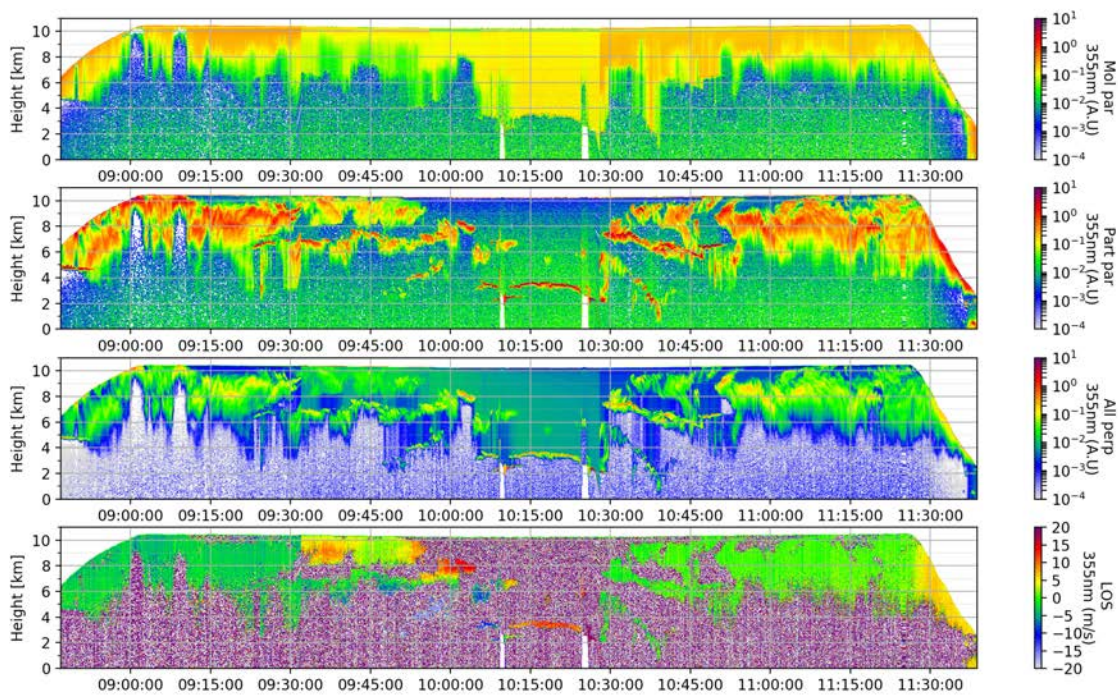


Figure 33 Raw 355nm LNG measurements. Top panel shows the raw molecular backscatter, second panel the particular parallel backscatter, third panel displays molecular and particular perpendicular backscatter. The bottom panel shows the raw line of sight Doppler.

4.3.2 Calibration of the lidar signals

In a first instance, the 4 channels of the interferometer have to be inter-calibrated to be able to retrieve the HSRL measurements at 355nm, namely the LIDAR molecular and particular signals in the parallel channel ($S_{par,part}$ and $S_{par,mol}$) and the Doppler measurement in the LIDAR line of sight (V_{LOS}). The coefficients a_i and M_i from **equation 12** have to be calibrated. Before each flight a recording is made with the reference signal when the laser is not injection seeded, which leads to no interference contrast and allows for a calibration of the 4 a_i coefficients. In practice, we need for each channel, a coefficient $a_{i,r}$ for the reference signal and a coefficient $a_{i,s}$ for the atmospheric signal. Therefore, a recording of a clear sky signal with the laser not injection seeded is also made (particles will create interferences).

The calibration of M_i has to be made in laboratory conditions prior to the field campaign (the calibration method is detailed in [Bruneau et al, 2015](#)). It may change during the

flights, however, in the measurement process, the reference signal is recorded prior to the atmospheric signal, which can be used to normalize the measured contrast and get rid of this uncertainty. This procedure allows for a calibrated measurement of the radial wind, which is then corrected from the offset due to the aircraft motion.

The cross and parallel channels are also intercalibrated in laboratory conditions. However, additional post-processing is needed to retrieve the lidar particular and molecular backscatter coefficients in $[m^{-1} \cdot sr^{-1}]$. The calibration of the signals is performed on each averaged profile on a clear sky area of 500m (~50 lidar gates) between the aircraft and the cloud top using a model of molecular backscatter:

$$\beta_m(t, z) = \hat{\beta}_m(t, z) * T^2(t, z), \quad (\text{eq13})$$

with $\hat{\beta}_m$ the “true” (unattenuated) backscatter. It is derived from the atmospheric density and depolarization following [Bodhaine et al. \(1999\)](#) and [She \(2001\)](#).

Temperature and pressure fields are from ERA-interim reanalysis. The reanalysis data are available at 0h, 6h, 12h and 18h UTC and the flights are between 2.5 and 4 hours long so only 1 ERA file is used for each flight. The reanalysis data are linearly interpolated over an [altitude, latitude, longitude] grid similar to that of the RASTA measurements (e.g. ~ [60m, 0.01°, 0.01°]) and then for each radar gate, the closest pixel from the ERAI file is selected. The ERAI file used for each flight is the one corresponding to the reanalysis for which the time is the closest in a least square sense to all the measurements performed during the flight.

The molecular transmittance along the laser path is given by:

$$T^2(t, z) = e^{-2 \int_z^{z^{aircraft}} \alpha_m(t, z') dz'}, \quad (\text{eq14})$$

with α_m the molecular extinction, also derived from [Bodhaine et al. \(1999\)](#).

A calibration constant is defined for each channel (532, 1064 and 355 parallel) as the ratio of the averaged signal over a 500m distance at a distance z_0 below the aircraft and the molecular backscatter calculated from the atmospheric reanalysis density and the lidar model presented above:

$$C_\lambda(t) = \text{mean}_{z_0 < z < z_0 - 500m} \left(\frac{S_\lambda(t, z)}{\beta_m(t, z, \lambda)} \right). \quad (\text{eq15})$$

For profiles where the cloud top is too close from the aircraft, the average of the constants computed for the current leg is used. And if there is no clear sky at all during the current flight, we use the average of all the calibration constants computed during the campaign. One must distinguish between legs performed in the ADM-like configuration (lidar pointing at 37° off-nadir) and legs performed in the classic nadir-pointing configuration.

The calibrated signals are:

$$\begin{aligned} \beta_{532} &= S_{532} / C_{532}, \\ \beta_{1064} &= S_{1064} / C_{1064}, \\ \beta_{par} &= S_{par} / C_{355}, \\ \beta_{perp} &= S_{perp} / C_{355} * \delta_{th} / \delta_{meas}, \end{aligned}$$

$$\begin{aligned}
\beta_{355} &= \beta_{par} + \beta_{perp}, \\
\beta_{part} &= (1 + \delta_{th}) * S_{par,part} / C_{355} + S_{perp} / C_{355} * \delta_{th} / \delta_{meas} - \delta_{th} * S_{par} / C_{355}, \\
\beta_{mol} &= (1 + \delta_{th}) * S_{par,mol} / C_{355}.
\end{aligned} \tag{eq16}$$

with δ_{th} , the theoretical value for the molecular depolarization ratio and δ_{meas} the average value of the measured depolarization ratio over the calibration distance.

4.3.3 Measurement errors

Error analysis - Level 0

The statistical error of the measurement, σ_{S_λ} , estimated at the output of the detectors, is derived from the photon noise on the detectors.

For the parallel UV channel, which is a linear combination of the 4 detectors at the output of the MZI, the statistical variance is also given by a linear combination of the variance computed for each detector (the random errors of the detectors are uncorrelated):

$$\sigma_{S_{par}}^2 = \left(\frac{4}{M_1^{-1} + M_2^{-1} + M_3^{-1} + M_4^{-1}} \right)^2 * \left(\frac{\sigma_{S_1}^2}{M_1^2 a_1^2} + \frac{\sigma_{S_2}^2}{M_2^2 a_2^2} + \frac{\sigma_{S_3}^2}{M_3^2 a_3^2} + \frac{\sigma_{S_4}^2}{M_4^2 a_4^2} \right). \tag{eq17}$$

It is a bit more complicated for the particular signal and the Doppler measurement, which involve non-linear operations. Following the formalism described previously, the variance of the particular signal can be expressed as follows:

$$\begin{aligned}
\sigma_{S_{par,part}}^2 &= \frac{q_1^2 * \sigma_{q_1}^2 + q_2^2 * \sigma_{q_2}^2}{q_1^2 + q_2^2}, \\
\text{with } \sigma_{q_1}^2 &= 4 * \frac{(1 + X_{pol})^2}{(M_2 + M_4)^2} * \left(\frac{\sigma_{S_4}^2}{a_4^2} - \frac{\sigma_{S_2}^2}{a_2^2} \right) \\
\text{and } \sigma_{q_2}^2 &= 4 * \frac{(1 + X_{pol})^2}{X_{pol}^2 (M_1 + M_3)^2} * \left(\frac{\sigma_{S_1}^2}{a_1^2} - \frac{\sigma_{S_3}^2}{a_3^2} \right).
\end{aligned} \tag{eq18}$$

The random error on the molecular signal, $\sigma_{S_{par,mol}}^2$, can be estimated as the sum of $\sigma_{S_{par}}^2$ and $\sigma_{S_{par,part}}^2$ although this is not completely true as S_{par} and $S_{par,part}$ are not independent.

The variance of the Doppler signal is expressed by:

$$\sigma_V^2 = \frac{q_1^2 * \sigma_{q_2}^2 + q_2^2 * \sigma_{q_1}^2}{(q_1^2 + q_2^2)^2} + \overline{\sigma_{Q_r}^2}. \tag{eq19}$$

Uncertainty of the molecular depolarization ratio ($\sigma(\delta_{mol,th})$)

Following [Behrendt and Nakamura \(2002\)](#) and [Placzek \(1934\)](#), we assume that the depolarization ratio of the atmospheric signal, $\delta_{mol,th}$, is independent of the wavelength. The theoretical depolarization measured in clear sky by the LIDAR depends on its receiver

bandwidth. Indeed, 75% of the depolarized fraction of the emission spectrum of molecules, due to Raman rotational processes, are located in the wings of the spectrum. When the LIDAR measures the entire spectrum, the depolarization ratio due to air molecules equals 1.45% (She 2001). For LNG, the spectral bandwidth of the receiver is not precisely known: $1.8\text{nm} < \text{FWHM}_{355\text{nm}} < 2.5\text{nm}$ (the full width at half-maximum of the Gaussian-shaped filter centered at 355nm) $< 2.5\text{nm}$, which corresponds to a filter bandwidth in cm^{-1} between 142.8cm^{-1} and 198.3cm^{-1} . This can then be translated back to nanometers to assess the corresponding size of the filter for a 532nm reception channel: $4\text{nm} < \text{FWHM}_{532\text{nm}} < 5.6\text{nm}$. Using the results presented by Behrendt and Nakamura (2002), the filtered molecular depolarization ratio can be estimated between 1.05% and 1.15%, for a given temperature of -30°C . As a conclusion, the uncertainty on the filter bandwidth leads to an error of 10% on the theoretical value of the molecular depolarization ratio. As a comparison, if we combine the statistic of temperatures in the calibration regions (Figure 34) with the variations of $\delta_{mol,th}$ as a function of temperature described by Behrendt and Nakamura (2002), the uncertainty due to the change in temperature is less than 5%.

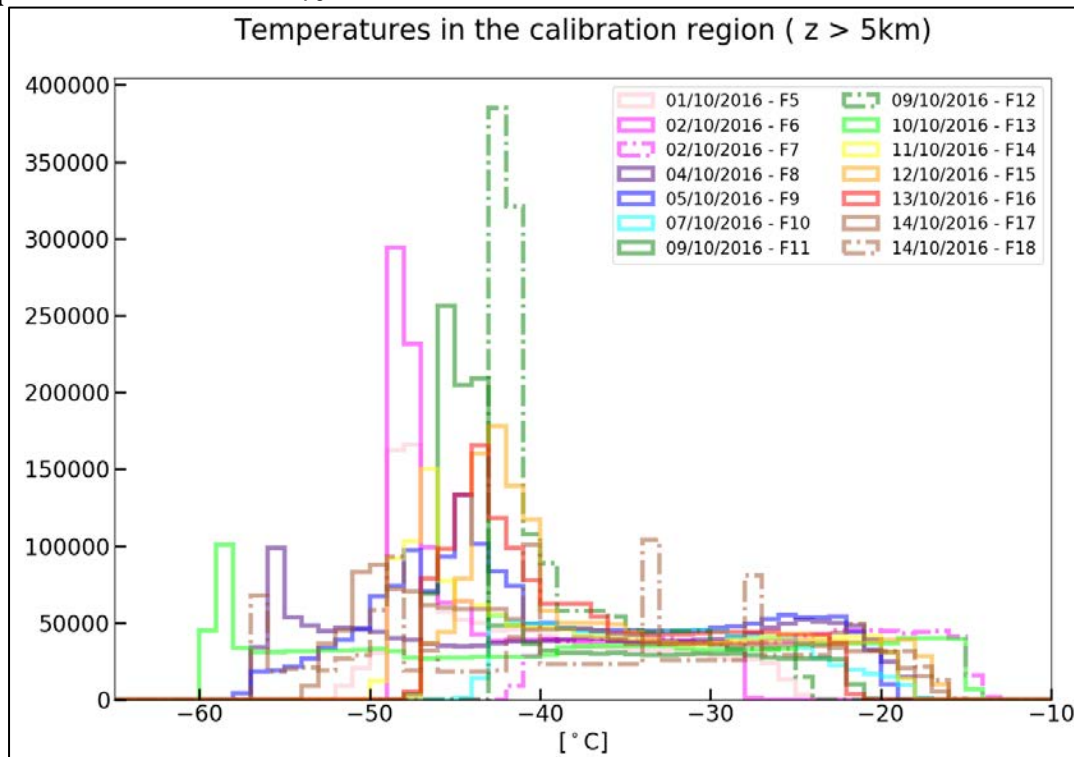


Figure 34 ERAI Temperatures at altitudes between 5km and 12km during the EPATAN field campaign

Uncertainty of the calibration ($\sigma(C_\lambda)$) - Level 1

The uncertainty in the calibration process is given in terms of relative error.

Averaging over 500m allows to get rid of the uncertainty of the measurement due to the detection noise, σ_{S_λ} . We can therefore assume that the fluctuations in calibration error, $\sigma(C_\lambda)$, and in σ_{S_λ} are independent.

Uncertainty in the calibration can be found because of:

- (1). the uncertainty on the reanalysis fields and their colocation with the airborne measurements,

- (2). low evolutions of the laser source in time (alignment),
- (3). possible icing on the aircraft window.

(1) can be estimated by comparing the reanalysis data to the temperature and pressure measurements made at the altitude of the aircraft during the flights. Figure 35 shows the histograms of the relative difference between ERAI fields and aircraft measurements for the EPATAN campaign. For both the pressure and the temperature fields, the mean value is close to 0% and the standard deviation is 2.3%. Figure 37 shows the evolution of these mean values and standard deviations as a function of the difference in time (ERAI fields are only available every 6 hours). The values do not seem to vary strongly when the time in the ERAI fields less corresponds to the one of the aircraft measurement. As a result, only one ERAI file is used for each flight, corresponding to the reanalysis for which the time is the closest in a least square sense to all the measurements performed during the flight. Moreover, the calibration constant is assumed to have at best a statistical error of 2.3% due to the uncertainty in the ERAI re-analysis.

Uncertainties due to (2) and (3) are more difficult to assess. Tables Table 12 and Table 13 present the relative standard deviation of the calibration constants for the 532nm and 1064nm channels, determined during the EPATAN campaign of October 2016, and the quantity of data used for this statistic. Those values can be considered as the result of the sum of the 3 sources of errors presented here (1, 2 and 3). When the quantity of data is < 100, the assumption of a Gaussian distribution is not valid leading to less confidence in the values of the mean and standard deviation. This error analysis is used when the calibration process could not be performed directly on the profile.

For the 355nm parallel and cross channels, the calibration constant also depends on $\delta_{mol,th}$:

$$C_{355} = S_{par} * (1 + \delta_{mol,th}) / \beta_{mol}(355). \quad (\text{eq20})$$

However, $\delta_{mol,th} \ll 1$, therefore, its influence on the calibration error can be neglected.

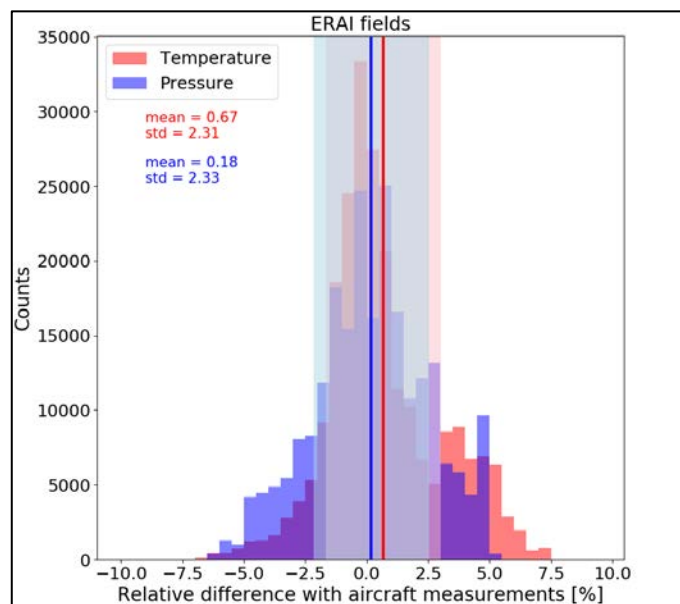


Figure 35 ERAI versus Safire temperature and pressure data - histogram

Version 1.2 EPATAN DATA ACQUISITION REPORT

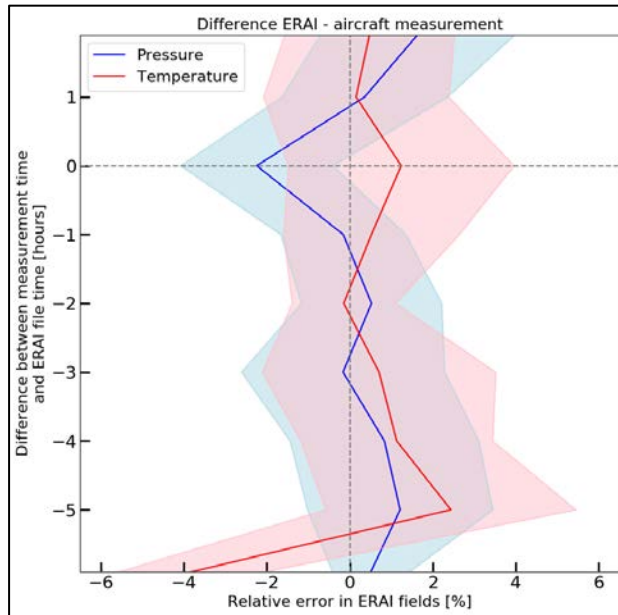


Figure 36 ERAI versus Safire temperature and pressure data – mean and standard deviation as a function of time delay between the reanalysis run and the measurement

Table 12 Statistic of the calibration constants: number of profiles (for the 532 and the 355 channels) where the calibration could be performed, in clear sky conditions.

Flight	Number of profiles to determine the standard deviation of the calibration constant [NADIR, ADM] #		
	355nm	532nm	1064nm
5	[511, 216]	[579, 357]	[478, 215]
6	[23, 297]	[93, 318]	[2, 217]
7	285	285	285
8	141	736	141
9	1441	1646	922
10	1008	1208	882
11	1114	1437	1114
12	[398, —]	[409, —]	[394, —]
13	[1027, 53]	[1075, 50]	[1027, 53]
14	[609, 23]	[1235, 148]	[344, —]
15	[353, 432]	[386, 528]	[350, 383]
16	[874, 105]	[1043, 105]	[858, 105]
17	[733, 189]	[1123, 309]	[733, 189]
18	[369, 628]	[443, 635]	[369, 628]

Table 13 Statistic of the calibration constants: relative standard deviation

Flight	Relative standard deviation of the calibration constants [NADIR, ADM] %		
	355nm	532nm	1064nm
5	[15, 10]	[3, 2]	[15, 24]
6	[2, 4]	[5, 2]	[6, 21]
7	3	3	8
8	4	4	18

Version 1.2 EPATAN DATA ACQUISITION REPORT

9	10	5	15
10	18	5	9
11	34	3	13
12	[25, —]	[3, —]	[11, —]
13	[52, 2]	[52, 3]	[45, 25]
14	[6, 2]	[3, 3]	[15, —]
15	[3, 7]	[2, 4]	[14, 26]
16	[10, 3]	[3, 2]	[18, 22]
17	[7, 5]	[3, 2]	[15, 30]
18	[5, 10]	[2, 4]	[15, 26]

Error propagation - Level 1

The raw outputs from the detectors are given with a statistical error, σ_{S_λ} , due to detection noise, which varies along the profile. The calibration relative uncertainty, $\sigma_{rel}(C_\lambda)$, has to be added to estimate the final error of the calibrated signal. The final attenuated backscatters, in $m^{-1}.sr^{-1}$, are given, for the 532nm and 1064nm channels, by $\beta_\lambda[t, z] = S_\lambda[t, z]/C_\lambda[t]$ and the corresponding errors, assuming the fluctuations in σ_{S_λ} and $\sigma_{rel}(C_\lambda)$ uncorrelated, are given by:

$$\sigma_{\beta_\lambda} = \beta_\lambda * \sqrt{\frac{\sigma_{S_\lambda}^2}{S_\lambda^2} + \sigma_{rel}^2(C_\lambda)}. \quad (\text{eq21})$$

For the 355nm outputs, the final errors on the corresponding attenuated backscatters (σ_{par} and σ_{perp}) depend on the calibration of the parallel channel, the uncertainty on the theoretical value of the molecular depolarization ratio (δ_{th}) and the uncertainty on its measurement (δ_{meas}).

They can be expressed as follows:

$$\sigma_{par} = \beta_{par} * \sqrt{\frac{\sigma_{S_{par}}^2}{S_{par}^2} + \sigma_{rel}^2(C_{355})} \quad (\text{eq22})$$

$$\sigma_{perp} = \beta_{perp} * \sqrt{\frac{\sigma_{S_{perp}}^2}{S_{perp}^2} + \sigma_{rel}^2(C_{355}) + \sigma_{rel}^2(\delta_{mol,th}) + \sigma_{rel}^2(\delta_{mol,meas})} \quad (\text{eq23})$$

Given the expression of the total, particular and molecular backscattered signal at 355nm presented in the previous section and following the propagation error procedure presented in **Bevington and Robinson (2003)**, the final uncertainties can be expressed using equation (28):

$$\begin{aligned} \sigma_{355}^2 = & \sigma_{S_{par}}^2 * F_{\Delta 355}(S_{par})^2 + \sigma_{S_{perp}}^2 * F_{\Delta 355}(S_{perp})^2 \\ & + \sigma_{rel}^2(C_{355}) * C_{355}^2 * F_{\Delta 355}(C_{355})^2 \\ & + \sigma_{rel}^2(\delta_{mol,th}) * \delta_{mol,th}^2 \\ & * F_{\Delta 355}(\delta_{mol,th})^2 + \sigma_{rel}^2(\delta_{mol,meas}) * \delta_{mol,meas}^2 \\ & * F_{\Delta 355}(\delta_{mol,meas})^2 \end{aligned} \quad (\text{eq24})$$

Version 1.2 EPATAN DATA ACQUISITION REPORT

$$\begin{aligned}
 \sigma_{355,part}^2 = & \sigma_{S_{par,part}}^2 * \mathbf{F}_{\Delta 355,part}(S_{par,part})^2 + \sigma_{S_{par,mol}}^2 * \mathbf{F}_{\Delta 355,part}(S_{par,mol})^2 \\
 & + \sigma_{S_{perp}}^2 * \mathbf{F}_{\Delta 355,part}(S_{perp})^2 \\
 & + \sigma_{rel}^2(C_{355}) * C_{355}^2 * \mathbf{F}_{\Delta 355,part}(C_{355})^2 \\
 & + \sigma_{rel}^2(\delta_{mol,th}) * \delta_{mol,th}^2 \\
 & * \mathbf{F}_{\Delta 355,part}(\delta_{mol,th})^2 + \sigma_{rel}^2(\delta_{mol,meas}) * \delta_{mol,meas}^2 \\
 & * \mathbf{F}_{\Delta 355,part}(\delta_{mol,meas})^2
 \end{aligned} \tag{eq25}$$

$$\begin{aligned}
 \sigma_{355,mol}^2 = & \sigma_{S_{par,mol}}^2 * \mathbf{F}_{\Delta 355,mol}(S_{par,mol})^2 \\
 & + \sigma_{rel}^2(C_{355}) * C_{355}^2 * \mathbf{F}_{\Delta 355,mol}(C_{355})^2
 \end{aligned} \tag{eq26}$$

$\mathbf{F}_{\Delta x}(\mathbf{u})$ accounts for $\left(\frac{\partial x}{\partial \mathbf{u}}\right)$ and the detailed expressions can be found below.

If we have $x = u * v * w$ and we measure the estimates $x_0 = u_0 * v_0 * w_0$, the error on the measurement of x is:

$$\Delta x = x - x_0 \approx \Delta u * \left(\frac{\partial x}{\partial u}\right)_{v_0 w_0} + \Delta v * \left(\frac{\partial x}{\partial v}\right)_{u_0 w_0} + \Delta w * \left(\frac{\partial x}{\partial w}\right)_{v_0 u_0}, \tag{eq27}$$

which is the first term of the Taylor expansion of x about the point (u_0, v_0, w_0) .

In general, we have several measurements x_i of the quantity x and we look at the variance or the standard deviation of those measurements to have an estimate of the error on the measurement.

The error propagation equation is defined as:

$$\sigma_x^2 = \sigma_u^2 \left(\frac{\partial x}{\partial u}\right)^2 + \sigma_v^2 \left(\frac{\partial x}{\partial v}\right)^2 + \dots + 2\sigma_{uv}^2 \left(\frac{\partial x}{\partial u}\right) \left(\frac{\partial x}{\partial v}\right) + \dots \tag{eq28}$$

When the fluctuations in the measured quantities u and v are uncorrelated in average, the covariance terms can be neglected.

Table 14 Coefficients for the error propagation equations

$F_{\Delta x}$ $= \left(\frac{\partial x}{\partial \mathbf{u}}\right)$	\mathbf{u}						
	S_{par}	S_{perp}	S_{par}^p	S_{par}^m	C_{355}	$\delta_{mol,th}$	$\delta_{mol,meas}$
β_{355}	$\frac{1}{C_{355}}$	$\frac{\delta_{mol,th}/\delta_{mol,meas}}{C_{355}}$			$-\frac{S_{par} + S_{perp} * (\delta_{mol,th}/\delta_{mol,meas})}{(C_{355})^2}$	$\frac{S_{perp}/\delta_{mol,meas}}{C_{355}}$	$-\frac{S_{perp} * \delta_{mol,th}}{C_{355} * (\delta_{mol,meas})}$
β_{355}^p		$\frac{\delta_{mol,th}/\delta_{mol,meas}}{C_{355}}$	$\frac{1}{C_{355}}$	$\frac{-\delta_{mol,th}}{C_{355}}$	$-\frac{S_{par}^p + S_{perp} * (\delta_{mol,th}/\delta_{mol,meas}) - \delta_{mol,th}}{(C_{355})^2}$	$\frac{S_{perp}/\delta_{mol,meas} - S_{par}^m}{C_{355}}$	$-\frac{S_{perp} * \delta_{mol,th}}{C_{355} * (\delta_{mol,meas})}$
β_{355}^m				$\frac{1 + \delta_{mol,th}}{C_{355}}$	$-\frac{(1 + \delta_{mol,th}) * S_{par}^m}{(C_{355})^2}$		

4.3.4 Masks

A mask is available for each LNG channel, as well as for the Doppler measurement (1=signal/ 0=noise). The mask defined for the 532 and 1064 channels is determined using thresholds on the raw (uncalibrated) 1064 signal from the L0 files ($\log_{10}(S_{1064}) > -3$) and

Version 1.2 EPATAN DATA ACQUISITION REPORT

on the relative error also from the L0 files ($\sigma_{S_{1064}}/S_{1064} < 0.2$). Concerning the HSRL measurements, the mask for the particular backscatter is based on thresholds determined for the particular parallel uncalibrated signal ($\log_{10}(S_{par,part}) > -2$) and the corresponding relative error ($\sigma_{S_{par,part}}/S_{par,part} < 0.4$). For the molecular backscatter, the thresholds are: $\log_{10}(S_{par,mol}) > -2$ and $\sigma_{S_{par,mol}}/S_{par,mol} < 1$. The first 100 meters below the aircraft are also removed from all the masks. The mask for the wind measurement is determined using a threshold on the Doppler measurement standard error ($V_{err} < 4$ m/s) and removing outliers (measurements above 90 m/s).

Figure 37 gives an illustration of L1 data derived for LNG with a focus on the 355nm measurements.

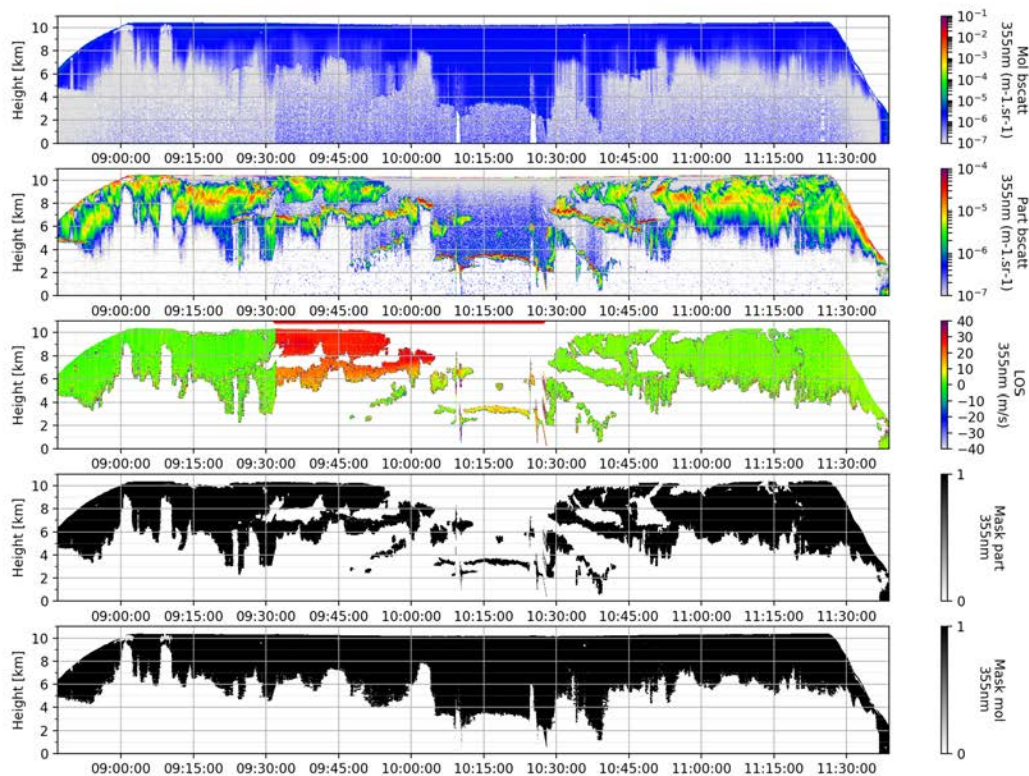


Figure 37 L1 LNG data. The calibrated attenuated molecular backscatter at 355nm is shown in top panel. The second panel illustrates the calibrated particular backscatter at 355nm. The Doppler measurement at 355nm which has been corrected from aircraft motion is shown in middle, the red line corresponds to the ADM pointing. Third and Fourth panels indicate valid particular and molecular signal.

4.4 RALI products

4.4.1 Co-located measurements product

The merged product consists in the combination of the radar and le lidar measurements, as shown in Figure 38. As radar and lidar are not working at the same vertical and horizontal resolution, the data are interpolated on a [Time x Altitude] grid with the lidar time step (5sec) and the radar range (60m). For every time step, the closest profile in

Version 1.2 EPATAN DATA ACQUISITION REPORT

time from each instrument is selected. We can find similar measurements as previously shown in L2 RASTA wind data and L1 LNG data but on the same grid.

Input and output files:

- INPUTS: From LNG Level 1 and RASTA Wind product (not all the variables are included, only those of interest for phase categorization and retrieval processing).
- OUPUT: RALI collocated netCDF files.

For every instrument, the position of each gate in the profile is known (latitude, longitude, altitude above sea level). We use the information on the altitude of the instrument gates to interpolate the data on the new grid using the nearest neighbour method.

This information is also used to determine for every gate of the new grid the distance between the measurements of both instruments.

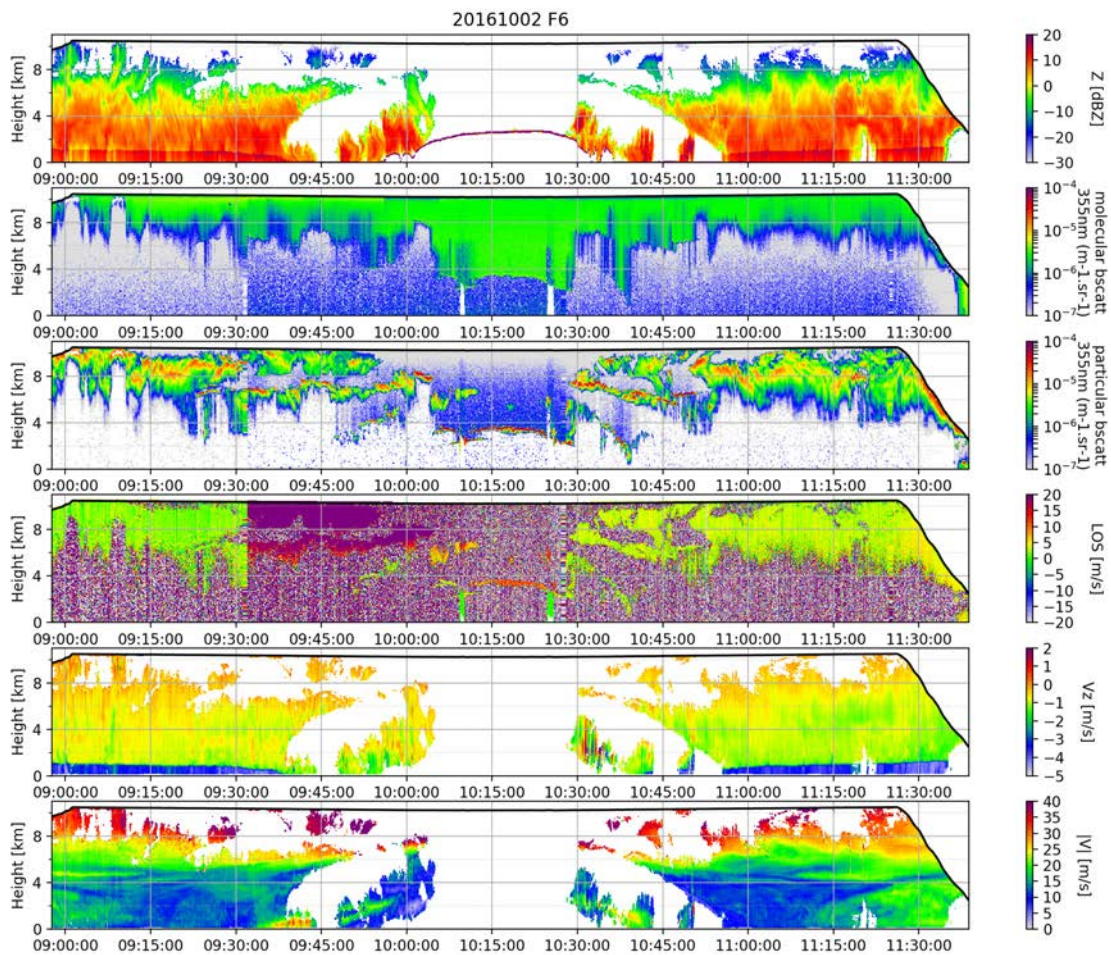


Figure 38 Merged radar-lidar product, L2 wind data from RASTA are on the same grid as the L1 LNG data.

4.4.2 Phase categorization

Version 1.2 EPATAN DATA ACQUISITION REPORT

The phase categorization relies on the synergy between two active sensors, the radar and the lidar. Indeed, radar and lidar have complementary properties: in the Rayleigh scattering regime, when particles are much smaller than the observing wavelength, the radar return signal is proportional to the sixth moment of the particle size distribution; hence, within a volume it is most sensitive to the largest particles. On the other hand, lidar backscatter is proportional to the second moment of the particle size distribution; therefore, it is most sensitive to particle concentration and backscattering cross section. Lidar signals are thus sensitive to optically thin clouds but are rapidly attenuated in optically thick clouds, whereas radar signals are able to penetrate even optically thick clouds, such as liquid water clouds, but are less sensitive to optically thin clouds composed of small particles.

OUTPUT: RALImask netCDF files.

INPUT: RALI collocated netCDF files.

INPUT mask variables:

- From RASTA processing: RASTA_Radar_Mask = 0 (no cloud) / 1 (ice) / 2 (rain) / 3 (melting layer) / 4 (ground) / 5 (underground)
- From LNG processing: LNG_Mask_Signal = for every channel, a 0 (no signal or molecular signal) / 1 (cloud or aerosol or ground detected) flag is defined using a threshold on the raw signal and/or the relative statistical error.

The default phase categorization is processed using the 532nm total attenuated backscatter.

a. Phase categorization – step 1: the melting layer

The melting layer is defined as the limit between ice cloud and rain. It can be detected using the Doppler signal of the cloud radar: the terminal fall velocity of rain drops is much higher than that of the ice crystals. In our case, the melting layer is determined using thresholds on the vertical gradients of Vz (vertical velocity) and Z (reflectivity in dBZ) and on the temperature field T.

Thresholds:

- $dV_z > 3 \text{ m/s}$
- $dZ < -8 \text{ dBZ}$
- $-4 \text{ °C} < T < 10 \text{ °C}$

➔ Warm flag: 1=below melting layer / 0=above

b. Phase categorization – step 2: the lidar masks

- Ground detection: $\log_{10}(\text{backscatter}) > -3$ and altitude $< 4 \text{ km}$ OR lidar signal where ground detected by the radar
- Attenuation / extinction of the lidar signal:
 - If the lidar can see the ground but at some point, the radar sees cloud and the lidar does not, then from this point to the ground, the lidar is attenuated. Otherwise, we consider that whatever is not a cloud is clear sky.
 - If the lidar does not see the ground, when there is no more information from this instrument but there is a radar measurement, then the lidar is attenuated and if there is cloud detected by the lidar below more than 1km of radar only measurement, then it is likely to be strongly attenuated.

- ➔ For every channel, backscatter flag: 0=clear sky / 1=cloud or aerosol / 3=particles detected but lidar signal attenuated / -1=lidar attenuated / -2=lidar extinguished / 5=ground

c. Phase categorization – step 3: layers with strong backscatter signal

Supercooled layers can be observed between 0°C and -40°C and are characterized by a strong lidar signal and small vertical extension. They are totally transparent for the radar (very small droplets). Their detection is important for the retrieval of ice clouds as the lidar signal coming from regions below is strongly attenuated and therefore must not be included in the retrieval scheme.

A threshold of $5 \times 10^{-4} \text{ m}^{-1} \cdot \text{sr}^{-1}$ on the lidar backscatter signal is used to select pixels which can potentially be part of supercooled layers. Then, one must make a distinction between supercooled layers, warm liquid clouds and highly concentrated ice.

For every selected pixel, a layer is defined using the strongest gradient in the 300m below and in the 300m above. When the selected gates are below the melting layer, then, it is warm liquid cloud.

The remaining gates are converted into objects with a given length and height. If the layer is more than 300m high or its length is less than 4 times its height, then it is not detected as supercooled water but highly concentrated ice.

- ➔ Layers: 0=signal not strong enough / 1=warm liquid water / 2=supercooled / 4=ice /

d. Phase categorization – step 4: separate ice from rain

Rain is determined from the radar mask.

Ice cloud is determined either from the radar mask or from whatever is detected by the lidar and is above the melting layer.

Ice and Rain pixels are then converted into objects and if a rain object shares some edge pixels with an ice cloud object then, it is cold rain. Otherwise, it is flagged as warm rain.

- ➔ Ice/Rain flag: 0=ground / 1=no ice, no rain / 2=ice / 4=warm rain / 5=cold rain / 6=multiple scattering suspected

e. Phase categorization – step 5: aerosol and liquid cloud detection

Aerosol is detected if the lidar backscatter is $\leq 10 \times 10^{-5}$ and the depolarization ratio is < 0.02 . This threshold was defined for the NAWDEX campaign where only marine aerosols with very low depolarization ratios were measured.

Liquid cloud is detected either when a supercooled layer is detected or if there is a lidar signal below the melting layer that is not flagged as aerosols or if there is a radar signal < -17 dBZ previously flagged as rain.

- ➔ Aerosol/Liquid flag: 0=ice, ground or clear sky / 1=liquid / 4=aerosol / 9=unknown (lidar attenuated)

f. Phase categorization – step 6: final step

Combination of all the previous flags:

- 3= subsurface
- 2= lidar attenuated or extinguished
- 1= ground
- 0= clear sky
- 1= ice cloud
- 2= 2d plates / spherical crystals
- 3= supercooled water
- 4= liquid cloud + ice
- 5= cold rain
- 6= aerosol
- 7= warm rain
- 8= stratospheric clouds (undetected by RALI)
- 9= strong ice concentration
- 10= top of convective towers (undetected by RALI)
- 11= liquid cloud
- 12= warm rain + liquid cloud
- 13= cold rain + liquid cloud
- 14= warm rain that could be mixed with liquid clouds but we don't know because the lidar is too extinguished
- 15= multiple scattering

4.4.3 Ice clouds retrieval

The retrieval algorithm, **Varcloud**, is based on a variational method (Delanoë and Hogan 2008, 2010).

The method relies on the synergy between the radar and the lidar to better constrain the retrieval of ice cloud variables and each cloud profile is retrieved independently.

The inverse problem

The inverse problem in remote sensing observation can be expressed as follows: we have a measurement which is indirectly linked to the cloud properties and can be expressed as

$$y = F(x) + \varepsilon,$$

with y the array containing the measured profiles (for example the radar reflectivity profile and the lidar backscatter profile at 532nm), x the state vector containing the cloud variables we want to retrieve, F the forward model (non-linear) simulating the observations and ε the errors and uncertainties on the model and the measurements.

As it is not possible to inverse F and directly retrieve x , and because many uncertainties have to be taken into account, we look for the state vector that will minimize the following cost function:

$$2J = (y - F(x))R^{-1}(y - F(x))^T + (x - x^a)B^{-1}(x - x^a)^T.$$

In the first term of this expression, we try to be as close to the observations (y) as possible using the forward model $F(x)$ and taking into account the uncertainties on the model and

the measurements in the error covariance matrix R . The higher the values of R , the less the algorithm will depend on this first term to determine the best state vector x .

The second term of the cost function accounts for an *a priori* information x^a that we have on the state vector (and B is the error covariance matrix associated to this *a priori*). This *a priori* makes it possible to retrieve seamlessly the cloud properties from areas where both instruments are available to regions where there is only one measurement left. Indeed, typically, the lidar can measure the top of the cloud where the particles are too small to be detected by the radar, then, when we go further down in the cloud profile, we get to a region detected by both the lidar and the radar and at the bottom of the cloud, there is only radar measurements as the lidar is totally extinguished. As a result, using *a priori* information allows us to simulate a second observation whenever one of the instruments is missing.

In order to find the optimal estimate that will minimize the cost function, the forward model expression has to be linearized. A Gauss-Newton method ([Rogers 2000](#)) is used to do this iteratively: at iteration k , we have the estimate of the state vector x_k and the corresponding forward model estimate of the observations $F(x_k)$. The linearized version of the cost function to get to the next (hopefully better) estimate of the state vector is obtained by replacing $F(x)$ by $F(x_k) + K(x - x_k)$, where K is the jacobian, a matrix containing the partial derivative of each observation with respect to each element of the state vector:

$$K_{x_k} = \begin{pmatrix} \frac{\partial y_1}{\partial x_{k_1}} & \dots & \frac{\partial y_1}{\partial x_{k_n}} \\ \vdots & \ddots & \vdots \\ \frac{\partial y_m}{\partial x_{k_1}} & \dots & \frac{\partial y_m}{\partial x_{k_n}} \end{pmatrix}$$

The new estimate of the state vector can then be determined as follows:

$$x_{k+1} = x_k + A^{-1}[K^T R^{-1}(y - F(x_k)) - B^{-1}(x_k - x^a)],$$

with $A = K^T R^{-1} K + B^{-1}$ and A^{-1} is a matrix containing the statistical error on the retrieval.

A χ^2 test is performed to determine when convergence is reached.

The state vector and microphysical assumptions

The state vector is composed of visible extinction (α_v) [$m^{-1}.sr^{-1}$], lidar extinction-to-backscatter ratio (S) [sr] and N'_0 , a variable related to the normalized number concentration parameter N_0^* [m^{-4}] via the relationship $N'_0 = N_0^*/\alpha_v^b$, with b a coefficient to determine. The choice of this state vector lies in the fact that first, in the geometric optics limit, α_v has the advantage to be directly linked to the lidar measurements. Then, the apparent lidar backscatter at range r from the instrument can be expressed in the single-scattering limit as $\beta(r) = \alpha_v(r)/S(r) * e^{-2\tau}$, where τ is the total optical thickness of the atmospheric layer between the lidar and range r . And finally, Delanoë et al. (2005) showed that one could find a robust relationship linking α_v/N_0^* to any extensive and intensive variable describing the cloud.

Indeed, the retrieved cloud properties are all linked to the particle size distribution (PSD) $N(D)$, representing the concentration of particle as a function of diameter. Delanoë et al. (2005, 2014) introduced the concept of PSD double normalization for ice cloud: both diameter and concentration are scaled. Diameter is scaled by the mean volume weighted diameter

$$D_m = \frac{\int_0^\infty N(D_{eq}) D_{eq}^4 dD_{eq}}{\int_0^\infty N(D_{eq}) D_{eq}^3 dD_{eq}} [m],$$

with D_{eq} the equivalent diameter (in meters) of the melted particle computed from the mass of the particle and the density of ice. The number concentration is scaled by N_0^* which can be written as follows:

$$N_0^* = \frac{4^4 \left(\int_0^\infty N(D_{eq}) D_{eq}^3 dD_{eq} \right)^5}{6 \left(\int_0^\infty N(D_{eq}) D_{eq}^3 dD_{eq} \right)^4}.$$

It is then possible to find a functional form F fitting any measured size distribution appropriately normalized by D_m and N_0^* :

$$N(D_{eq}) = N_0^* F\left(\frac{D_{eq}}{D_m}\right).$$

Delanoë et al. (2005) found this function could be approximated by a two-parameter modified gamma shape, the two parameters being determined by a statistic of in-situ measurements. With this normalized size distribution and for a given range of D_m , it is then possible to create a one-dimensional look-up table linking all the cloud microphysical variables to the ratio of α_v by N_0^* .

To compute D_{eq} for an ice crystal it is necessary to have the mass of the particle as a function of its maximum diameter. $M(D)$, the mass-diameter relationship is usually described as a power-law relationship. Several mass-diameter relationships have been obtained for different types of clouds, temperature ranges and from different data sets. In our case, we use a relationship developed by **Heymsfield et al. (2010)**:

$$M_{[g]} = 7.10^{-3} (D_{[cm]})^{2.2}$$

N_0' was shown to have a very good temperature dependence (**Delanoë and Hogan 2008**). For this reason, it was chosen over N_0^* as part of the state vector and the *a priori* of $\ln(N_0')$ can be expressed with good confidence as a linear function of T :

$$\ln(N_0') = \ln(N_0^*/\alpha_v^{0.67}) = -0.095 * T + 21.94$$

To account for the variability of the lidar ratio in the cloud profile, the *a priori* of $\ln(S)$ is assumed to vary linearly with temperature:

$$\ln(S) = -0.014 * T + 3$$

The visible extinction does not need *a priori* information as it is already well constrained by the measurements. Moreover, without HSRL measurement, the molecular signal located below the cloud and measured by the lidar is also used as an extra constraint on α , with a maximum of 5 additional lidar gates.

The forward model

The radar reflectivity Z is computed for a wide range of diameters, using the Rayleigh theory for small particles and the T-matrix calculation for the biggest spheroids. The 1-D lookup table formerly described is then used to link Z/N_0^* to α_v/N_0^* .

A model accounting for multiple scattering developed by Hogan 2006 is used to simulate the lidar backscatter.

Errors

The errors on the forward model are 1 dBZ and 0.3 for the radar reflectivity and the logarithm of the lidar backscatter, respectively.

Concerning the measurements, the calibration is assumed to be the leading source of error on the radar side and is estimated to a constant value of 1.

A statistical error is calculated on every gate of the lidar profile, considering the noise of the photon detectors and the standard deviations of the background noise measurement and the calibration constant. The instrument channels are assumed independent and the calibration unbiased.

The error on the *a priori* is estimated using the standard deviations of the datasets used to determine the *a priori* relationships of S and N_0' . Those errors are 1, 0.1 and $1e^{-4}$ for the logarithm of the *a priori* of N_0' and the coefficients a_S and b_S from the lidar ratio relationship $\ln(S) = a_S + b_S * T$.

Additional tricks for a smoother retrieval

- First of all, to avoid the unphysical possibility of retrieving negative values, the logarithm of the entities is used instead of the entities themselves.

- As lidar measurements may be noisy, an additional smoothing constrain is added to the retrieved extinction through a third term in the cost function using a “Twomey-Tikhov” matrix (Rogers 2000, $\kappa = 1$) which penalizes the second derivative of the α_v profile.

- To improve the computational efficiency, we seek to reduce the number of elements in x . To do so, N_0' is not retrieved directly at each gate, but rather represented by a reduced set of m basis functions N_b such that smooth variation in range is guaranteed. The number of basis functions is $m = n/4$, with n the number of cloud gates detected by either the lidar or the radar.

- Following the assumptions made for the *a priori*, the logarithm of the lidar ratio is assumed to vary linearly with the temperature. Therefore, only the two coefficients of this relationship are retrieved.

4.4.4 Reported errors in merge products

The errors reported in the merge radar-lidar product are identical to those reported in L1, error propagation has not been taken into account.

4.5 Dropsondes

The raw data are available but we recommend to use the data that have been processed using the Aspen software (<https://www.eol.ucar.edu/software/aspen>). An example of dropsonde measurements which have been corrected using the aspen software is given in Figure 39. We notice that unphysical measurements have been removed. However, the main modification is done for the relative humidity profile (please refer to aspen documentation).

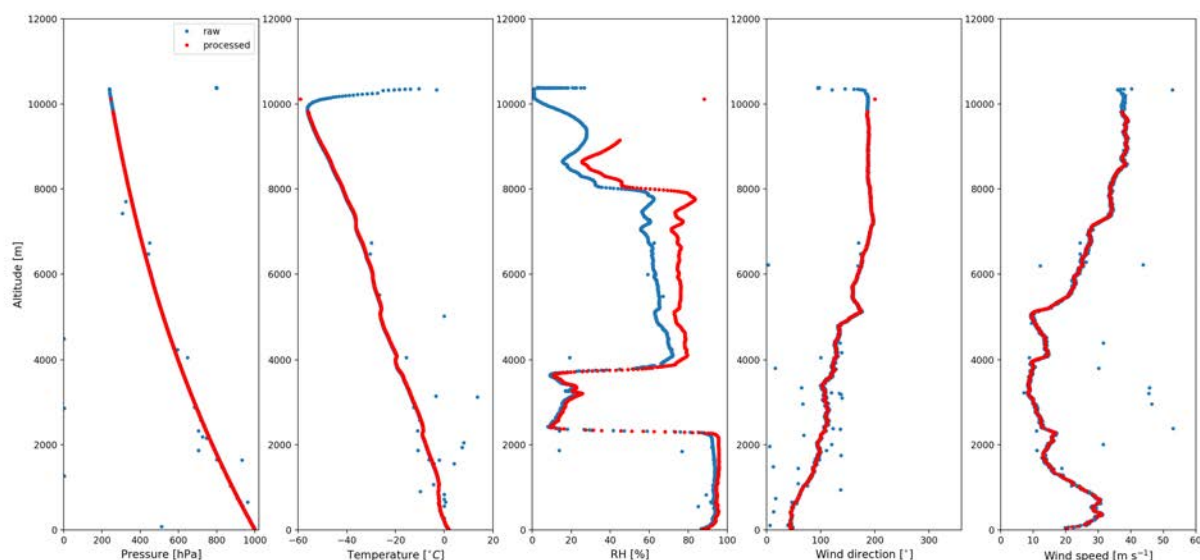


Figure 39: Example of the correction applied to raw DS data (Flight 6). Raw data are presented in blue and processed data are shown in red.

A selection of dropsonde measurements is available in Annex A.

5. HALO products

Several products of the HALO measurements for the dedicated common flight legs will be available:

- Radar: Calibrated and quality checked reflectivity
- Lidar: Calibrated attenuated backscatter profiles at 532 nm, particle backscatter and extinction profiles at 532 nm
- Radar-Lidar: Cloud mask, ice water content, effective radius
- specMACS*: Spectral radiances between 400 – 2500 nm

*The specMACS system is owned and deployed by the Ludwig-Maximilians-Universität (LMU) München. The data can only be requested within direct collaboration with LMU (contact: Prof. Dr. Bernhard Mayer, bernhard.mayer@lmu.de).

During the common flight legs the WALES lidar system and the MIRA36 cloud radar on HALO worked without major technical problems and yielded high quality data. However, unforeseen small data gaps might be caused by software issues or, in case of the lidar, system shut down due to strong intensity of the backscattered light. The lidar system is

very well calibrated and characterized. The system parameters and the systems performance are monitored during the entire measurement. Information about error calculation and calibration of the lidar system can be found in [Wirth et al., 2009](#), [Esselborn et al., 2008](#) and [Esselborn et al., 2009](#). A basic description of the WALES data processing is given in the following. The cloud radar MIRA36 was calibrated during the prior campaign and checked against the well calibrated RASTA and Global Precipitation Measurement (GPM) systems. The calibration of the system is described in the following.

5.1 Basic of WALES Data Processing

As the light pulse emitted from a lidar propagates through the atmosphere its intensity is reduced by scattering and absorption by the molecular constituents of the air and by aerosol and cloud particles. Part of the light is also scattered in a backward direction and propagates back to the lidar system, again undergoing the same extinction process. In this way the signal of a lidar depends on the local ability of the atmosphere to scatter light and on the integral light extinction along the complete light path between the system and the probed volume. This can be seen in a more formal way from the so called lidar equation, which gives the power P received from an atmospheric volume at distance r :

$$P(r) = \left(\frac{E_0 c}{2} \cdot \frac{A}{r^2} \right) \cdot (\beta_m(r) \cdot T_a^2(r) + \beta_p(r) \cdot T_a^2(r))$$

Here the first term in brackets contains system-specific parameters: the laser pulse energy E_0 and the area of the receiving telescope A (c is the speed of light). The atmospheric parameters are described by the backscatter coefficients for light scattering from air molecules β_m and particles β_p as well as the total atmospheric transmission T_a from the system to the probed volume. For a monochromatic light source and in the absence of multiple scattering T_a can be written in the form (Beer's law):

$$T_a(r) = \exp\left(\int_0^r (\alpha_m(r') + \alpha_p(r')) \cdot dr'\right)$$

where $\alpha_m(r)$ and $\alpha_p(r)$ are the molecular or particle extinction coefficients.

The molecular coefficients β_m and α_m are proportional to the air density and can be calculated from the molecular scattering cross-sections obtained from laboratory measurements and the pressure and temperature profile from numerical weather prediction (NWP) models or independent collocated measurements, e.g., from radiosondes.

In sharp contrast to the molecular case, the coefficients describing light scattering by particles β_p and α_p are extremely sensitive to the size, shape and refractive index of the particles. Especially there is no simple general relation between the two parameters, as for molecular (Rayleigh) scattering. The HSRL method uses the fact that air molecules have a much lower mass and therefore a much higher thermal velocity than aerosol or cloud particles. This high random velocity leads to a significant spectral broadening of the laser light scattered by the molecules due to the Doppler Effect. If plotted against the wavelength shift, the spectrum of the light scattered back to the lidar receiver looks like the dashed curve shown in Figure 40. It consists of a broad, nearly Gaussian-shaped part coming from scattering by molecules and a narrow central peak from particle scattering.

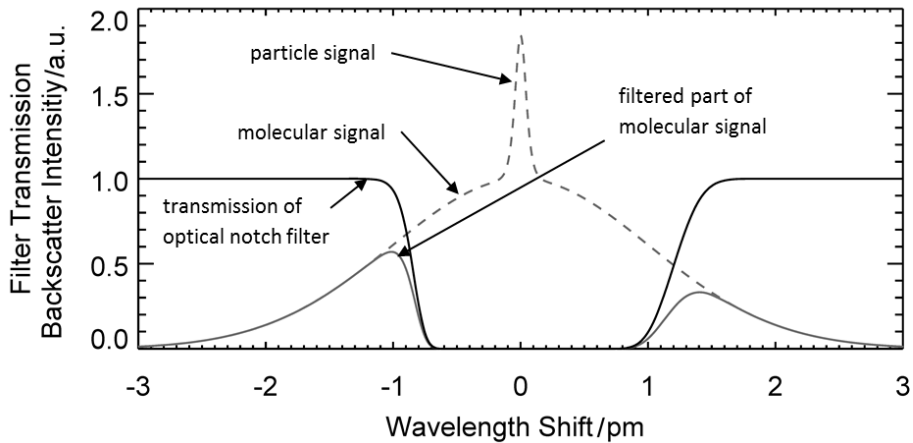


Figure 40: Spectral signatures of the light backscattered from the atmosphere. Figure adapted from [Groß et al., 2012](#).

Using HSRL the received atmospheric backscatter is split into two channels. The narrow bandwidth optical filter in the molecular channel suppresses the aerosol backscatter, whereas the combined channel detects the intensity of both aerosol and molecular backscatter. Therefore the emitted laser frequency must be tuned to match the filter absorption line. The iodine absorption filter eliminates the aerosol backscatter and transmits the wings of the Doppler broadened molecular backscatter spectrum. To determine the amount of molecular backscatter absorbed by the iodine filter, the HSRL system needs to be calibrated. This is done by measuring the filter transmission spectrum and calculating the atmospheric temperature and pressure-dependent filter transmission with an appropriate molecular backscatter model. For measuring the iodine filter transmission spectrum, a highly attenuated reflection of the pulsed green laser emission is directed through the receiver assembly and the laser frequency is scanned. The filter transmission is determined by the product of the iodine filter transmission and the calculated molecular backscatter spectrum.

The lidar equation for the filtered signal is then reduced to the first term:

$$P_{\text{HSRL}}(r) = C \cdot \left(\frac{E_0 c}{2} \cdot \frac{A}{r^2} \right) \cdot \beta_m(r) \cdot T_a^2(r)$$

where the calibration constant C accounts for the fact that also part of the molecular scattered light is rejected by the notch filter. The big advantage of this reduced equation is that from the particle scattering parameters it only contains α_p (wrapped into T_a). Since all other parameters are known or can be calculated with good accuracy, the atmospheric transmission between the lidar and an arbitrary point along the laser beam can be directly measured. From this data product it is straightforward to calculate α_p by simple numerical differentiation with a relative systematic error of typically less than 5%. Since we not only want to measure the extinction coefficient α_p but also the backscatter coefficient β_p the signal in a HSRL receiver is split into two parts, one for the total signal and one with the optical notch filter. As the transmission from the HSRL channel is known, the lidar equation can be solved for β_p .

Uncertainties

Systematic errors in the measurement of the backscatter coefficient arise from uncertainties of the measured quantities and the calculated quantities are mainly due to

normalization, where the magnitude of background aerosol at a reference height within the free troposphere has to be estimated. The assumption of the background backscatter coefficient is based on the analysis of in situ measured aerosol size distributions. Further uncertainties are induced by laser frequency fluctuations and variations in the atmospheric temperature.

5.2 Basic of MIRA Data Processing

The processing of cloud radar I-Q-signals to calibrated radar reflectivity includes the following steps:

Calculation of FFT power spectra in each range gate

Received pulses are sampled with the range sampling period of 15 m, 30 m, or 60 m depending on the transmitted pulse length – 100 ns, 200 ns, or 400 ns, respectively. Samples of the received pulses from a given range gate produce a complex signal, sampled with the pulse repetition frequency of 5 kHz. By the complex notation, the signal can be written as:

$$y(kT) = I(kT) + iQ(kT), \quad k = 0, 1, \dots, N_{FFT} - 1.$$

$y(kT)$ is called “I-Q-signal”, and T is the pulse repetition period. $N_{FFT} = 256$ is the length of the Fast Fourier Transform (FFT). Subsequently, the power spectrum $p(N_{FFT})$ from $y(kT)$ is calculated.

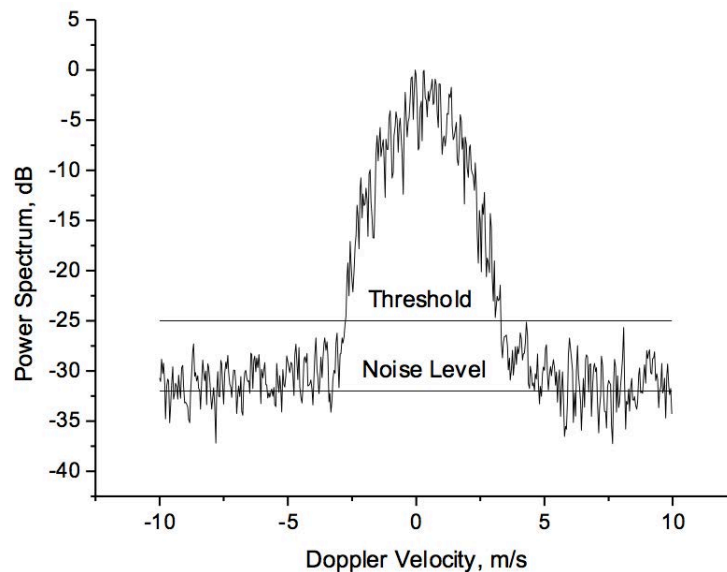


Figure 41: Power spectrum of the Doppler velocity.

Non-coherent averaging of FFT power spectra

Before peak identification and moment estimation are performed, $K_{sum} = 20$ power spectra are averaged non-coherently to improve the signal-to-noise ratio.

Estimation of signal moments

The Doppler velocity v and signal power PR can be estimated from the power spectrum of the scattered signal.

The threshold value S_{TH} used to separate the signal S_n and the noise parts of the spectrum is calculated from the noise power P_N (with $Q=7$). While the mean Doppler velocity v results from the 1st moment of S_n the signal power P_R is the 0st moment of S_n :

$$S_{TH} = \langle N_n \rangle + Q \cdot \sigma_{SUM}(N_n) = \frac{P_N}{N_{FFT}} \left(1 + \frac{Q}{\sqrt{K_{SUM}}} \right).$$

$$S_n = \begin{cases} S[k] - S_{NL}, & S_n \geq S_{TH}, \\ 0, & S_n < S_{TH}. \end{cases}$$

$$v = -\frac{\lambda}{2} \frac{1}{P_0} \sum_{n=0}^{N_{FFT}-1} f_n S_n, \quad P_R = \sum_{n=0}^{N_{FFT}-1} S_n.$$

Calculation of calibrated radar reflectivity

After that, the SNR is calculated by dividing P_R by the receiver noise level:

$$SNR = 10 \log \left(\frac{P_R}{P_{RecNoise}} \right)$$

Here, the noise power $P_{RecNoise}$ is obtained from the noise gate. The equivalent radar reflectivity factor Z_e is then calculated from the estimated SNR values using the radar equation for meteorological radars:

$$Z_e = C_0 \left(\frac{H}{H_0} \right)^2 \frac{F}{F_0} \frac{\tau_0 P_{TAV0}}{\tau P_{TAV}} SNR$$

For convenience, following reference values were used here ($H_0 = 5$ km, $P_{TAV0} = 30$ W, $F_0 = 5$ kHz, and $\tau_0 = 200$ ns). Using the radar parameters listed in the following table, the specific radar constant C_0 is -26.1 dB:

$$C_0 = \frac{1024 \ln 2 \lambda^2 K_B T_0}{\pi^3 c |K_w|^2} 10^{18} \frac{L F_N}{G_0^2 \theta_0^2} \frac{F_0 H_0^2}{P_{TAV0} \tau_0}$$

5.2.1 Internal/Budget calibration

For a similar cloud radar, the monitoring of the system specific parameters and the subsequent estimation of radar reflectivity is described in detail by [Görsdorf et.al. \(2015\)](#). The internal calibration (budget calibration) strategy for the HAMP MIRA is therefore only briefly summarized here:

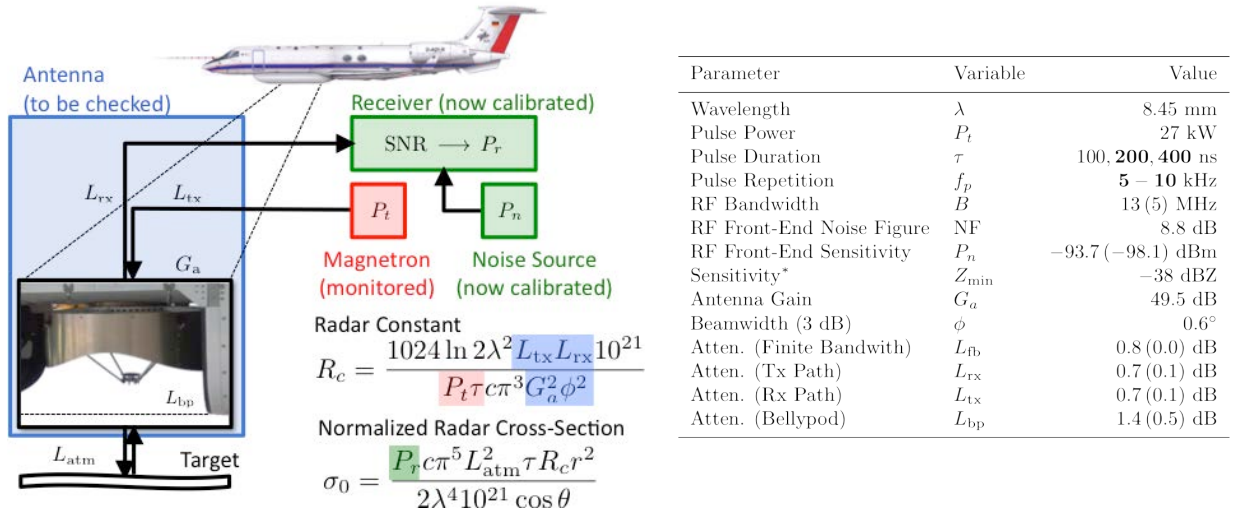


Figure 42: (left) Characterized instrument components (right) Technical specifications of the HAMP cloud radar as characterized in this work or as given by the manufacturer (in brackets).

First, the instrument components (see Figure 42, left) like transmitter, receiver, waveguides, antenna and radome are characterized individually in the laboratory (see Table in Figure 42, right). During in-flight measurements, variable component parameters are then monitored and corrected for drifts to correct the radar constant and to calculate a normalized radar cross-section which can be checked with external calibration sources like the ocean surface.

Antenna, radome and waveguides

- **Antenna:** The gain 49.5 dBi and the beam pattern (-3 dB beamwidth at 0.6°) was determined by the manufacturer.
- **Radome:** The thickness of the epoxy quartz radome in the belly pod was designed with a thickness of 4.53mm to limit the one-way attenuation to around 0.5 dB. Deviations during manufacturing increased the thickness to 4.84mm, with a one-way attenuation of around 1.4 dB. Laboratory measurements confirmed this 1.8 dB higher two-way attenuation.
- **Waveguides:** Initial calibration only accounted for a transmitting and receiving waveguide length of 20cm. Actually, the waveguides has a length of 1.15m. With a specified attenuation of 0.65 dB/m, the two-way attenuation by waveguides is thus 1.3 dB higher than the initially assumed one.

Transmitted and received signal power

- **Transmitter peak power P_t :** Due to strong variations in ambient temperatures in the cabin, in-flight thermistor measurements proved to be unreliable. For this reason, thermally stabilized measurements of P_t were conducted on the ground which were correlated with measured magnetron currents I_m .
- **Received signal power P_r :** The SNR response of the receiver to an input power P_r is described by a receiver transfer function $SNR = T(P_r)$. When T is known, an unknown received signal power P_r can be derived from a measured SNR by the inversion T^{-1} :

$$P_r = T^{-1}(SNR) \approx P_n SNR \quad (1)$$

- **Receiver sensitivity P_n :** Ideally, T^{-1} can be approximated by a signal independent receiver sensitivity P_n , which translates a measured SNR to an absolute signal power P_r in dBm. It includes the inherent thermal noise within the receiver bandwidth, the overall noise figure of the receiver and mixer circuitry and all losses occurring between ADC and antenna port.

Measured Receiver Sensitivity

A key component of this work was to replace the estimated receiver sensitivity P_n with an actual measured value. To this end, an analog signal generator E8257D from Agilent Technologies was used to determine the receiver bandwidth and the receiver transfer function.

Receiver Bandwidth

Figure 45 shows the obtained signal-to-noise ratio as a function of the frequency offset from the center frequency at 35.5 GHz .

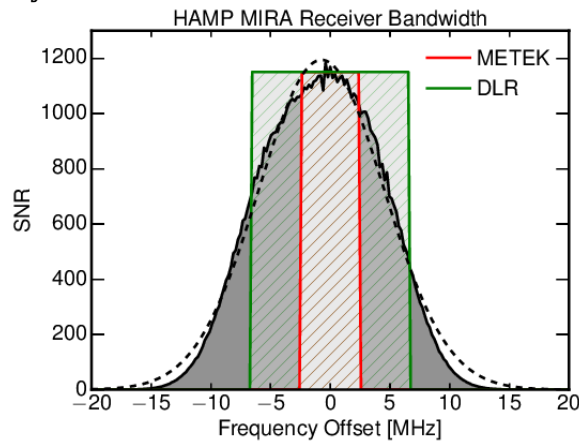


Figure 43: Measured radar receiver bandwidth (gray) as a function of the frequency offset from the center frequency at 35.5 GHz. The dashed line shows a gaussian fit to the measurements. While the green-hatched rectangle shows the actual equivalent noise bandwidth of 13MHz, the red-hatched rectangle shows the initial assumed bandwidth of 5MHz.

Centered on 35.5 GHz, the spectral response (black line) of the radar receiver approaches a Gaussian shape (dashed line). The equivalent noise bandwidth was determined to be 13 MHz, which is illustrated by the green-hatched rectangle in Fig. 2. In contrast, the red-hatched rectangle shows the assumed 5 MHz receiver bandwidth.

Receiver Transfer Function

Next, the amplitude ramp mode of the signal generator was used to determine the transfer function $P_r = T(\text{SNR})$ of the receiver. For this measurement, the frequency of the signal generator was set to 35.5 GHz, while the output power of the generator was increased steadily from -110 dBm to 10 dBm (see Fig. 3a). In order to test the linearity and the saturation behavior of the receiver for strong signals, this measurements were repeated for PiN attenuator settings of 15 dB and 30 dB .

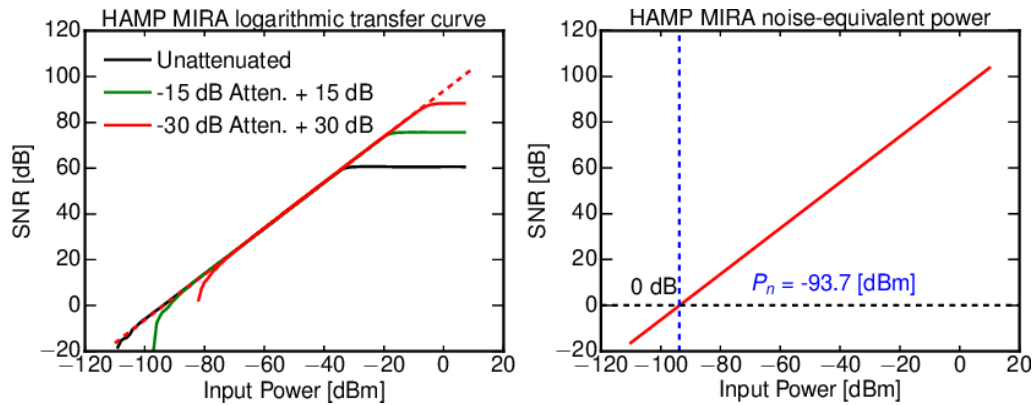


Figure 44: Measured receiver transfer functions for the three PiN attenuator settings of 0 dB (black), 15 dB (green) and 30 dB (red).

Subsequently, a linear regression to the results without PiN attenuator was performed between input powers of -70 dBm and -40 dBm, which is shown in Figure 46. With a slope m of $1.0009(\pm 0.0006)$ and a residual of 0.054 dB, the receiver behaved very linear for this input power region.

Receiver Sensitivity

Finally, the linear regression to the receiver transfer function can be used to derive the receiver sensitivity P_n . Its x-intercept ($\text{SNR} = 0$) directly yields the noise equivalent power, here called the inherent noise power $P_n^* = -93.7$ dBm. Compared to the estimated -98.1 dBm, this higher value for P_n^* increases the calculated radar reflectivity Z by 4.4 dB. Combined with the 1.8 dB higher two-way attenuation by the radome, the 1.3 dB higher two-way attenuation by the waveguides and including the finite receiver bandwidth loss $L_{fb} = 0.8$ dB, Z derived with the new calibration is larger by 8.3 dB compared to the initial calibration.

5.2.2 Radiometric calibration of the MIRA36

Li et al. (2005) demonstrated the radiometric absolute calibration of an airborne cloud radar by using the ocean surface backscatter, where measured Normalized Radar Cross Sections (NRCS) for different beam incident angles are compared to modeled NRCS. Figure 45 illustrates the calibration principle where measured Normalized Radar Cross Sections (NRCS) for different beam incident angles are compared to modeled NRCS.

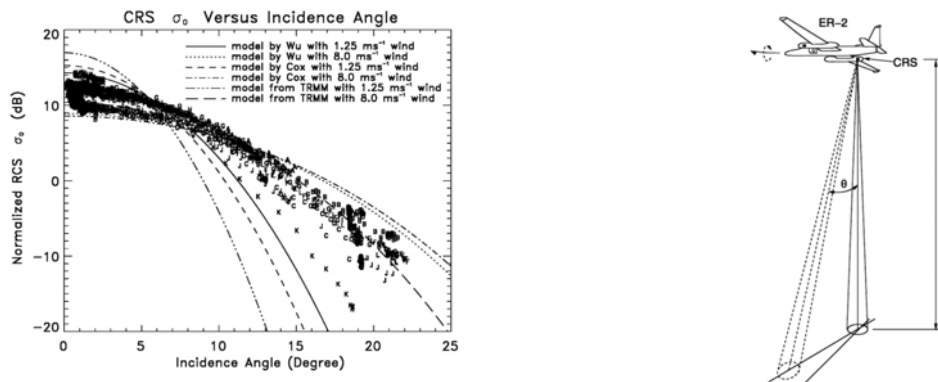


Figure 45 (left) Normalized Radar Cross Sections measured by Li et al. (2005) as a function of beam incidence angle with modelled NRCS for various surface wind speeds. (right) Measurement principle for the plot on the left, where the aircrafts executes alternating roll maneuvers to sample the NRCS for different beam incident angles.

During the NARVAL2 in 2016, alternating roll maneuvers were executed to apply the same technique to the cloud radar MIRA (Figure 46). Additionally, the radar receiver has been recalibrated by DLR in the lab. A systematic bias of -8 dB has been found for the manufacturer calibration. With the new calibration the NRCS fits much better to the modeled values as well as to measurements by the Global Precipitation Measurement satellite.

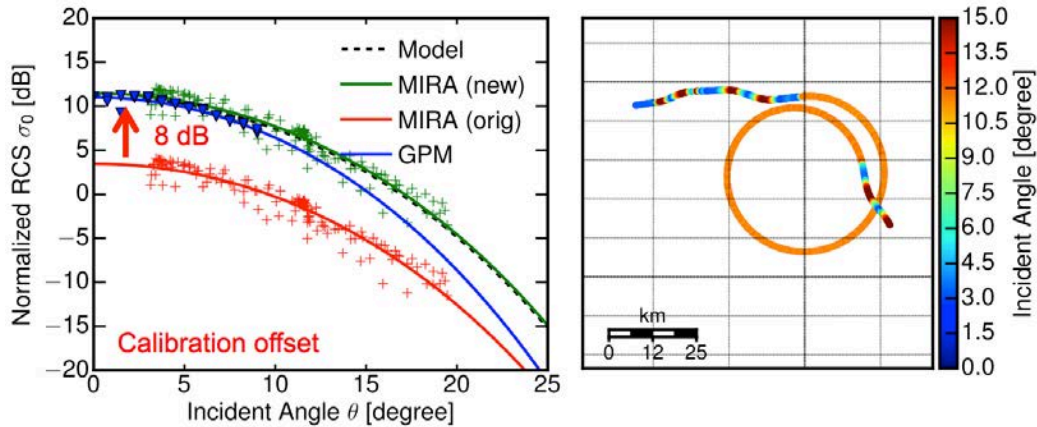


Figure 46 (left) Measured Normalized Radar Cross Sections returned by the sea surface. The red crosses correspond to the manufacturer calibration, the green crosses to the new calibration and the blue triangles represent measurements from the GPM satellite. (right) Radar calibration flight pattern with alternating roll maneuvers and a 10 degree bank circle.

Validation of MIRA36 calibration

To further validate the calibration of the MIRA36 radar a coordinated measurement flight together with the French F20 RASTA radar was used (Figure 47). During a coordinated flight on 19 December 2013 measurements of a well-defined cirrus cloud could be performed which is perfectly suited to compare both radar systems. Furthermore both systems had sampled the same cloud area so that the measurements can be directly compared.

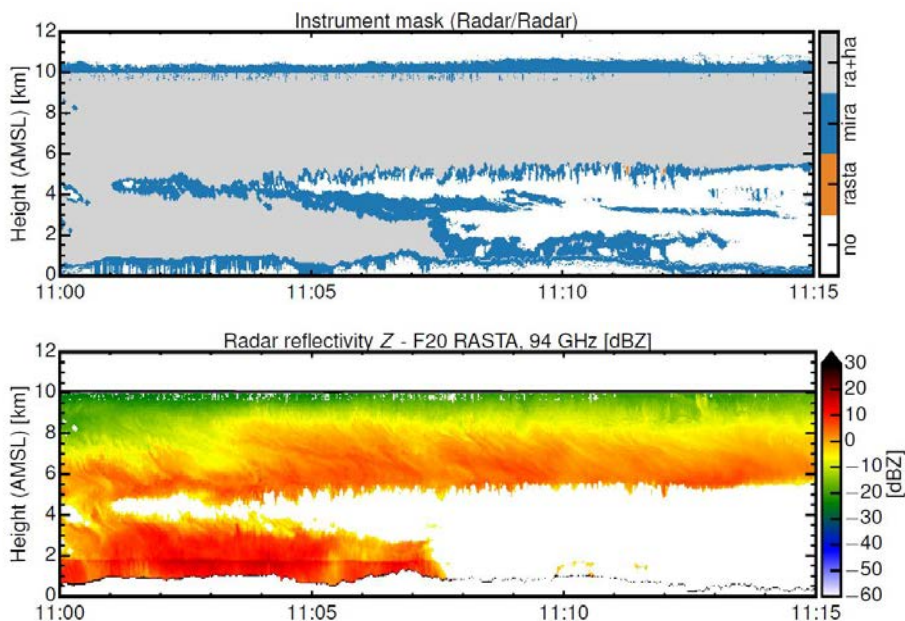


Figure 47 (upper panel) Instrument mask for RASTA and MIRA36 radar measurements. Grey areas indicate the part of the cloud where both instruments show overlapping measurements; the blue color indicates parts of the cloud that are only detected by the MIRA36 system. (lower panel) Calibrated Radar reflectivity measured with the RASTA system.

Taking the different sensitivity and attenuation of both systems due to their different wavelength into account, it is expected, that both measurements (especially at the top of the cloud, where different attenuation is negligible) should show the same values. In lower cloud regions or at higher reflectivity the measurements at 35 GHz are expected to be higher than the corresponding 95 GHz values.

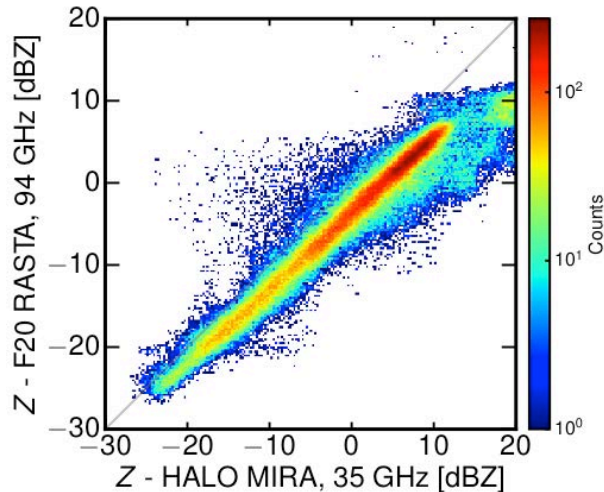


Figure 48 Comparison of the reflectivity at 94 GHz and 35 GHz measured with the RASTA and the MIRA36 radar systems during the flight shown in Figure 47.

Comparing the measurements of both systems for the collocated flight, the measurements of RASTA and the calibrated MIRA36 we see exactly the simulated and expected behavior (Figure 48). No bias is found for measurements of both systems in the upper and middle part of the cloud where both wavelengths are almost unaffected from attenuation. However, in the lower part of the measurement region where the shorter wavelength is already slightly affected by attenuation and thus showing slightly smaller values as the radar measurements at the longer wavelength.

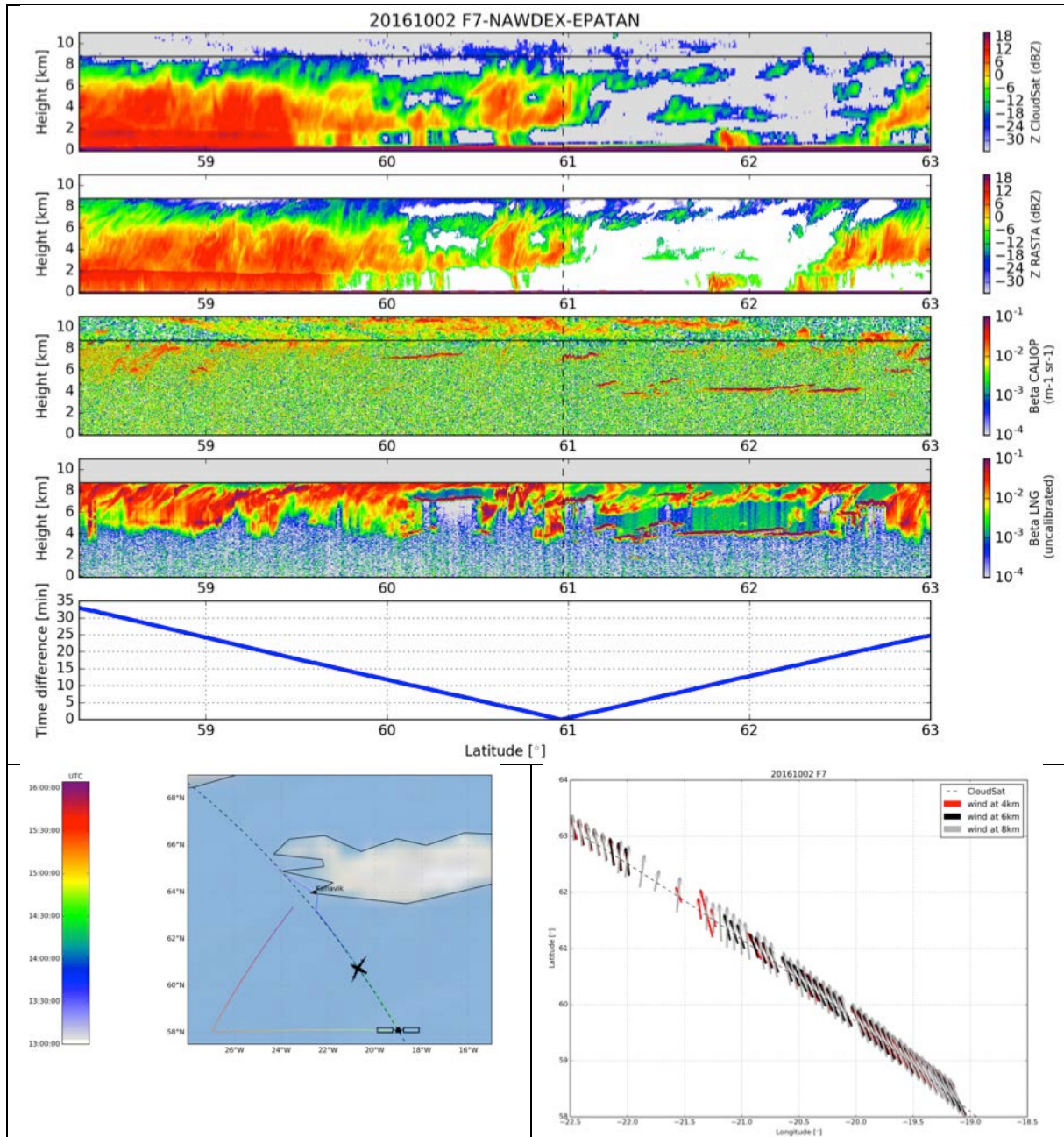
5.3 Co-located MIRA36 and WALES products and ice cloud retrieval

The co-located data products and the ice cloud retrieval will be done with the same algorithm as described in Sections 4.4.1.

6. Satellite underpasses

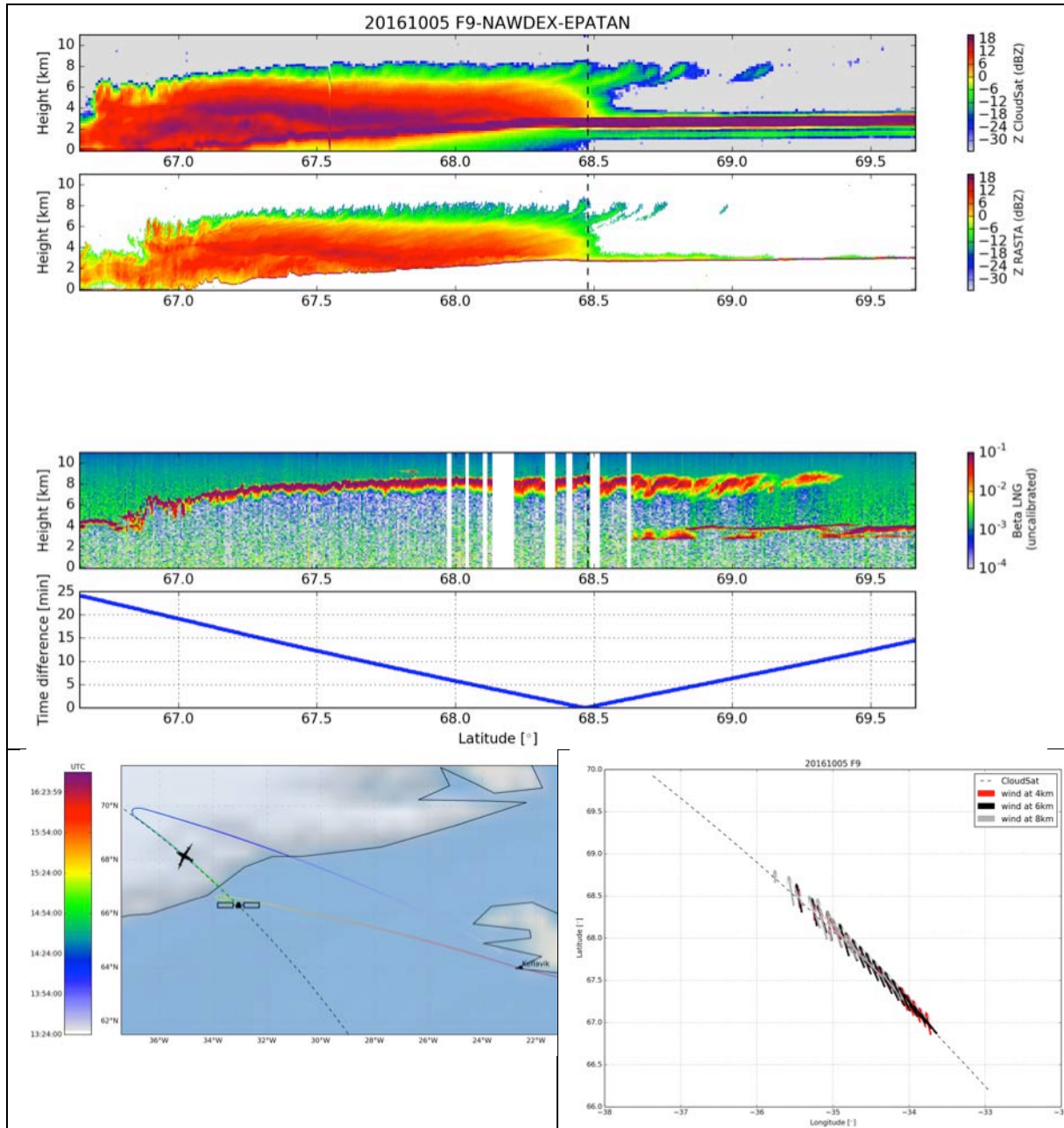
There were 3 satellite overpasses during the EPATAN-NAWDEX campaign. Calibration, validation purposes

6.1 Underpass #1 : 2016/10/02 (F7-French Falcon)

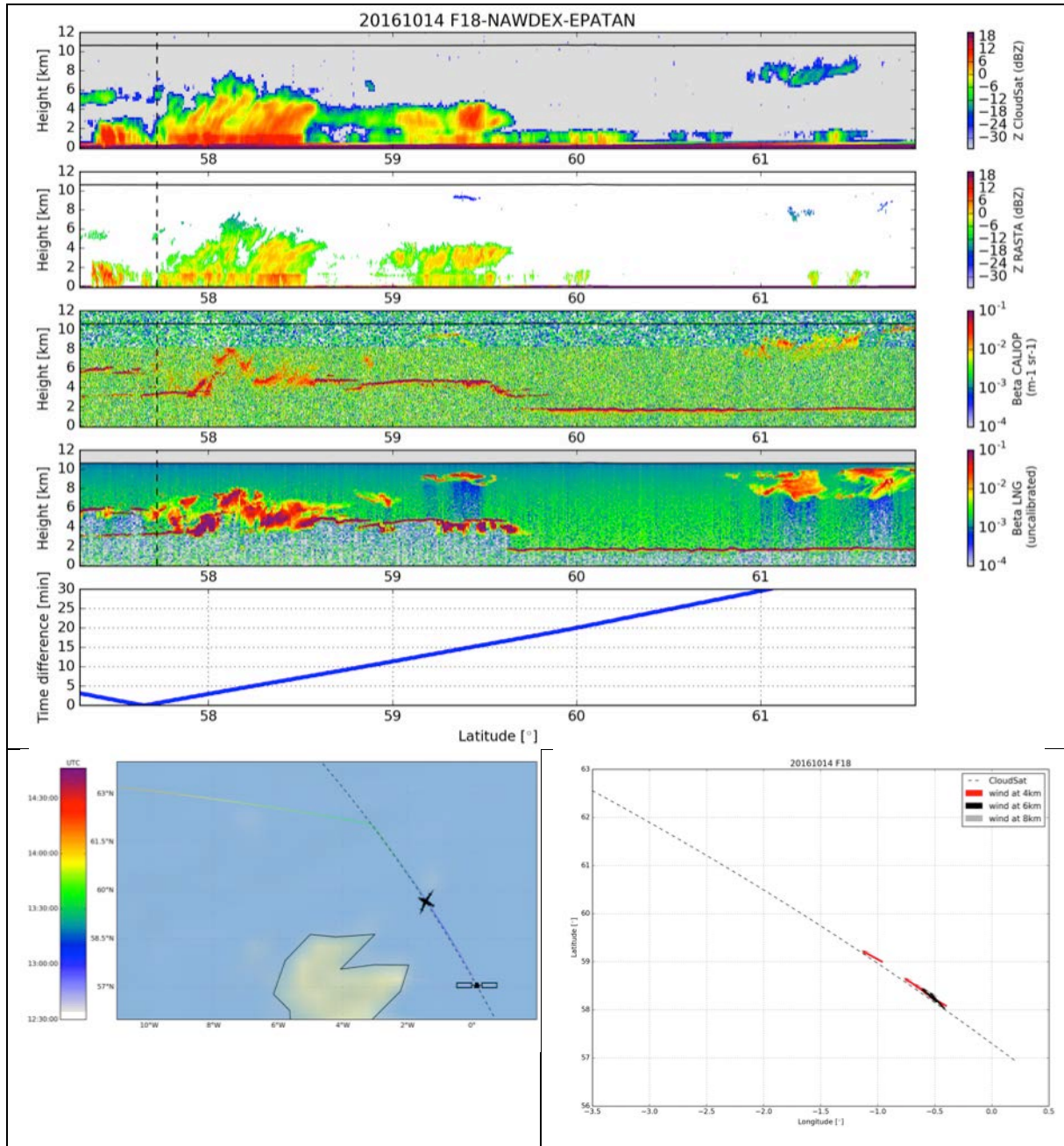


6.2 Underpass #2 : 2016/10/05 (F9-French Falcon)

Due to a system operation there is no CALIOP data during that overpass.



6.3 Underpass #3 : 2016/10/14 (F18-French Falcon)



References

- Brogniez, G., C. Pietras, M. Legrand, P. Dubuisson, and M. Haeffelin, 2003: A high-accuracy multiwavelength radiometer for in situ measurements in the thermal infrared. Part II: Behavior in field experiments. *J. Atmos. Oceanic Technol.*, **20**, 1023–1033.
- Brogniez, G., M. Legrand, B. Damiri, I. Behnert, and J.-P. Buis, 2005: Multi-channel ground based and airborne infrared radiometers. *NEWRAD Proc. Ninth Int. Conf. on New Developments and Applications in Optical Radiometry*, Davos, Switzerland, Physikalisch- Meteorologisches Observatorium Davos, World Radiation Center, 173–174.
- Bruneau D. and J. Pelon, “Simultaneous measurements of particle backscattering and extinction coefficients and wind velocity by lidar with a Mach–Zehnder interferometer: Principle of operation and performance assessment,” *Appl. Opt.* **42**, 1101–1114, 2003.
- Bruneau D., J. Pelon, F. Blouzon, J. Spatazza, P. Genau, G. Buchholtz, N. Amarouche, A. Abchiche, and O. Aouji, 355nm high spectral resolution airborne lidar LNG: system description and first results, *Appl. Opt.* **54**(29), 8776–8785, 2015.
- Cordeira JM, Ralph FM, Moore BJ. 2013. The development and evolution of two atmospheric rivers in proximity to western North Pacific tropical cyclones in October 2010. *Mon. Wea. Rev.*, **141**: 4234–4255.
- Delanoë, J., A. Protat, D. Bouniol, A. J. Heymsfield, A. Bansemmer and P. Brown. *The characterization of ice clouds properties from Doppler radar measurements. Journal of Applied Meteorology and Climatology*, 2007, **46**, 10, 1682-1698. DOI: 10.1175/JAM2543
- Delanoë, J., A. Protat, J. Testud, D. Bouniol, A. J. Heymsfield, A. Bansemmer, P. R. A. Brown, and R. M. Forbes, 2005. *Statistical properties of the normalized ice particle size distribution. J. Geophys. Res.*, 2005, **110**, D10201, doi:10.1029/2004JD005405.
- Delanoë, J., and R. J. Hogan. *A variational scheme for retrieving ice cloud properties from combined radar, lidar, and infrared radiometer. J. Geophys. Res.*, 2008, **113**, D07204, doi:10.1029/2007JD009000.
- Delanoë, J., and R. J. Hogan (2010), *Combined CloudSat-CALIPSO-MODIS retrievals of the properties of ice clouds*, *J. Geophys. Res.*, **115**, D00H29, doi:10.1029/2009JD012346.
- Delanoë J., Protat A., Jourdan O., Pelon J., Papazzoni M., Dupuy R., Gayet J.-F., Jouan C.. *Comparison of airborne in-situ, airborne radar-lidar, and spaceborne radar-lidar retrievals of polar ice cloud properties sampled during the POLARCAT campaign. Journal of Atmospheric and Oceanic Technology*, American Meteorological Society, 2013, **30** (1), pp.57-73. <10.1175/JTECH-D-11-00200.1> - [hal-00730535](https://doi.org/10.1175/JTECH-D-11-00200.1)
- Delanoë J., Heymsfield A. J., Protat A., Bansemmer A., Hogan R. J. . *Normalized particle size distribution for remote sensing application. Journal of Geophysical Research : Atmospheres*, American Geophysical Union (AGU), 2014, **119** (7), pp.4204-4227. <10.1002/2013JD020700> - [hal-00979328](https://doi.org/10.1002/2013JD020700)
- Delanoë J., A. Protat, J.-P. Vinson, W. Brett, C. Caudoux, F. Bertrand, J. Parent du Chatelet, R. Hallali, L. Barthes, M. Haeffelin, and J.-C. Dupont, 2016: BASTA: A 95-GHz FMCW Doppler Radar for Cloud and Fog Studies. *J. Atmos. Oceanic Technol.* **33**, 1023–1038, doi: 10.1175/JTECH-D-15-0104.1.
- Esselborn, M., Wirth, M., Fix, A., Tesche, M., and Ehret, G.: Air-borne high spectral resolution lidar for measuring aerosol extinction and backscatter coefficients, *Appl. Opt.*, **47**, 346–358, doi:10.1364/AO.47.000346, 2008.
- Ewald, F., Kölling, T., Baumgartner, A., Zinner, T., and Mayer, B.: Design and characterization of specMACS, a multipurpose hyperspectral cloud and sky imager, *Atmos. Meas. Tech.*, **9**, 2015-2042, doi:10.5194/amt-9-2015-2016, 2016.
- Görsdorf, U., Lehmann, V., Bauer-Pfundstein, M., Peters, G., Vavriv, D., Vinogradov, V., and Volkov, V.: A 35- GHz Polarimetric Doppler Radar for Long-Term Observations of Cloud Parameters—Description of System and Data Processing, *Journal of Atmospheric and Oceanic Technology*, **32**, 675–690, doi:10.1175/JTECH-D-14-00066.1.
- Haimov, S., and A. Rodi, 2013: Fixed-antenna pointing-angle calibration of airborne Doppler cloud radar. *Journal of Atmospheric and Oceanic Technology*, **30** (10), 2320–2335, doi:10.1175/JTECH-D-12-00262.1, URL <http://dx.doi.org/10.1175/JTECH-D-12-00262.1>.
- Legrand, M., C. Pietras, G. Brogniez, and M. Haeffelin, 2000: A high-accuracy multiwavelength radiometer for in situ measurements in the thermal infrared. Part I: Characterization of the instrument. *J. Atmos. Oceanic Technol.*, **17**, 1203–1214.

Version 1.2 EPATAN DATA ACQUISITION REPORT

- Li, L., G. M. Heymsfield, L. Tian, and P. E. Racette, 2005: Measurements of Ocean Surface Backscattering Using an Airborne 94-GHz Cloud Radar—Implication for Calibration of Airborne and Spaceborne W-Band Radars. *Journal of Atmospheric and Oceanic Technology*, 22, 1033–1045.
- Mech, M., Orlandi, E., Crewell, S., Ament, F., Hirsch, L., Hagen, M., Peters, G., and Stevens, B.: HAMP – the microwave package on the High Altitude and Long range research aircraft (HALO), *Atmos. Meas. Tech.*, 7, 4539-4553, doi:10.5194/amt-7-4539-2014, 2014.
- Paffrath U, Lemmerz C, Reitebuch O, Witschas B, Nikolaus I, Freudenthaler V. 2009. The airborne demonstrator for the direct-detection Doppler wind lidar ALADIN on ADM-Aeolus: II. Simulations and Rayleigh receiver radiometric performance. *J. Atmos. Ocean. Tech.*, 26: 2516-2530.
- Protat, A., and I. Zawadzki, 1999: A Variational Method for Real-Time Retrieval of Three-Dimensional Wind Field from Multiple-Doppler Bistatic Radar Network Data. *Journal of Atmospheric and Oceanic Technology*, 16, 432–449.
- Ralph F. M., M. D. Dettinger, and G. A. Wick, 2004: Satellite and CALJET aircraft observations of atmospheric rivers of the eastern North Pacific Ocean during the winter of 1997/98. *Mon. Wea. Rev.*, 132, 1721–1745.
- Reitebuch O, Lemmerz C, Nagel E, Paffrath U, Durand Y, Endemann M, Fabre F, Chaloupy M. 2009. The airborne demonstrator for the direct-detection Doppler wind lidar ALADIN on ADM-Aeolus: I. Instrument design and comparison to satellite instrument. *J. Atmos. Ocean. Tech.*, 26: 2501-2515
- Sourdeval, O., Brogniez, G., Pelon, J., C.-Labonnote, L., Dubuisson, P., Parol, F., Josset, D., Garnier, A., Faivre, M., and Minikin, A.: Validation of IIR/CALIPSO Level 1 measurements by comparison with collocated airborne observations during CIRCLE-2 and Biscay '08 campaigns, *J. Atmos. Ocean. Tech.*, 29, 653–667, doi:10.1175/JTECH-D-11-00143.1, 2012.
- Tanelli, S., S. L. Durden, E. Im, K. S. Pak, D. G. Reinke, P. Partain, J. M. Haynes, and R. T. Marchand, 2008: Cloudsat's cloud profiling radar after 2 years in orbit: Performance, external calibration, and processing. *IEEE Trans. Geosci. Remote Sens.*, 46, 3560–3573.
- Testud, J., H. P. H., and L. W.-C., 1995: A procedure to correct airborne doppler radar data for navigation errors, using the echo returned from the earth surface. *J. Atmos. Oceanic Technol.*, 12, 800–820.
- Weissmann M, Busen R, Dörnbrack, A, Rahm S, Reitebuch O. 2005. Targeted Observations with an Airborne Wind Lidar. *J. Atmos. Ocean. Tech.*, 22: 1706-1719.
- Wirth, M., Fix, A., Mahnke, P. et al., "The airborne multi-wavelength water vapor differential absorption lidar WALES: system design and performance", *Appl. Phys. B*, 96: 201., (2009), doi:10.1007/s00340-009-3365-7

Annexe A: Flights description

In this annex we illustrate the RALI measurements and dropsonde measurements (when available).

Note that the red line in the RALI measurements plots indicates when LNG is working in ADM mode, blue line when the F20 has a roll larger than 10° in absolute value.

Top panel gives an overview of the flight track, the time is coded in colours (cf colourbar), dropsondes are marked with a green dot with the launch time.

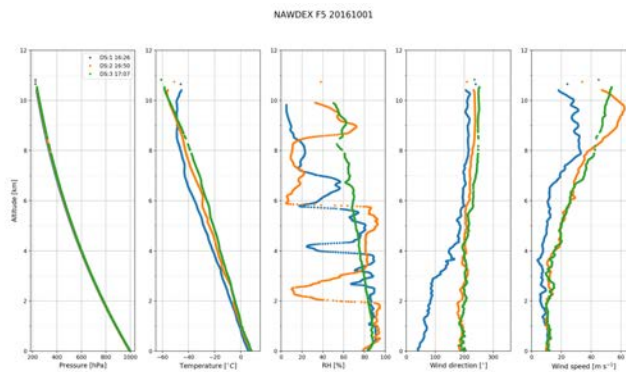
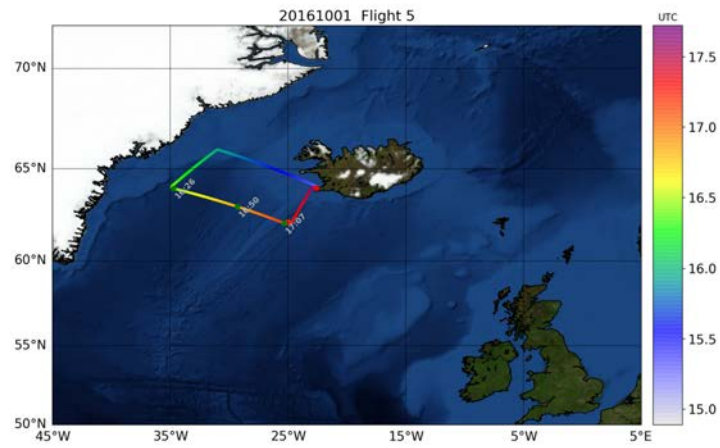
The second panel shows the main dropsondes measurements (if available).

The bottom panel description is described below:

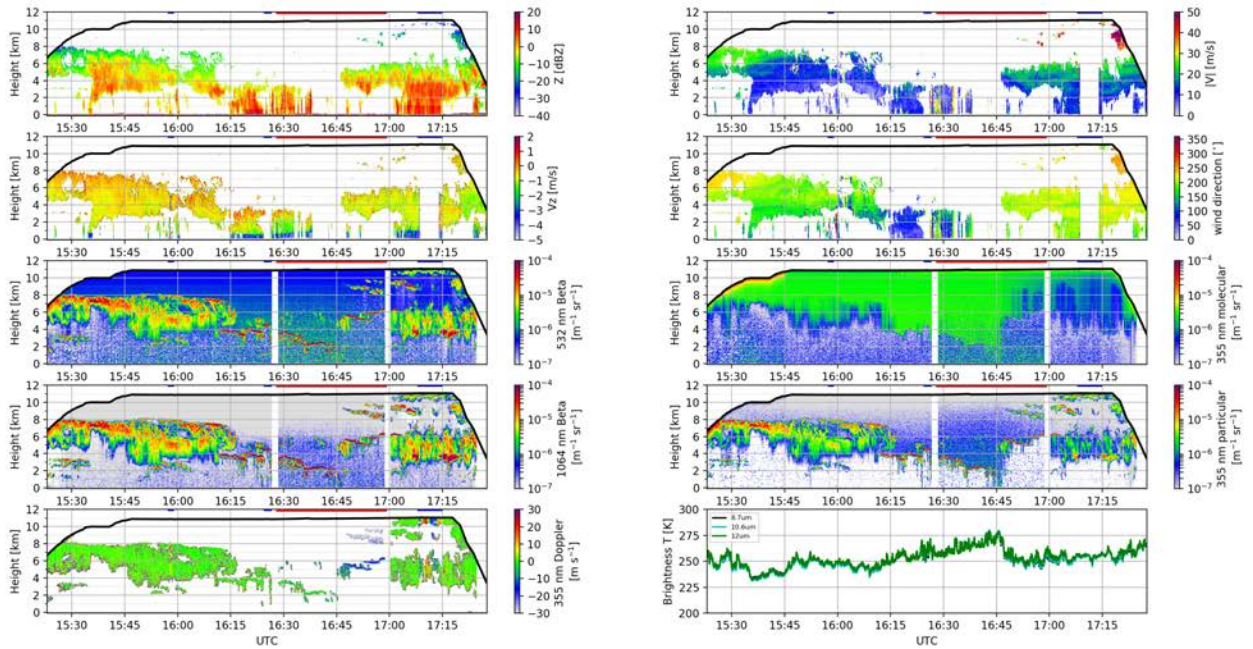
RASTA vertical reflectivity	Horizontal wind speed retrieved by RASTA
RASTA Vertical velocity, derived from the 3 antennas combination	Horizontal wind direction retrieved by RASTA
LNG attenuated backscatter at 532 nm	LNG attenuated molecular backscatter at 355 nm
LNG attenuated backscatter at 1064 nm	LNG attenuated particular backscatter at 355 nm
LNG Doppler measurement at 355 nm	Climat brightness temperatures

Version 1.2 EPATAN DATA ACQUISITION REPORT

F5: 2016/10/01

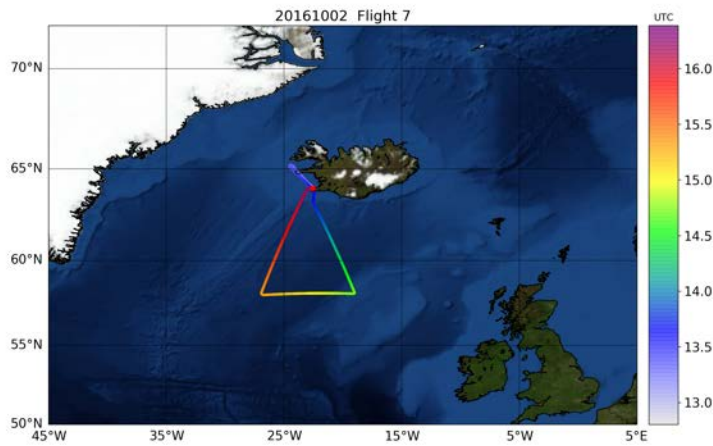


NAWDEX F5 20161001

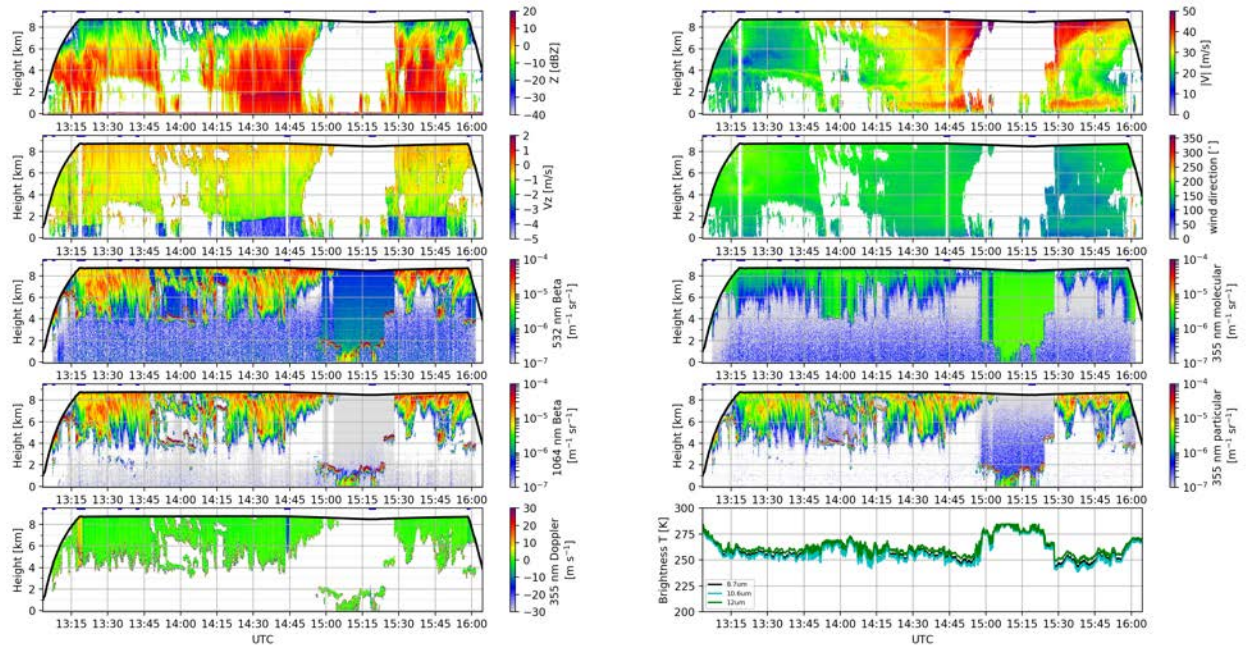


Version 1.2 EPATAN DATA ACQUISITION REPORT

F7: 2016/10/02

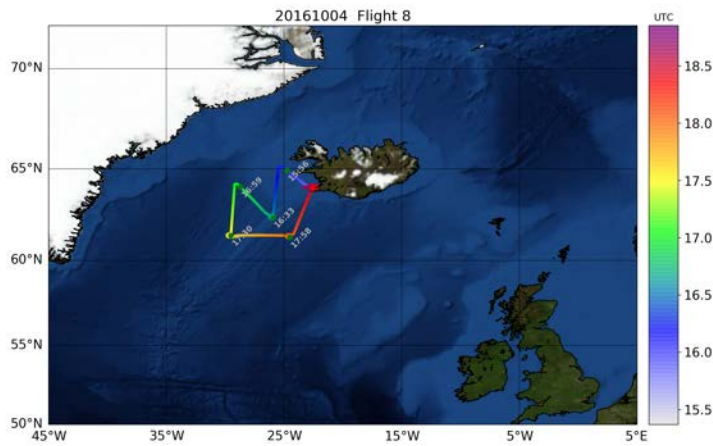


NAWDEx F7 20161002

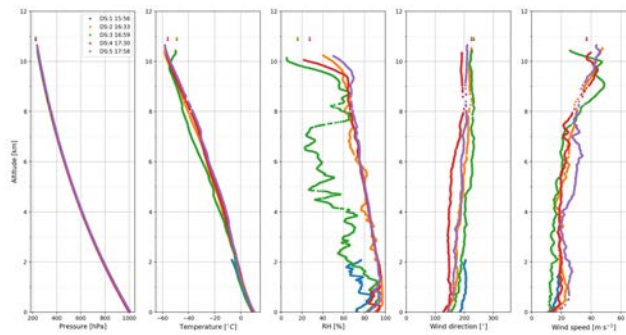


Version 1.2 EPATAN DATA ACQUISITION REPORT

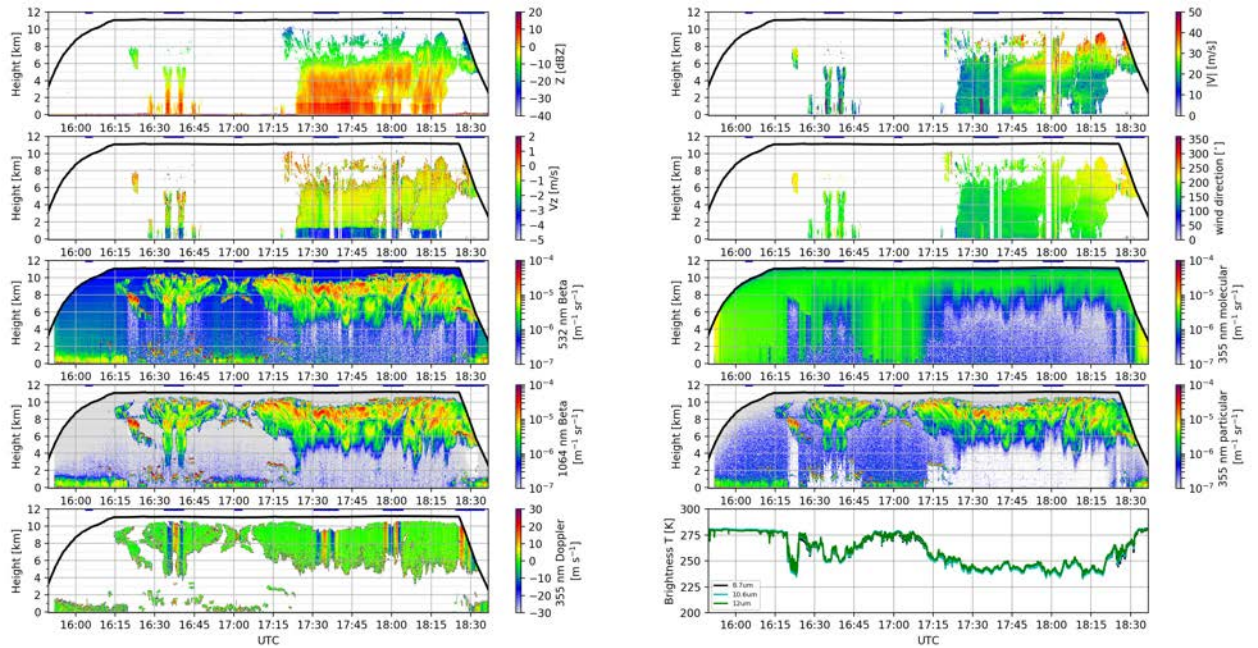
F8: 2016/10/04



NAWDEX F8 20161004

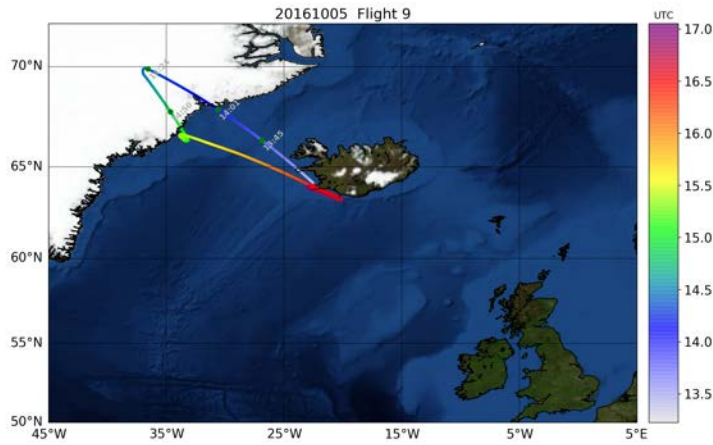


NAWDEX F8 20161004

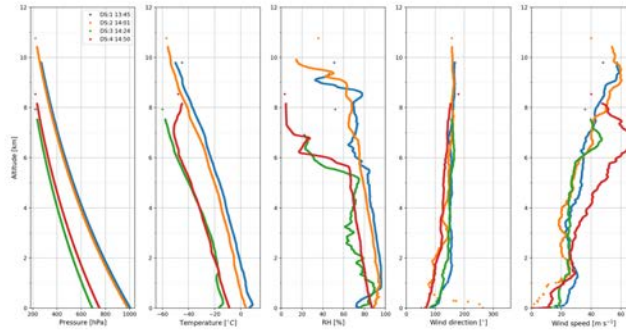


Version 1.2 EPATAN DATA ACQUISITION REPORT

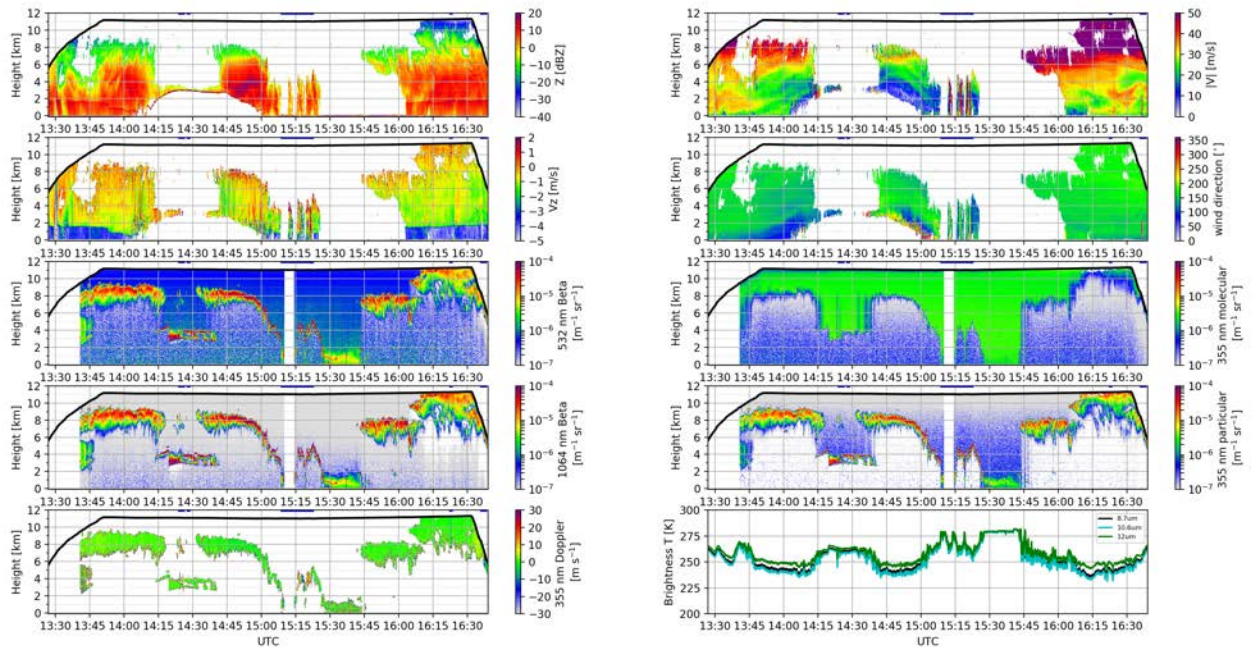
F9: 2016/10/05



NAWDEX F9 20161005

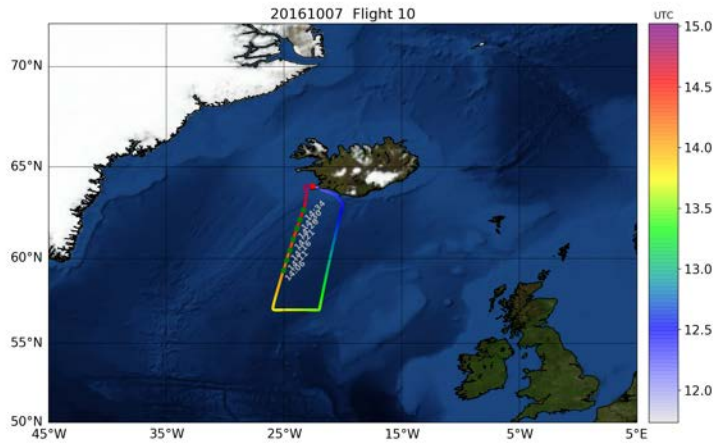


NAWDEX F9 20161005

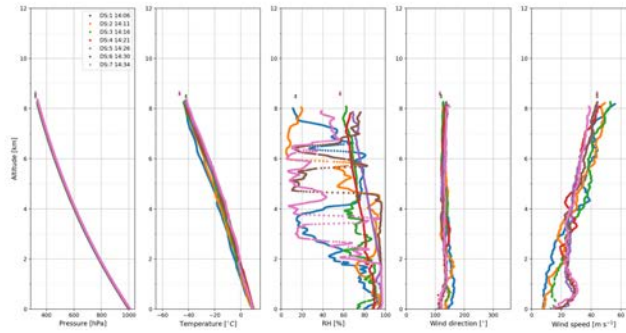


Version 1.2 EPATAN DATA ACQUISITION REPORT

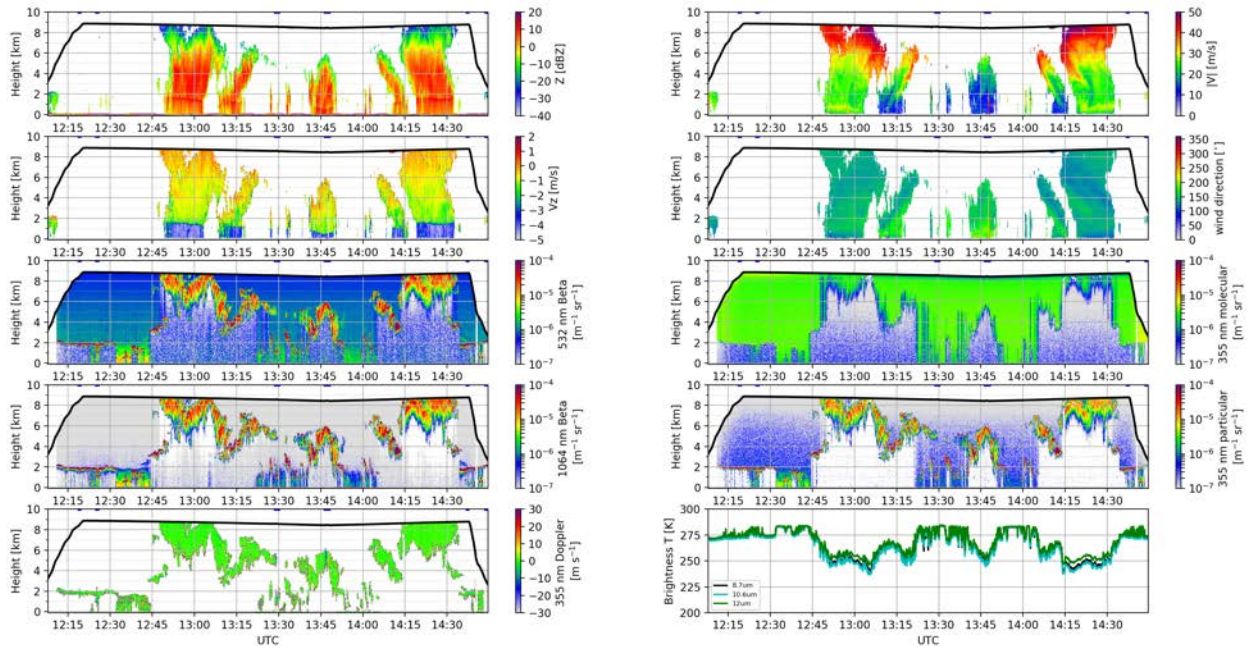
F10: 2016/10/07



NAWDEX F10 20161007

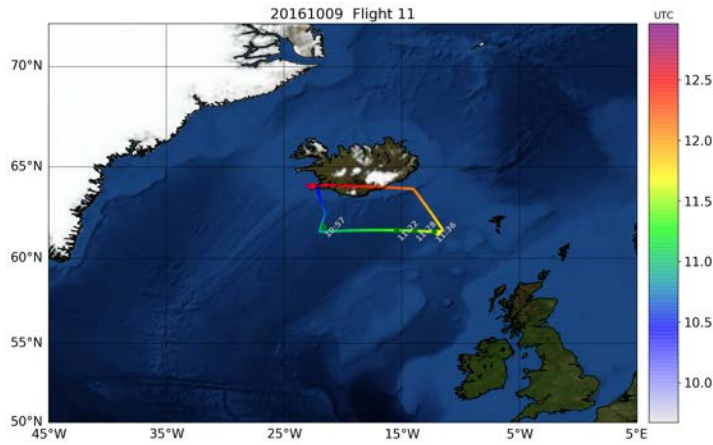


NAWDEX F10 20161007

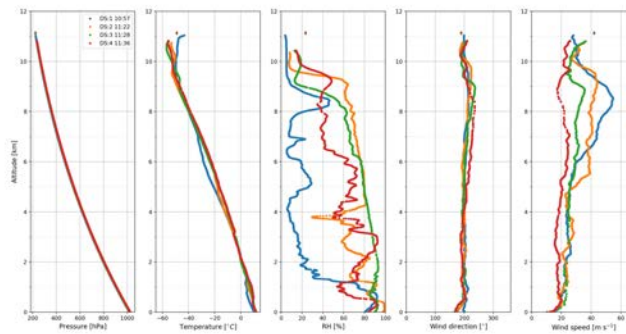


Version 1.2 EPATAN DATA ACQUISITION REPORT

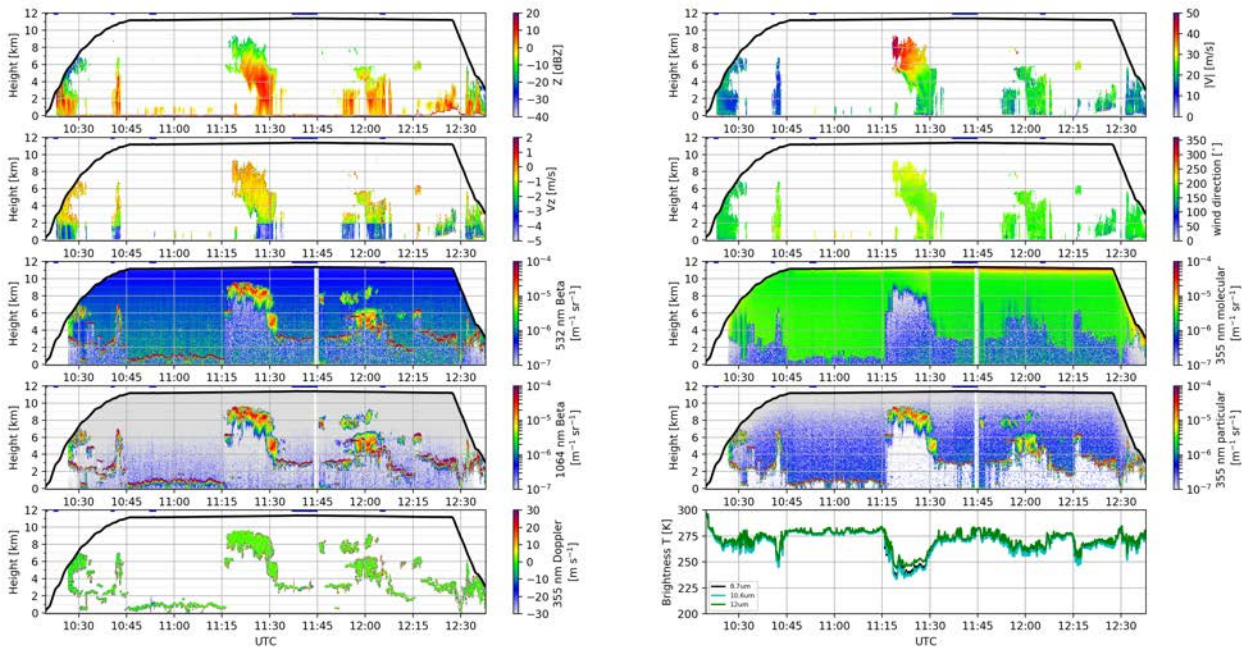
F11: 2016/10/09



NAWDEX F11 20161009

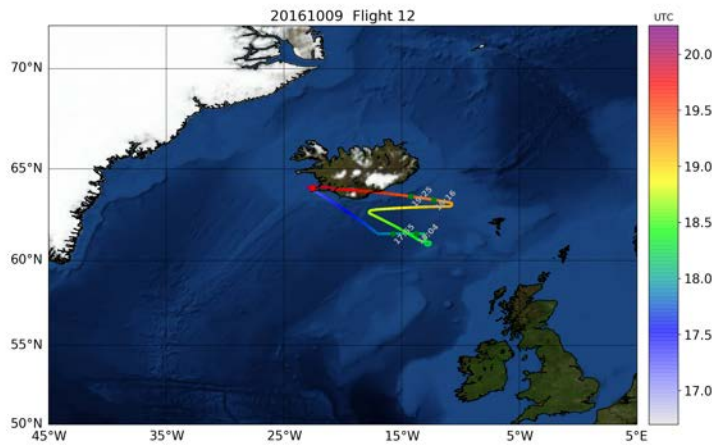


NAWDEX F11 20161009

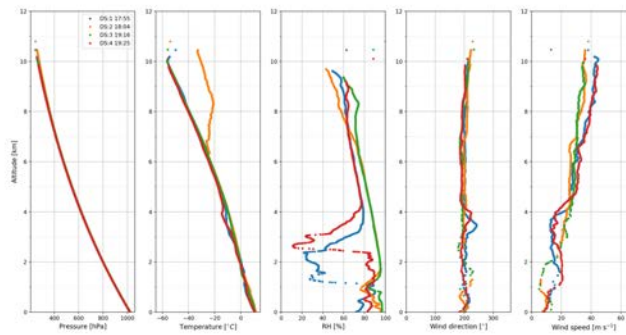


Version 1.2 EPATAN DATA ACQUISITION REPORT

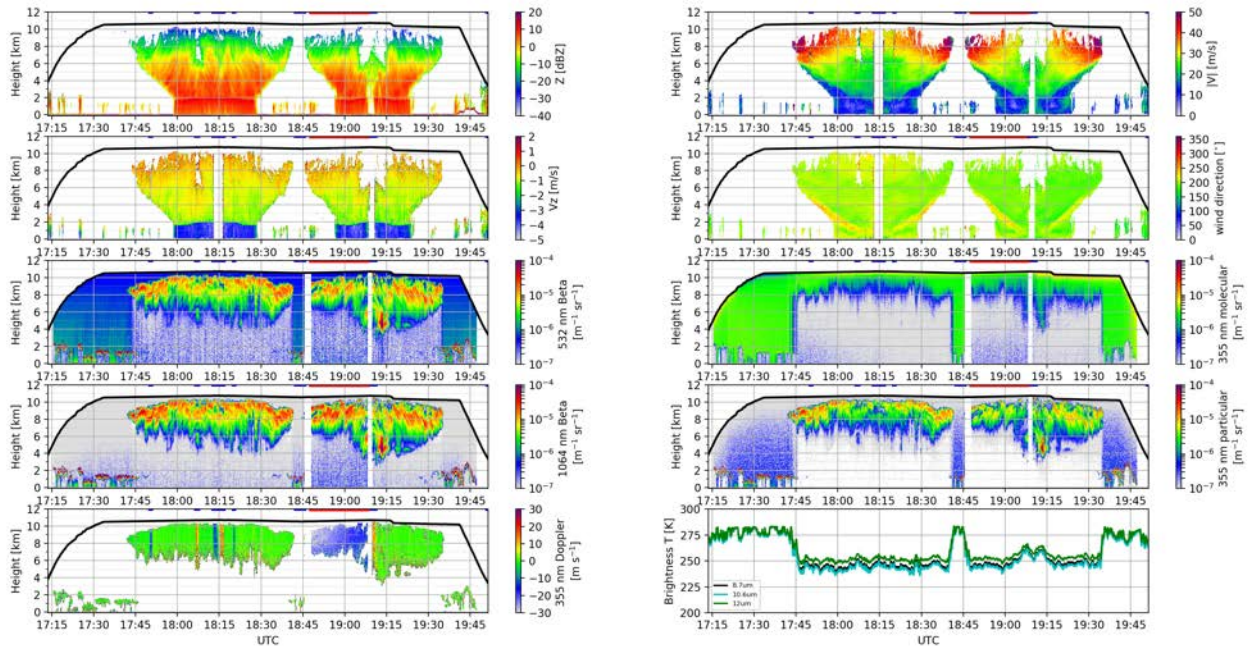
F12: 2016/10/09



NAWDEX F12 20161009

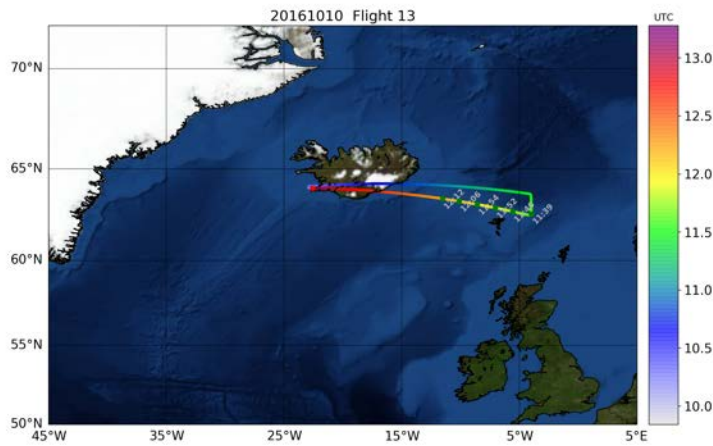


NAWDEX F12 20161009

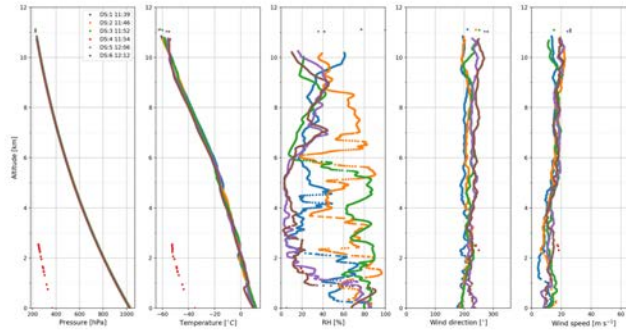


Version 1.2 EPATAN DATA ACQUISITION REPORT

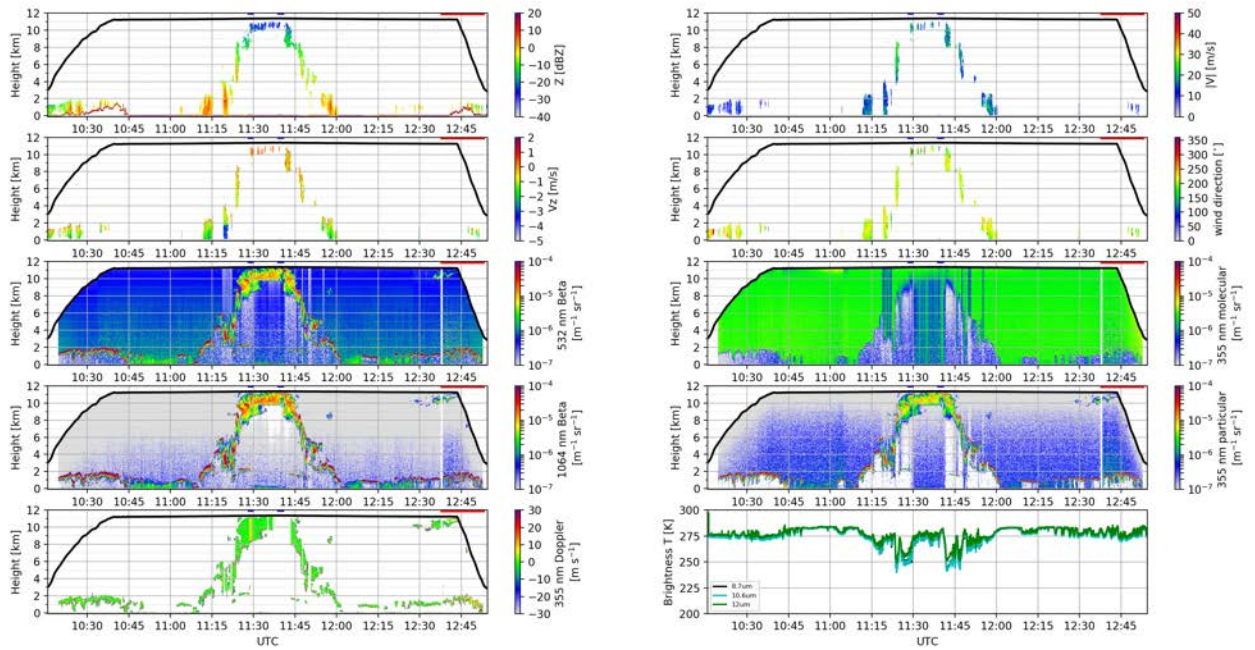
F13: 2016/10/10



NAWDEX F13 20161010

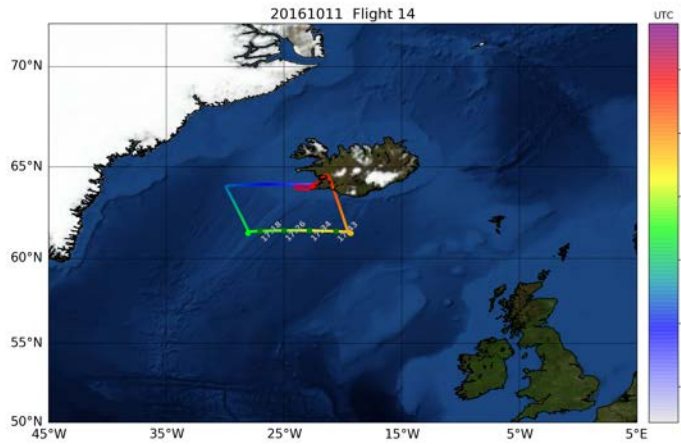


NAWDEX F13 20161010

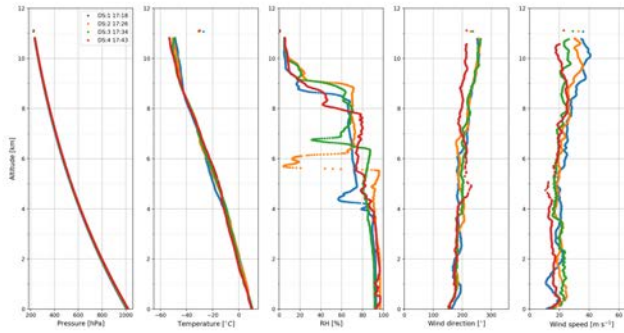


Version 1.2 EPATAN DATA ACQUISITION REPORT

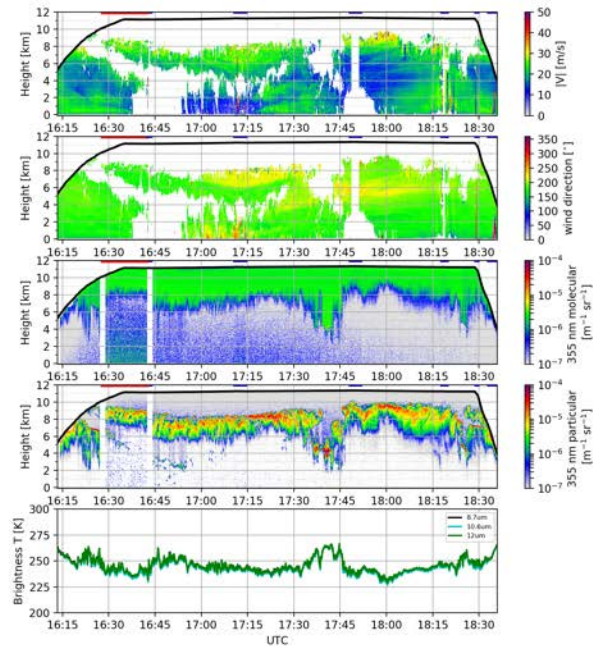
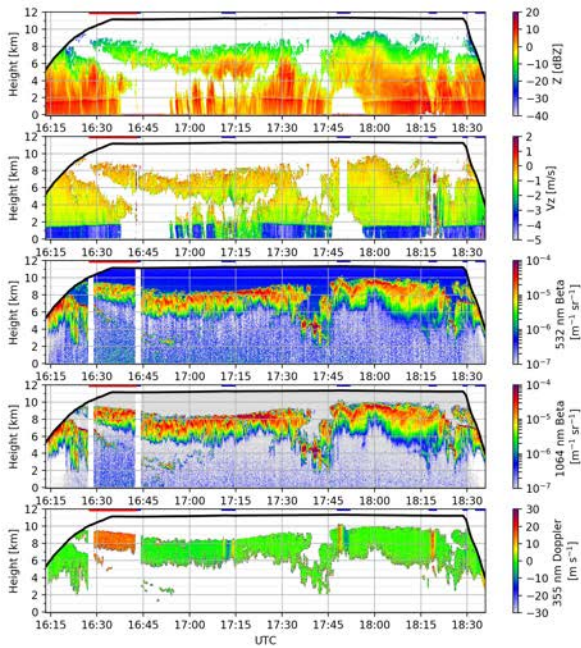
F14: 2016/10/11



NAWDEX F14 20161011

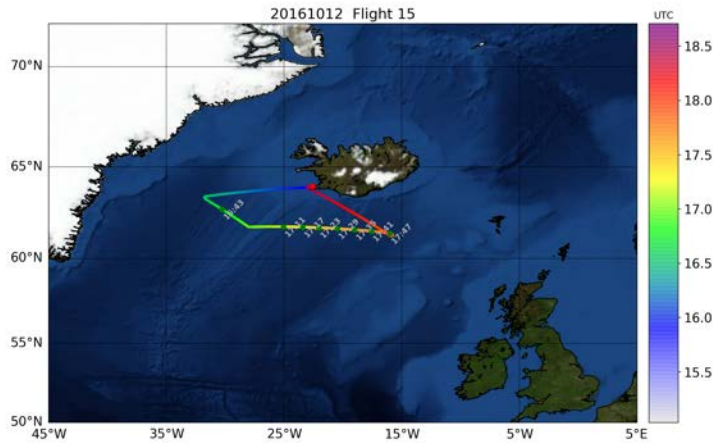


NAWDEX F14 20161011

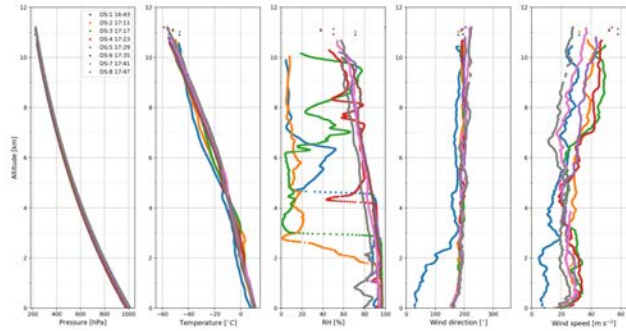


Version 1.2 EPATAN DATA ACQUISITION REPORT

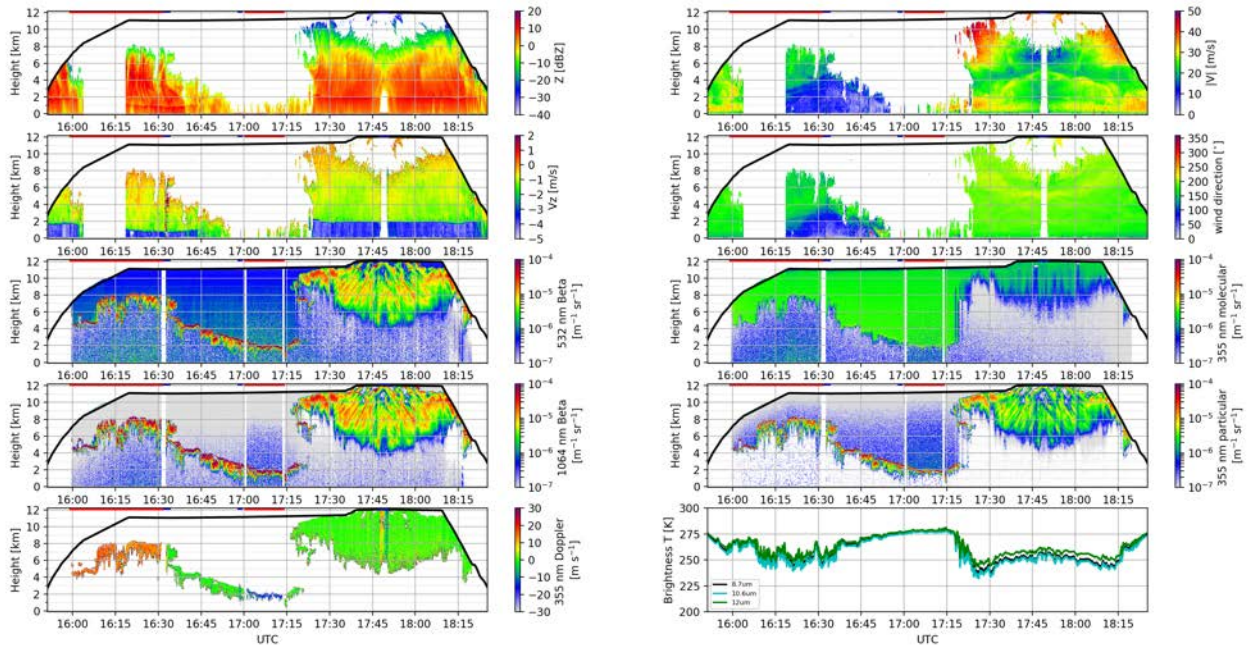
F15: 2016/10/12



NAWDEX F15 20161012

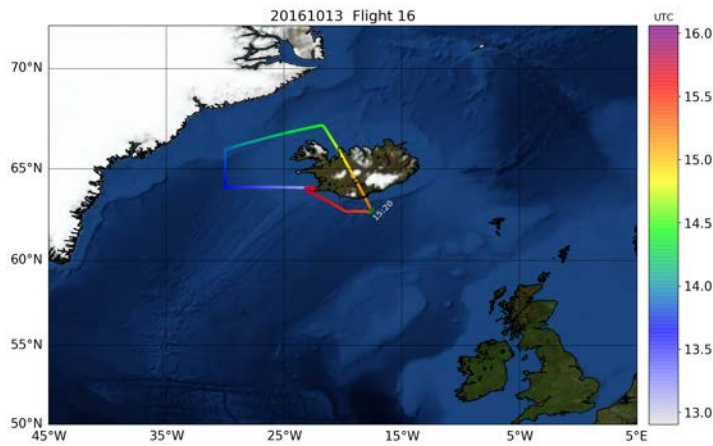


NAWDEX F15 20161012

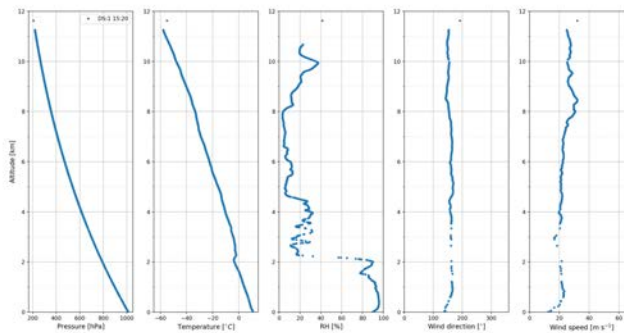


Version 1.2 EPATAN DATA ACQUISITION REPORT

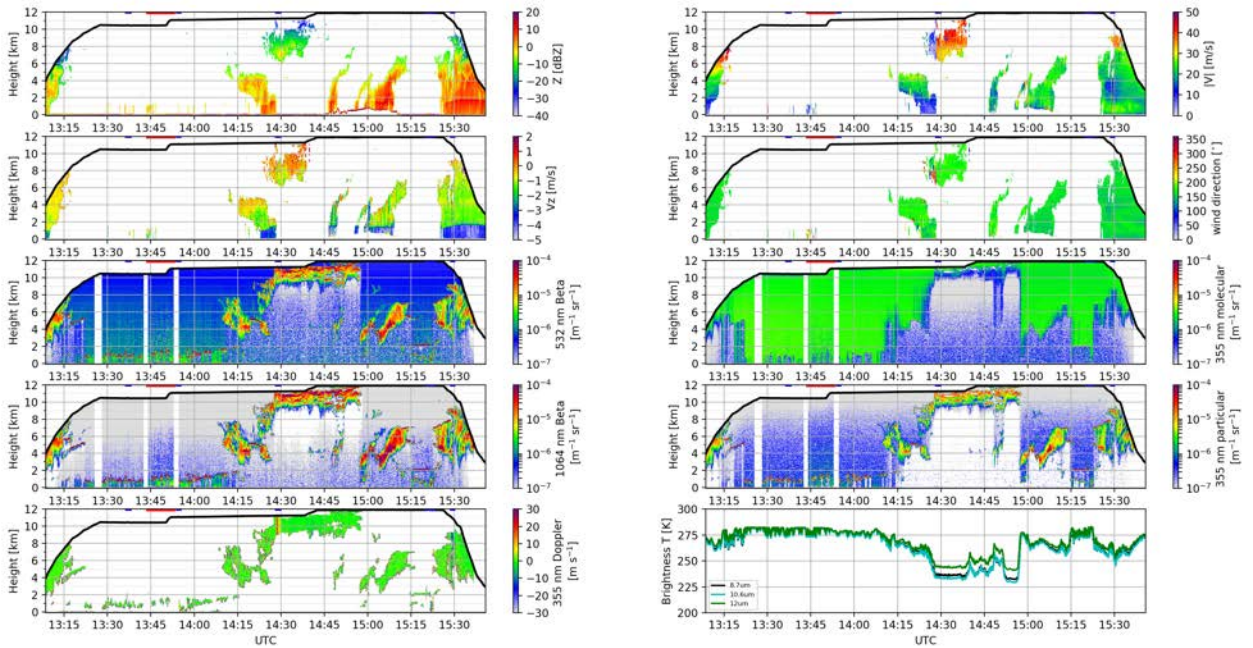
F16: 2016/10/13



NAWDEX F16 20161013

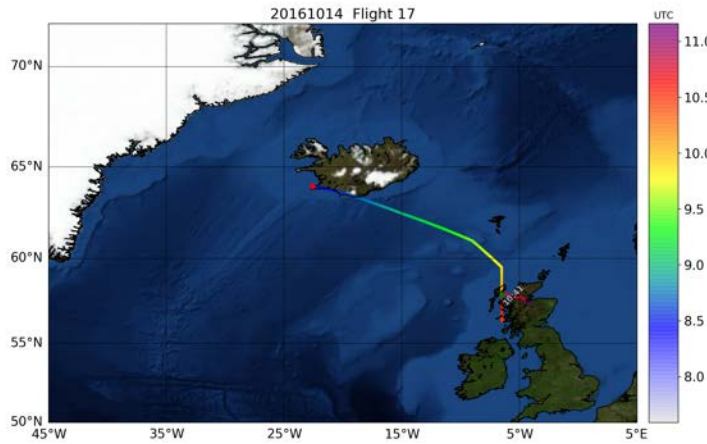


NAWDEX F16 20161013

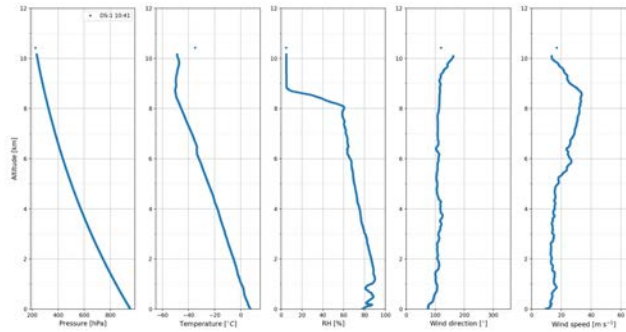


Version 1.2 EPATAN DATA ACQUISITION REPORT

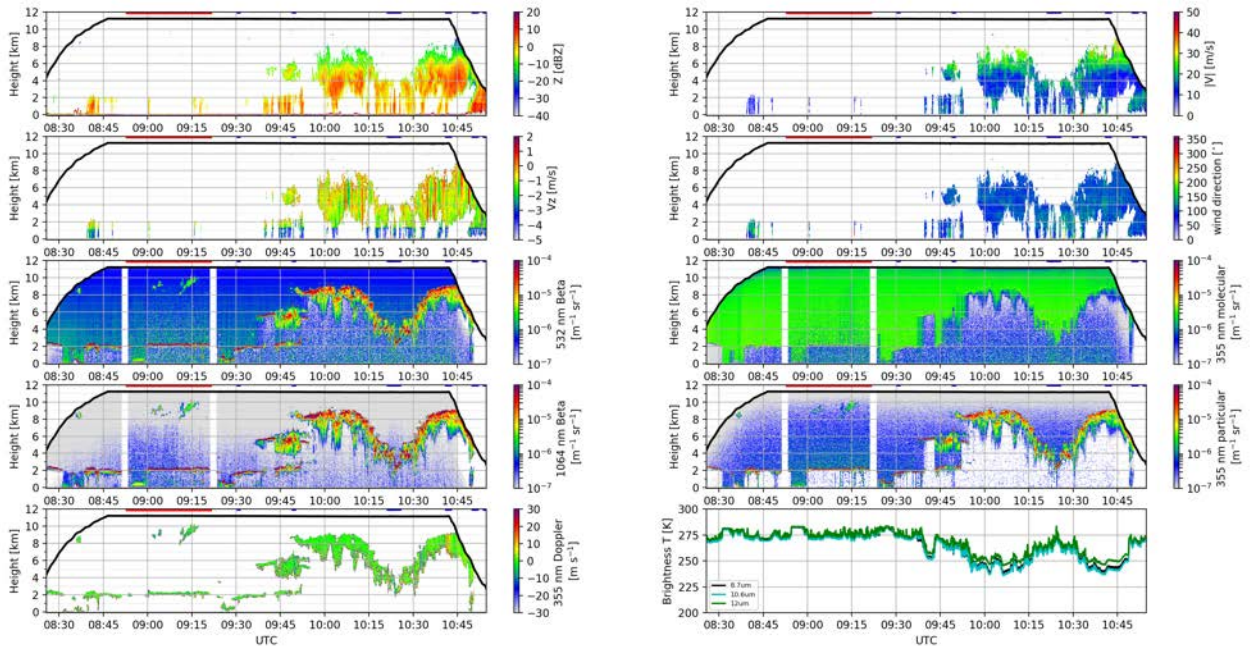
F17: 2016/10/14



NAWDEX F17 20161014

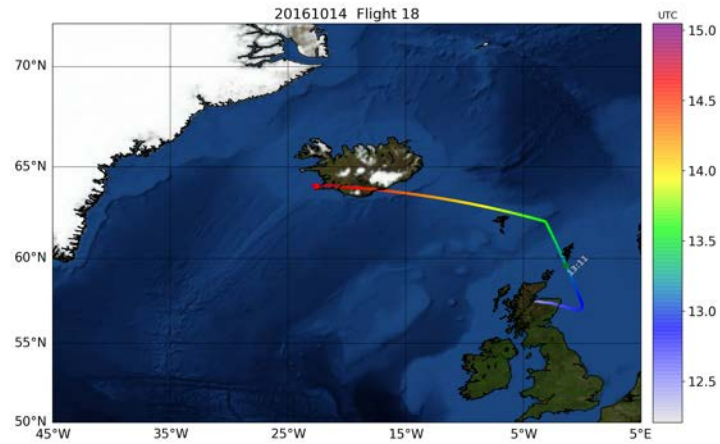


NAWDEX F17 20161014

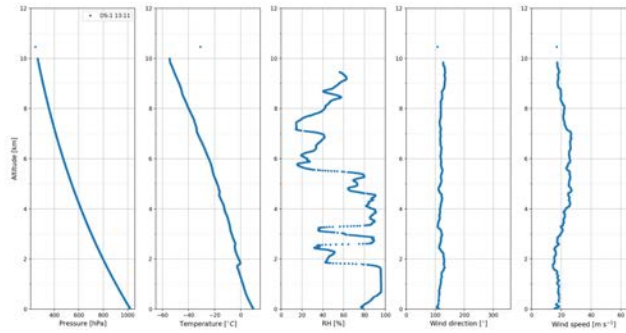


Version 1.2 EPATAN DATA ACQUISITION REPORT

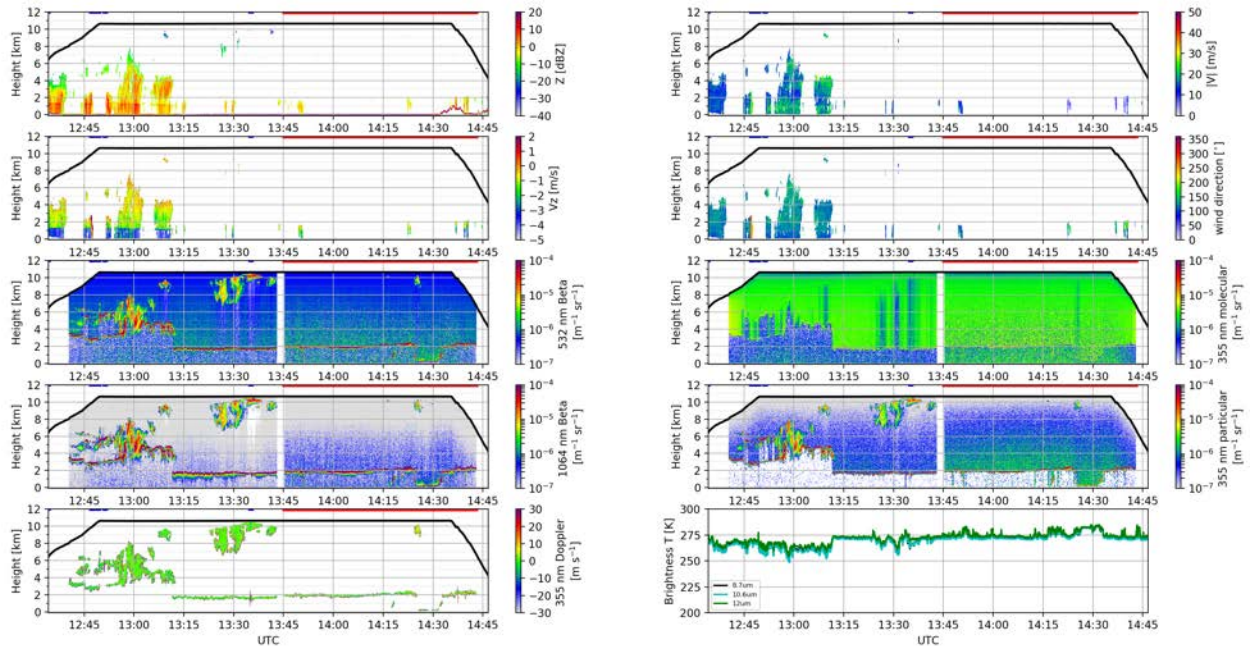
F18: 2016/10/14



NAWDEX F18 20161014



NAWDEX F18 20161014



Annexe B: content of the files

SAFIRE aircraft product

```

netcdf core_safire-fa20_20161002_r3_fs160006 {
dimensions:
    time = UNLIMITED ; // (12595 currently)
variables:
    double time(time) ;
        time:units = "seconds since 2016-10-02 00:00:00 UTC" ;
        time:long_name = "time" ;
        time:standard_name = "time" ;
    float topnb_cal_1(time) ;
        topnb_cal_1:units = "count" ;
        topnb_cal_1:FillValue = -9.e+33 ;
        topnb_cal_1:proposed_standard_name = "event_marker" ;
        topnb_cal_1:long_name_fr = "top de l evenement" ;
        topnb_cal_1:valid_max = 3.e+38 ;
        topnb_cal_1:fct_origin = "Dec_CAM95_TOP (12595, TOPNB, [3.40282e+38,
3.40282e+38, 3.40282e+38 ..])" ;
        topnb_cal_1:Category = "housekeeping" ;
    float pos_lat_aipov_1(time) ;
        pos_lat_aipov_1:units = "degree" ;
        pos_lat_aipov_1:FillValue = -9.e+33 ;
        pos_lat_aipov_1:long_name = "Latitude AIRINS synchronised on Sampling
times (GPS synchronised clock" ;
        pos_lat_aipov_1:standard_name = "latitude" ;
        pos_lat_aipov_1:long_name_fr = "Latitude AIRINS synchronise sur Temps
des echantillons (horloge calee sur reference GPS" ;
        pos_lat_aipov_1:fct_origin = "CnvDbl2Flt (pos_lat_aipov_dbl_1,
pos_lat_aipov_1)" ;
        pos_lat_aipov_1:Category = "position" ;
    float pos_lon_aipov_1(time) ;
        pos_lon_aipov_1:units = "degree" ;
        pos_lon_aipov_1:FillValue = -9.e+33 ;
        pos_lon_aipov_1:long_name = "Longitude AIRINS synchronised on
Sampling times (GPS synchronised clock" ;
        pos_lon_aipov_1:standard_name = "longitude" ;
        pos_lon_aipov_1:long_name_fr = "Longitude AIRINS synchronise sur
Temps des echantillons (horloge calee sur reference GPS" ;
        pos_lon_aipov_1:fct_origin = "CnvDbl2Flt (pos_lon_aipov_dbl_1,
pos_lon_aipov_1)" ;
        pos_lon_aipov_1:Category = "position" ;
    float alt_alti_gps_1(time) ;
        alt_alti_gps_1:units = "meter" ;
        alt_alti_gps_1:FillValue = -9.e+33 ;
        alt_alti_gps_1:long_name = "Altitude corrected from the geoid undulation
interpolated on Sampling times (GPS synchronised clock" ;

```

Version 1.2 EPATAN DATA ACQUISITION REPORT

```
alt_alti_gps_1:positive = "up" ;
alt_alti_gps_1:standard_name = "altitude" ;
alt_alti_gps_1:long_name_fr = "Altitude corrigee ondulation geoid
interpolle sur Temps des echantillons (horloge calee sur reference GPS" ;
alt_alti_gps_1:fct_origin = "Interpol_irreg_mnq (rft_TIME_1,
rft_LLATIME_utc_1, alt_altigps_geoid84_1, $Arg3.NbVal, 2.6, 1., alt_alti_gps_1)" ;
alt_alti_gps_1:Category = "position" ;
float alt_aipov_1(time) ;
alt_aipov_1:units = "meter" ;
alt_aipov_1:_FillValue = -9.e+33 ;
alt_aipov_1:long_name = "Altitude from AIRINS synchronised on Sampling
times (GPS synchronised clock" ;
alt_aipov_1:positive = "up" ;
alt_aipov_1:standard_name = "altitude" ;
alt_aipov_1:long_name_fr = "Altitude AIRINS synchronise sur Temps des
echantillons (horloge calee sur reference GPS" ;
alt_aipov_1:fct_origin = "MoyEch_tps_impos (alt_altaipov_cal_100,
rft_TIMEAIPOV_100, 1./2., 1./2., $Arg1.sample/2, rft_TIME_1, $Arg6.NbVal, alt_aipov_1)"
;
alt_aipov_1:Category = "position" ;
float att_roll_aipov_1(time) ;
att_roll_aipov_1:units = "degree" ;
att_roll_aipov_1:_FillValue = -9.e+33 ;
att_roll_aipov_1:long_name = "Roll angle AIRINS synchronised on
Sampling times (GPS synchronised clock" ;
att_roll_aipov_1:standard_name = "platform_roll_angle" ;
att_roll_aipov_1:long_name_fr = "Roulis AIRINS synchronise sur Temps des
echantillons (horloge calee sur reference GPS" ;
att_roll_aipov_1:fct_origin = "MoyEch_tps_impos (att_rollaipov_cal_100,
rft_TIMEAIPOV_100, 1./2., 1./2., $Arg1.sample/2, rft_TIME_1, $Arg6.NbVal,
att_roll_aipov_1)" ;
att_roll_aipov_1:Category = "platform_dynamics" ;
float att_pitch_aipov_1(time) ;
att_pitch_aipov_1:units = "degree" ;
att_pitch_aipov_1:_FillValue = -9.e+33 ;
att_pitch_aipov_1:long_name = "Pitch angle AIRINS synchronised on
Sampling times (GPS synchronised clock" ;
att_pitch_aipov_1:standard_name = "platform_pitch_angle" ;
att_pitch_aipov_1:long_name_fr = "Tangage AIRINS synchronise sur Temps
des echantillons (horloge calee sur reference GPS" ;
att_pitch_aipov_1:fct_origin = "MoyEch_tps_impos (att_pitchaipov_cal_100,
rft_TIMEAIPOV_100, 1./2., 1./2., $Arg1.sample/2, rft_TIME_1, $Arg6.NbVal,
att_pitch_aipov_1)" ;
att_pitch_aipov_1:Category = "platform_dynamics" ;
float att_capgeo_aipov_1(time) ;
att_capgeo_aipov_1:units = "degree" ;
att_capgeo_aipov_1:_FillValue = -9.e+33 ;
att_capgeo_aipov_1:long_name = "True Heading AIRINS sampled on the
variable named rft_TIME_100 averaged and sampled" ;
```

Version 1.2 EPATAN DATA ACQUISITION REPORT

```
att_capgeo_aipov_1:standard_name = "platform_orientation" ;
att_capgeo_aipov_1:long_name_fr = "cap géographique AIRINS
echantillonne sur la variable rft_TIME_100 moyenne et echantillonne" ;
att_capgeo_aipov_1:fct_origin = "MoyEch_Angl_auto_unit
(att_capaipov_sync_100, 1./$Arg1.sample, -$Arg1.sample/(1*2), $Arg1.unit,
att_capgeo_aipov_1)" ;
att_capgeo_aipov_1:Category = "platform_dynamics" ;
float pre_s_av_adc_fitpch_1(time) ;
pre_s_av_adc_fitpch_1:units = "hPa" ;
pre_s_av_adc_fitpch_1:FillValue = -9.e+33 ;
pre_s_av_adc_fitpch_1:long_name = "Nose boom front static pressure
averaged at 1 Hz minus Static defect V 2006" ;
pre_s_av_adc_fitpch_1:standard_name = "air_pressure" ;
pre_s_av_adc_fitpch_1:long_name_fr = "Pression brute statique avant
perche moyenne a 1 Hz moins Erreur de statique V 2006" ;
pre_s_av_adc_fitpch_1:fct_origin = "Moins (pre_sb_av_1,
ctl_errstat_av_adc_fitpch_1, pre_s_av_adc_fitpch_1)" ;
pre_s_av_adc_fitpch_1:Category = "pressure" ;
float tpr_srd_adc_fitpch_1(time) ;
tpr_srd_adc_fitpch_1:units = "Celsius" ;
tpr_srd_adc_fitpch_1:FillValue = -9.e+33 ;
tpr_srd_adc_fitpch_1:long_name = "Static air temperature from Deiced
Rosemount impact temperature averaged at 1 Hz" ;
tpr_srd_adc_fitpch_1:standard_name = "air_temperature" ;
tpr_srd_adc_fitpch_1:long_name_fr = "temperature statique a partir de
Temperature degivree Rosemount moyenne a 1 Hz" ;
tpr_srd_adc_fitpch_1:fct_origin = "Tair (tpr_total_rd_1, vit_dp_adc_fitpch_1,
pre_s_av_adc_fitpch_1, 0.97, Ra/cpa, tpr_srd_adc_fitpch_1)" ;
tpr_srd_adc_fitpch_1:Category = "temperature" ;
float tpr_aero_adc_fitpch_1(time) ;
tpr_aero_adc_fitpch_1:units = "Celsius" ;
tpr_aero_adc_fitpch_1:FillValue = -9.e+33 ;
tpr_aero_adc_fitpch_1:long_name = "Static air temperature from
Temperature averaged at 1 Hz" ;
tpr_aero_adc_fitpch_1:standard_name = "air_temperature" ;
tpr_aero_adc_fitpch_1:long_name_fr = "temperature statique a partir de
Temperature moyenne a 1 Hz" ;
tpr_aero_adc_fitpch_1:fct_origin = "Tair (tpr_total_aero_1,
vit_dp_adc_fitpch_1, pre_s_av_adc_fitpch_1, 0.97, Ra/cpa, tpr_aero_adc_fitpch_1)" ;
tpr_aero_adc_fitpch_1:Category = "temperature" ;
float tpr_total_rd_1(time) ;
tpr_total_rd_1:units = "Celsius" ;
tpr_total_rd_1:FillValue = -9.e+33 ;
tpr_total_rd_1:long_name = "Deiced Rosemount impact temperature
averaged at 1 Hz" ;
tpr_total_rd_1:proposed_standard_name = "air_total_temperature" ;
tpr_total_rd_1:long_name_fr = "Temperature degivree Rosemount
moyenne a 1 Hz" ;
```

Version 1.2 EPATAN DATA ACQUISITION REPORT

```
tpr_total_rd_1:fct_origin = "MoyEch (tpr_ttbtrtd_cal_200, 1/$Arg1.sample, -
$Arg1.sample/(2*1), tpr_total_rd_1)";
tpr_total_rd_1:Category = "temperature";
float tpr_tatadc_1(time);
tpr_tatadc_1:units = "Celsius";
tpr_tatadc_1:FillValue = -9.e+33;
tpr_tatadc_1:long_name = "Total air temperature from Air Data Computer
synchronised on Sampling times (GPS synchronised clock";
tpr_tatadc_1:proposed_standard_name = "air_total_temperature";
tpr_tatadc_1:long_name_fr = "Temperature totale air Data Computer
synchronise sur Temps des echantillons (horloge calee sur reference GPS";
tpr_tatadc_1:fct_origin = "MoyEch_tps_impos (tpr_tatadc_cal_16,
rft_TIME_ARINC0_RX4_16, 0.5, 0.5, 8, rft_TIME_1, $Arg6.NbVal, tpr_tatadc_1)";
tpr_tatadc_1:Category = "temperature";
float hum_tdc2_rs_sync_1(time);
hum_tdc2_rs_sync_1:units = "Celsius";
hum_tdc2_rs_sync_1:FillValue = -9.e+33;
hum_tdc2_rs_sync_1:long_name = "CR2 mirror temperature interpolated
on Sampling times (GPS synchronised clock";
hum_tdc2_rs_sync_1:standard_name = "dew_point_temperature";
hum_tdc2_rs_sync_1:long_name_fr = "temperature miroir td cryo CR2
interpolle sur Temps des echantillons (horloge calee sur reference GPS";
hum_tdc2_rs_sync_1:fct_origin = "Interpol_irreg_mnq (rft_TIME_1,
rft_TIME_NAI_0_CH1_0, hum_tdc2_rs_cal_0, $Arg3.NbVal, 2.6, 1., hum_tdc2_rs_sync_1)"
;
hum_tdc2_rs_sync_1:Category = "humidity";
float hum_rel_stat_aero_1(time);
hum_rel_stat_aero_1:units = "%";
hum_rel_stat_aero_1:FillValue = -9.e+33;
hum_rel_stat_aero_1:long_name = "Static rel. hum. from Relative humidity
averaged at 1 Hz";
hum_rel_stat_aero_1:standard_name = "relative_humidity";
hum_rel_stat_aero_1:long_name_fr = "Hum. rel. statique a partir de
Humidite relative moyenne a 1 Hz";
hum_rel_stat_aero_1:fct_origin = "Calc_Static_RH_From_Dynamic_RH_V1
(hum_rel_aero_1, tpr_aero_1, tpr_total_aero_1, hum_rel_stat_aero_1)";
hum_rel_stat_aero_1:Category = "humidity";
float hum_RapM_td_cr2_num_1(time);
hum_RapM_td_cr2_num_1:units = "gram/kg";
hum_RapM_td_cr2_num_1:FillValue = -9.e+33;
hum_RapM_td_cr2_num_1:long_name = "Water vapor mixing ratio from
CR2 mirror temperature interpolated on Sampling times (GPS synchronised clock";
hum_RapM_td_cr2_num_1:standard_name = "humidity_mixing_ratio";
hum_RapM_td_cr2_num_1:long_name_fr = "Rapport de melange a partir de
temperature miroir td cryo CR2 interpolle sur Temps des echantillons (horloge calee sur
reference GPS";
hum_RapM_td_cr2_num_1:fct_origin = "RapM_Tdf (hum_tdc2_rs_sync_1,
pre_s_av_1, hum_RapM_td_cr2_num_1)";
hum_RapM_td_cr2_num_1:Category = "humidity";
```

Version 1.2 EPATAN DATA ACQUISITION REPORT

```
float hum_RapM_aero_1(time) ;
    hum_RapM_aero_1:units = "gram/kg" ;
    hum_RapM_aero_1: FillValue = -9.e+33 ;
    hum_RapM_aero_1:long_name = "Water vapour mixing ratio from Static
rel. hum. from Relative humidity averaged at 1      Hz" ;
    hum_RapM_aero_1:standard_name = "humidity_mixing_ratio" ;
    hum_RapM_aero_1:long_name_fr = "Rapport de melange a partir de Hum.
rel. statique a partir de Humidite relative moyenne a 1      Hz" ;
    hum_RapM_aero_1:fct_origin = "RapM_Hu (hum_rel_stat_aero_1,
tpr_aero_1, pre_s_av_1, hum_RapM_aero_1)" ;
    hum_RapM_aero_1:Category = "humidity" ;
float vit_tasadc_cal_ms_1(time) ;
    vit_tasadc_cal_ms_1:units = "m/s" ;
    vit_tasadc_cal_ms_1: FillValue = -9.e+33 ;
    vit_tasadc_cal_ms_1:long_name = "True Air Speed from Air Data Computer
synchronised on Sampling times (GPS synchronised clock" ;
    vit_tasadc_cal_ms_1:standard_name = "platform_speed_wrt_air" ;
    vit_tasadc_cal_ms_1:long_name_fr = "Vitesse vraie air Air Data Computer
synchronise sur Temps des echantillons (horloge calee sur reference GPS" ;
    vit_tasadc_cal_ms_1:fct_origin = "Poly_1_ft (vit_tasadc_cal_1, 0.0, KtMs,
\"m/s\", $Arg1.name, $Arg1.english_name, vit_tasadc_cal_ms_1)" ;
    vit_tasadc_cal_ms_1:Category = "platform_dynamics" ;
float acc_gz_aipov_1(time) ;
    acc_gz_aipov_1:units = "meter-second^-2" ;
    acc_gz_aipov_1: FillValue = -9.e+33 ;
    acc_gz_aipov_1:long_name = "Z-axis aircraft acceleration AIRINS
synchronised on Sampling times (GPS synchronised clock" ;
    acc_gz_aipov_1:proposed_standard_name =
"platform_acceleration_along_z_axis" ;
    acc_gz_aipov_1:long_name_fr = "Acceleration axe Z avion AIRINS
synchronise sur Temps des echantillons (horloge calee sur reference GPS" ;
    acc_gz_aipov_1:fct_origin = "MoyEch_tps_impos (acc_gzaipov_cal_100,
rft_TIMEAIPOV_100, 1./2., 1./2., $Arg1.sample/2, rft_TIME_1, $Arg6.NbVal,
acc_gz_aipov_1)" ;
    acc_gz_aipov_1:Category = "platform_dynamics" ;
float nav_route_aipov_1(time) ;
    nav_route_aipov_1:units = "degree" ;
    nav_route_aipov_1: FillValue = -9.e+33 ;
    nav_route_aipov_1:long_name = "Track AIRINS sampled on the variable
named rft_TIME_100 averaged and sampled" ;
    nav_route_aipov_1:standard_name = "platform_course" ;
    nav_route_aipov_1:long_name_fr = "Route AIRINS echantillonne sur la
variable rft_TIME_100 moyenne et echantillonne" ;
    nav_route_aipov_1:fct_origin = "MoyEch_Angl_auto_unit
(nav_traipov_sync_100, 1./$Arg1.sample, -$Arg1.sample/(1*2), $Arg1.unit,
nav_route_aipov_1)" ;
    nav_route_aipov_1:Category = "navigation" ;
float vit_s_aipov_1(time) ;
    vit_s_aipov_1:units = "m/s" ;
```

Version 1.2 EPATAN DATA ACQUISITION REPORT

```
vit_s_aipov_1: FillValue = -9.e+33 ;
vit_s_aipov_1:long_name = "AIPOV ground speed" ;
vit_s_aipov_1:standard_name = "platform_speed_wrt_ground" ;
vit_s_aipov_1:long_name_fr = "Vitesse/sol AIPOV" ;
vit_s_aipov_1:fct_origin = "Module_2D_flt (vit_e_aipov_1, vit_n_aipov_1,
\"Vitesse/sol AIPOV\", \"AIPOV ground speed\", vit_s_aipov_1)\" ;
vit_s_aipov_1:Category = "platform_dynamics" ;
float nav_route_gps_1(time) ;
nav_route_gps_1:units = "degree" ;
nav_route_gps_1: FillValue = -9.e+33 ;
nav_route_gps_1:long_name = "Principal value of the arc tangent of GPS
East speed interpolated on Sampling times (GPS synchronised clock, with isolated peaks
removed / GPS north speed interpolated on Sampling times (GPS synchronised clock,
with isolated peaks removed" ;
nav_route_gps_1:standard_name = "platform_course" ;
nav_route_gps_1:long_name_fr = "Arctangente du rapport de vitesse GPS
selon l_axe Est interpolle sur Temps des echantillons (horloge calee sur reference GPS
sans pics isolés sur vitesse GPS selon l_axe Nord interpolle sur Temps des echantillons
(horloge calee sur reference GPS sans pics isolés" ;
nav_route_gps_1:fct_origin = "Atan2 (vit_e_gps_1, vit_n_gps_1, \"degree\",
nav_route_gps_1)\" ;
nav_route_gps_1:Category = "navigation" ;
float vit_s_gps_1(time) ;
vit_s_gps_1:units = "m/s" ;
vit_s_gps_1: FillValue = -9.e+33 ;
vit_s_gps_1:long_name = "GPS ground speed" ;
vit_s_gps_1:standard_name = "platform_speed_wrt_ground" ;
vit_s_gps_1:long_name_fr = "Vitesse/sol GPS" ;
vit_s_gps_1:fct_origin = "Module_2D_flt (vit_e_gps_1, vit_n_gps_1,
\"Vitesse/sol GPS\", \"GPS ground speed\", vit_s_gps_1)\" ;
vit_s_gps_1:Category = "platform_dynamics" ;
float vit_v_aipov_1(time) ;
vit_v_aipov_1:units = "m/s" ;
vit_v_aipov_1: FillValue = -9.e+33 ;
vit_v_aipov_1:long_name = "Vertical speed AIRINS synchronised on
Sampling times (GPS synchronised clock" ;
vit_v_aipov_1:proposed_standard_name =
"platform_vertical_velocity_wrt_ground" ;
vit_v_aipov_1:long_name_fr = "Vitesse verticale AIRINS synchronise sur
Temps des echantillons (horloge calee sur reference GPS" ;
vit_v_aipov_1:fct_origin = "MoyEch_tps_impos (vit_vvaipov_cal_100,
rft_TIMEAIPOV_100, 1./2., 1./2., $Arg1.sample/2, rft_TIME_1, $Arg6.NbVal,
vit_v_aipov_1)\" ;
vit_v_aipov_1:Category = "platform_dynamics" ;
float att_incid_c15hyb_pch_deg_1(time) ;
att_incid_c15hyb_pch_deg_1:units = "degree" ;
att_incid_c15hyb_pch_deg_1: FillValue = -9.e+33 ;
att_incid_c15hyb_pch_deg_1:long_name = "Angle of attack ()" ;
```

Version 1.2 EPATAN DATA ACQUISITION REPORT

```
att_incid_c15hyb_pch_deg_1:proposed_standard_name = "angle_of_attack"
;
att_incid_c15hyb_pch_deg_1:long_name_fr = "Incidence (hybride
dP_horiz/dP_ADC, coefs 2015)";
att_incid_c15hyb_pch_deg_1:fct_origin = "Poly_1_ft
(att_incid_c15hyb_pch_1, 0, RadDeg, \"degree\", $Arg1.name, $Arg1.english_name,
att_incid_c15hyb_pch_deg_1)";
att_incid_c15hyb_pch_deg_1:Category = "platform_dynamics";
float att_derap_e1hyb_pch_deg_1(time);
att_derap_e1hyb_pch_deg_1:units = "degree";
att_derap_e1hyb_pch_deg_1:FillValue = -9.e+33;
att_derap_e1hyb_pch_deg_1:long_name = "Sideslip angle ()";
att_derap_e1hyb_pch_deg_1:proposed_standard_name =
"angle_of_sideslip";
att_derap_e1hyb_pch_deg_1:long_name_fr = "Derapage (hybride
dP_horiz/dP_ADC)";
att_derap_e1hyb_pch_deg_1:fct_origin = "Poly_1_ft
(att_derap_e1hyb_pch_1, 0, RadDeg, \"degree\", $Arg1.name, $Arg1.english_name,
att_derap_e1hyb_pch_deg_1)";
att_derap_e1hyb_pch_deg_1:Category = "platform_dynamics";
float ven_e_aipovtaer_1(time);
ven_e_aipovtaer_1:units = "m/s";
ven_e_aipovtaer_1:FillValue = -9.e+33;
ven_e_aipovtaer_1:long_name = "Zonal wind component";
ven_e_aipovtaer_1:standard_name = "eastward_wind";
ven_e_aipovtaer_1:long_name_fr = "Composante zonale du vent";
ven_e_aipovtaer_1:fct_origin = "CalcVent_repgeo (11.0, vit_p_pavtaer_1,
att_incid_c2015_pch_val_1, att_derap_estim1_pch_val_1, vit_e_aipov_1, vit_n_aipov_1,
vit_v_aipov_1, vit_ry_aipov_rad_1, vit_rz_aipov_rad_1, att_tang_aipov_rad_1,
att_roul_aipov_rad_1, att_capgeo_aipov_rad_1, ven_e_aipovtaer_1, ven_n_aipovtaer_1,
ven_v_aipovtaer_1)";
ven_e_aipovtaer_1:Category = "wind";
float ven_n_aipovtaer_1(time);
ven_n_aipovtaer_1:units = "m/s";
ven_n_aipovtaer_1:FillValue = -9.e+33;
ven_n_aipovtaer_1:long_name = "Meridional wind component";
ven_n_aipovtaer_1:standard_name = "northward_wind";
ven_n_aipovtaer_1:long_name_fr = "Composante meridienne du vent";
ven_n_aipovtaer_1:fct_origin = "CalcVent_repgeo (11.0, vit_p_pavtaer_1,
att_incid_c2015_pch_val_1, att_derap_estim1_pch_val_1, vit_e_aipov_1, vit_n_aipov_1,
vit_v_aipov_1, vit_ry_aipov_rad_1, vit_rz_aipov_rad_1, att_tang_aipov_rad_1,
att_roul_aipov_rad_1, att_capgeo_aipov_rad_1, ven_e_aipovtaer_1, ven_n_aipovtaer_1,
ven_v_aipovtaer_1)";
ven_n_aipovtaer_1:Category = "wind";
float ven_v_aipovtaer_1(time);
ven_v_aipovtaer_1:units = "m/s";
ven_v_aipovtaer_1:FillValue = -9.e+33;
ven_v_aipovtaer_1:long_name = "Vertical wind component";
ven_v_aipovtaer_1:standard_name = "upward_air_velocity";
```

Version 1.2 EPATAN DATA ACQUISITION REPORT

```
ven_v_aipovtaer_1:long_name_fr = "Composante verticale du vent" ;
ven_v_aipovtaer_1:fct_origin = "CalcVent_repgeo (11.0, vit_p_pavtaer_1,
att_incid_c2015_pch_val_1, att_derap_estim1_pch_val_1, vit_e_aipov_1, vit_n_aipov_1,
vit_v_aipov_1, vit_ry_aipov_rad_1, vit_rz_aipov_rad_1, att_tang_aipov_rad_1,
att_roul_aipov_rad_1, att_capgeo_aipov_rad_1, ven_e_aipovtaer_1, ven_n_aipovtaer_1,
ven_v_aipovtaer_1)" ;
ven_v_aipovtaer_1:Category = "wind" ;
float ven_DD_aipovtaer_1(time) ;
ven_DD_aipovtaer_1:units = "degree" ;
ven_DD_aipovtaer_1: FillValue = -9.e+33 ;
ven_DD_aipovtaer_1:long_name = "Wind direction" ;
ven_DD_aipovtaer_1:standard_name = "wind_from_direction" ;
ven_DD_aipovtaer_1:long_name_fr = "Direction du vent" ;
ven_DD_aipovtaer_1:fct_origin = "UV2ddff (ven_e_aipovtaer_1,
ven_n_aipovtaer_1, ven_DD_aipovtaer_1, ven_FF_aipovtaer_1)" ;
ven_DD_aipovtaer_1:Category = "wind" ;
float ven_FF_aipovtaer_1(time) ;
ven_FF_aipovtaer_1:units = "m/s" ;
ven_FF_aipovtaer_1: FillValue = -9.e+33 ;
ven_FF_aipovtaer_1:long_name = "Wind speed" ;
ven_FF_aipovtaer_1:standard_name = "wind_speed" ;
ven_FF_aipovtaer_1:long_name_fr = "Vitesse du vent" ;
ven_FF_aipovtaer_1:fct_origin = "UV2ddff (ven_e_aipovtaer_1,
ven_n_aipovtaer_1, ven_DD_aipovtaer_1, ven_FF_aipovtaer_1)" ;
ven_FF_aipovtaer_1:Category = "wind" ;
float mic_msofreqice_rs_sync_1(time) ;
mic_msofreqice_rs_sync_1:units = "Hz" ;
mic_msofreqice_rs_sync_1: FillValue = -9.e+33 ;
mic_msofreqice_rs_sync_1:long_name = "MSO frequency of ice detector
synchronised on Sampling times (GPS synchronised clock" ;
mic_msofreqice_rs_sync_1:proposed_standard_name =
"frequency_of_the_magnetostrictive_oscillator" ;
mic_msofreqice_rs_sync_1:long_name_fr = "Frequence MSO du detecteur
de glace synchronise sur Temps des echantillons (horloge calee sur reference GPS" ;
mic_msofreqice_rs_sync_1:fct_origin = "MinEch_tps_impos
(mic_msofreqice_rs_cal_2, rft_TIME_NAI_1_CH0_2, 1./2., 1./2., $Arg1.sample/2,
rft_TIME_1, $Arg6.NbVal, mic_msofreqice_rs_sync_1)" ;
mic_msofreqice_rs_sync_1:Category = "microphysics" ;
float ray_tb_ce332_c1_1(time) ;
ray_tb_ce332_c1_1:units = "kelvin" ;
ray_tb_ce332_c1_1: FillValue = -9.e+33 ;
ray_tb_ce332_c1_1:long_name = "brightness temp. from first channel (12
µm) synchronised on Sampling times (GPS synchronised clock" ;
ray_tb_ce332_c1_1:standard_name = "brightness_temperature" ;
ray_tb_ce332_c1_1:long_name_fr = "tempé de brillance dans le canal 1 (12
µm) synchronise sur Temps des echantillons (horloge calee sur reference GPS" ;
ray_tb_ce332_c1_1:fct_origin = "MoyEch_tps_impos (ray_tb_ce332_c1_6,
rft_time_ce332_6, 0.5, 0.5, 3, rft_TIME_1, $Arg6.NbVal, ray_tb_ce332_c1_1)" ;
ray_tb_ce332_c1_1:Category = "radiation" ;
```

Version 1.2 EPATAN DATA ACQUISITION REPORT

```
float ray_tb_ce332_c2_1(time) ;
    ray_tb_ce332_c2_1:units = "kelvin" ;
    ray_tb_ce332_c2_1:FillValue = -9.e+33 ;
    ray_tb_ce332_c2_1:long_name = "brightness temp. from second channel
(10.6 µm) synchronised on Sampling times (GPS synchronised clock" ;
    ray_tb_ce332_c2_1:standard_name = "brightness_temperature" ;
    ray_tb_ce332_c2_1:long_name_fr = "tempé de brillance dans le canal 2
(10.6 µm) synchronise sur Temps des echantillons (horloge calee sur reference GPS" ;
    ray_tb_ce332_c2_1:fct_origin = "MoyEch_tps_impos (ray_tb_ce332_c2_6,
rft_time_ce332_6, 0.5, 0.5, 3, rft_TIME_1, $Arg6.NbVal, ray_tb_ce332_c2_1)" ;
    ray_tb_ce332_c2_1:Category = "radiation" ;
float ray_tb_ce332_c3_1(time) ;
    ray_tb_ce332_c3_1:units = "kelvin" ;
    ray_tb_ce332_c3_1:FillValue = -9.e+33 ;
    ray_tb_ce332_c3_1:long_name = "brightness temp. from third channel (8.7
µm) synchronised on Sampling times (GPS synchronised clock" ;
    ray_tb_ce332_c3_1:standard_name = "brightness_temperature" ;
    ray_tb_ce332_c3_1:long_name_fr = "tempé de brillance dans le canal 3 (8.7
µm) synchronise sur Temps des echantillons (horloge calee sur reference GPS" ;
    ray_tb_ce332_c3_1:fct_origin = "MoyEch_tps_impos (ray_tb_ce332_c3_6,
rft_time_ce332_6, 0.5, 0.5, 3, rft_TIME_1, $Arg6.NbVal, ray_tb_ce332_c3_1)" ;
    ray_tb_ce332_c3_1:Category = "radiation" ;

// global attributes:
:Conventions = "CF-1.0" ;
:institution = "SAFIRE : Service des Avions Francais Instrumentes pour la
Recherche en Environnement" ;
:history = "Final data processing by CNRM-GAME(Meteo-France/CNRS)
with AIDA;Conversion to netCDF with vec2df.R by piguet on 2017-08-02 14:49:49" ;
:project = "EPATAN" ;
:references = "" ;
:comments = "" ;
:title = "falconcore measurements for the EPATAN campaign" ;
:source = "safire-fa20 airborne observation" ;
:geospatial_lat_min = 63.5687103271484 ;
:geospatial_lat_max = 65.2085571289062 ;
:geospatial_lon_min = -43.5517730712891 ;
:geospatial_lon_max = -22.3994064331055 ;
}
```

RASTA L2 single antenna product

Data format and variables for the L2 RASTA product

File name:

NAWDEX_YYYYMMDD_Fflightnumber_RASTA_2B_04_1_new_system_antenna.nc

version 4.4

“new_system_” pulse pair technique and use the new acquisition system

Version 1.2 EPATAN DATA ACQUISITION REPORT

Available for each antenna, “Nadir”, “Down-Backward”, “Down-Transverse” (variable names will change in the file depending of the antenna)

Short description:

This file contains aircraft measurement (P, T, H, wind and position) and radar measurements (Z, V and flag). Raw Doppler velocity and reflectivity are also available. Radar reflectivity is calibrated and range corrected. Doppler velocity is corrected from aircraft motion and folding. Position (altitude, longitude, latitude) of each radar gate is available.

File size and format: ~100Mo for one flight

Time resolution depends on the number of antennas used. For example, 3 antennas x 0.25 s leads to a 0.75 s time resolution.

range = 250

Name	dimension	units	comments
	s		
calibration_value	1	dBZ	Calibration value used for Z
azimuth_relative	1	degrees	Azimuth angle of the antenna beams with respect to the right wing (positive counter clockwise)
elevation_relative	1	degrees	Elevation angle of the antenna beams with respect to the aircraft horizontal plane (positive when above aircraft)
time	time	hour	Decimal hours UTC since midnight
range	range	km	Range from the radar to the centre of each range gate
latitude	time	degrees north	Latitude of the aircraft, from Global Positioning System (GPS)
longitude	time	degrees east	Longitude of the aircraft, from Global Positioning System (GPS)
altitude	time	km	Height of the aircraft above geoid, from Global Positioning System (GPS)
altitude_ins	time	km	Height of the aircraft above geoid, from Inertial Navigation System (INS)
pitch	time	degrees	Aircraft pitch angle, From Inertial Navigation System (INS): positive when the aircraft nose is up
roll	time	degrees	Aircraft roll angle, from Inertial Navigation System (INS): positive when the starboard wing is down
drift	time	degrees	Aircraft drift angle, from Inertial Navigation System (INS): positive if track is more clockwise than heading

Version 1.2 EPATAN DATA ACQUISITION REPORT

heading	time	degrees	Aircraft heading angle, from Inertial Navigation System (INS): relative to geographical North, positive clockwise
track	time	degrees	Aircraft track angle, from Inertial Navigation System (INS): relative to geographical North, positive clockwise, track = heading + drift
aircraft_vh	time	m s-1	Aircraft horizontal speed, from Global Positioning System (GPS)
aircraft_vz	time	m s-1	Aircraft vertical speed, from Global Positioning System (GPS)
aircraft_vh_ins	time	m s-1	Aircraft horizontal speed (INS), from Inertial Navigation System (INS)
pressure	time	hPa	Static air pressure at flight level
temperature	time	deg C	Static air temperature at flight level
relative_humidity	time	percent	Relative humidity at flight level
u_wind	time	m s-1	Eastward Wind Component (positive when westerly)
v_wind	time	m s-1	Northward Wind Component (positive when southerly)
w_wind	time	m s-1	Vertical Wind Component (positive when upward)
u_wind_raw	time	m s-1	Raw Eastward Wind Component (positive when westerly)
v_wind_raw	time	m s-1	Raw Northward Wind Component (positive when southerly)
w_wind_raw	time	m s-1	Raw Vertical Wind Component (positive when upward)
eastward_wind	time	m s-1	Eastward Wind Component (positive when westerly),
northward_wind	time	m s-1	Northward Wind Component (positive when southerly)
proj_insitu_wind_speed	time	m s-1	Projected in-situ wind speed along the radial
azimuth_east_Nadir	time	degrees	Azimuth angle of the Nadir antenna beams with respect to the horizontal plane (positive when above aircraft)
elevation_hor_Nadir	time	degrees	Elevation angle of the Nadir antenna beams with respect to the horizontal plane (positive when above aircraft)
Data_longitude	time, range	degrees	Longitude of the data, obtained with the equation: $\text{Data_longitude} = \text{Longitude} + (\text{Range} * \cos(\text{Azimuth}) * \cos(\text{Elevation})) * 360. / (40000. * \cos(\text{Latitude}))$
Data_latitude	time, range	degrees	Latitude of the data, obtained with the equation: $\text{Data_latitude} = \text{Latitude} + (\text{Range} * \sin(\text{Azimuth}) * \cos(\text{Elevation})) * 360. / 40000.$

Version 1.2 EPATAN DATA ACQUISITION REPORT

Data_altitude	time, range	km	Altitude of the data, obtained with the equation: $Data_altitude = Altitude + Range * \sin(Elevation)$
Zraw_Nadir	time, range	dB	Raw radar reflectivity factor from the Nadir antenna, produced using the Pulse-Pair Processing. Not Range-corrected and not calibrated
vraw_Nadir	time, range	m s-1	Raw Doppler velocity from the Nadir antenna (positive when target moves away from the radar) - not corrected for aircraft motion and folding, produced using the Pulse-Pair Processing. Counted positive when target moves away from radar
Z_Nadir	time, range	dBZ	Radar reflectivity factor from the Nadir antenna, produced using the Pulse-Pair Processing. Range-corrected and calibrated but not interpolated (interpolated if zenith antenna available)
v_Nadir	time, range	m s-1	Doppler velocity from the Nadir antenna (positive when target moves away from the radar) - not corrected for aircraft motion and folding, produced using the Pulse-Pair Processing. Counted positive when target moves away from radar
Z_Nadir_processed	time, range	dBZ	Radar reflectivity factor from the Nadir antenna, produced using the Pulse-Pair Processing. Range-corrected and calibrated
v_Nadir_corr_ac	time, range	m s-1	Doppler velocity from the Nadir antenna (positive when target moves away from the radar) - corrected for aircraft motion, produced using the Pulse-Pair Processing. Counted positive when target moves away from radar
v_Nadir_corr_ac_fold	time, range	m s-1	Doppler velocity from the Nadir antenna (positive when target moves away from the radar) - corrected for aircraft motion and first folding correction, produced using the Pulse-Pair Processing. Counted positive when target moves away from radar
v_Nadir_processed	time, range	m s-1	Doppler velocity from the Nadir antenna (positive when target moves away from the radar) - corrected for aircraft motion and folding, produced using the Pulse-Pair Processing. Counted positive when target moves away from radar
v_Nadir_processed_corr	time, range	m s-1	Doppler velocity from the Nadir antenna (positive when target moves away from the radar) - corrected for aircraft motion and folding, produced using the Pulse-Pair

Version 1.2 EPATAN DATA ACQUISITION REPORT

			Processing. Counted positive when target moves away from radar
Flag	time, range	none	Flag - Data description, 0 if no cloud; 1 if cloud; 2 Z is corrected; 3 if ground echo; 4 if ghost ground echo; 5 Z is interpolated
leg	time	none	Leg identifier, each leg corresponds to a straight line
leg_nb_profiles	time	none	Number of profiles per leg, each leg corresponds to a straight line

global attributes

Description = "95GHz Cloud Radar (RASTA) - L2B"
Airport_latitude = 63.9986277778
Airport_longitude = -22.5663472222
Antenna = "Nadir looking antenna diameters: 0.45m"
Frequency = "95.04 GHz"
Peak_power = "1.8 kW"
Pulse_width = "0.4 us"
Ambiguous_distance = "15 km"
Pulse_repetition_frequency = "PRF=25kHz"
Beamwidth = "0.7 degrees"
Range_resolution = "60 m"
Reflectivity = "not corrected for attenuation, calibrated following Li & al (2005,J.Atmos.Oceanic.Tech.)"
Doppler_Velocity = "corrected for aircraft motion and folding"
Real_time_processing = "Pulse Pair Technique"
Experiment = "NAWDEX EPATAN (29/09/16-16/10/12), Airport: Keflavik"
Flight = "5"
Day = "20161001"
contact = "contact email: julien.delanoe@latmos.ipsl.fr"
created = "2017-02-08"

Note: Data which are coloured in grey are for internal use only

RASTA wind product

Description of the file product:

```
netcdf NAWDEX_20161002_F6_RASTA_WIND_hr_04_4_new_system {  
dimensions:
```

```
    range = 250 ;  
    parameter = 1 ;  
    time = UNLIMITED ; // (12962 currently)  
    height = 250 ;
```

```
variables:
```

```
    float range(range) ;  
        range:units = "km" ;  
        range:long_name = "Range from the radar to the centre of each range gate"
```

```
;
```

Version 1.2 EPATAN DATA ACQUISITION REPORT

```
float time(time) ;
    time:units = "hours UTC" ;
    time:long_name = "Decimal hours UTC since midnight" ;
    time:missing_value = -999.f ;
float latitude(time) ;
    latitude:units = "degrees north" ;
    latitude:long_name = "Latitude of the aircraft" ;
    latitude:missing_value = -999.f ;
    latitude:comments = "from Global Positioning System (GPS)" ;
float longitude(time) ;
    longitude:units = "degrees east" ;
    longitude:long_name = "Longitude of the aircraft" ;
    longitude:missing_value = -999.f ;
    longitude:comments = "from Global Positioning System (GPS)" ;
float altitude(time) ;
    altitude:units = "km" ;
    altitude:long_name = "Height of the aircraft above geoid" ;
    altitude:missing_value = -999.f ;
    altitude:comments = "from Global Positioning System (GPS)" ;
float pitch(time) ;
    pitch:units = "degrees" ;
    pitch:long_name = "Aircraft pitch angle" ;
    pitch:missing_value = -999.f ;
    pitch:comments = "From Inertial Navigation System (INS): positive when
the aircraft nose is up" ;
float roll(time) ;
    roll:units = "degrees" ;
    roll:long_name = "Aircraft roll angle" ;
    roll:missing_value = -999.f ;
    roll:comments = "From Inertial Navigation System (INS): positive when
the starboard wing is down" ;
float drift(time) ;
    drift:units = "degrees" ;
    drift:long_name = "Aircraft drift angle" ;
    drift:missing_value = -999.f ;
    drift:comments = "From Inertial Navigation System (INS): positive if track
is more clockwise than heading" ;
float heading(time) ;
    heading:units = "degrees" ;
    heading:long_name = "Aircraft heading angle" ;
    heading:missing_value = -999.f ;
    heading:comments = "From Inertial Navigation System (INS): relative to
geographical North, positive clockwise" ;
float track(time) ;
    track:units = "degrees" ;
    track:long_name = "Aircraft track angle" ;
    track:missing_value = -999.f ;
    track:comments = "From Inertial Navigation System (INS): relative to
geographical North, positive clockwise, track = heading + drift" ;
```

Version 1.2 EPATAN DATA ACQUISITION REPORT

```
float aircraft_vh(time) ;
    aircraft_vh:units = "m s-1" ;
    aircraft_vh:long_name = "Aircraft horizontal speed" ;
    aircraft_vh:missing_value = -999.f ;
    aircraft_vh:comments = "from Global Positioning System (GPS)" ;
float aircraft_vz(time) ;
    aircraft_vz:units = "m s-1" ;
    aircraft_vz:long_name = "Aircraft vertical speed" ;
    aircraft_vz:missing_value = -999.f ;
    aircraft_vz:comments = "from Global Positioning System (GPS)" ;
float pressure(time) ;
    pressure:units = "hPa" ;
    pressure:long_name = "Static air pressure" ;
    pressure:missing_value = -999.f ;
    pressure:comments = "Pressure in hPa at flight level" ;
float temperature(time) ;
    temperature:units = "deg C" ;
    temperature:long_name = "Static air temperature" ;
    temperature:missing_value = -999.f ;
    temperature:comments = "Temperature in deg C at flight level" ;
float relative_humidity(time) ;
    relative_humidity:units = "%" ;
    relative_humidity:long_name = "Relative humidity" ;
    relative_humidity:missing_value = -999.f ;
    relative_humidity:comments = "Relative Humidity in % at flight level" ;
float eastward_wind(time) ;
    eastward_wind:units = "m s-1" ;
    eastward_wind:long_name = "In-situ Eastward Wind Component (positive
when westerly)" ;
    eastward_wind:missing_value = -999.f ;
float northward_wind(time) ;
    northward_wind:units = "m s-1" ;
    northward_wind:long_name = "In-situ Northward Wind Component
(positive when southerly)" ;
    northward_wind:missing_value = -999.f ;
float u_wind(time) ;
    u_wind:units = "m s-1" ;
    u_wind:long_name = "Along track Wind Component" ;
    u_wind:missing_value = -999.f ;
float v_wind(time) ;
    v_wind:units = "m s-1" ;
    v_wind:long_name = "Cross track Wind Component" ;
    v_wind:missing_value = -999.f ;
float w_wind(time) ;
    w_wind:units = "m s-1" ;
    w_wind:long_name = "Vertical Wind Component (positive when upward)"
;
    w_wind:missing_value = -999.f ;
float u_wind_fuselage(time) ;
```

Version 1.2 EPATAN DATA ACQUISITION REPORT

```
u_wind_fuselage:units = "m s-1" ;
u_wind_fuselage:long_name = "Along fuselage Wind Component" ;
u_wind_fuselage:missing_value = -999.f ;
float v_wind_fuselage(time) ;
v_wind_fuselage:units = "m s-1" ;
v_wind_fuselage:long_name = "Cross fuselage Wind Component" ;
v_wind_fuselage:missing_value = -999.f ;
float proj_insitu_wind_speed(time) ;
proj_insitu_wind_speed:units = "m s-1" ;
proj_insitu_wind_speed:long_name = "Projected in-situ wind speed along
the radial" ;
proj_insitu_wind_speed:missing_value = -999.f ;
byte land_water_flag(time) ;
land_water_flag:units = "none" ;
land_water_flag:long_name = "0 means Land, 1 means Water" ;
land_water_flag:missing_value = -9b ;
land_water_flag:comments = "Derived from Very High Resolution land/sea
tag map with distance from land, Naval Oceanographic Office (NAVOCEANO) 2007-06-
28" ;
float height_2D(time, height) ;
height_2D:units = "km" ;
height_2D:long_name = "Altitude of the centre of each range gate" ;
float Z_vertical(time, height) ;
Z_vertical:units = "dBZ" ;
Z_vertical:long_name = "Radar reflectivity factor from Nadir and Zenith
antennas" ;
Z_vertical:missing_value = -999.f ;
Z_vertical:fill_value = -999. ;
Z_vertical:comments = "Produced using the Pulse-Pair Processing. Range-
corrected and calibrated" ;
float Z_L1_vertical(time, height) ;
Z_L1_vertical:units = "dBZ" ;
Z_L1_vertical:long_name = "L1 Radar reflectivity factor from Nadir and
Zenith antennas" ;
Z_L1_vertical:missing_value = -999.f ;
Z_L1_vertical:fill_value = -999. ;
Z_L1_vertical:comments = "Produced using the Pulse-Pair Processing.
Range-corrected and calibrated" ;
float V_vertical(time, height) ;
V_vertical:units = "m s-1" ;
V_vertical:long_name = "Doppler velocity from Nadir and Zenith antennas
(positive when target moves away from the radar) - not corrected for aircraft motion
and folding" ;
V_vertical:missing_value = -999.f ;
V_vertical:fill_value = -999. ;
V_vertical:comments = "Produced using the Pulse-Pair Processing.
Counted positive when target moves away from radar" ;
float R_vertical(time, height) ;
R_vertical:units = "m" ;
```

Version 1.2 EPATAN DATA ACQUISITION REPORT

```
R_vertical:long_name = "Range from aircraft (Nadir and Zenith)" ;
R_vertical:missing_value = -999.f ;
R_vertical:fill_value = -999. ;
float latitude_vertical(time, height) ;
    latitude_vertical:units = "degrees north" ;
    latitude_vertical:long_name = "Latitude of nadir and zenith data" ;
    latitude_vertical:missing_value = -999.f ;
    latitude_vertical:comments = "from Global Positioning System (GPS)" ;
float longitude_vertical(time, height) ;
    longitude_vertical:units = "degrees east" ;
    longitude_vertical:long_name = "Longitude of nadir and zenith data" ;
    longitude_vertical:missing_value = -999.f ;
    longitude_vertical:comments = "from Global Positioning System (GPS)" ;
float azimuth_east_vertical(time, height) ;
    azimuth_east_vertical:units = "degrees" ;
    azimuth_east_vertical:long_name = "Azimuth angle of Nadir and Zenith
antenna beams with respect to the horizontal plane (positive when above aircraft)" ;
    azimuth_east_vertical:missing_value = -999.f ;
float elevation_hor_vertical(time, height) ;
    elevation_hor_vertical:units = "degrees" ;
    elevation_hor_vertical:long_name = "Elevation angle of Nadir and Zenith
antenna beams with respect to the horizontal plane (positive when above aircraft)" ;
    elevation_hor_vertical:missing_value = -999.f ;
float Z_backward(time, height) ;
    Z_backward:units = "dBZ" ;
    Z_backward:long_name = "Radar reflectivity factor from Down and and Up
backward antennas" ;
    Z_backward:missing_value = -999.f ;
    Z_backward:fill_value = -999. ;
    Z_backward:comments = "Produced using the Pulse-Pair Processing.
Range-corrected and calibrated" ;
float Z_L1_backward(time, height) ;
    Z_L1_backward:units = "dBZ" ;
    Z_L1_backward:long_name = "L1 Radar reflectivity factor from Down and
and Up backward antennas" ;
    Z_L1_backward:missing_value = -999.f ;
    Z_L1_backward:fill_value = -999. ;
    Z_L1_backward:comments = "Produced using the Pulse-Pair Processing.
Range-corrected and calibrated" ;
float V_backward(time, height) ;
    V_backward:units = "m s-1" ;
    V_backward:long_name = "Doppler velocity from Down and and Up
backward antennas (positive when target moves away from the radar) - not corrected
for aircraft motion and folding" ;
    V_backward:missing_value = -999.f ;
    V_backward:fill_value = -999. ;
    V_backward:comments = "Produced using the Pulse-Pair Processing.
Counted positive when target moves away from radar" ;
float R_backward(time, height) ;
```

Version 1.2 EPATAN DATA ACQUISITION REPORT

```
R_backward:units = "m" ;
R_backward:long_name = "Range from aircraft (Down and and Up
backward)" ;
R_backward:missing_value = -999.f ;
R_backward:fill_value = -999. ;
float latitude_backward(time, height) ;
latitude_backward:units = "degrees north" ;
latitude_backward:long_name = "Latitude of Down and and Up backward
data" ;
latitude_backward:missing_value = -999.f ;
latitude_backward:comments = "from Global Positioning System (GPS)" ;
float longitude_backward(time, height) ;
longitude_backward:units = "degrees east" ;
longitude_backward:long_name = "Longitude of Down and and Up
backward data" ;
longitude_backward:missing_value = -999.f ;
longitude_backward:comments = "from Global Positioning System (GPS)" ;
float azimuth_east_backward(time, height) ;
azimuth_east_backward:units = "degrees" ;
azimuth_east_backward:long_name = "Azimuth angle of Down and and Up
backward antenna beams with respect to the horizontal plane (positive when above
aircraft)" ;
azimuth_east_backward:missing_value = -999.f ;
float elevation_hor_backward(time, height) ;
elevation_hor_backward:units = "degrees" ;
elevation_hor_backward:long_name = "Elevation angle of Down and and
Up backward antenna beams with respect to the horizontal plane (positive when above
aircraft)" ;
elevation_hor_backward:missing_value = -999.f ;
float Z_transverse(time, height) ;
Z_transverse:units = "dBZ" ;
Z_transverse:long_name = "Radar reflectivity factor from Down and and
Up transverse antennas" ;
Z_transverse:missing_value = -999.f ;
Z_transverse:fill_value = -999. ;
Z_transverse:comments = "Produced using the Pulse-Pair Processing.
Range-corrected and calibrated" ;
float Z_L1_transverse(time, height) ;
Z_L1_transverse:units = "dBZ" ;
Z_L1_transverse:long_name = "L1 Radar reflectivity factor from Down and
and Up transverse antennas" ;
Z_L1_transverse:missing_value = -999.f ;
Z_L1_transverse:fill_value = -999. ;
Z_L1_transverse:comments = "Produced using the Pulse-Pair Processing.
Range-corrected and calibrated" ;
float V_transverse(time, height) ;
V_transverse:units = "m s-1" ;
```

Version 1.2 EPATAN DATA ACQUISITION REPORT

```
V_transverse:long_name = "Doppler velocity from Down and and Up
transverse antennas (positive when target moves away from the radar) - not corrected
for aircraft motion and folding" ;
V_transverse:missing_value = -999.f ;
V_transverse:fill_value = -999. ;
V_transverse:comments = "Produced using the Pulse-Pair Processing.
Counted positive when target moves away from radar" ;
float R_transverse(time, height) ;
R_transverse:units = "m" ;
R_transverse:long_name = "Range from aircraft (Down and and Up
transverse)" ;
R_transverse:missing_value = -999.f ;
R_transverse:fill_value = -999. ;
float latitude_transverse(time, height) ;
latitude_transverse:units = "degrees north" ;
latitude_transverse:long_name = "Latitude of Down and and Up transverse
data" ;
latitude_transverse:missing_value = -999.f ;
latitude_transverse:comments = "from Global Positioning System (GPS)" ;
float longitude_transverse(time, height) ;
longitude_transverse:units = "degrees east" ;
longitude_transverse:long_name = "Longitude of Down and and Up
transverse data" ;
longitude_transverse:missing_value = -999.f ;
longitude_transverse:comments = "from Global Positioning System (GPS)"
;
float azimuth_east_transverse(time, height) ;
azimuth_east_transverse:units = "degrees" ;
azimuth_east_transverse:long_name = "Azimuth angle of Down and and Up
transverse antenna beams with respect to the horizontal plane (positive when above
aircraft)" ;
azimuth_east_transverse:missing_value = -999.f ;
float elevation_hor_transverse(time, height) ;
elevation_hor_transverse:units = "degrees" ;
elevation_hor_transverse:long_name = "Elevation angle of Down and and
Up transverse antenna beams with respect to the horizontal plane (positive when above
aircraft)" ;
elevation_hor_transverse:missing_value = -999.f ;
float distance_vertical_backward(time, height) ;
distance_vertical_backward:units = "km" ;
distance_vertical_backward:long_name = "Distance between vertical and
backward gates" ;
distance_vertical_backward:missing_value = -999.f ;
distance_vertical_backward:fill_value = -999. ;
float distance_vertical_tranverse(time, height) ;
distance_vertical_tranverse:units = "km" ;
distance_vertical_tranverse:long_name = "Distance between vertical and
transverse gates" ;
distance_vertical_tranverse:missing_value = -999.f ;
```

Version 1.2 EPATAN DATA ACQUISITION REPORT

```
distance_vertical_tranverse:fill_value = -999. ;
float Z(time, height) ;
  Z:units = "dBZ" ;
  Z:long_name = "Radar reflectivity" ;
  Z:missing_value = -999.f ;
  Z:fill_value = -999. ;
  Z:comments = "Produced using the Pulse-Pair Processing. Range-corrected
and calibrated" ;
float Vx(time, height) ;
  Vx:units = "m s-1" ;
  Vx:long_name = "Vx, Horizontal component of the retrieved 3D wind" ;
  Vx:missing_value = -999.f ;
  Vx:fill_value = -999. ;
  Vx:comments = "The Vx component is along the aircraft fuselage, positive
towards the aircraft nose" ;
float Vy(time, height) ;
  Vy:units = "m s-1" ;
  Vy:long_name = "Vy, Horizontal component of the retrieved 3D wind" ;
  Vy:missing_value = -999.f ;
  Vy:fill_value = -999. ;
  Vy:comments = "The Vy component is perpendicular the aircraft fuselage,
positive towards the left aircraft wing" ;
float Vz(time, height) ;
  Vz:units = "m s-1" ;
  Vz:long_name = "Vz, Vertical component of the retrieved 3D wind" ;
  Vz:missing_value = -999.f ;
  Vz:fill_value = -999. ;
  Vz:comments = "Vz, positive upward" ;
float VE(time, height) ;
  VE:units = "m s-1" ;
  VE:long_name = "VE, Eastward Wind component of the retrieved 3D wind"
;
  VE:missing_value = -999.f ;
  VE:fill_value = -999. ;
float VN(time, height) ;
  VN:units = "m s-1" ;
  VN:long_name = "VN, Northward Wind component of the retrieved 3D
wind" ;
  VN:missing_value = -999.f ;
  VN:fill_value = -999. ;
float wind_direction(time, height) ;
  wind_direction:units = "degree" ;
  wind_direction:long_name = "Direction of the retrieved 3D wind" ;
  wind_direction:missing_value = -999.f ;
  wind_direction:fill_value = -999. ;
float wind_speed(time, height) ;
  wind_speed:units = "m s-1" ;
  wind_speed:long_name = "Speed of the retrieved 3D wind" ;
  wind_speed:missing_value = -999.f ;
```

Version 1.2 EPATAN DATA ACQUISITION REPORT

```
wind_speed:fill_value = -999. ;
byte Mask_Vx(time, height) ;
    Mask_Vx:units = "none" ;
    Mask_Vx:long_name = "Mask for the Vx component of the wind" ;
    Mask_Vx:missing_value = -9b ;
    Mask_Vx:fill_value = -9b ;
    Mask_Vx:comments = "1: good confidence /2: should not be used" ;
byte Mask_Vy(time, height) ;
    Mask_Vy:units = "none" ;
    Mask_Vy:long_name = "Mask for the Vy component of the wind" ;
    Mask_Vy:missing_value = -9b ;
    Mask_Vy:fill_value = -9b ;
    Mask_Vy:comments = "1: good confidence /2: should not be used" ;
byte Mask_Vz(time, height) ;
    Mask_Vz:units = "none" ;
    Mask_Vz:long_name = "Mask for the Vz component of the wind" ;
    Mask_Vz:missing_value = -9b ;
    Mask_Vz:fill_value = -9b ;
    Mask_Vz:comments = "1: good confidence /2: should not be used /3: could
be used but carefully" ;
float Vx_error(time, height) ;
    Vx_error:units = "m s-1" ;
    Vx_error:long_name = "Error in Vx, Horizontal component of the retrieved
3D wind" ;
    Vx_error:missing_value = -999.f ;
    Vx_error:fill_value = -999. ;
float Vy_error(time, height) ;
    Vy_error:units = "m s-1" ;
    Vy_error:long_name = "Error in Vy, Horizontal component of the retrieved
3D wind" ;
    Vy_error:missing_value = -999.f ;
    Vy_error:fill_value = -999. ;
float Vz_error(time, height) ;
    Vz_error:units = "m s-1" ;
    Vz_error:long_name = "Error in Vz, Vertical component of the retrieved 3D
wind" ;
    Vz_error:missing_value = -999.f ;
    Vz_error:fill_value = -999. ;
float Temperature_field_ERAI(time, height) ;
    Temperature_field_ERAI:units = "deg C" ;
    Temperature_field_ERAI:long_name = "Air temperature ERAI" ;
    Temperature_field_ERAI:missing_value = -999.f ;
    Temperature_field_ERAI:comments = "Averaged temperature ERAI" ;
float Pressure_field_ERAI(time, height) ;
    Pressure_field_ERAI:units = "hPa" ;
    Pressure_field_ERAI:long_name = "Air pressure field ERAI" ;
    Pressure_field_ERAI:missing_value = -999.f ;
    Pressure_field_ERAI:comments = "Averaged pressure ERAI" ;
float RH_field_ERAI(time, height) ;
```

Version 1.2 EPATAN DATA ACQUISITION REPORT

```
RH_field_ERAI:units = "percent" ;
RH_field_ERAI:long_name = "Relative humidity ERAI" ;
RH_field_ERAI:missing_value = -999.f ;
RH_field_ERAI:comments = "Relative humidity ERAI" ;
float Temperature_field(time, height) ;
  Temperature_field:units = "deg C" ;
  Temperature_field:long_name = "Air temperature" ;
  Temperature_field:missing_value = -999.f ;
  Temperature_field:comments = "Averaged temperature" ;
float Pressure_field(time, height) ;
  Pressure_field:units = "hPa" ;
  Pressure_field:long_name = "Air pressure field" ;
  Pressure_field:missing_value = -999.f ;
  Pressure_field:comments = "Averaged pressure" ;
float RH_field(time, height) ;
  RH_field:units = "percent" ;
  RH_field:long_name = "Relative humidity" ;
  RH_field:missing_value = -999.f ;
  RH_field:comments = "Relative humidity" ;
byte Mask_domain(time, height) ;
  Mask_domain:units = "none" ;
  Mask_domain:long_name = "Domain Mask" ;
  Mask_domain:missing_value = -9b ;
  Mask_domain:fill_value = -9b ;
  Mask_domain:comments = "This mask identifies the valid data above and
below the aircraft (1:down/2:down and nadir only/3:up/4:up but zenith only)" ;
byte convective_index(time) ;
  convective_index:units = "none" ;
  convective_index:long_name = "Convective index" ;
  convective_index:missing_value = -9b ;
  convective_index:comments = "Convective index
(0:stratiform/1:convective)" ;
byte Mask_wind(time, height) ;
  Mask_wind:units = "none" ;
  Mask_wind:long_name = "Wind Mask" ;
  Mask_wind:missing_value = -9b ;
  Mask_wind:fill_value = -9b ;
  Mask_wind:comments = "This mask identifies areas where wind retrieval
is expected to be bad, good confidence when abs(roll) < 10 deg. (1: confident /2: less
confident upper domain /3: less confident lower domain)" ;
byte attenuation_phase_flag(time, height) ;
  attenuation_phase_flag:units = "none" ;
  attenuation_phase_flag:long_name = "Attenuation and phase flag" ;
  attenuation_phase_flag:missing_value = -9b ;
  attenuation_phase_flag:fill_value = -9b ;
  attenuation_phase_flag:comments = "0: no cloud / 1: ice / 2: rain / 3: ice
but likely attenuated / 4: ground / 5: ghost ground / 6: interpolated" ;
float RainRate(time, height) ;
  RainRate:units = "mm/h" ;
```

Version 1.2 EPATAN DATA ACQUISITION REPORT

```
RainRate:long_name = "Rain rate" ;
RainRate:missing_value = -999.f ;
RainRate:fill_value = -999. ;
RainRate:comments = "Similar to CloudSat basic retrieval using
attenuation below the melting layer - Matrosov et al 2007" ;
float Gaseous_twowayatt(time, height) ;
Gaseous_twowayatt:units = "dB" ;
Gaseous_twowayatt:long_name = "Gaseous two way attenuation" ;
Gaseous_twowayatt:missing_value = -999.f ;
Gaseous_twowayatt:fill_value = -999. ;
Gaseous_twowayatt:comments = "From Liebe at 95GHz" ;
float Gaseous_twowayatt_ERAI(time, height) ;
Gaseous_twowayatt_ERAI:units = "dB" ;
Gaseous_twowayatt_ERAI:long_name = "Gaseous two way attenuation" ;
Gaseous_twowayatt_ERAI:missing_value = -999.f ;
Gaseous_twowayatt_ERAI:fill_value = -999. ;
Gaseous_twowayatt_ERAI:comments = "From Liebe at 95GHz and
computed from ERAI-ECMWF" ;

// global attributes:
:Description = "95GHz Cloud Radar (RASTA) - Wind DATA" ;
:Airport_latitude = 63.9986277777778 ;
:Airport_longitude = -22.5663472222222 ;
:Frequency = "95.04 GHz" ;
:Peak_power = "1.8 kW" ;
:Pulse_width = "0.4 us" ;
:Ambiguous_distance = "15 km" ;
:Pulse_repetition_frequency = "PRF=25kHz" ;
:Beamwidth = "0.7 degrees - downward antennas" ;
:Range_resolution = "60 m" ;
:Reflectivity = "not corrected for attenuation, calibrated following Li & al
(2005,J.Atmos.Oceanic.Tech.)" ;
:Doppler_Velocity = "corrected for aircraft motion and folding" ;
:Real_time_processing = "Pulse Pair Technique" ;
:Experiment = "NAWDEX EPATAN (29/09/16-16/10/12), Airport:
Keflavik" ;
:Flight = "6" ;
:Day = "20161002" ;
:contact = "contact email: julien.delanoe@latmos.ipsl.fr" ;
:created = "2018-01-28" ;
:data_policy = "If you intend to use these data for any communication or
publication please contact Julien Delanoe" ;
}
```

RASTA microphysical product

Version 1.2 EPATAN DATA ACQUISITION REPORT

Variable	Dimension	unit	Comment
Dimensions			
time	time	h	Decimal hours UTC since midnight
range	range (250)	km	Range from the radar to the centre of each range gate
height	height (500)	km	Altitude above and below the aircraft have been concatenated
height_2D	time, height	km	Altitude above and below the aircraft have been concatenated as a function of time 0:249 below the aircraft toward the aircraft 250:499 above the aircraft toward the sky
Aircraft position and in-situ from SAFIRE file (B. Piguet)			
latitude	time	degree	Latitude of the aircraft, from Global Positioning System (GPS)
longitude	time	degree	Longitude of the aircraft, from Global Positioning System (GPS)
altitude	time	km	Altitude of the aircraft above geoid, from Global Positioning System (GPS)
pitch	time	degree	Aircraft pitch angle, from Inertial Navigation System (INS): positive when the aircraft nose is up
roll	time	degree	Aircraft roll angle, from Inertial Navigation System (INS): positive when the starboard wing is down
drift	time	degree	Aircraft drift angle, from Inertial Navigation System (INS): positive if track is more clockwise than heading
heading	time	degree	Aircraft heading angle, from Inertial Navigation System (INS): relative to geographical North, positive clockwise
track	time	degree	Aircraft track angle, from Inertial Navigation System (INS): relative to geographical North, positive clockwise, track = heading + drift
aircraft_vh	time	m s-1	Aircraft horizontal speed

Version 1.2 EPATAN DATA ACQUISITION REPORT

Variable	Dimension	unit	Comment
aircraft_vz	time	m s-1	Aircraft vertical speed
pressure	time	hPa	Pressure at flight level
temperature	time	degree C	Temperature at flight level
relative_humidity	time	%	Relative Humidity at flight level
eastward_wind	time	m s-1	In-situ Eastward Wind Component (positive when westerly)
northward_wind	time	m s-1	In-situ Northward Wind Component (positive when southerly)
u_wind	time	m s-1	Along track Wind Component
v_wind	time	m s-1	Cross track Wind Component
w_wind	time	m s-1	Vertical Wind Component (positive when upward)
u_wind_fuselage	time	m s-1	Along fuselage Wind Component
v_wind_fuselage	time	m s-1	Cross fuselage Wind Component
proj_insitu_wind_speed	time	m s-1	Projected in-situ wind speed along the nadir radial
land_water_flag	time	none	0 means Land, 1 means Water Derived from Very High Resolution land/sea tag map with distance from land, Naval Oceanographic Office (NAVOCEANO) 2007-06-28
RADAR measurements	Upward antennas are collocated with Zenith grid Downward antennas are collocated with Nadir grid Vertical: Nadir and Zenith Backward: Down and Up Transverse: Down and Up		
Z_vertical	time, height	dBZ	Radar reflectivity factor from Nadir and Zenith antennas
v_vertical	time, height	m s-1	Doppler velocity from Nadir and Zenith antennas (positive when target moves away from the radar)
R_vertical	time, height	m	Range from aircraft (Nadir and Zenith)
Z_L1_vertical	time, height	dBZ	L1 Radar reflectivity factor from Nadir and Zenith antennas
latitude_vertical	time, height	degree	Latitude of Nadir and Zenith data

Version 1.2 EPATAN DATA ACQUISITION REPORT

Variable	Dimension	unit	Comment
longitude_vertical	time, height	degree	Longitude of Nadir and Zenith data
Z_backward	time, height	dBZ	Radar reflectivity factor from Down and Up Backward antennas
v_backward	time, height	m s-1	Doppler velocity from the Down and Up Backward antennas (positive when target moves away from the radar)
R_backward	time, height	m	Range from aircraft (Down and Up Backward)
Z_L1_backward	time, height	dBZ	L1 Radar reflectivity factor from Down and Up Backward antennas
latitude_backward	time, height	degree	Latitude of Down and Up Backward data
longitude_backward	time, height	degree	Longitude of Down and Up Backward data
distance_vertical_backward	time, height	km	Distance between vertical and backward gates
Z_transverse	time, height	dBZ	Radar reflectivity factor from Down and Up Transverse antennas
v_transverse	time, height	m s-1	Doppler velocity from Down and Up Transverse antennas (positive when target moves away from the radar)
R_transverse	time, height	m	Range from aircraft (Down and Up Transverse)
Z_L1_transverse	time, height	dBZ	L1 Radar reflectivity factor from Down and Up Transverse antennas
latitude_transverse	time, height	degree	Latitude of Down and Up Transverse data
longitude_transverse	time, height	degree	Longitude of Down and Up Transverse data
distance_vertical_transverse	time, height	km	Distance between vertical and transverse gates
azimuth_east_vertical	time, height	degree	Azimuth angle of Nadir and Zenith antenna beams with respect to the right wing (positive counterclockwise)
elevation_hor_vertical	time, height	degree	Elevation angle of Nadir and Zenith antenna beams with respect to the aircraft horizontal plane (positive when above aircraft)

Version 1.2 EPATAN DATA ACQUISITION REPORT

Variable	Dimension	unit	Comment
azimuth_east_backward	time, height	degree	Azimuth angle of Down and Up Backward antenna beams with respect to the right wing (positive counterclockwise)
elevation_hor_backward	time, height	degree	Elevation angle of Down and Up Backward antenna beams with respect to the aircraft horizontal plane (positive when above aircraft)
azimuth_east_transverse	time, height	degree	Azimuth angle of Down and Up Transverse antenna beams with respect to the right wing (positive counterclockwise)
elevation_hor_transverse	time, height	degree	Elevation angle of Up and Down Transverse antenna beams with respect to the aircraft horizontal plane (positive when above aircraft)
Geophysical parameters WIND	WIND and masks 0:249 below the aircraft toward the aircraft 250:499 above the aircraft toward the sky		
Z	time, height	dBZ	Radar reflectivity (vertical, above and below the aircraft)
Vx	time, height	m s-1	Horizontal component of the retrieved 3D wind, along track
Vy	time, height	m s-1	Horizontal component of the retrieved 3D wind, cross track
Vz	time, height	m s-1	Vertical component of the retrieved 3D wind
VE	time, height	m s-1	Eastward Wind component of the retrieved 3D wind
VN	time, height	m s-1	Northward Wind component of the retrieved 3D wind
Mask_domain	time, height		This mask identifies the valid data above and below the aircraft (1:down/2:down and nadir only/3:up/4:up but zenith only)
altitude_melting	time, height	km	Altitude of the melting layer (derived from Z and V)
convective_index	time		Convective index (0:stratiform/1:convective)

Version 1.2 EPATAN DATA ACQUISITION REPORT

Variable	Dimension	unit	Comment
Mask_wind	time, height		This mask identifies areas where wind retrieval is expected to be bad, good confidence when $\text{abs}(\text{roll}) < 10$ deg. (1: confident /2: less confident upper domain /3: less confident lower domain)
Mask_Vx	time, height		Mask for the Vx component of the wind 1: good confidence /2: should not be used
Mask_Vy	time, height		Mask for the Vy component of the wind 1: good confidence /2: should not be used
Mask_Vz	time, height		Mask for the Vz component of the wind 1: good confidence /2: should not be used /3: could be used but carefully
attenuation_phase_flag	time, height		Attenuation and Phase flag 0: no cloud / 1: ice / 2: rain / 3: ice but likely attenuated / 4: ground / 5: ghost ground / 6: interpolated
Gaseous_twowayatt	time, height	dBZ	Two way attenuation, From Liebe at 95GHz
Pressure_field	time, height	hPa	
Temperature_field	time, height	degree C	
Vx_error	time, height		Error in Vx, Horizontal component of the retrieved 3D wind
Vy_error	time, height		Error in Vy, Horizontal component of the retrieved 3D wind
Vz_error	time, height		Error in Vz, Horizontal component of the retrieved 3D wind
RainRate	time, height	mm/h	Similar to CloudSat basic retrieval using attenuation below the melting layer - Matrosov et al 2007
Inputs of the retrieval of the Geophysical parameters (Radonvar)	0:249 below the aircraft toward the aircraft 250:499 above the aircraft toward the sky		

Version 1.2 EPATAN DATA ACQUISITION REPORT

Variable	Dimension	unit	Comment
T_in	time, height	degree C	Input temperature (used in the algorithm)
Z_in	time, height	dBZ	Input radar reflectivity
V_in	time, height	m s-1	Input vertical velocity
Geophysical parameters (Radonvar)	Microphysical and vertical air motion products 0:249 below the aircraft toward the aircraft 250:499 above the aircraft toward the sky		
w_ret	time, height	m s-1	Retrieved Vertical Wind Component (positive when upward)
iwc_ret	time, height	g m-3	Retrieved Ice water content
iwc_IWC_Z_T	time, height	g m-3	Retrieved Ice water content using IWC-Z-T relationship
Dm_ret	time, height	m	Retrieved Mean volume weighted diameter
N0_ret	time, height	m-4	Retrieved Intercept parameter of the normalised PSD
extinction_ret	time, height	m-1	Retrieved visible extinction
re_ret	time, height	m	Retrieved effective radius
Nt_ret	time, height	# m-3	Retrieved total number concentration
Z_fwd	time, height	mm6m-3	Forward modelled reflectivity
Z_noatt_fwd	time, height	mm6m-3	Forward modelled reflectivity corrected from attenuation
V_fwd	time, height	m s-1	Forward modelled vertical velocity
Z_Xband	time, height	dBZ	Simulated X band Radar reflectivity. Derived using microphysical parameterization and radonvar
Error and control parameters Geophysical parameters (Radonvar)	Microphysical and vertical air motion products 0:249 below the aircraft toward the aircraft 250:499 above the aircraft toward the sky		
error_v	time, height		
error_lnz	time, height		ln(z) error

Version 1.2 EPATAN DATA ACQUISITION REPORT

Variable	Dimension	unit	Comment
lniwc_error	time, height		fractional error in IWC (lniwc error)
w_error	time, height		error in w
lniwc_apriori	time, height		ln(iwc) apriori from IWC-Z-T relationship
error_lniwc_apriori	time, height		ln(iwc) apriori error
Jd	time, niter		cost function below the aircraft
Ju	time, niter		cost function above the aircraft
ijd	time		index of the min cost function below the aircraft
iju	time		index of the min cost function above the aircraft

Example of global attributes:

```

:Description = "95GHz Cloud Radar (RASTA) - Microphysics and Wind DATA" ;
:frequency = "95.04 GHz" ;
:peak_power = "1.8 kW" ;
:pulse_width = "0.4 us" ;
:ambiguous_distance = "15 km" ;
:pulse_repetition_frequency = "PRF=25kHz" ;
:beamwidth = "0.7 degrees" ;
:range_resolution = "60 m" ;
:reflectivity = "not corrected for attenuation, calibrated following Li & al
(2005,J.Atmos.Oceanic.Tech.)" ;
:doppler_velocity = "corrected for aircraft motion and folding" ;
:real_time_processing = "Pulse Pair Technique" ;
:flight = "21" ;
:day = "DDMMYEAR" ;
:campaign = "XXX" ;
:year = "2014" ;
:experiment = "XXXX" ;
:airport_latitude = XX;
:airport_longitude = XX ;
:contact = "contact email: julien.delanoe@latmos.ipsl.fr" ;
:created = "YEAR-MM-DD" ;
:data_policy = "If you intend to use these data for any communication or publication
please contact Julien Delanoe" ;

```

RASTA Spectral product

Version 1.2 EPATAN DATA ACQUISITION REPORT

File size and format:

~290Mo, 1min file, for size sake

Algorithms:

- wind retrieval
- FFT processing
- Pulse pair processing

File name: spectral_analysis_YYYY_MM_DD_hh_min.nc

3 dimensions: range = 250, time = (79 currently), shot = 2048

Name	dimensions	units	comments
time	time	s	second UTC since midnight
range	range	km	Range from the radar to the centre of each range gate
vbin	shot	s	FFT spectrum velocity bins
height_2D	time, range	km	Altitude of the centre of each range gate
latitude	time	degrees north	Latitude of the aircraft from Global Positioning System (GPS)
longitude	time	degrees east	Longitude of the aircraft from Global Positioning System (GPS)
altitude	time	km	Height of the aircraft above geoid
pitch	time	degrees	Aircraft pitch angle, From Inertial Navigation System (INS): positive when the aircraft nose is up
roll	time	degrees	Aircraft roll angle, From Inertial Navigation System (INS): positive when the starboard wing is down
drift	time	degrees	Aircraft drift angle, From Inertial Navigation System (INS): positive if track is more clockwise than heading
heading	time	degrees	Aircraft heading angle, From Inertial Navigation System (INS): relative to geographical North, positive clockwise
track	time	degrees	Aircraft track angle, From Inertial Navigation System (INS): relative to geographical North, positive clockwise, track = heading + drift
aircraft_vh	time	m s-1	Aircraft horizontal speed, from Global Positioning System (GPS)
aircraft_vz	time	m s-1	Aircraft vertical speed, from Global Positioning System (GPS)
azimuth_east	time	degrees	Azimuth angle of Nadir antenna beam
elevation_hor	time	degrees	Elevation angle of Nadir antenna beam
Data_longitude	time, range	degrees	Longitude of the data
Data_latitude	time, range	degrees	Latitude of the data
I	time, range, shot		raw radar data from nadir antenna: I data, I data, I + jQ
Q	time, range, shot		raw radar data from nadir antenna: Q data, I data, I + jQ
Temperature_field_ERAI	time, range	deg C	Co-located temperature from ECMWF reanalysis ERAI
Pressure_field_ERAI	time, range	hPa	Co-located pressure from ECMWF reanalysis ERAI
RH_field_ERAI	time, range	percent	Co-located relative humidity from ECMWF reanalysis ERAI
Gaseous_twowayatt_ERAI	time, range	dB	Gaseous two way attenuation, from Liebe at 95GHz and computed from ERAI-ECMWF
attenuation_phase_flag	time, range	none	Attenuation and phase flag, 0: no cloud / 1: ice / 2: rain / 3: ice but likely attenuated / 4: ground / 5: ghost ground / 6: interpolated / 7: ice retrieval should not be used

Version 1.2 EPATAN DATA ACQUISITION REPORT

land_water_flag	time	none	0 means Land, 1 means Water Derived from Very High Resolution land/sea tag map with distance from land, Naval Oceanographic Office (NAVOCEANO) 2007-06-28
Z	time, range	dBZ	95GHz Radar reflectivity factor from Nadir antenna (calculated on board). Produced using the Pulse-Pair Processing (calculated on board). Range-corrected and calibrated
V	time, range	m s-1	Doppler velocity from Nadir antenna (positive when target moves away from the radar) - corrected for aircraft motion and folding, Produced using the Pulse-Pair Processing. Counted positive when target moves away from radar
VN	time, range	m s-1	VN, Northward Wind component of the retrieved 3D wind – combination of Nadir, backward and transverse antennas Doppler measurements
VE	time, range	m s-1	VE, Eastward Wind component of the retrieved 3D wind – combination of Nadir, backward and transverse antennas Doppler measurements
Vspeed	time, range	m s-1	Horizontal wind module of the retrieved 3D wind – combination of Nadir, backward and transverse antennas Doppler measurements
Vdir	time, range	degrees	Horizontal wind direction of the retrieved 3D wind – combination of Nadir, backward and transverse antennas Doppler measurements
Vz	time, range	m s-1	Vz, Vertical component of the retrieved 3D wind– combination of Nadir, backward and transverse antennas Doppler measurements - Vz, positive upward
V_pp	time, range	m s-1	Doppler velocity from Nadir and Zenith antennas - PP post-processed using I and Q - (positive when target moves away from the radar) - not corrected for aircraft motion and folding. Produced using the Pulse-Pair Processing. Counted negative when target moves away from radar
Z_pp	time, range	dBZ	95GHz Radar reflectivity factor from Nadir antenna (post-processed using I and Q) - Produced using the Pulse-Pair Processing (post-processed using I and Q). Range-corrected and calibrated
V_fft	time, range	m s-1	Doppler velocity from Nadir and Zenith antennas - FFT post-processed using I and Q - (positive when target moves away from the radar) - not corrected for aircraft motion and folding. Produced using FFT Processing. Counted negative when target moves away from radar
Z_fft	time, range	dBZ	95GHz Radar reflectivity factor from Nadir antenna (FFT post-processed using I and Q),
sw_fft	time, range	m s-1	Spectral width, produced using the FFT Processing (post-processed using I and Q)
fft_spectrum	time, range, shot	none	Doppler spectrum - calibrated but not range corrected, use vbin to know the velocity distribution

Example of global attributes

- **description = "Cloud Radar data (RASTA)"**
- **frequency = "95.04 GHz"**
- **peak_power = "1.8 kW"**
- **pulse_width = "0.4 us"**
- **ambiguous_distance = "15 km"**
- **pulse_repetition_frequency = "PRF=25kHz"**
- **beamwidth = "0.7 degrees"**
- **range_resolution = "60 m"**
- **airport_latitude = 63.9986277778**
- **airport_longitude = -22.5663472222**

Version 1.2 EPATAN DATA ACQUISITION REPORT

- **experiment = "NAWDEX EPATAN (29/09/16-16/10/12), Airport: Keflavik"**
- **flight = "6"**
- **day = "20161002" ;**
- **contact = "contact email: julien.delanoe@latmos.ipsl.fr" ;**
- **created = "2017-05-01" ;**
- **data_policy = "EPATAN project: If you intend to use these data for any communication or publication please contact Julien Delanoe"**

Level 1 LNG file

LNG_HSRL_L1_NAWDEX_YYYYMMDD_Flightnumber.nc

Short description:

This file contains aircraft position, lidar measurements (backscatter, Doppler, depolarization ratio and errors), additional information on the instrument and atmospheric 2D fields from ERAI (P, T). Lidar attenuated backscatter is calibrated and range corrected. Position (altitude, longitude, latitude) of each lidar gate is available.

Level 0 LNG measurements are:

Total attenuated signal from the 1064nm channel

Total attenuated signal from the 532nm channel

From the 355nm channel:

- Perpendicular signal (attenuated)
- Parallel particular signal (HSRL / attenuated)
- Parallel molecular signal (HSRL / attenuated)
- Doppler Velocity (HSRL)

Current version:

The profiles are defined in range coordinates (i.e. with the distance from the aircraft on the line of sight of the lidar beam).

The 4 channels (532, 1064, 355parallel and 355cross) are calibrated over aerosol and cloud free regions, with respects to a model of molecular backscatter and depolarization.

The pointing angle of the lidar antenna was refined to correct from the bias observed in the Doppler compared to the radar measurements.

File size and format:

netCDF file

~400Mo for one flight

time resolution ~ 5s

range = 6m

Name	dimensions	units	comments
Time	Dimensions	time	seconds UTC
Range	height	seconds UTC	Seconds UTC since midnight
Latitude	time	degrees north	Range from the lidar to the center of each gate
			Latitude of the aircraft from Global Positioning System (GPS)

Version 1.2 EPATAN DATA ACQUISITION REPORT

Longitude	time	degrees east	Longitude of the aircraft from Global Positioning System (GPS)
Aircraft_Altitude	time	degrees	Altitude of the aircraft above geoid
Aircraft_Pitch	time	degrees	Pitch angle of the aircraft
Aircraft_Roll	time	degrees	Roll angle of the aircraft
Aircraft_Heading	time	degrees	Heading angle of the aircraft
Aircraft_Track	time	degrees	Track angle of the aircraft
LNG_Lidar_Wavelength	wavelengths	nm	
LNG_Lidar_Telescope_Field_Of_View	wavelengths	nm	
LNG_Lidar_Beam_Divergence	wavelengths	nm	
LNG_elev_hor	time	degrees	Elevation angle of LNG beam with respect to the horizontal, positive when pointing upward
LNG_azim_east	time	degrees	Azimuth angle of LNG beam with respect to the East, positive when pointing northward
HSR_Offset_Radial_Wind	time	m/s	Offset of the radial wind due to the speed of the aircraft
Energy_532_channel	time	mJ	
Energy_1064_channel	time	mJ	
Energy_355_channel	time	mJ	
Height	time, height	km	Altitude of the lidar gates
LNG_DLAt	time, height	degrees north	Latitude of the lidar gates
LNG_DLon	time, height	degrees east	Longitude of the lidar gates
LNG_UpDown	time, height	AU	Pointing of the antenna: 1=down / 2=up / 3=ADM
raw_HSR_Signal_1064	time, height	AU	Uncalibrated signal detected on the 1064 channel
raw_Signal_1064_error	time, height	AU	Detection noise
raw_HSR_Signal_532	time, height	AU	Uncalibrated signal detected on the 532 channel
raw_Signal_532_error	time, height	AU	Detection noise
raw_HSR_Signal_355_perpendicular	time, height	AU	Uncalibrated signal detected on the 355-perpendicular channel
raw_Signal_355_perpendicular_error	time, height	AU	Detection noise
raw_HSR_Signal_355_parallel	time, height	AU	Uncalibrated signal detected on the 355-parallel channel
raw_Signal_355_parallel_error	time, height	AU	Detection noise
raw_HSR_Particular_Signal_355_parallel	time, height	AU	Uncalibrated signal from aerosols and clouds (output from the interferometer)
raw_Particular_Signal_355_parallel_error	time, height	AU	Detection noise and standard error due to the HSRL processing
raw_HSR_Molecular_Signal_355_parallel	time, height	AU	Uncalibrated signal from molecules (output from the interferometer)

Version 1.2 EPATAN DATA ACQUISITION REPORT

raw_Molecular_Signal_355_parallel_error	time, height	AU	Detection noise and standard error due to the HSRL processing
HSR_PBR	time, height	AU	Interference contrast due to the atmosphere - corresponds to the particular to total backscatter ratio
HSR_Doppler	time, height	m/s	Uncorrected Doppler measurement clouds (output from the interferometer)
HSR_Doppler_Error	time, height	m/s	Doppler standard error (from HSRL processing)
Temperature	time, height	K	Temperature field (from ERAI)
Pressure	time, height	Pa	Pressure field (from ERAI)
Model_Molecular_Backscatter_532	time, height	m-1.sr-1	
Model_Molecular_Backscatter_1064	time, height	m-1.sr-1	
Model_Molecular_Backscatter_355	time, height	m-1.sr-1	
Model_Molecular_Extinction_532	time, height	m-1	
Model_Molecular_Extinction_1064	time, height	m-1	
Model_Molecular_Extinction_355	time, height	m-1	
Model_Molecular_Attenuation_532	time, height	AU	
Model_Molecular_Attenuation_1054	time, height	AU	
Model_Molecular_Attenuation_355	time, height	AU	
LNG_calibration_constant_532	time, height	AU	a mean normalisation constant is determined using a modelled molecular signal for each profile provided a clear sky area (500m) below the aircraft can be found
LNG_calibration_constant_1064	time, height	AU	
LNG_calibration_constant_355	time, height	AU	Calibration constant for the parallel channel
LNG_calibration_constant_532_relative_error	time, height	%	relative standard deviation determined for every profile depending on the quality of the calibration
LNG_calibration_constant_1064_relative_error	time, height	%	
LNG_calibration_constant_355_relative_error	time, height	%	
LNG_calibration_constant_532_distance	time, height	km	distance from the aircraft where the calibration constant is determined
LNG_calibration_constant_1064_distance	time, height	km	
LNG_calibration_constant_355_distance	time, height	km	
LNG_raw_measured_molecular_depolarization	time, height	AU	
LNG_raw_measured_molecular_depolarization_relative_error	time, height	%	
LNG_Total_Attenuated_Backscatter_532	time, height	m-1.sr-1	

Version 1.2 EPATAN DATA ACQUISITION REPORT

LNG_Total_Attenuated_Backscatter_532_Error	time, height	m-1.sr-1	Statistical error
LNG_Total_Attenuated_Backscatter_1064	time, height	m-1.sr-1	
LNG_Total_Attenuated_Backscatter_1064_Error	time, height	m-1.sr-1	Statistical error
LNG_Total_Attenuated_Backscatter_355	time, height	m-1.sr-1	
LNG_Total_Attenuated_Backscatter_355_Error	time, height	m-1.sr-1	Statistical error
LNG_Parallel_Attenuated_Backscatter_355	time, height	m-1.sr-1	
LNG_Parallel_Attenuated_Backscatter_355_Error	time, height	m-1.sr-1	Statistical error
LNG_Perpendicular_Attenuated_Backscatter_355	time, height	m-1.sr-1	
LNG_Perpendicular_Attenuated_Backscatter_355_Error	time, height	m-1.sr-1	Statistical error
LNG_Molecular_Attenuated_Backscatter_355	time, height	m-1.sr-1	
LNG_Molecular_Attenuated_Backscatter_355_Error	time, height	m-1.sr-1	Statistical error
LNG_Particular_Attenuated_Backscatter_355	time, height	m-1.sr-1	
LNG_Particular_Attenuated_Backscatter_355_Error	time, height	m-1.sr-1	Statistical error
LNG_Depolarization_Ratio_355	time, height	AU	Volumic depolarization ratio at 355nm
LNG_Depolarization_Ratio_355_Error	time, height	AU	Statistical error
LNG_Particular_Depolarization_Ratio_355	time, height	AU	Aerosol/clouds depolarization ratio at 355nm
LNG_Particular_Depolarization_Ratio_355_Error	time, height	AU	Statistical error
LNG_Parallel_Backscatter_Ratio_355	time, height	AU	Lidar parallel backscatter ratio (Parallel Backscatter / Molecular Parallel Backscatter) at 355nm
LNG_Backscatter_Ratio_355	time, height	AU	Lidar backscatter ratio (Total Backscatter / Molecular Backscatter) at 355nm
LNG_LOS_Doppler_Velocity	time, height	m/s	Lidar line of sight doppler measurement corrected from aircraft motion
Mask_Signal_532	time, height	AU	1= Signal (cloud/ground) / 0= Clear sky or noise
Mask_Signal_1064	time, height	AU	
Mask_Signal_355	time, height	AU	
Mask_Signal_Molecular	time, height	AU	1= Signal (atmospheric) / 0= noise
Saturated_Shots_355_channel	time, height	AU	Ratio of saturated shots (over the 100 averaged for one profile)
LNG_Misalignment_532	time	AU	0= OK / 1= the gradient in altitude of the molecular signal does not match with the model / 2= misalignment

Version 1.2 EPATAN DATA ACQUISITION REPORT

			suspected (visible on the UV channel) / 3= both
LNG_Misalignment_355	time	AU	
LNG_Quality_Calib_532	time	AU	Quality of the calibration - 0= good: average of 500m of clear sky measurement / 1= OK: no clear sky available for calibration - linear interpolation using the 20 nearest good profiles / 2= Higher uncertainty: average value on the ongoing leg / 3= Not so good: the reference calibration area was used
LNG_Quality_Calib_1064	time	AU	
LNG_Quality_Calib_355	time	AU	
LNG_Overlap_532	time, height	AU	Size of the overlap region
LNG_Overlap_1064	time, height	AU	
LNG_Overlap_355	time, height	AU	

File Description for MIRA36

typedef netCDF //netCDF data format

YYYYMMDD_hhmm.mmclx {

dimensions:

time = UNLIMITED ; // (25078 currently)

range = 487 ;

variables:

[...]

float SNRg(time, range) ;

SNRg:long_name = "Reflectivity SNRg" ;

SNRg:units = " " ;

Version 1.2 EPATAN DATA ACQUISITION REPORT

```
SNRg:yrange = -22.90047f, 70.f ;
SNRg:db = 1s ;
float VELg(time, range) ;
  VELg:long_name = "Doppler Velocity VELg" ;
  VELg:units = "m/s" ;
  VELg:yrange = -12.66761f, 12.66761f ;
  VELg:db = 0s ;
float RMSg(time, range) ;
  RMSg:long_name = "Peak Width RMSg" ;
  RMSg:units = "m/s" ;
  RMSg:yrange = 0.f, 3.f ;
  RMSg:db = 0s ;
float LDRg(time, range) ;
  LDRg:long_name = "Linear De-Polarization Ratio LDRg" ;
  LDRg:units = " " ;
  LDRg:yrange = -35.f, 5.f ;
  LDRg:db = 1s ;
float SNRCx(time, range) ;
  SNRCx:long_name = "Reflectivity SNR Cx-Channel" ;
  SNRCx:units = " " ;
  SNRCx:yrange = -35.f, 70.f ;
  SNRCx:db = 1s ;
float Ze(time, range) ;
  Ze:long_name = "Equivalent Radar Reflectivity Factor Ze of Hydrometeors" ;
  Ze:units = "Z" ;
  Ze:yrange = -60.f, 30.f ;
  Ze:db = 1s ;
float Zg(time, range) ;
  Zg:long_name = "Equivalent Radar Reflectivity Factor Ze of all Targets" ;
  Zg:units = "Z" ;
  Zg:yrange = -60.f, 30.f ;
  Zg:db = 1s ;
float RadarConst(time) ;
  RadarConst:long_name = "Radar Constant related to 5 km Height, and 200 ns pulses. Z =
  SNR * RadarConst * (range/5 km)^2 * SNRCorFaCo. It changes slightly in time due to the
  measured transmit power" ;
  RadarConst:units = "Z" ;
  RadarConst:yrange = -35.f, -20.f ;
  RadarConst:db = 1s ;
```

File description for WALES

```
typedef netCDF //netCDF data format
YYYYMMDDhhmmss_ADLR_WVDIAL_BACKSC_D_V1.0.nc {
```

dimensions:

```
time = UNLIMITED ; // (18240 currently)
range = 859 ;
```

variables:

```
double time(time) ;
  time:long_name = "seconds since 1970-01-01 00:00:00 00:00 UTC" ;
  time:units = "seconds since 1970-01-01 00:00:00 00:00 UTC" ;
double time_resolution(time) ;
  time_resolution:long_name = "time resolutions" ;
  time_resolution:units = "s" ;
float height_above_sea_level(time) ;
  height_above_sea_level:long_name = "height_above_sea_level" ;
  height_above_sea_level:units = "m" ;
  height_above_sea_level:missing_value = -9.e+33f ;
```

Version 1.2 EPATAN DATA ACQUISITION REPORT

```
height_above_sea_level: FillValue = -9.e+33f ;  
float latitude(time) ;  
latitude:long_name = "latitude" ;  
latitude:units = "degree_north" ;  
latitude:standard_name = "latitude" ;  
float longitude(time) ;  
longitude:long_name = "longitude" ;  
longitude:units = "degree_east" ;  
longitude:standard_name = "longitude" ;  
float range(range) ;  
range:long_name = "range" ;  
range:units = "m" ;  
range:standard_name = "range" ;  
float range_resolution(time, range) ;  
range_resolution:long_name = "range_resolution" ;  
range_resolution:units = "m" ;  
range_resolution:standard_name = "vertical_resolution" ;  
float emission_wavelength ;  
emission_wavelength:long_name = "emission_wavelength" ;  
emission_wavelength:units = "nanometer" ;  
emission_wavelength:standard_name = "emission_wavelength" ;  
float instrument_elevation_angle(time) ;  
instrument_elevation_angle:long_name = "elevation" ;  
instrument_elevation_angle:units = "degree" ;  
instrument_elevation_angle:description = "elevation angle from  
-90 to +90 degrees" ;  
instrument_elevation_angle:missing_value = -9.e+33f ;  
instrument_elevation_angle:_FillValue = -9.e+33f ;  
float backscatter_due_to_aerosol(time, range) ;  
backscatter_due_to_aerosol:long_name = "backscatter  
coefficient at 532 nm" ;  
backscatter_due_to_aerosol:units = "m-1 sr-1" ;  
backscatter_due_to_aerosol:missing_value = -9.e+33f ;  
backscatter_due_to_aerosol:_FillValue = -9.e+33f ;
```

File Description for VARCLOUD Output on HALO**typedef netCDF** //netCDF data format

NAWDEX_RFXX_AYYMMDD_VARCLOUD_L2_HHMMSS_HHMMSS_V1_PYYYYMMDD.nc {

dimensions:**time** = UNLIMITED ; // (25078 currently)**height** = 867 ;**wvl** = 3 ;**iter** = 20 ;**variables:****double** **time**(time) ;

time:units = "s" ;

time:long_name = "UTC time" ;

float **latitude**(time) ;

latitude:units = "degree" ;

float **longitude**(time) ;

longitude:units = "degree" ;

float **height**(height) ;

height:units = "m" ;

float **lidar_wavelength**(wvl) ;

lidar_wavelength:units = "m" ;

float **N_coeff** ;**float** **A_ln_N_apriori** ;**float** **B_ln_N_apriori** ;**int** **smoothing** ;**int** **N_spacing** ;**int** **N_decorr_dist** ;**float** **a_ln_k_apriori** ;**float** **b_ln_k_apriori** ;**float** **ln_alpha_apriori** ;**float** **ln_alpha_first_guess** ;**float** **a_ln_k_apriori_error** ;**float** **b_ln_k_apriori_error** ;**float** **ln_alpha_apriori_error** ;**float** **ln_N_apriori_error** ;**float** **extinction**(time, height) ;

extinction:_FillValue = -999.f ;

extinction:units = "m-1" ;

float **N0star**(time, height) ;

N0star:_FillValue = -999.f ;

N0star:units = "m-4" ;

float **lidar_ratio**(time, height) ;

lidar_ratio:_FillValue = -999.f ;

lidar_ratio:units = "sr" ;

float **iwc**(time, height) ;

iwc:_FillValue = -999.f ;

iwc:units = "kg.m-3" ;

float **effective_radius**(time, height) ;

effective_radius:_FillValue = -999.f ;

effective_radius:units = "m" ;

float **error_ln_extinction**(time, height) ;

error_ln_extinction:_FillValue = -999.f ;

error_ln_extinction:units = "ln(m-1)" ;

float **error_ln_Nprime**(time, height) ;

error_ln_Nprime:_FillValue = -999.f ;

error_ln_Nprime:units = "ln(m-3)" ;

float **error_ln_lidar_ratio**(time, height) ;

error_ln_lidar_ratio:_FillValue = -999.f ;

error_ln_lidar_ratio:units = "ln(sr)" ;

float **error_ln_iwc**(time, height) ;

Version 1.2 EPATAN DATA ACQUISITION REPORT

```
error_ln_iwc: FillValue = -999.f ;
error_ln_iwc:units = "ln(kg.m-3)" ;
float error_ln_effective_radius(time, height) ;
error_ln_effective_radius: FillValue = -999.f ;
error_ln_effective_radius:units = "ln(m)" ;
float temperature(time, height) ;
temperature: FillValue = -999.f ;
temperature:units = "K" ;
float pressure(time, height) ;
pressure: FillValue = -999.f ;
pressure:units = "Pa" ;
float bscat_532_fwd(time, height) ;
bscat_532_fwd: FillValue = -999.f ;
bscat_532_fwd:units = "m-1.s-1" ;
float ln_bscat_532_fwd_error(time, height) ;
ln_bscat_532_fwd_error: FillValue = -999.f ;
ln_bscat_532_fwd_error:units = "ln(m-1.s-1)" ;
float bscat_1064_fwd(time, height) ;
bscat_1064_fwd: FillValue = -999.f ;
bscat_1064_fwd:units = "m-1.s-1" ;
float ln_bscat_1064_fwd_error(time, height) ;
ln_bscat_1064_fwd_error: FillValue = -999.f ;
ln_bscat_1064_fwd_error:units = "ln(m-1.s-1)" ;
float bscat_355_fwd(time, height) ;
bscat_355_fwd: FillValue = -999.f ;
bscat_355_fwd:units = "m-1.s-1" ;
float ln_bscat_355_fwd_error(time, height) ;
ln_bscat_355_fwd_error: FillValue = -999.f ;
ln_bscat_355_fwd_error:units = "ln(m-1.s-1)" ;
float bscat_mol_fwd(time, height) ;
bscat_mol_fwd: FillValue = -999.f ;
bscat_mol_fwd:units = "m-1.s-1" ;
float ln_bscat_mol_fwd_error(time, height) ;
ln_bscat_mol_fwd_error: FillValue = -999.f ;
ln_bscat_mol_fwd_error:units = "ln(m-1.s-1)" ;
float Z_fwd(time, height) ;
Z_fwd: FillValue = -999.f ;
Z_fwd:units = "dBZ" ;
float ln_Z_fwd_error(time, height) ;
ln_Z_fwd_error: FillValue = -999.f ;
ln_Z_fwd_error:units = "ln(mm6.m-3)" ;
int instrument_flag(time, height) ;
instrument_flag: FillValue = -999 ;
int iteration(time) ;
iteration: FillValue = -999 ;
float cost_function(time, phony_dim_4) ;
cost_function: FillValue = -999.f ;
float chi2(time, phony_dim_4) ;
chi2: FillValue = -999.f ;
float running_time(time) ;
running_time: FillValue = -999.f ;
running_time:units = "s" ;
```

// global attributes:

```
:Description = "Test varcloud Python - HALO" ;
>Date = "20170707" ;
:Convergence_test = "chi-squared" ;
:S_profile = "k: lidar ratio ; lnk = a + b*T" ;
:Running_time = "Total running time: 11296.4439712s" ;}
```

File Description for VARMASK Output on HALO

typedef netCDF //netCDF data format

NAWDEX_RFXX_AYYMMDD_VARMASK_L2_HHMMSS_HHMMSS_V1_PYYYYMMDD.nc {

dimensions:

time = UNLIMITED ; // (25078 currently)

height = 867 ;

variables:

double time(time) ;

time:units = "s" ;

time:long_name = "UTC time" ;

float latitude(time) ;

latitude:units = "degree" ;

float longitude(time) ;

longitude:units = "degree" ;

float height(height) ;

height:units = "m" ;

float lidar_wavelength(wvl) ;

lidar_wavelength:units = "m" ;

float Radar_Mask(time, height) ;

Radar_Mask: FillValue = -999.f ;

Radar_Mask:units = "None" ;

Radar_Mask:long_name = "Radar Mask (MIRA product)" ;

Radar_Mask:comments = "0: no cloud / 1: ice / 2: rain /

3: ice but likely attenuated / 4: ground / 5: ghost ground / 6: interpolated" ;

float Simplified_Categorization(time, height) ;

Simplified_Categorization: FillValue = -999.f ;

Simplified_Categorization:units = "None" ;

Simplified_Categorization:long_name = "Cloud Mask" ;

Simplified_Categorization:comments = "-2=presence of liquid unknown / -1=surface and subsurface / 0=clear sky / 1=ice clouds / 2=spherical or 2D ice / 3=supercooled water / 4=supercooled + ice / 5=cold rain / 6=aerosol / 7=warm rain / 8=stratospheric clouds / 9=highly concentrated ice / 10=top of convective towers / 11=liquid cloud / 12=warm rain + liquid clouds / 13=cold rain+ liquid clouds / 14=rain may be mixed with liquid / 15=Multiple scattering due to supercooled water" ;

float Aerosol_Liquid(time, height) ;

Aerosol_Liquid: FillValue = -999.f ;

Aerosol_Liquid:units = "None" ;

Aerosol_Liquid:long_name = "Aerosol/Liquid Mask" ;

Aerosol_Liquid:comments = "0=no data / 1=liquid / 4=aerosol / 9=don't know" ;

float Ice_Rain(time, height) ;

Ice_Rain: FillValue = -999.f ;

Ice_Rain:units = "None" ;

Ice_Rain:long_name = "Ice/Rain Mask" ;

Ice_Rain:comments = "0=ground / 1=no ice, no rain / 2=ice / 4=warm rain / 5=cold rain / 6=multiple scattering" ;

float Instruments_Mask(time, height) ;

Instruments_Mask: FillValue = -999.f ;

Instruments_Mask:units = "None" ;

Instruments_Mask:long_name = "Instruments available" ;

Instruments_Mask:comments = "1-3:no radar and number of lidar available channels / 4: radar only / 5-7: radar + 1 to 3 lidar wavelengths" ;

float Target_Lidar_532_Mask(time, height) ;

Target_Lidar_532_Mask: FillValue = -999.f ;

Target_Lidar_532_Mask:units = "None" ;

Target_Lidar_532_Mask:long_name = "Target_Lidar_532_Mask" ;

Target_Lidar_532_Mask:comments = "-2=extinguished / -1=attenuated / 5=ground / 0=no data or clear sky / 1=cloud" ;

float Target_Lidar_1064_Mask(time, height) ;

Target_Lidar_1064_Mask: FillValue = -999.f ;

Version 1.2 EPATAN DATA ACQUISITION REPORT

```
Target_Lidar_1064_Mask:units = "None" ;  
Target_Lidar_1064_Mask:long_name = "Target_Lidar_1064_Mask" ;  
Target_Lidar_1064_Mask:comments = "-2=extinguished / -1=attenuated / 5=ground / 0=no data or  
clear sky / 1=cloud" ;
```

```
float Target_Lidar_Part_Mask(time, height) ;
```

```
Target_Lidar_Part_Mask:FillValue = -999.f ;  
Target_Lidar_Part_Mask:units = "None" ;  
Target_Lidar_Part_Mask:long_name = "Target_Lidar_Part_Mask" ;  
Target_Lidar_Part_Mask:comments = "-2=extinguished / -1=attenuated / 5=ground / 0=no data or  
clear sky / 1=cloud" ;
```

```
float Target_Lidar_Mol_Mask(time, height) ;
```

```
Target_Lidar_Mol_Mask:FillValue = -999.f ;  
Target_Lidar_Mol_Mask:units = "None" ;  
Target_Lidar_Mol_Mask:long_name = "Target_Lidar_Mol_Mask" ;  
Target_Lidar_Mol_Mask:comments = "-2=extinguished / -1=attenuated / 5=ground / 0=no data /  
1=signal" ;
```

// global attributes:

```
:Description = "HALO VARMAK Classification" ;  
:created = "20180201" ;  
:Author = "florian.ewald@dlr.de" ;  
:Campaign = "NAWDEX" ;  
:Day = "20161015" ;  
:Flight = "12" ;  
:Airport_Latitude = 63.9986277778 ;  
:Airport_Longitude = -22.5663472222 ;  
:Time_grid = "Lidar" ;  
:Height_grid = "Lidar" ;  
:Reference_Altitude = "altitude of the aircraft" ;  
:Time_colocation_method = "closest profile" ;  
:Height_colocation_method = "closest" ;  
:Categorization = "Cloud categorization using radar and lidar 532nm channel" ;  
:Lidar_Masks_Methods = "Filtering methods for the attenuated backscatter at 532nm: from WALES  
L1 file: using thresholds on raw signal and relative error ; 1064nm: from WALES L1 file:  
using thresholds on raw signal and relative error" ;}
```